UNIVERSITÀ
DEGLI STUDI
DI PADOVA

Head Office: Università degli Studi di Padova

Department of Geosciences

Ph.D. COURSE IN: EARTH SCIENCES
SERIES XXXI

THE CARNIAN (LATE TRIASSIC) EXTREME CLIMATE EVENT: COMPARISON OF THE ITALIAN TETHYS AND SOUTH CHINA GEOLOGICAL RECORDS

Thesis written with the financial contribution of China Scholarship Council (grant number 201508510096)

Coordinator: Ch. mo Prof. Claudia Agnini
Supervisor: Ch. mo Prof. Nereo Preto
Co-Supervisor: Ch. mo Prof. Piero Gianolla

Ph.D. student: Xin Jin

CONTENTS

ACKNOWLEDGMENTS

The first time I met my supervisor Prof. Nereo Preto and co-supervisor Prof. Piero Gianolla (University of Ferrara) was in the summer of 2012 in Chengdu. I was inspired and benefited from their guidance when we were in the field for investigating the Carnian Pluvial Episode (CPE) in the northwestern Sichuan Basin. Since then, we have been studying the CPE. Here, I would like to thank these two professors who gave their guidance, constructive discussion, critical comments and reviews during my PhD project.

I would like to express my most sincere thanks to Prof. Zhiqiang Shi (Chengdu University of Technology) who organized the field work and provided samples for my PhD project. I also deeply appreciate my co- collaborators who gave much help to contribute to the present work: Prof. Paolo Mietto, Prof. Christopher A. McRoberts (State University of New York at Cortland), Prof. Manuel Rigo, Dr. Guido Roghi (CNR), Dr. Marco Franceschi, Dr. Marcello Caggiati (University of Ferrara). And I would like to thank Dr. Anna Breda, Dr. Giuseppa Forte, Yixing Du for their support and help during my PhD programs.

I would like to thank Prof. Claudia Agnini, Prof. Andrea D'alpaos, Prof. Nicola Surian who interviewed and gave me an opportunity to study in the Department of Geoscience, University of Padova. I would like to thank Prof. Fabrizio Nestola and Prof. Claudia Agnini who arranged my PhD courses and activities. I would like to thank Prof. Cristina Stefani, the Director of the Department of Geoscience, who gave me many support when I was applying my research funds. Many thanks also go to Dr. Luca Peruzzo (CNR), Dr. Mr. Stefano Castelli, Mr. Leonardo Tauro and Mrs. Sandra Boesso for helping me to preparing my samples and giving me many assistance during my lab work.

Finally, I want to express my deep gratefulness to my wife Xueqin Yan who gave me her utmost support and concern during my three-year study in Italy. I am also much grateful to her for giving me newborn daughter Yumo Jin who brings many happiness to my family. I will love you forever. I also want to express my deep gratefulness to my father Youhuai Jin, mother Xiliu Guo, my parents in law Nengwu Yan and Yunshu Li, and my little brother in law Yibin Yan, for their constant support and inspiration during my life in ltaly. I also want to express my thankfulness to all my relatives and friends in China for their attention and support.

ABSTRACT

As one of the most complex climate events in Triassic, the Carnian extreme climate event or Carnian Pluvial Episode (CPE) has been widely documented in the Tethyan regions. It occurred at the boundary of the two substages of the Carnian: Julian 1 and Julian 2. The CPE was mainly characterized by Tethys-wide humid climate associated with abundant terrigenous sediment and freshwater input to the shallow marine carbonate platforms. A contemporary crisis of carbonate production was recognized in the marginal sea in western Tethys. The CCD in Lagonegro Basin (southern Apennines, southern Italy) arose temporarily. A remarkable temperature was inferred from oxygen isotopes of conodont apatite during this interval. The onset of the CPE was found coincident with a major negative $\delta^{13}C$ perturbation recorded by bulk organic matter and n-alkanes. This was interpreted as a massive injection of CO_2 into the atmosphere-ocean system, possibly linked to the eruption of the large igneous province of Wrangellia. The CPE has been studied for decades in western Tethys, but much less data are available from other parts of Paleo-Tethys. In this thesis, I focused on the yet poorly investigated Sichuan Basin, which was located at the margin of South China Block in the eastern Tethys. We selected four stratigraphic sections encompassing the Carnian: Ma'antang (MAT), Qingyan Gou (HWQ), Guanyin Ya (HWG) and Jushui (JS) with the goal of determining their biostratigraphy and retrieving carbon and oxygen stable isotope record. Quantitative modal analysis was also carried out for comparing the carbonate facies of the Sichuan Basin with those from the Dolomites, northern Italy, that in the Carnian occupied a paleogeorgraphic position in the western Tethys. New diagnostic fossil findings were presented together with carbonate $\delta^{13}C$ and $\delta^{18}O$ records and organic carbon isotopes from bulk organic matters and woods from the MAT, HWQ, HWG and JS sections in northwestern Sichuan Basin. The late Carnian conodonts associations indicated that the demise of the hexactinellid sponge reef in Hanwang and Jushui areas was late Carnian in age. A late Carnian ammonoid association with tropitids was found at the boundary between carbonates and siliciclastics, overlain by late Carnian ammonoid associations. Along with ammonoids, the late Carnian bivalve *Halobia* cf. *H. septentrionalis* was found. These new biostratigraphic data suggested a late Carnian to early Norian age for the base of the siliciclastic succession, which was confirmed by the occurrence of the DKC and DLC palynological associations of Li and Wang (2016) in the HWQ and HWG sections. In light of this comprehensive biochronologic evidence, we concluded that major facies changes of the Upper Triassic of the Sichuan Basin should not be ascribed to the CPE. Moreover, the Carnian/Norian boundary interval was pinpointed in a short stratigraphic interval around 10 meters thick of the HWQ section in the Sichuan Basin. The carbon isotopic excursions recorded by bulk carbonate rock and microbial grains of the HWQ section were interpreted and discussed in the light of a petrographic evaluation of the diagenetic overprint. Smooth positive trends of carbon stable isotopes recorded by wood and bulk organic matter of the HWQ, HWG and JS sections implied that no isotopic excursion was present across the Carnian/Norian transition. The wood samples showed dispersed values, in agreement with the normal variability of isotopic composition of wood tissue. A strong negative isotopic perturbation of organic carbon isotopes at the MAT was dated by early Carnian ammonoid and conodont associations, and was comparable with other CPE records of South China. A quantitative petrological study was performed on carbonate microfacies of the MAT, HWQ and HWG sections from Sichuan Basin and sections of Southern Apls. The results revealed that the demise of microbial factories within CPE was not a local phenomenon, but interested the entire Tethy. The microbial carbonate platforms totally recovered between the latest Carnian to early Norian, both in western and eastern Tethys.

RIASSUNTO

Uno degli eventi climatici più complessi del Triassico è il Carnian Pluvial Episode (CPE), che si colloca nel Carnico inferiore ed è un periodo caratterizzato in Tetide da un clima umido e apporto di abbondanti sedimenti terrigeni e acqua dolce alle piattaforme carbonatiche. Contemporaneamente, una crisi della produzione di carbonati è stata riconosciuta in Tetide occidentale. La CCD è temporaneamente risalita nel Bacino di Lagonegro (Appennino meridionale). Un aumento della temperatura è stato dedotto dagli isotopi stabili dell'ossigeno nell'apatite dei conodonti. L'insorgenza del CPE coincide con una perturbazione negativa del $\delta^{13}C$ della materia organica e degli n-alcani. Ciò è stato interpretato come una iniezione di CO_2 nel sistema atmosfera-oceano, innescato dall'eruzione della provincia magmatica di Wrangellia. Il CPE è stato studiato a lungo nella Tetide occidentale, ma sono molti meno i dati disponibili da altre porzioni della Tetide, tra le quali il Bacino del Sichuan in Cina meridionale. Sono state selezionate quattro sezioni carniche in Sichuan: Ma'antang (MAT), Qingyan Gou (HWQ), Guanyin Ya (HWG) e Jushui (JS). Su queste è stato condotto uno studio biostratigrafico, degli isotopi stabili del carbonio e dell'ossigeno. L'analisi modale quantitativa delle microfacies carbonatiche ha permesso il confronto tra la produzione carbonatica del Bacino del Sichuan e del Sudalpino. Nuovi fossili diagnostici sono stati raccolti, e un nuovo record del $\delta^{13}C$ e $\delta^{18}O$ è stato ottenuto per le sezioni MAT, HWQ, HWG e JS. I conodonti indicano che la scomparsa delle biocostruzioni a spugne silicee in Sichuan avvenne nel Carnico superiore. Ammonoidi raccolti al limite tra carbonati e rocce silicoclastiche comprendono tropitidi, *Gonionotites* sp., *Griesbachites* sp., *Griesbachites* cf. *G. laevis*., *Guembelites philostrati*, *Thisbites* cf. *T. petralis*., *Hadrothisbites* n. sp. e il bivalve *Halobia* cf. *H. septentrionalis*. Questi suggeriscono una età da tardo-carnica a norica per la base della successione siliciclastica, che è confermata dalle associazioni palinologiche. Alla luce di questa biostratigrafia integrata, si deve concludere che i drastici cambiamenti di facies del Triassico Superiore del Bacino del Sichuan non vanno associati al CPE. Inoltre, il limite Carnico/Norico è stato individuato in un breve intervallo stratigrafico di circa 10 metri a HWQ. Le escursioni isotopiche del carbonio nel carbonato di HWQ sono interpretate e discusse alla luce di una valutazione petrografica della diagenesi. Al contrario dei dati ottenuti dalla roccia totale, il $\delta^{13}C$ di brachiopodi ben conservati, che rappresentano la composizione isotopica dell'acqua marina originale, non mostra oscillazioni. Il $\delta^{13}C$ di legno fossile e materia organica a HWQ, HWG e JS invece presenta un trend positivo, che si esaurisce prima del passaggio alle rocce silicoclastiche. Non è stata identificata alcuna escursione isotopica al limite Carnico-Norico. Il legno mostra valori dispersi del $\delta^{13}C$, in accordo con la normale variabilità della composizione isotopica di questo tessuto. Una pronunciata perturbazione isotopica negativa degli isotopi di carbonio organico a MAT è stata datata con ammonoidi e conodonti al Carnico inferiore, ed è paragonabile per età e struttura ad altri record del CPE della Cina meridionale. Infine, uno studio petrologico quantitativo è stato condotto sulle microfacies carbonatiche delle sezioni MAT, HWQ e HWG, e da sezioni delle Alpi Giulie nel nord Italia e Slovenia. I risultati rivelano che la scomparsa delle associazioni carbonatiche microbiali all'inizio del CPE ha interessato tutta la Tetide, non è stato influenzato dalle condizioni ambientali locali e dal contesto geologico o geodinamico. Le piattaforme carbonatiche microbiali si sono completamente riprese tra la fine del Carnico e il Norico basale, sia nella Tetide occidentale che orientale.

INTRODUCTION

The onset of this PhD project was in October 2015. This project was supported by a scholarship awarded by the China Scholarship Council (grant number 201508510096). The bulk rock samples and fossils from Chinese sections were mainly collected by Xin Jin and his supervisor Prof. Nereo Preto during their field work in Sichuan Basin, part of samples were collected and mailed by Prof. Zhiqiang Shi (Chengdu University of Technology). The field work in China were funded by Prof. Zhiqiang Shi from his the National Natural Science Foundation of China grants (grant numbers 41272131, 41572085). The samples from Dolomites were collected by Xin Jin, Prof. Nereo Preto, Prof. Piero Gianolla (Ferrara University), Dr. Marco Franceschi, and Dr. Marcello Caggiati (University of Ferrara). The field work in the Alps were funded by the PhD School of Earth Sciences of the University of Padova and by the research funds of Prof. Nereo Preto. All the analyses and lab work were carried out in the Department of Geoscience, Padova University. Some thin sections from Chinese sections were donated by Prof. Zhiqiang Shi, and part of thin sections from the Alps were courtesy of Dr. Marcello Caggiati and Prof. Piero Gianolla (Ferrara University).

Within this PhD, I performed stable isotopic analyses, petrological studies with Scanning Electron Microscope, Cathodoluminescence, and Binocular Polarized Microscope. I took part in all processes of fossil preparation and determination. The present thesis was supervised by Prof. Nereo Preto in the Department of Geoscience, Padova University.

Approximately 234 million years ago in the middle of the Carnian stage of the Upper Triassic, a climate event with global relevance occurred, termed Carnian Pluvial Episode (CPE) (Simms and Ruffell, 1989, 2018). It is widely reported in western Tethys and marked by a temporarily termination or crisis of shallow carbonate production, by humid weather and associated increased runoff and coarser clastic sediments into the marginal basins (Ogg, 2015; Ruffell *et al.*, 2016, and references therein). An episode of extinction coincides with a sharp negative shift of $\delta^{13}C$ from bulk organic matter and n-alkanes (e.g., Dal Corso *et al.*, 2012, 2015, 2018; Mueller *et al.*, 2016; Sun *et al.*, 2016; Miller *et al.*, 2017; Baranyi *et al.*, 2018; Shi *et al.*, 2018). While being one of most important parts of Paleo-Tethys, the Sichuan Basin of South China is still poorly understood. Therefore, this PhD thesis mainly focuses on the CPE in northwestern Sichuan Basin, and the comparisons with the CPE sections from the Alps.

The Carnian of the Sichuan Basin is comprised of a thick carbonate platform succession, from oolitic-bioclastic limestones to sponge reef mounds (Wu, 1989, Jin *et al.*, 2018a, b), which top is overlain by dark grey shales and marls with rich fossils. This sharp lithological transition was suggested to be related to the "CPE" in Sichuan Basin (Shi *et al.*, 2017). Due to the scarcity of available data, the reported "CPE" in Sichuan Basin is in need of re-examination. To this end,

comprehensive geological data from the Carnian of Sichuan Basin including ammonoids, conodonts, bivalves, sporepollen, quantitative petrography, microfacies, and carbon and oxygen isotopes are provided in this thesis. These multidisciplinary data will contribute to reconstruct the Carnian paleogeography, palaeoenvironment, and palaeoclimate in Sichuan Basin, and the stratigraphic position and character of the CPE in Sichuan Basin, South China will be pinpointed and displayed.

This thesis is structured as four different papers, which are presented in chapters 2 to 5. Three of these papers are published, and one is in preparation. The five chapters of this thesis are briefly introduced below.

Chapter 1: This chapter is aimed to guide the reader throughout the characters and research status of the CPE. It includes all reported information about the CPE to date.

Chapter 2: This chapter has been published on the Journal of Asian Earth Sciences with the title "Carbonate platform crisis in the Carnian (Late Triassic) of Hanwang (Sichuan Basin, South China): insights from conodonts and stable isotope data" (DOI: doi.org/10.1016/j.jseaes.2018.06.021). This chapter is a study on the conodont biostratigraphy, microfacies, and carbonate carbon and oxygen isotopes from bulk rock, microbial grains, and brachiopods in the HWQ section, northwestern Sichuan Basin. Through the determination of conodonts, we provide a late Carnian age (Tuvalian 3) of the carbonate platform in Hanwang area, which implies the carbonate platform crisis was much younger than the CPE. A strong negative excursion of carbonate carbon isotopes is reported from the microbial grains which has been considered to be related to the diagenesis on the base of petrology and a flat trend of $\delta^{13}C$ from well preserved brachiopods. Moreover, the results of microfacies analysis did not provide arguments for a karst surface near the top of Carnian limestones. Instead, it is found that the local sea level was rising during the Carnian.

Chapter 3: This chapter has been published on the Journal of the Geological Society with the title "The aftermath of the CPE and the Carnian/Norian transition in northwestern Sichuan Basin, South China" (DOI: doi.org/10.1144/jgs2018-104). To characterize the Carnian/Norian boundary and the composition of carbon isotopes of organic matter after the CPE in northwestern Sichuan Basin, three Carnian/Norian sections were investigated in Hanwang and Jushui. This Chapter shows the results of ammonoids, bivalves, sporopollen, and organic carbon isotopes of bulk rock and woods from the HWQ, HWG, and JS sections. We pinpointed the Carnian/Norian boundary in a short interval at the HWQ section basing on biostratigraphy and recalibration of the magnetic polarity patterns of Zhang *et al*. (2015). Moreover, the tail of a negative carbon isotopic excursion was documented in the lowest part of the HWG section, which was attributed to the fading phase of the CPE. The subsequent long positive trend of organic carbon isotopes was reported from the HWQ and JS sections. Finally, no excursion of carbon isotopes was recorded in the Carnian/Norian interval in the Sichuan Basin due to the mixed organic carbon sources.

Chapter 4: It has been published on the Journal of the Geological Society and titled "The Carnian Pluvial Episode at Ma'antang, Jiangyou in Upper Yangtze Block, Southwestern China" (DOI: doi.org/10.1144/jgs2018-038). This paper was designed by Prof. Zhiqiang. I am not the first author in this paper but I performed the geochemistry and biostratigraphy with our Padova research group, and I prepared the relative texts. In this chapter, the contributions of Prof. Zhiqiang were reported in a summarized form, while my contributions correspond to the published text.

In this chapter, the MAT section, which is ca. 75 km away from the other three sections, was studied for its ammonoids, conodonts, and organic carbon isotopes. A negative shift of the stable isotopes of organic carbon, with an amplitude of ca. 4 ‰, in the lower part of the MAT section is attributed to the CPE. Its shape and duration are similar in the Nanpanjiang Basin, located on the other side of the South China Block (Sun *et al.,* 2016). While the occurrence of a single carbon isotopic excursion (CIE) is different from the multiple CIEs which have been reported in western Tethys.

Chapter 5: "A new perspective for Carnian Pluvial Episode (Late Triassic): tracing of microbial carbonate abundance variations reveals synchronized modifications in shallow water carbonate production", is a manuscript draft. In this chapter, we performed the quantitative petrographic study of carbonate microfacies from the MAT, HWQ, and HWG sections from Sichuan Basin, South China, and two Carnian sections from the Dolomites and Julian Alps, Northern Italy, and one section from Julian Alps of Slovenia. The point-counting results indicate that microbial carbonate production occurs before and after the CPE in the whole Tethys. The early Carnian prolific microbial carbonate production came to an end at the beginning of the CPE, and was replaced by dominant skeletal carbonate production. This process occurred irrespective of the different local environmental conditions and geologic settings that characterize these two regions during the CPE. The recovery of microbial factories is in the late Carnian/early Norian both in the Southern Alps and Sichuan Basin.

CHAPTER 1

What is the Carnian Pluvial Episode (CPE)?

1. The terminology and age of CPE

As one of the most prominent climatic events in the Triassic with global relevance (Preto *et al.*, 2010), the CPE was first reported in the Northern Calcareous Alps (NCA), Austria, and termed "Reingrabener Wende" (Schlager and Schöllnberger, 1974). Subsequently, This term was redefined by many researchers: "Carnian Pluvial Episode" (CPE) (Simms and Ruffell, 1989), "Black Shale Events" (Hornung and Brandner, 2005), "Reingraben Event" (Hornung *et al.*, 2007a), "Mid-Carnian Carbonate Productivity Crisis" (Hornung *et al.*, 2007b), "Middle Carnian Wet Intermezzo" (Kozur and Bachmann, 2010), "Carnian Humid Phase" (Rostási *et al.*, 2011), "Early Carnian Anoxic Event" (Soua, 2014), "Carnian Humid Episode" (CHE) (Ruffell *et al.*, 2016). In this thesis, we used the term "Carnian Pluvial Episode" (CPE) (Simms and Ruffell, 1989) (Note: in Chapter 2, we used the CHE basing on the reviewers' suggestion). The CPE has been described in detailed reviews by Ogg (2015), Ruffell *et al*. (2016), and Simms and Ruffell (2018).

The Carnian (Late Triassic) was named in the Carinthia region, Austria, which yielded the ammonoids genera Trachyceras and Tropites (Mojsisovics von Mojsvár, 1869). The First Appearance Datum of *Daxatina canadensis* was chosen for the definition of the Carnian Stage (Broglio Loriga *et al.*, 1999). The GSSP of the Carnian is placed at Prati di Stuores (Italy) (Mietto *et al.*, 2012). It was subdivided initially into three substages: Cordevolian, Julian, and Tuvalian (Mojsisovics von Mojsvár *et al.*, 1895). Krystyn (1980) incorporated the Cordevolian into the Julian, but the Cordevolian was still used as the first substage of Carnian in some publications (e.g., Korte *et al.*, 2005; Kozur and Bachmann, 2010; Rostási *et al.*, 2011). In this thesis, the subdivision into two substages of the Carnian was used. Its base and top are dated at 237 Ma and 229.6 Ma (Bernardi *et al.*, 2018). The Julian substage is subdivided into Julian 1 and Julian 2 (Krystyn, 1980). The Julian 1 corresponds to the *Daxatina canadensis*, *Trachyceras aon* and *Trachyceras aonoides* ammonoid zones: the Julian 2 is instead coinciding with the *Austrotrachyceras austricum* ammonoid zone (Gallet *et al.*, 1994; Broglio Loriga *et al.*, 1999).

Many researchers regarded the uppermost *Trachyceras aonoides* ammonoid zone and the *Ma. Carnicus* conodont zone as the onset of the CPE (Hornung *et al.*, 2007a, b, c). The duration of the CPE may include entire *Austrotrachyceras austriacum* ammonoid zone with a period of approximate 1 Ma (Hornung and Brandner, 2005; Hornung *et al.*, 2007b, c). Kozur and Bachmann (2010) found

sandstones related to the CPE in the Germanic Basin above an unconformity, which were dated at the upper subzone of the *A. austriacum* zone with the duration of 0.7-0.8 Myr. In Dolomites, the onset of terrigenous discharge is at the boundary between Julian 1 and Julian 2 (Breda *et al.*, 2009; Dal Corso *et al.*, 2015, 2018, and references therein). Lukeneder *et al*. (2012) reported a delay of the CPE on the equatorial Cimmerian terrane in Turkey, near the boundary between Julian and Tuvalian. A recent astronomical timescale set the duration of the CPE at 1.21 Myr (Miller *et al.*, 2017).

2. Carnian regression and paleokarst

An early Carnian sea level drop caused an extensive palaeokarst which was widely observed in the shallow marine carbonate platforms of the Southern Alps (western Tethys) (Bosellini, 1984; De Zanche *et al.*, 1993, 2000; Mutti and Weissert, 1995; Gianolla *et al.*, 1998a; Keim *et al.*, 2001; Breda *et al.*, 2009; Gattolin *et al.*, 2015). An increased supply of terrigenous siliciclastics occurred during and after this sea-level drop, and as a consequence, Carnian interplatforms were filled (De Zanche *et al.*, 1993; Gianolla *et al.*, 1998a; Bosellini *et al.*, 2003; Preto and Hinnov, 2003). Paleosols of this age were associated with paleokarst, which was considered to the result of a humid tropical climate, which was also identified beyond the Southern Alps region (Arche and López-Gómez, 2014; López-Gómez *et al.*, 2017; Barrenechea *et al.*, 2018). In continental areas (e.g., Germanic Basin and Iberian Peninsula), abundant fluvial deposits are found (Kozur and Bachmann, 2010; Arche and López-Gómez, 2014; López-Gómez *et al.*, 2017; Barrenechea *et al.*, 2018). A recent study showed that the CPE initiated before this dramatic sea level drop and consequent subaerial exposure in the Dolomites region (Gattolin *et al.*, 2015).

The decomposition of Pangea synchronized with the closure of the Palaeotethys and the Indosinian orogeny were considered for a possible cause for the global sea level fluctuations (Hornung *et al.*, 2007c).

3. Carbonate crisis and coarse terrigenous and freshwater input in CPE

The demise of early Carnian rimmed carbonate platforms and reduction of carbonate sedimentation was recognized in shallow marine to basinal environments of Tethyan region, followed by an exceptional input of mixed siliciclastic-carbonate and increased rainfall associated to the CPE. This deposition of siliciclastics was considered to reflect a pluvial episode (Simms and Ruffell, 1989, 1990, 2018), which caused the enhancement of the hydrological cycle (Dal Corso *et al.*, 2012, and references therein). However, the CPE as a pluvial event has been questioned by Visscher *et al.* (1994). This critical view, however, was not shared by subsequent literature and the sharp lithological

transition from carbonates to clays-sandstones was related to the CPE in many locations: Northern Calcareous Alps (Austria: Schlager and Schöllnberger, 1974; Hornung and Brandner, 2005; Hornung, 2007; Hornung *et al.*, 2007a; Roghi *et al.*, 2010; Dal Corso *et al.*, 2015; Mueller *et al.*, 2016; Hungary: Haas *et al.*, 2012; Dal Corso *et al.*, 2015); Southern Alps (Julian Alps: De Zanche *et al.*, 2000; Preto *et al.*, 2005; Roghi *et al.*, 2010; Dolomites: De Zanche *et al.*, 1993; Keim *et al.*, 2001, 2006; Gianolla *et al.*, 1998a, 2003; Preto and Hinnov, 2003; Breda *et al.*, 2009; Roghi *et al.*, 2010; Dal Corso *et al.*, 2015; Gattolin *et al.*, 2015); Lombardian Prealps (Berra and Jadoul, 2002); Slovakia (Sýkora *et al.*, 2011); China (Sun *et al.*, 2016; Wang *et al.*, 2017); Turkey (Lukeneder *et al.*, 2012); Tunisia (Soua, 2014); Southern Israel (Bialik *et al.*, 2013). In most positions of the Northern Calcareous Alps and the Dolomites, the siliciclastic input was organized into multiple pulses (Hornung *et al.*, 2007c; Breda *et al.*, 2009; Roghi *et al.*, 2010; Stefani *et al.*, 2010).

The carbonate sedimentation crisis and input of fine siliciclastic materials can be also observed in the hemipelagic settings of Spiti in Himalaya (India), Lagonegro Basin (Italy), in Hungary, and Japan (Hornung *et al.*, 2007b; Rigo *et al.*, 2007; Rostási *et al.*, 2011; Preto *et al.*, 2013; Nakada *et al.*, 2014).

In continental areas, the evaporitic playas and playa-lakes were temporarily substituted by fluvial sandy deposits, and river systems occupied vast surfaces, for example, in the Germanic Basin (Kozur and Bachmann, 2010), southern UK (Simms and Ruffell, 1989; Miller *et al.*, 2017), Iberian Peninsula (Spain, Portugal, Morocco, Algeria, summarized in Arche and López-Gómez, 2014; López-Gómez *et al.*, 2017; Barrenechea *et al.*, 2018), Southwestern USA (Prochnow *et al.*, 2006; Lucas and Tanner, 2018). In North America, the CPE should correspond to thick fluvial deposits at the base of the Newark Supergroup, which infills continental rifting basins (Olsen *et al.*, 1996). Fluvial or deltaic sandstones also occur during the CPE in transitional environments of Norway (Mueller *et al.*, 2015).

Recent research found that not all carbonate platforms were shut off, but on the contrary, the type of carbonate production was changed, and microbial carbonates were replaced by ooids and skeletal grains (Dal Corso *et al.*, 2015; Gattolin *et al.*, 2015).

4. Humid weather during the CPE inferred from mineral composition and quantitative palynological studies

The CPE was characterized by wet weather conditions and an increase in rainfall and runoff, in between two extended periods of arid climate. These humid conditions were challenged by Franz *et al.* (2018), and Baranyi *et al.* (2018) also proposed that the climate history was more complex during the CPE. However, humidification and enhanced freshwater runoff were widely reported in continental Europe and in the western Tethys realm, (Simms and Ruffell, 1989, 1990; Roghi, 2004,

2010; Hornung and Brandner, 2005; Rigo *et al.*, 2007; Rostási *et al.*, 2011; Bialik *et al.*, 2013; Mueller *et al.*, 2015, 2016; López-Gómez *et al.*, 2017; Barrenechea *et al.*, 2018). Climatic conditions were mainly inferred from evidences of palynological assemblages and the changes of mineral composition of paleosols and arenites.

Quantitative analyses of palynological investigations showed a switch from xerophytic elements toward hygrophytic elements suggesting a humid climate perturbation from late Julian to the early Tuvalian, and an abrupt return to the increase of hygrophytic associations in the lower Tuvalian (Hochuli and Frank, 2000; Roghi, 2004; Mueller *et al.*, 2015, 2016). More palynological studies suggested that multiple humid climate pulses occurred in the CPE (Roghi, 2010; Mueller *et al.*, 2016). The CPE was thus not a single humid event (Breda *et al.*, 2009; Stefani *et al.*, 2010; Kozur and Bachmann, 2010; Arche and López-Gómez, 2014). In addition, a humid and warm climate was demonstrated in light of elevated kaolinite contents or coal beds from siliciclastic intervals (Simms and Ruffell, 1989; Rostási *et al.*, 2011; Barrenechea *et al.*, 2018; Lucas and Tanner, 2018), the character of palaeosol horizons (Prochnow *et al.*, 2006; Breda *et al.*, 2009; Barrenechea *et al.*, 2018), and occurrences of amber (Gianolla *et al.*, 1998b).

5. Carbon and oxygen isotopic perturbations in CPE

A strong negative perturbation of carbon isotopes, recorded in terrestrial and marine organic matter, was synchronous with the crisis of the microbial factories and has been reported from Italy, Austria and Hungary (Dal Corso *et al.*, 2012, 2015, 2018; Mueller *et al.*, 2016). In South China, an abrupt carbon isotope excursion in organic matter and subsequently a long positive trend were both documented in Guizhou (Sun *et al.*, 2016) and Sichuan Basin (Shi *et al.*, 2018). Recently, multiple negative shifts in organic carbon isotopes were reported in terrestrial stratigraphic successions of the UK and marine successions of Alpine region (Miller *et al.*, 2017; Baranyi *et al.*, 2018; Dal Corso *et al.*, 2018). The multiple negative shifts were also reported in the carbonate carbon isotopes from Oman and Guizhou (Sun *et al.*, 2016, 2018), which is in agreement with, e.g., Kozur and Bachmann (2010) who concluded that the CPE was a prolonged and multi-phase event. Dal Corso *et al.* (2012, 2015, 2018) and Sun *et al.* (2016, 2018) speculated that negative carbon isotope perturbations were related to the eruption of Wrangellia flood basalts, which injected a massive amount of ^{13}C-depleted CO_2 into the atmosphere-ocean system, thus causing a disequilibrium of the carbon cycle. A significant negative shift of oxygen isotopes in conodont apatite suggested that the CPE corresponded to a warm temperature and/or a change in seawater salinity (Hornung *et al.*, 2007c; Rigo and Joachimski, 2010; Trotter *et al.*, 2015; Sun *et al.*, 2016).

6. Anoxic and black shales in CPE

During the CPE, dysaerobic to anoxic conditions have been documented in many regions of western Tethys (e.g., Reingraben Shales in NCA: Hornung and Brandner, 2005; basal Heiligkreuz Formation in the Dolomites: Keim, 2006), southern Tethyan margin (Tunisian basin: Soua, 2014), eastern Tethys (Guizhou: Wang *et al.*, 2008; Minzoni *et al.*, 2015; Sun *et al.*, 2016). The anoxic conditions are suggested by organic matter rich marlstones, black shales or black limestones (Schlager and Schöllnberger, 1974; Bellanca *et al.*, 1995; Nagy, 1999; Hornung and Brandner, 2005; Keim *et al.*, 2006; Hornung *et al.*, 2007a, b; Wang *et al.*, 2008; Rostási *et al.*, 2011; Soua, 2014; Sun *et al.*, 2016). Anoxic and/or brackish waters were also inhabited by a low diversity biota ostracod fauna (Keim *et al.*, 2001), as a result of elevated nutrient input, enhanced freshwater runoff, and salinity change (Hallock and Schlager 1986; Gerry *et al.*, 1990; Keim *et al.*, 2006). However, there are no indications so far for low-oxygen conditions in open oceans (Rigo *et al.*, 2007; Nakada *et al.*, 2014).

7. Biological extinction and occurrence in CPE

The CPE was also a biotic turnover or extinction event (Simms and Ruffell, 1989, 1990; Simms *et al.*, 1995). Some groups showed high extinction rates, such as the conodonts, ammonoids, bivalves, crinoids and bryozoans (Simms and Ruffell, 1989, 1990; Simms *et al.*, 1995), and terrestrial flora and fauna (e.g., Benton, 1991; Seyfullah *et al.*, 2018). The turnover or the reduction of conodont diversity and abundance were reported in the CPE (Rigo *et al.*, 2007; Chen *et al.*, 2015; Martínez-Pérez *et al.* 2015; Zhang *et al.*, 2018), while Hornung *et al.* (2007c) reported a delayed extinction of ammonites and conodonts around the Julian/Tuvalian boundary.

The causes of the extinctions are still under discussion, but some researchers supposed that the abrupt change to more humid weather conditions may have been the cause of this crisis (Simms and Ruffell, 1989, 1990; Simms *et al.*, 1995). Zhang *et al.* (2018) concluded that warm climate and deteriorating environments of seawater suppressed the conodont diversity.

Some important groups originated within or shortly after the CPE, for example, the first known dinosaurs and calcareous nannoplankton (e.g., Benton, 1991, 2018; Erba, 2006; Furin *et al.*, 2006; Bernardi *et al.*, 2018), first occurrence of scleractinian corals as reef builders (Stanley, 2003), the first global appearance of millimetre-sized droplets of amber (Roghi *et al.*, 2006; Breda *et al.*, 2009; Seyfullah *et al.*, 2018), the earliest record of turtles (Reolid *et al.*, 2018). Moreover, the calcispheres (calcareous nannofossils) were suddenly abundant (Preto *et al.*, 2013).

8. What caused the CPE?

The leading cause of the CPE is still under debate (Simms and Ruffell 1989; Simms *et al.*, 1995; Keim *et al.*, 2001; Hornung and Brandner, 2005; Rigo *et al.*, 2007; Dal Corso *et al.*, 2015; Miller *et al.*, 2017; Sun *et al.*, 2018). Generally, there are three hypotheses, as follow:

First, “monsoonal hypothesis", Hornung and Brandner (2005) speculated that the CPE was ascribed to an enhancement of the monsoonal circulation as a consequence of the Cimmerian orogeny, which changed the plate constellations, and triggered a more intense monsoonal climate near the forming Cimmerian orogen. The high landmasses would provide the source areas for increased terrigenous discharge (Hornung and Brandner, 2005). This megamonsoonal system that was marked by increased moisture and northwesterly flowing trade winds in Europe (Kozur and Bachmann, 2010) may record the peak of the Pangaean mega-monsoon (Parrish, 1993; Colombi and Parrish, 2008). The megamonsoonal atmospheric circulation may generate the increase in rainfall and river runoff (Simms and Ruffel, 1989), and it may enhance the production of siliciclastics in epicontinental areas, moreover, an increase in influx of freshwater may decrease the salinity of surface water in shallow marine of Tethyan sea and enhanced nutrification (Simms and Ruffell, 1989; Hornung *et al.*, 2007a, b, c). These factors may cause carbonate productivity crisis (Hornung *et al.*, 2007b, c; Hornung, 2007).

Second, "sea-level drop hypothesis", the sea level fall associated with consequent subaerial exposure was thought to overcome the regional subsidence, and subsequently triggered elevated siliciclastics and freshwater input to the shallow marine environments (Bosellini, 1984; De Zanche *et al.*, 1993; Keim *et al.*, 2001). This could have had a series of consequences: excessive nutrients, anoxia and salinity fluctuations (Keim *et al.*, 2001), and, finally, the carbonate platform demise.

Third, "large igneous province hypothesis", the global climate perturbation in the CPE was attributed to additional CO_2 releasing into the ocean-atmosphere system and subsequent climatic warming and enhanced rainfall, which were induced by the coeval Wrangellia large igneous province (Furin *et al.*, 2006; Dal Corso *et al.* 2012, 2015, 2018; Xu *et al.*, 2014; Mueller *et al.*, 2016; Sun *et al.*, 2016, 2018). The Wrangellia LIP has been estimated the volume of ca. 1×106 km3 (Panuska, 1990), and the $^{187}Os/^{188}Os$ data concluded that the initial onset of Wrangellia LIP was likely to be the late Ladinian (Xu *et al.*, 2014). The $^{40}Ar/^{39}Ar$ and U-Pb dating gave a close age range between 233 and 227 Ma (Greene *et al.*, 2010, and references therein). Moreover, Eastern Mediterranean alkaline volcanics may be one additional source of CO_2 (Hornung *et al.*, 2007b, c). These contemporary alkaline basalts were recorded in many locations: China (Huang *et al.*, 2013) and Italy (Furin *et al.*, 2006). The excessive CO_2 supply may has produced the rise of the carbonate compensation depth (CCD) and missing carbonate participation during the CPE in Lagonegro Basin, Sicily (Rigo *et al.*, 2007).

CHAPTER 2

Carbonate platform crisis in the Carnian (Late Triassic) of Hanwang (Sichuan Basin, South China): insights from conodonts and stable isotope data

Xin Jin [a], [b], *, Zhiqiang Shi [c], Manuel Rigo [a], Marco Franceschi [a], Nereo Preto [a]

a. Dipartimento di Geoscienze, Università degli Studi di Padova, Via G. Gradenigo 6, Padova, Italy
b. Shandong Provincial Key Laboratory of Depositional Mineralization & Sedimentary Minerals, Shandong University of Science and Technology, Qingdao, Shandong 266590, China
c. State Key Laboratory of Oil and Gas Reservoir Geology and Exploitation, Chengdu University of Technology, Chengdu, Sichuan 610059, China
*Corresponding author. E-mail address: xin.jin@studenti.unipd.it, Tel: +39 3891476394

Received 27 September 2017; Received in revised form 4 June 2018; Accepted 9 June 2018

Abstract

During the Carnian, the Hanwang area in the northwestern Sichuan Basin (South China) was characterized by shallow water carbonate sedimentation that underwent an abrupt demise associated to a sudden input of terrigenous sediments. This major facies change was considered to be the expression of the onset of the Carnian Humid Episode, a most remarkable environmental crisis in Late Triassic that is well recognized in northwestern Tethys margins and coincides with a major global perturbation of the carbon stable isotope record. However, the lack of detailed biostratigraphic constraints have so far prevented a precise dating of the carbonate platform demise in western Sichuan Basin.

In this work, the Qingyan Gou (HWQ) section, cropping out in Hanwang, was investigated for its facies and microfacies, carbonate carbon and oxygen isotopes on brachiopods, microbial grains and bulk matrix. Facies analysis shows a marine transgression from inner ramp oolitic shoal to middle ramp siliceous sponge mound, then overlain by shale and calcareous siltstone with interbedded silty mudstones. Refined biostratigraphic data from the HWQ and Guanyin Ya (HWG) sections imply that the demise of sponge mounds occurs in the late Tuvalian or later.

A negative carbon isotope perturbation was found in the bulk matrix immediately below the sponge mounds demise, but it was not found on the isotope record from brachiopods. This suggests that the negative shift in the bulk carbonate was probably related to diagenesis. Given the late

Tuvalian (last substage of Carnian) age attributed to the demise of the sponge mounds and the absence of a carbon isotopic excursion, we infer that the carbonate platform crisis and strong terrigenous input in Hanwang cannot be related to the onset of the Carnian Humid Episode. These the demise of the carbonate platform and the facies deepening trend could be rather due to the interplay between accelerating subsidence rates, environmental chants and enhanced siliciclastic input related to the formation of a foreland basin during Indosinian orogenesis.

Keywords: Carnian Humid Episode; Stable isotopes; Carbonate ramp; Biostratigraphy

1. Introduction

During the Mesozoic, siliceous (Hexactinellida) sponges played an accessory role in carbonate reefs, in contrast to calcareous sponges, which were widely distributed in carbonate platforms and constructed carbonate buildups (Pratt, 1995; Stenzel and James, 1995; Wendt *et al.*, 1997). The first reports of hexactinellid sponges as major Mesozoic reef builders were made by Wendt *et al.* (1989) and Wu (1989) in Hanwang and Jushui areas, within the northwestern Sichuan Basin (Carnian, Late Triassic, China). Since then, hexactinellid sponges spread continuously in the geological record and are found commonly on continental shelves (Krautter *et al.*, 2006).

The Sichuan Basin hosts a thick Middle to Upper Triassic sedimentary succession, deposited in a foreland basin related to the Indosinian orogenesis (Luo and Long, 1992; Li *et al.*, 2003, 2014). Hexactinellid sponges formed spectacular mounds in Hanwang and Jushui areas, which soon underwent an abrupt demise and were overlain by a thick terrigenous succession. Their age so far was constrained to the Carnian only by scarce fossils (Wu, 1989; Wang, 1992; Shi *et al.*, 2017). The disappearance of sponge mounds coincides with a sharp transition to terrigenous sedimentation that was correlated to the Carnian Humid Episode (Shi *et al.*, 2009, 2017; Wang *et al.*, 2015). The Carnian Humid Episode (CHE sensu Ruffell *et al.*, 2016), also known as Carnian Pluvial Event, is a major global Triassic climate event which was recognized in shallow carbonate platforms (Ogg, 2015; Ruffell *et al.*, 2016, and references therein), and in deep-water environments (Rigo *et al.*, 2007; Nakada *et al.*, 2014). The CHE testifies to an increase in rainfall that caused input of terrigenous sediments and black shales deposition into sedimentary basins (e.g., Simms and Ruffell, 1989). At the same time, carbonate production crises occurred worldwide (e.g., Keim *et al.*, 2006; Hornung *et al.*, 2007b, c; Breda *et al.*, 2009; Lukeneder *et al.*, 2012). The onset of the CHE was found coincident with a major negative $\delta^{13}C$ perturbation (CIE) recorded by bulk organic matter and n-alkanes (e.g., Dal Corso *et al.*, 2012, 2015; Mueller *et al.*, 2015, 2016; Sun *et al.*, 2016; Miller *et al.*, 2017). This led to interpret the climate change towards wetter conditions as related to an injection of CO_2 in the

atmosphere-ocean system, possibly triggered by massive volcanism (Furin *et al.*, 2006; Dal Corso *et al.*, 2012, 2015). Biochronostratigraphic investigations allowed dating the CHE to around the boundary between Julian 1 (*Trachyceras* ammonoid zone) and Julian 2 (*Austrotrachyceras ammonoid* zone, Fig. 1) in most locations of northwestern Tethys (e.g., Hornung and Brandner, 2005; Hornung *et al.*, 2007a, c; Breda *et al.*, 2009; Dal Corso *et al.*, 2015), in southern Tethys (Spiti basin, Hornung *et al.*, 2007b) and in eastern Tethys (Nanpanjiang Basin, Sun *et al.*, 2016). These studies suggest synchronicity of climate change, terrigenous input and demise of carbonate platforms. This synchronicity was questioned by Lukeneder *et al.* (2012), who found that the carbonate platform crisis in Turkey has been younger, at the boundary between Julian and Tuvalian.

Despite the broad coincidence in terms of age between the CHE and the facies changes observed in the Carnian of the Sichuan Basin, the precise temporal relationship is still unclear. Thus, the causes and time of the demise of the hexactinellid sponge reefs and potential relationships with the ongoing Indosinian orogenesis are obscure. A discussion of these open questions would require a precise correlation of the Carnian of Sichuan Basin with the western Tethyan domain, and a finer biostratigraphic framework, which are still lacking. Moreover, a stable isotope record was not retrieved yet that could confirm the presence of the major isotope shift at the onset of the CHE. These data are provided in this paper.

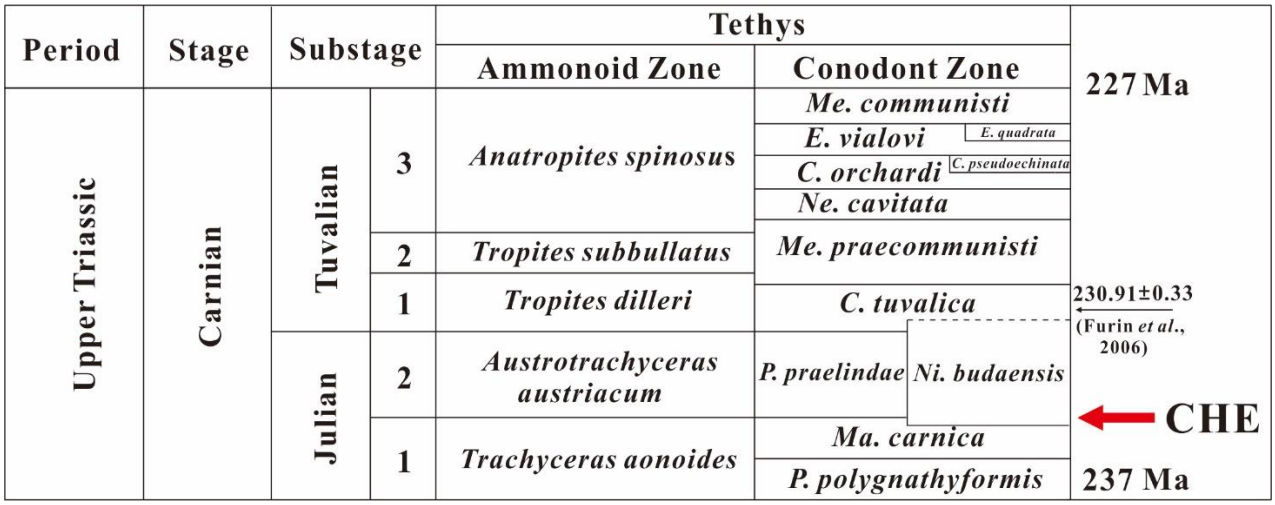

Fig. 1. Tethysian Carnian chronostratigraphy. Ammonoid biozonation follows Gallet *et al.* (1994), conodont biozonation follows Rigo *et al.* (2018). The top and base of Carnian age are based on Cohen *et al.* (2013). "CHE"= Carnian Humid Episode.

2. Geological setting

The Sichuan Basin is a portion of eastern Tethys, located on the northern margin of South China Plate (Fig. 2A). Sedimentation on this plate was dominated by extensive carbonate platforms during the Triassic. Two sections are studied in this work and are situated in Hanwang region, in the middle

of the Longmen Shan Thrust Belt at the boundary between the Sichuan Basin and Tibetan Plateau (Fig. 2B). The first section is named Qingyan Gou (HWQ) (N31°27'46.85"/E104°09'35.40") and is located at 7 km SSW of Mianzhu city, northwestern Sichuan Basin. The other is named Guanyin Ya (HWG) which is around 1.5 km to the northwest of the HWQ (Fig. 2C). Due to the collision between North China and South China plates (Zhang *et al.*, 1996), which was considered the first stage of the Indosinian orogenesis (Li *et al.*, 2003), an extensive unconformity formed between Middle and Upper Triassic sediments (Li *et al.*, 2003). During the Late Triassic, a carbonate ramp dipping west and surrounded by local uplifted areas formed in the middle to western Sichuan Basin (Wu, 2009). In the meantime, the Middle Triassic carbonates suffered intense karst dissolution in the shallow parts of the Sichuan Basin (Li *et al.*, 2003).

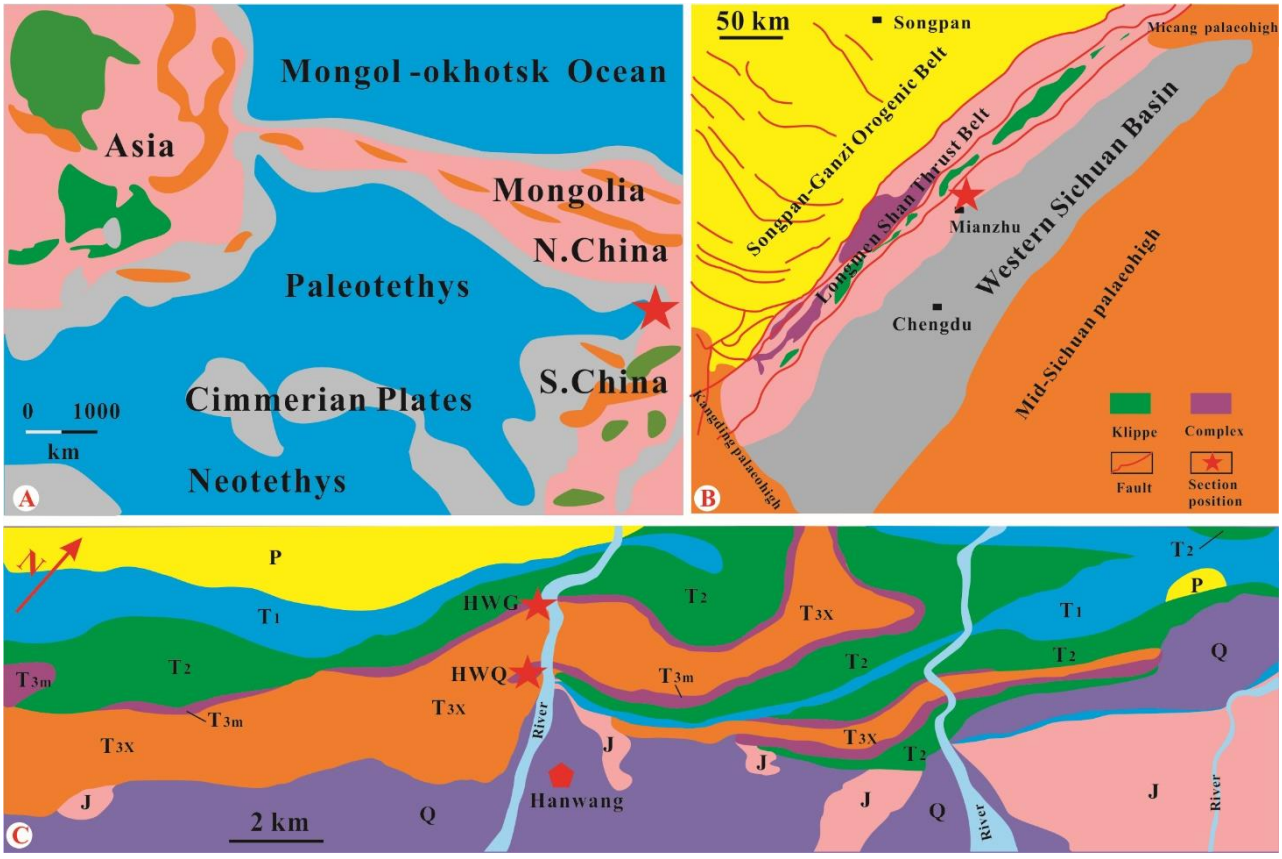

Fig. 2. Maps of the study area during the Late Triassic. **A**) General position of study area during the Late Triassic period (simplified from Golonka, 2007); **B**) Geological and tectonic map of the Sichuan Basin and adjacent areas (Li *et al.*, 2003); **C**) Geological map showing the location of the study sections apart 4 km from northwest of Hanwang town (simplified from Wu, 1989). J: Jurassic; P: Permian; T_1: Lower Triassic; T_2: Middle Triassic; T_{3m}: Ma'antang Formation in Upper Triassic (study interval); T_{3x}: Xujiahe Formation in Upper Triassic; Q: Quaternary. HWG: Guanyin Ya section; HWQ: Qingyan Gou section.

A second phase of the Indosinian orogenesis at the end of Carnian caused a minor and local unconformity between Carnian and Norian (Zhang *et al.*, 2013). Some consider this minor unconformity as the initiation of the western Sichuan foreland basin (Zeng and Li, 1995). According

to these authors, the entire Sichuan Basin could have been mainly subjected to extension, not compression, during the early Carnian (Liu *et al.*, 1995; Li *et al.*, 2011c). In the early Carnian, seawater from the eastern Tethys Ocean was entering the western Sichuan Basin from the Ganzi deep marine basin, which thus became a large bay (Wu, 1984). This bay was the only channel connecting the Sichuan Basin with the eastern Tethys Ocean through an island chain (Deng *et al.*, 1982; Wu, 1984). Because of the complex sea level changes during the Carnian (e.g., De Zanche *et al.*, 1993; Gianolla *et al.*, 1998a; Li *et al.*, 2011a, 2014) and the inherited rugged landforms, the thickness and lithological features of Carnian rocks are extremely variable both laterally and stratigraphically in the Sichuan Basin (Shi *et al.*, 2015).

3. Carnian/Norian Stratigraphy of Hanwang area in Sichuan Basin

The subaerial unconformity between Middle and Upper Triassic is well documented in the Hanwang region, and is exposed at the base of the HWG section. Above the unconformity, the Upper Triassic succession is divided into three formations: the Ma'antang Formation (T_{3m}) consists of oolitic limestones, bioclastic limestones and microbial - sponge mounds, subsequently overlain by dark grey shales, calcareous silty mudstones and muddy siltstones. It is interpreted as being deposited on a carbonate ramp (Wu, 2009). This formation is subdivided into 4 lithozones (unit 1 to 4 in Shi *et al.*, 2017). Above, the Xiaotangzi Member (T_{3xt}) is assigned to the lower Xujiahe Formation (T_{3x}) and dated to Norian (Li *et al.*, 2003), on the basis of limited biostratigraphic data (Deng *et al.*, 1982). It mainly consists of quartz arenite, coarse lithic arenite with calcite cement and is widely distributed in the Sichuan Basin. Its sedimentary environment is thought to be transitional between littoral and delta (Wu, 1989; Li *et al.*, 2003). The boundary between T_{3m} and T_{3xt} is marked by a local unconformity (Fig. 3, Zhang *et al.*, 2013). Above it, the rest of Xujiahe Formation (T_{3x}) mainly consists of hundreds of meters of fluvial sandstone with common horizontal-, cross-, and ripple bedding (Wu, 1989; Mei and Liu, 2017).

The age of the Ma'antang Formation in the HWQ is Carnian, based on scarce biostratigraphic data (Wu, 1989; Wang, 1992). In units 1 and 2 (Fig. 3), a distinct Carnian bryozoan subspecies, *Paralioclema dagysi Ma'antanggense*, was determined by Yang (1979). Wu (1989) described *Protrachyceras* cf. *victoria* Moijsisovics, *Clionites* sp., *Sandlingites* sp., *Californites?* sp.. In Unit 1 and Unit 2 of the Ma'antang Formation in Hanwang and adjacent areas but there is no illustration of his ammonoids. Wang (1992) reported *Thisbites borellii* Mojs., *T. haushoferi* Mojs., *T.*cf. *borni* Mojs., *T. agricolae* Mojs., *Anatomites herici* Mojs., *Discotropites plinii* (Mojs.), *Timortropites dubvosus* (Welter)., *Anatibetites* sp., *Thisbites* sp., *Juvavites* sp. above the sponge mound (Bed B4 in Fig. 3). This ammonoid association may be attributed to the Late Carnian (late Tuvalian), but Wang (1992)

did not draw a conclusion about the age determination.

In previous work, the lower limestone units (units 1 to 2, in this paper) were assigned to lower Carnian and units 3 and 4 were dated to late Carnian, based on ammonoid biostratigraphy (Wu, 1989; Shi *et al.*, 2017) and magneto stratigraphy (Zhang *et al.*, 2015; Shi *et al.*, 2017).

In the two study sections, a marine to continental succession is exposed above the unconformity, which begins with carbonates, followed by mainly siliciclastics (Fig. 3). At the HWQ, only the upper part of the carbonates and the siliciclastics are exposed, while the basal limestone is mostly covered. Available biostratigraphic data in these localities only consist of a long-range conodont (*Quadralella polygnathiformis*) which is not useful for precise dating, apart for marking the Carnian stage (Mietto *et al.*, 2012; Shi *et al.*, 2017).

4. Methods

The HWQ section was sampled for conodonts, moreover, all the limestone layers occurring in the lower part of this section were sampled for microfacies analysis (Fig. 3), Scanning Electron Microscope (SEM) imaging, cathodoluminescence, and carbonate carbon and oxygen isotopes analyses. The HWG section was only studied for conodont biostratigraphy, carbonate microfacies data are given in Wu (2009) and Shi *et al.* (2017).

4.1. Sample preparation

Sample preparation was carried out at the Department of Geosciences of the University of Padova (Italy) and Institute of Sedimentary Geology of the Chengdu University of Technology (China). Bulk samples collected at 17 positions in the HWQ (Fig. 3) were cut in two halves. One half was used for making thin sections, the other was cleaned by ultrasonic bath for 15 mins to remove surface contamination, repeatedly washed by deionized water, and then oven-dried at 50 °C for 2 hours. Powders for isotope analyses were collected from separated rock components on the polished surface of these samples with a hand-held drill.

Forty-two fragments of brachiopods from 22 layers of the HWQ were separated from the host rock with a steel needle, and 15 brachiopods were collected in debris. Brachiopods from the HWQ were examined with an optical microscope to check the integrity of the shell structure, and it was observed that only the secondary layer of the brachiopod shells was preserved. Therefore, no HCl treatment was carried out (Ullmann and Korte, 2015). Shell fragments were then cleaned and sampled by a hand-held micro-drill.

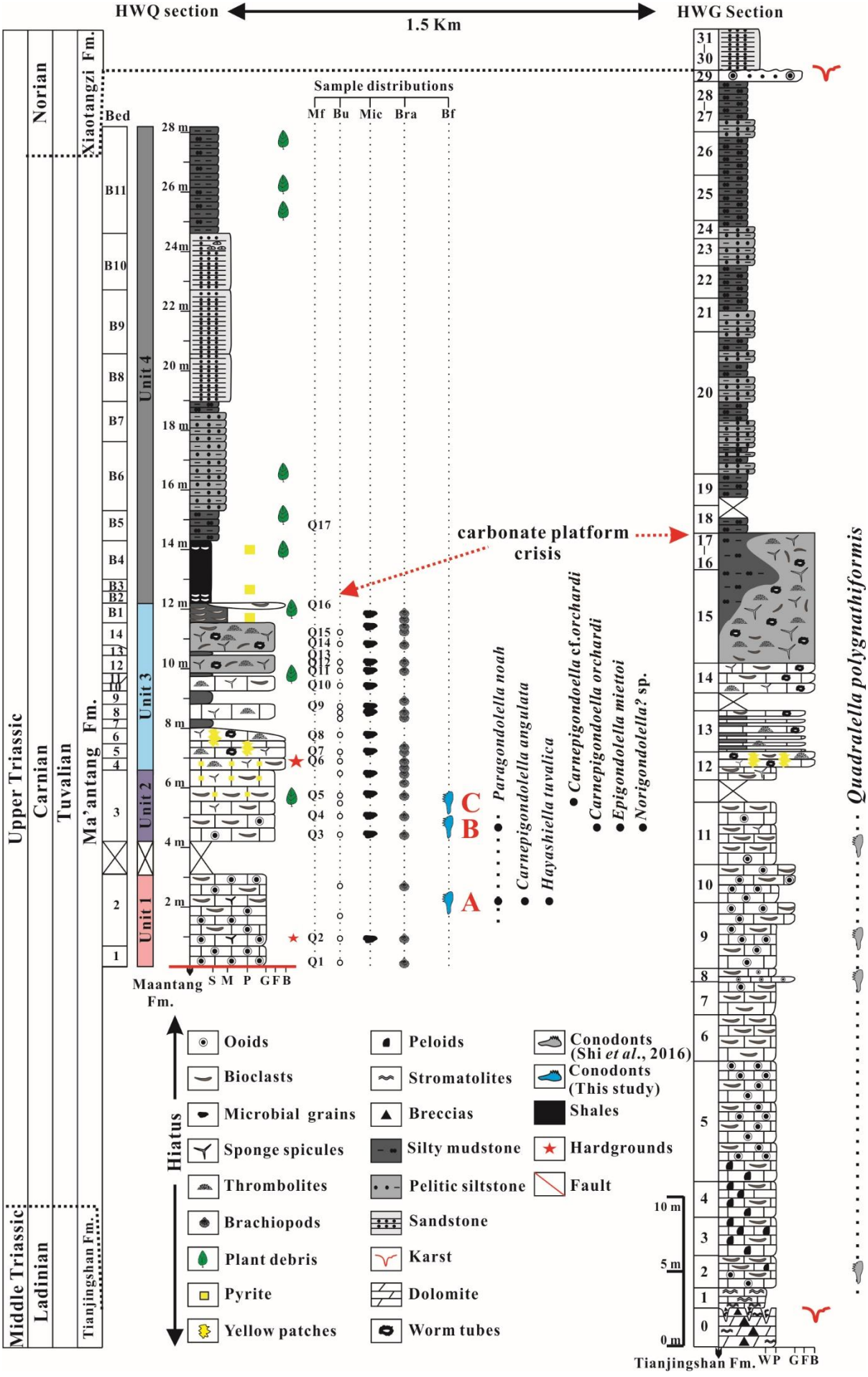
HWQ section
1.5 Km
HWG Section
Upper Triassic
Middle Triassic
Norian
Carnian
Ladinian
Tuvalian
Xiaotangzi Fm.
Ma'antang Fm.
Tianjingshan Fm.
Bed
Unit 4
Unit 3
Unit 2
Unit 1
Sample distributions
Mf Bu Mic Bra Bf
carbonate platform crisis
Paragondolella noah
Carnepigondolella angulata
Hayashiella tuvalica
Carnepigondoella cf.orchardi
Carnepigondoella orchardi
Epigondolella miettoi
Norigondolella? sp.
Quadralella polygnathiformis
Maantang S M P GFB
Tianjingshan Fm. WP GFB
Hiatus
Ooids
Bioclasts
Microbial grains
Sponge spicules
Thrombolites
Brachiopods
Plant debris
Pyrite
Yellow patches
Peloids
Stromatolites
Breccias
Silty mudstone
Pelitic siltstone
Sandstone
Karst
Dolomite
Worm tubes
Conodonts (Shi et al., 2016)
Conodonts (This study)
Shales
Hardgrounds
Fault

Fig. 3. Lithologic log of Qingyan Gou section (HWQ) and Guanyin Ya (HWG) section with sampled distributions. "Mf" = microfacies, "Bu" = bulk rock, "Mic" = microbial grains, "Bra" = brachiopods, "Bf" = biostratigraphic fossils (conodonts), "S" = shale, "M" = marlstone, "P" = packstone, "G" =grainstone, "F" = floatstone, "B" = boundstone, "W" = wackestone.

4.2. SEM imaging and cathodoluminescence

Selected brachiopods were imaged using a CamScan MX 2500 SEM in order to assess preservation (Korte *et al.*, 2005; Brand *et al.*, 2012; Ullmann and Korte, 2015). Alterations in the elongate fibers of the secondary layer (Merkel *et al.*, 2009; Brand *et al.*, 2011; Korte and Hesselbo, 2011) were observed only in few cases, while many brachiopods have punctated shells. Punctae are often filled by carbonate cement. When a shell is micro-drilled, it is unavoidable to incorporate the carbonates filling the punctae, and this may impact the results of isotopic analyses (see below). Shells displaying evidence of dissolution could also be identified, and powders from these samples were thus discarded. Smooth fibrous surfaces of most shells were considered as well preserved (Korte *et al.*, 2004, 2005, 2017). Microdrill sampling traces are clearly identifiable under the SEM, thus, image inspection was used to ensure that matrix or diagenetic carbonate in cracks were not sampled.

Cathodoluminescence (CL) was used for the monitoring of diagenetic alteration (Bates and Brand, 1990; Grossman *et al.*, 1996). Carbonate thin sections were observed under an 8200 mk3 cold cathodoluminescence device linked to a Nikon Eclipse 50i polarizing microscope and a Canon EOS 600D digital camera at the IGG-CNR Institute hosted in Padova. The voltage was set at 20 kV and the cathode current intensity was maintained at ca. 250-300 mA.

4.3. Conodonts

Fifteen samples, 3-5 kg each, were collected from limestones both in the HWQ and HWG sections for conodonts. The limestone samples were dissolved, and the obtained residues dried at the Institute of Sedimentary Geology, Chengdu University of Technology. Residues were then concentrated with heavy liquids, conodonts were separated manually at the binocular microscope, and photographed at the SEM of at the Department of Geosciences, Padova University.

4.4. Stable isotope analyses

Powder sampling was carried out by a micro-drill (0.4 mm) to manually extract from freshly broken surfaces ca. 0.2-2 mg of powder from different rock components (e.g., microbial carbonates, ooids, calcite veins, bulk matrix, crinoids). All the obtained powders were then weighted into

exetainer vials. CO_2 was produced at 70 °C by complete reaction with >99% H_3PO_4 in a Gasbench II device linked to a Thermo Delta V Advance isotopic ratio mass spectrometer at the Department of Geosciences, Padova University. Two internal calcite standards were employed for calibration to the VPDB scale, i.e, MAQ 1 ($\delta^{13}C$= +2.58 ‰; $\delta^{18}O$= -1.15 ‰) and SUPP ($\delta^{13}C$= -49.69 ‰; $\delta^{18}O$= -16.38 ‰). A quality control standard (Gr 1, Triassic marble from the Monzoni contact aureole) was ran along with the samples, and indicates a reproducibility of better than 0.1‰ (1σ) for both carbon and oxygen.

4.5. Facies analysis methods

17 thin sections from the HWQ section were studied and photographed with a polarizing microscope at the Department of Geosciences, Padova University. The methods and principles of microfacies analysis for carbonate rocks follow Flügel (2010).

5. Results

5.1. Sedimentological and facies description of the HWQ section

HWQ section (Fig. 3) consists of about 12 m of calcareous beds, beginning with limestone in the lower part, followed by > 20 m of marly limestones interbedded with marls. HWQ section was subdivided into four lithological units (Fig. 3), i.e., an oolitic limestone unit (Unit 1), a bioclastic limestone unit (Unit 2), a microbial-sponge reef unit (Unit 3), and a terrigenous clastic unit (Unit 4). The section described here corresponds to the lower part of the HWQ section illustrated in Shi *et al.* (2017).

5.1.1. Unit 1: oolitic limestone unit

Unit 1 begins with mainly oolitic grainstones (microfacies type RMF 29 of Flügel, 2010). Bed 1 outcrops for a thickness of 0.7 meters (Fig. 3, 4A). Its base is not visible because it is cut by a fault (Fig. 3: microfacies sample Q1). In thin section, ooids display bimodal size distribution (Fig. 5A). The majority of ooids are radial and micritized (Fig. 5A), some are deformed and exhibit different bioclasts at their nuclei (e.g., foraminifera, brachiopods, echinoderms, crinoids). Some are encrusted by sessile foraminifera (Fig. 5A). Most ooids show sutured contacts with stylolites (Fig. 5A).

Bed 2 consists of bioclastic-oolitic packstone and grainstone (Fig. 3: 0.7-3.1 m; Q2), attributed to microfacies RMF 28 of Flügel (2010). Ooids are still dominant, but bioclasts, reef-derived

intraclasts and carbonate mud are also present. Grains are poorly sorted and with no preferential orientation. Limestone chips some cm in size form breccias embedded in the oolitic matrix (Fig. 4B). In thin section, the microfacies is characterized by ooids, peloids (often micritized), brachiopods, foraminifera, bivalves, fragments (intraclasts) of thrombolites, and reworked hexactinellid siliceous sponges embedded in microsparite cement (Fig. 5B). The upper boundary of Bed 2 is covered.

5.1.2. Unit 2: bioclastic limestone unit

Bed 3 is a bioclastic and intraclastic floastone (Fig. 3: 4.2-6.7 m; Q3-Q5) and corresponds to RMF 15 (Flügel, 2010). It is approximately 2.5 m in thickness, with fragments of marine fossils and plant debris, and is covered by a gray thin limestone (Bed 4 in Fig. 4C). In thin section, intraclasts are 2-5 mm in diameter, while bioclasts are mainly brachiopods, foraminifera, bivalves, with fewer ostracods and gastropods (Fig. 5C). Microbial grains also occur and are dominated by oncoids and peloids. Large fragments of siliceous sponges and intraclasts with thrombolitic fabric are present as well (Fig. 5C). Peloids may be found in interstices between bioclasts. Moreover, pyrite is common as framboids 3-7 μm in diameter and small euhedral crystals ca. 20 μm in size. In sample Q5 (Fig. 3), Pyrite is often oxidized and pervades microbial grains or surrounds them forming envelopes (Fig. 5D, E).

5.1.3. Unit 3: inter-reef unit

Unit 3 starts at the 6.7 m level (Fig. 2), with a thickness of 5.5 m (Q6-Q16). It is composed from bottom to top of mound-shaped beds of microbial boundstones (beds 4 to 6 in Fig. 4C to E) and bioclastic-thrombolitic floatstones (Bed 8, 10 in Fig. 4G) with interbedded muddy clays, followed by a 1.6 meter-thick microbial sponge floatstone (Bed 12, 14 in Fig. 4H). This sponge floatstone facies is analogous to the microbial sponge mound described in the HWG section (Wu, 1989; Wang *et al.*, 2015; Shi *et al.*, 2017). Unit 3 terminates with a fossil-rich marly limestone layer of ca. 0.5 m interfingering with wedge-shaped sponge rudstones (Fig. 4J, K). Cm-scale pyrite nodules and abundant wood fragments are seen.

The microbial boundstones at the base of Unit 3 (Fig. 3: Q6 to Q8), correspond to RMF 12 of Flügel (2010). On the field, the lowest Bed 4 is a bioclastic-microbial boundstone or microbially-bounded grainstone-rudstone, ca. 0.3 m thick (Fig. 3: Q6). It can be interpreted as a microbially bound hardground, as in thin section skeletal grains are bound by dense micrite with irregular shapes and framework pores (Fig. 6A, B). Locally, microbialites with clotted peloidal micrite fabric form encrustations (Fig. 5F, 6A, B). The skeletal grains within the hardground often have oncolitic coatings

and are further bound by dense micrite and clotted peloidal micrite (Fig. 5F, G). Pyrite framboids and crystals are pervasive in grains and their interstices and are often oxidized, i.e., they are replaced by iron oxides (Fig. 5G).

Subsequently, the beds 5 and 6 (Fig. 3: Q7 and Q8) are characterized by yellow or pale patches (Fig. 4F) similar to those recognized in the HWG section below the siliceous sponge mound (HWG section Bed 12, Fig. 3). The patches are sub-vertical with irregular borders or cauliflower-shaped, and most of them are not interconnected (Fig. 4F). In thin section, the yellow and pale patches are composed of microsparite with oxidized pyrite framboids and crystals which fill in the framework pores between siliceous sponges and thrombolites, and often contain microbial grains and others marine organisms like bryozoans and worm tubes (Fig. 5H, I).

The overlying bioclastic-thrombolitic floatstones (Fig. 3: Q9-10) are mainly composed of fragments of thrombolites, bioclasts and intraclasts, attributed to RMF 9 (Flügel, 2010). Sorting is poor and there is no preferential orientation of grains. Interparticle spaces are filled with micrite, peloids and quartz silts (Fig. 5J-L). Allochthonous fragments of siliceous sponges 1-2 cm in diameter are present, which soft parts were partially substituted by micrite with thrombolitic fabric; the remaining voids are filled by microspar (Fig. 5J). Bioclasts 1-3 cm in diameter, mainly brachiopods and bivalves, are visible (Fig. 5J). Oncoids with thrombolitic coatings display an irregular shape (Fig. 5K), and in adjacent areas rounded allochthonous thrombolite fragments often include framboidal pyrite (Fig. 5L).

The layer of microbial sponge floatstone found at top of Unit 3 (Fig. 3: Q11-15) contains disk-shaped sponges between 3 mm and 8 mm in diameter (Fig. 4I). Within the sponge floatstones, diverse bioclasts, including reef-building organisms and brachiopods, are very common (Fig. 4I). In thin section, the material between sponges is a rudstone or breccia consisting of thrombolite fragments, broken bioclasts, worm tubes and siliceous sponges (Fig. 5M). This microfacies was attributed to RMF 9 (Flügel, 2010).

Above Q15, approximately 0.5 m of marly limestone contains abundant marine fossils such as crinoids, ammonoids, bivalves and brachiopods (Fig. 4J, K), and has wedge-shaped sponge rudstone intercalations. The sponge rudstones contain worm tubes, thrombolite fragments and siliceous sponges (Q16, Fig. 5N). This microfacies was attributed to RMF 11 (Flügel, 2010).

5.1.4. Unit 4: Terrigenous clastic unit

This unit is mainly composed of dark grey shales, calcareous siltstone and sandstones with interbedded silty mudstones (Fig. 3, 4L). Benthic marine fossils are abundant and less common at higher horizons. Large pyrite nodules (max 5 cm) and wood fragments become more common in this

unit. With respect to the underlying beds, pyrite nodules here are larger and more abundant. In thin section, burrowing traces are visible (Q17, Fig. 5O). This interval may be assigned to RMF 2 (Flügel, 2010).

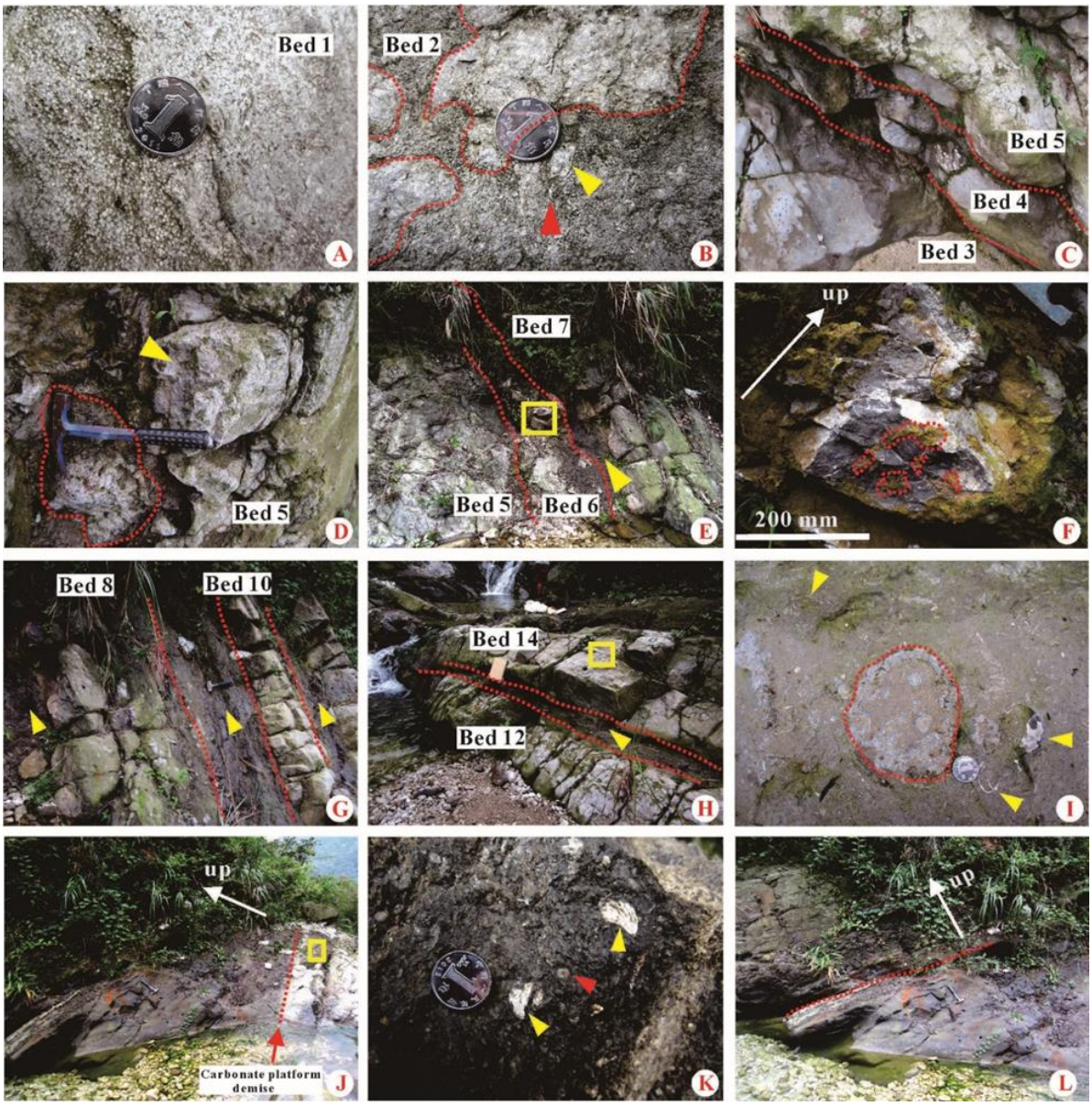

Fig. 4. Field photographs of Ma'antang Formation in the HWQ section. Coin diameter is 19 mm, hammer is ca. 30 cm long. (**A**)- Oolitic grainstones in Bed 1, the lowest part of the HWQ section. (**B**)- Limestone chips (red dashed lines) coexist with reworked intraclasts (yellow arrow) and skeletal grains (red arrow) from Bed 2. (**C**)- Contacts between beds 3, 4, 5 (indicated by red dashed lines). (**D**)- Mound-shaped bed or thrombolite head (red dashed lines) of microbial boundstone with clotted peloidal fabric (Bed 5) occur close to yellow patches (yellow arrow) at the base of Unit 3. (**E**)- Microbial boundstones (Bed 5 and Bed 6) are covered by muddy clay (Bed 7, yellow arrow). (**F**)- Close-up of poorly interconnected yellow patches from E (yellow square), exhibiting irregular shapes (red dashed lines). (**G**)- Bioclastic-thrombolitic floatstones (Bed 8, 10) with interbedded muddy clays (yellow arrows). (**H**)- Microbial sponge floatstones (Bed 12 and Bed 14) in Unit 3 with a thin clay interlayer (yellow arrow). (**I**)- Close-up of a disk-shaped sponge (red dashed line) from H (yellow square) that coexists with abundant brachiopods (yellow arrows). (**J**)- The boundary (red dashed

line) between limestone units of Unit 3 and overlying dark shales (Unit 4). (**K**)- Detail of a fossil-rich marly limestone (Bed B1) from J (yellow square), containing bivalves (yellow arrows) and crinoids (red arrow). (**L**)- The boundary (red dashed line) between dark shales and upper calcareous mudstones and siltstones.

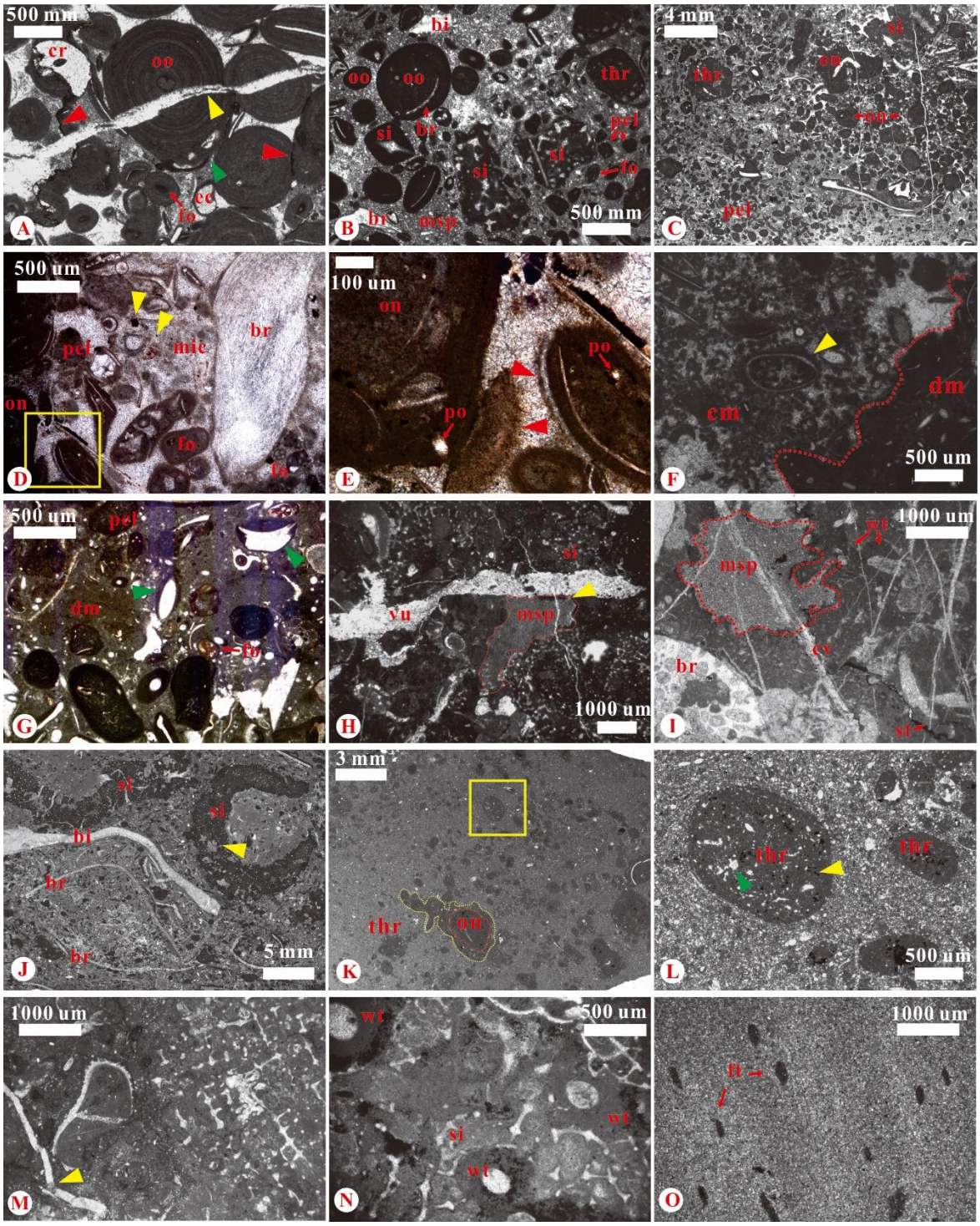

Fig. 5. Thin-section microphotographs of the Ma'antang Formation in the HWQ section. (**A**)- Sample Q1. Radial ooids (oo) which commonly have bioclast nuclei such as echinoderms (ec), crinoids (cr), foraminifera (fo), and may be encrusted by sessile foraminifera (green arrow). Stylolitic contacts are indicated by red arrows, and all components are cut by late veins filled of calcite spar (yellow arrow). (**B**)- Bioclastic-oolitic packstone and grainstone, sample Q2. Ooids (oo) are still dominant, and fragments of bivalves (bi) and brachiopods (br) are seen. Peloids (pel), reworked siliceous sponges (si) and thrombolites (thr) also occur embedded in microsparite cement (msp), and sorting is bad. (**C**)- Bioclastic and intraclastic floatstone, sample Q5. Bioclasts

and intraclasts as reworked siliceous sponges (si) and fragments of thrombolite (thr) occur along with oncoids (on). Intergranular spaces are filled with microsparry cement and small peloids (pel). (**D**)- Detail from sample Q5. Oxidized pyrite (yellow arrows) pervades oncoids (on), peloids (pl), foraminifera (fo) and micrite (mic). A well preserved brachiopod (br) is seen. (**E**)- Enlargement of D (yellow square). Oxidized pyrite pervades microbial grains (on) or surround them as envelopes (red arrows). Micropores (po) are commonly seen. (**F**)- Microbial boundstone and hardground surface in sample Q6. A clear boundary between lithified dense micrite incorporating skeletal grains (dm) and thrombolite or clotted peloidal micrite (cm) is highlighted by the red dashed line. In the center of the thrombolite part, a brachiopod fragment with oncolitic-microbial coating (yellow arrow). (**G**)- Detail of dense micrite (dm), sample Q6. Some skeletal grains have oncolitic coatings (green arrows). Oxydized pyrite, identified by its yellowish colour, is common in dense micrite, peloids (pel) and foraminifera (fo). (**H**)- Microbial boundstone of sample Q7 with in situ siliceous sponges (si) and framework pores (red dashed line). The pores are commonly filled with microsparite (msp) and contain oxidized pyrite, a late vein (vu) cuts everything. (**I**)- Microbial boundstone of sample Q8 with abundant reef-building organisms including bryozoans (br), worm tubes (wt), siliceous sponges (si). Framework pores (red dashed line) are filled with microsparite (msp) and contain oxidized pyrite. A stylolite (st) cuts, and is subsequently cut by, late calcite veins (cv). (**J**)- Bioclastic-thrombolitic floatstone of sample Q9 with reworked siliceous sponges (si) with soft parts substituted by clotted peloidal micrite with framework cavities (yellow arrow: note that substituted spicules are preserved also in the cavities, which excludes dissolution), and bioclasts as bivalves (bi) and brachiopods (br). Interstitial space is filled with micrite, peloids and fine terrigenous sediment. (**K**)- Microphotograph of sample Q10 displaying allochthonous oncoids (red dashed line) with thrombolitic coatings (yellow dashed line) of irregular shape. The allochthonous thrombolites (thr, intraclast) are more common and identified because they are worn and mildly rounded. (**L**)- Detail of allochthonous thrombolites (thr) from K (yellow square). Framboidal pyrite (yellow arrow) concentrate in grains. The green arrow points to framework or dissolution cavities in the thrombolite fabric. (**M**)- Microbial sponge floatstone or breccia from sample Q15. Bioclasts are often broken (yellow arrow). (**N**)- Sponge rudstone of sample Q16 mainly consists of worm tubes (wt) and siliceous sponges (si). (**O**)- Fossil traces (ft) filled with carbonate mud in the silty mudstone of sample Q17.

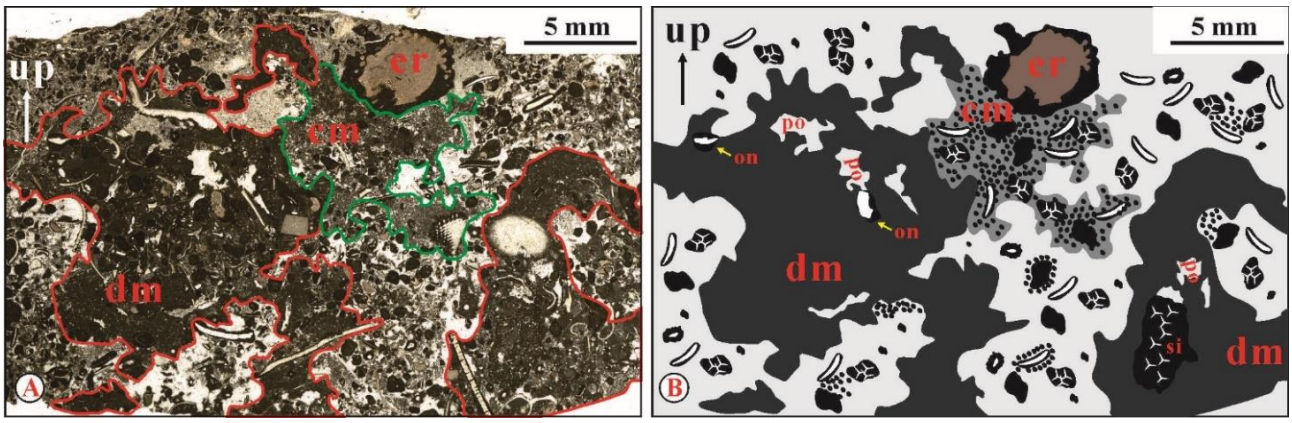

Fig. 6A-B. Hardground (sample Q6) as seen in thin section. The hardground part (red line) consists of dense micrite (dm) and various grains like oncoids (on), reworked siliceous sponge (si), bioclasts and peloids. Above the hardground, the infilling consists of an intra-bioclastic grainstone that is locally cemented by clotted peloidal micrite (cm, green line). po: framework pores; er: echinoderm.

5.2. Biostratigraphy

Several conodont elements were collected from the heavy residues. A conodont assemblage consisting of *Paragondolella noah* (Fig. 7/1), *Carnepigondolella angulata* (Fig. 7/2) and *Hayashiella tuvalica* (Fig. 7/3) was collected from Unit 1 (A in Fig. 3). Higher in Unit 2 (B and C in Fig. 3), a conodont association composed by *Epigondolella miettoi* (Fig. 7/4), *Carnepigondoella orchardi* (Fig. 7/5), *Carnepigondoella* cf. *orchardi* (Fig. 7/7) and *Paragondolella noah* (Fig. 7/8) was recovered. All conodonts show a Color Alteration Index (CAI) of 1.

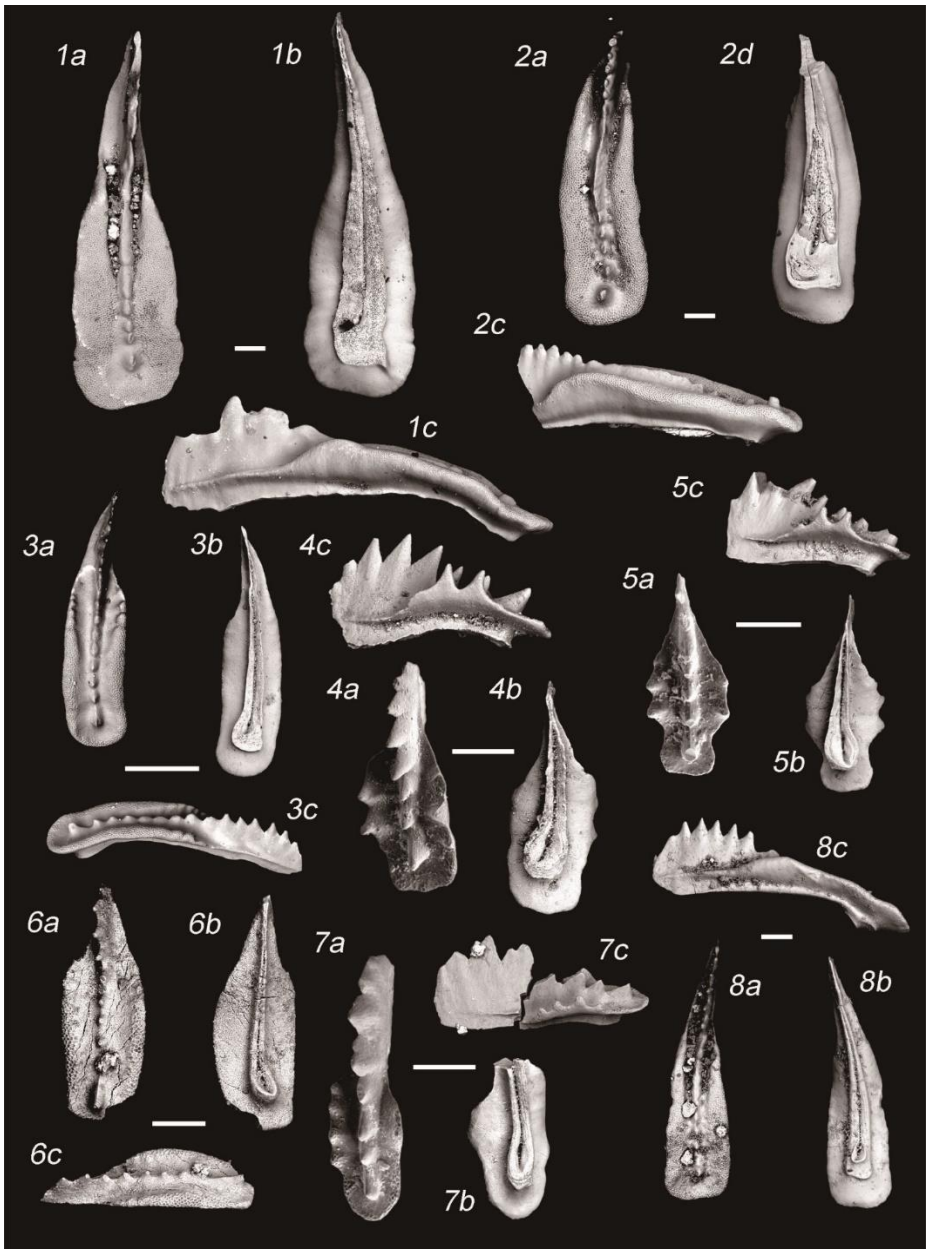

Fig. 7. S.E.M. Photomicrographs from the HWQ Section. (**1**) *Paragondolella noah*; (**2**) *Carnepigondolella angulata*; (**3**) *Hayashiella tuvalica*; (**4**) *Epigondolella miettoi*; (**5**) *Carnepigondoella orchardi*; (**6**) *Norigondolella?* sp.; (**7**) *Carnepigondoella* cf. *orchardi*; (**8**) *Paragondolella noah*. For each species: (a) upper view, (b) lower view, (c) lateral view. Specimen 1 to 3 (A in Fig. 3); Specimen 4 to 6, 8 (B in Fig. 3); Specimen 7 (C in Fig. 3) Scale bar 100 m. CAI=1.

5.3. Optical, SEM and CL microscopy for the assessment of diagenesis

5.3.1. Brachiopods

SEM images of brachiopods from the HWQ are shown in figure 8(A-I). In the articulate brachiopods sampled at the HWQ, shells exhibiting smooth or fibrous surface are inferred to be made of the original low magnesium calcite (LMC) of the secondary layer (Fig. 8A, B, F). In most cases shells have punctae (Fig. 8C-E), they are spaced by ca. 15 μm and between 10 and 40 μm in diameter. Microdrill sampling traces, cracks and dissolution are seen (Fig. 8F-I). In CL, most brachiopods from the HWQ display no luminescence, however the punctae or cracks have bright luminescence similar to that of the surrounding matrix and late cement (Fig. 8J-L).

To assess the influence of secondary carbonates that fills the punctae on the results from stable isotopic geochemistry, we considered 17 SEM images of brachiopod shells displaying no cracks or evidences of dissolution (Fig. 8C). Per each image, a region of the same size was selected and the area occupied by punctae was calculated (Fig. 9A; Table 1). The area covered by punctae ranges between 0 and 19 % of the total image area in these samples. The $\delta^{18}O$ and $\delta^{13}C$ versus area ratio is shown in figure 9B. A strong correlation between $\delta^{18}O$ and punctae area ratio is observed. In contrast, the $\delta^{13}C$ is not significantly correlated with the punctae area ratio.

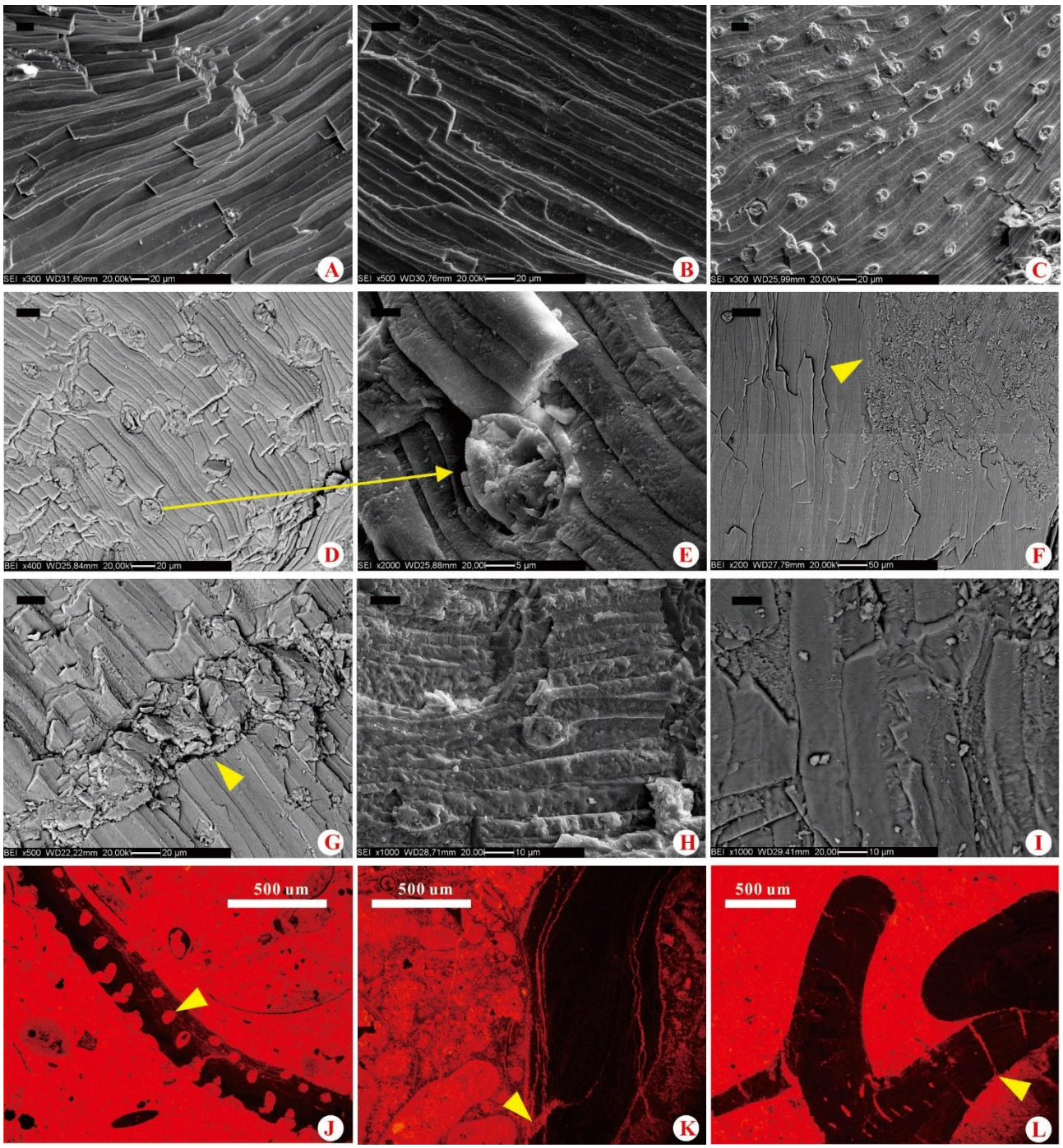

Fig. 8. SEM and CL images of brachiopod shells in the HWQ section. (**A-B**)- Low Mg-calcite secondary layer of well-preserved brachiopods displaying smooth fiber structure. Bar scale = 20 μm. (**C-D**)- Punctae structures. Bar scale = 20 μm. (**E**)- Enlarged detail of a punctae from D, which is filled with late calcite. Bar scale = 5 μm. (**F**)- Microdrill sampling traces (yellow arrow). Bar scale = 50 μm. (**G**)- Cracks (yellow arrow) in the secondary layer of a brachiopod shell. Bar scale = 20 μm. (**H-I**)- Dissolution in secondary layer, as highlighted by the irregular, etched texture of calcite fibers. Bar scale = 10 μm. (**J**)- Punctate brachiopod shell with no CL, while the punctae are filled with sediment or cement with bright CL (yellow arrow). (**K**)- Cracks in brachiopod filled by a cement with bright CL (yellow arrow). (**L**)- Well preserved brachiopod with small cracks which display bright CL (yellow arrow).

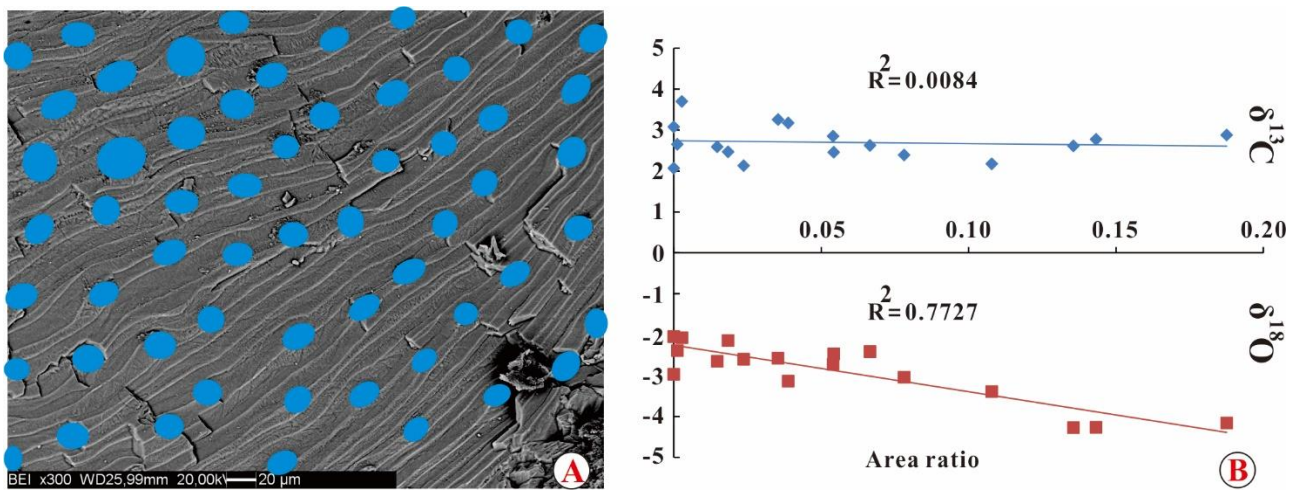

Fig. 9. Estimation of the influence of punctae on the carbon isotopic composition of powders sampled from brachiopod shells. (**A**)- An example of punctae distribution in a secondary layer of a brachiopod shell, the blue ellipses are punctae that were manually segmented. (**B**)- Stable isotopic composition of powders sampled from brachiopod shells versus the punctae area ratio. The value of 0.0084 for the R^2 between $\delta^{13}C$ and area ratio is not significantly different from 0 at the 95% confidence level.

Image area (px)	Punctae area (px)	Punctae (n)	Area ratio	$\delta^{13}C$	$\delta^{18}O$
1310720.00	31083.76	4	0.02	2.13	-2.60
1310720.00	177693.16	13	0.14	2.62	-4.27
1310720.00	70820.03	13	0.05	2.85	-2.72
1310720.00	141393.54	5	0.11	2.17	-3.39
1310720.00	71075.23	28	0.05	2.46	-2.47
1310720.00	3545.86	1	0.00	3.70	-2.07
1310720.00	102457.71	13	0.08	2.39	-3.04
1310720.00	0.00	0	0.00	2.07	-2.97
1310720.00	19274.88	3	0.01	2.59	-2.65
1310720.00	87223.93	13	0.07	2.62	-2.41
1310720.00	24159.65	2	0.02	2.47	-2.14
1310720.00	1569.81	1	0.00	2.65	-2.39
1310720.00	0.00	0	0.00	3.08	-2.05
1310720.00	245812.91	33	0.19	2.88	-4.16
1310720.00	50839.92	17	0.04	3.17	-3.13
1310720.00	187788.92	8	0.14	2.78	-4.26
1310720.00	46372.63	19	0.04	3.26	-2.57

Table. 1. Total image area, punctae area, number of punctae and carbon and oxygen isotopic values in brachiopod samples.

5.3.2. Other sedimentary components and cements

Grains and cements in the HWQ section were observed with optical and CL microscopy, in order to identify a sequence of cement phases and associate stable isotopic features to specific cements and sediment types (See in Table 2), whenever possible. The diagenetic phases shown in Table 2 are given in a chronological order. The CL expression of grains and cements is complex and varies with stratigraphy, and some cement phases only occur in specific stratigraphic intervals.

At the bottom of Bed 2 (sample Q2), ooid laminae show no CL, and their nuclei have patchy luminescence or uniformly bright CL (Fig. 10A). Interparticle spaces are filled by sparry calcite cements showing bright CL (b2). They are generally cut by calcite veins which display bright/patchy CL (v1 in Table 2 and Fig. 10A). A few centimeters below (sample Q1), all ooids display instead moderate CL, and the interparticle spaces are filled by two types of calcite cements. The b1 calcite cement grows atop the ooids showing moderate/patchy CL, and b4 calcite cements fill in the remaining pore space and show no CL. All components are cut by v1 calcite veins (Fig. 10B).

Microbial grains also can exhibit different CL in different layers. In Bed 3 (sample Q5), most oncoids (m1) show moderate CL and are rimmed by dog tooth calcite cements (c1) which have no luminescence. The b1 cements grow atop c1, and interstitial micrite showing moderate CL (m2) is abundant (Fig. 10C). Encrusting foraminifera have the same CL as m1 (Fig. 10C). In Bed 12 (sample Q12) most oncoids (m1) are instead non-luminescent, commonly encrusted by sessile foraminifera which chambers are filled by a bright CL cement, probably b2 (Fig. 10D).

In Bed 6 (sample Q8), the yellow fillings of framework pores are composed of microspar displaying very bright cathodoluminescence (Fig. 10E). The surrounding fine microbial grains (m1) have moderate to dull CL and coexist with bryozoans whose zooecia are filled by bright CL cement (b2?). The v2 calcite veins cut all grains and are filled by dull to non-luminescent calcite (Fig. 10E). In Bed 8 (sample Q9), fragments of siliceous sponges consist of non-luminescent spicules substituted by chalcedony and chert (ch), and the surrounding microbial carbonates (m1) showing dull CL (Fig. 10F).

In the hardground of Bed 4 (sample Q6 in Fig. 3), three generations of calcite cement fill the framework pores. The first are dull to non-luminescent rims of dog-tooth cement (c1), followed by a sparry calcite cement with moderate to dull CL (b1) (Fig. 10J). A third cement (b4), again a sparry calcite, occurs at the center of larger pores and shows no CL (Fig. 10J). In the oxidized part of this hardground, the microbial grains (m1) show no CL and coexist with brachiopods which shells show no luminescence; the intraparticle spaces are filled in microspar which has moderate CL (Fig. 10H).

Phase	Cement (sediment) type	Inferred original mineralogy	Crystal type and property	CL	Crystal size/cement size	Diagenetic phase	Sedimentary interval	Stable isotope signature
m1	Microbial carbonate (Fig. 10C-F, H)	Aragonite and/or high-Mg calcite	Oncolitic and thrombolitic structures	Moderate to no	20 μm to 5 mm	Marine phreatic	All intervals	$\delta^{13}C$: closed to brachiopods or lightly depleted, $\delta^{18}O$: moderate
m2	Micrite (Fig. 10C, D, J)	Aragonite and/or high-Mg calcite	Microcrystalline, partially filling intergranular pore space	Moderate to no	< 5 μm	Marine phreatic	All intervals	N/A
sc	Isopachous calcite cements	Aragonite and/or high-Mg calcite	Needle (thin and small),forming the rims of ooids and grains	Dull	< 20 μm	Marine phreatic	Q1 to Q3, Q5, Q7	N/A
c1	Dog tooth to fibrous calcite cements (Fig. 10C, J)	Calcite or high-Mg calcite	Elongated and pore-filling, some growing atop sc	Dull to no	20 μm to 150 μm	Marine phreatic/shallow burial	Q5, Q6	N/A
py1	Oxidized pyrite	Sulfide mineral	Framboids and crystals	No	From 1 μm to 50 μm	Marine phreatic/shallow burial	Q5 to Q8, Q15	N/A
py2	Unoxidized pyrite (Fig. 10D)	Sulfide mineral	Black framboids and crystals	No	Mainly 3 μm to 20 μm up to a few cm	Marine phreatic/shallow burial	All intervals (big crystals only exist in Q15 to Q16)	N/A
c2	Dog tooth to fibrous calcite cements	Calcite or high-Mg calcite	Elongated and pore- or crack-filling, somewhere growing atop c1	Bright	From 250 μm to 800 μm (elongate orientation)	Shallow burial	Q5, Q7	Both are closed to brachiopods
msp	Microspar (Fig. 10D-F, H)	Low-Mg calcite	Microcrystalline mosaic, replacing internal sediment of framework pores and interstices of grains, locally geopetal	Bright	Mainly 10 μm to 20 μm	Shallow burial	All intervals	N/A

Table. 2-A. Properties of diagenetic phases in HWQ section

b1	Sparry calcite cements (Fig. 10B, C, J)	Low -Mg calcite	Drusy to equant (late poikilotopic, small), pore-filling phases, somewhere growing atop c1 and m2	Moderate/patchy	From 50 μm to 100 μm	Shallow burial	Q1 to Q8	N/A
b2	Sparry calcite cements (Fig. 10A)	Low-Mg calcite	Equant (small), intergranular or framework pores filling, somewhere growing atop c1	Bright	Generally 20 to 100 μm	Shallow burial	All intervals	N/A
b3	Sparry calcite cements	Low-Mg calcite	Mosaic (big), growing atop previous moldic pore-filling, zonations are visible	Patchy or zoned	From 100 μm to 300 μm	Shallow burial	All intervals	N/A
b4	Sparry calcite cements (Fig. 10B, J)	Low-Mg calcite	Drusy to equant spar (late poikilotopic, big), growing atop b1,b2	No	From 150 μm to 300 μm	Shallow /deep burial	Q1 to Q6, Q16	N/A
ch	Chert, chalcedony (Fig. 10E, F)	Opal-A	Substitute sponge spicules and some carbonate shells and skeletons	No	20 μm to 200 μm up to more than 1 cm	Shallow /deep burial	Q4 to Q17	N/A
b5	Dog tooth to fibrous calcite cements	Low-Mg calcite	Elongated, substitute spicules and chalcedony	Patchy	From 20 μm to 100 μm (elongate orientation)	Shallow /deep burial	Q3 to Q8	N/A
v1	Calcite veins (Fig. 10A,B)	Low -Mg calcite	Drusy to equant (small to big),Veins cut grains and cements as late as b4, and stylolites	Bright/patchy	< 50 μm	Deep burial	Q1, Q3, Q5, Q7,Q15	N/A
v2	Calcite veins (Fig. 10E)	Low -Mg calcite	Drusy to equant spar (big),Veins cut everything up to v1	Dull/no	Generally 200 to 350 μm, few <50 um	Deep burial	Q7, Q8, Q16	$\delta^{13}C$: closed to brachiopods, $\delta^{18}O$: heavily depleted
v3	Calcite veins	Low -Mg calcite	Drusy to equant (small) cut v2	Strongly bright	From 10 μm to 25 μm	Deep burial or Telogenesis?	Q16	N/A

Table. 2-B. Properties of diagenetic phases in HWQ section

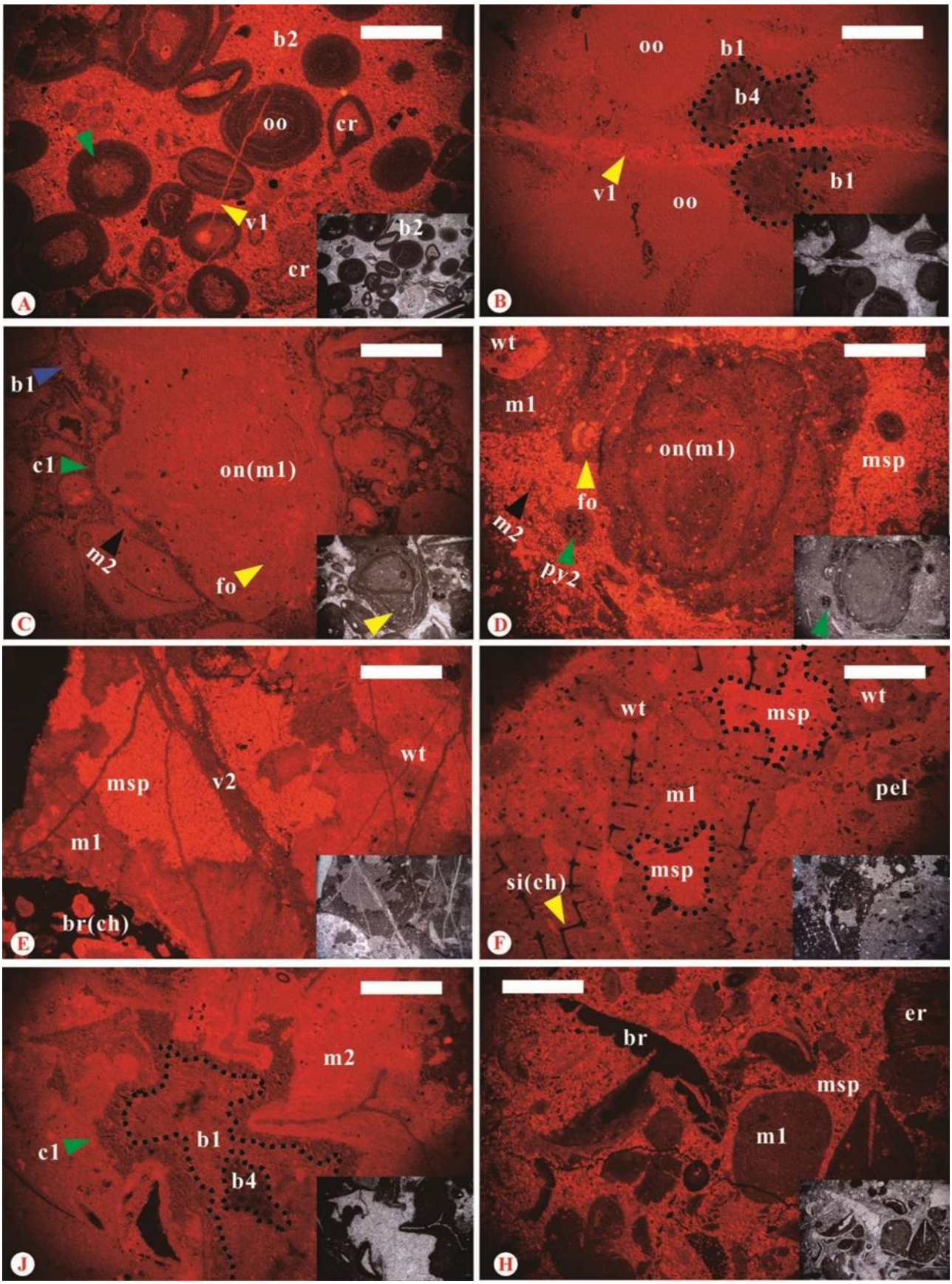

Fig. 10. CL images of different components in the HWQ section. (**A**)- Radial ooids (center) in Q2 exhibiting clear growth rims with alternate CL, intraclast nuclei showing patchy CL (green arrow). Crinoids (cr) have patchy CL. Intergranular pore space of ooids is filled with b2 sparry calcite cement showing bright CL. The v1 calcite vein (yellow arrow) cuts grains and b2 cement and has bright CL. (**B**)- Ooids (oo) displaying moderate CL in sample Q1.

The b1 calcite cements grow atop the rim of ooids and show moderate/patchy CL, followed by b4 calcite cements (dark dashed lines) with no CL. The v1 vein (yellow arrow) cuts the grains and shows patchy/bright CL. (**C**)- Sample Q5. Oncoid (on), assigned to m1 in Table 2, encrusted by sessile foraminifera (fo, yellow arrow). Both show moderate CL. C1 cements showing no CL (green arrows) are overlain by b1 cements (blue arrow) with patchy CL. Interstitial micrite (m2, black arrow) has moderate CL. (**D**)- Sample Q12. Oncoid and thrombolitic coatings (m1) are non-luminescent. Microspar (msp) with bright C also fills the chambers of sessile foraminifera (yellow arrow) and a worm tube (wt). Micrite (m2, black arrow) randomly distributes within microsparite and shows no CL. The framboidal pyrite aggregations (py2, green arrow) show no CL. (**E**)- Sample Q8. Microspar (msp) with iron oxides (from oxydation of pyrite) fills a framework pore, a worm tube (wt) and the zooecia of a bryozoan (ch) and have bright CL. Microbial carbonates (m1) have moderate to dull CL. The walls of a bryozoan (ch) have no CL. The v2 calcite veins cut everything showing dull to no CL. (**F**)- Sample Q9. Reworked siliceous sponges (si), assigned to ch in Table 2, and peloids (pel) have no CL, while the microspar (msp) in framework pores (dark dashed lines) and worm tubes (wt) shows bright CL. The microbial carbonates (m1) have moderate to dull CL. (**J**)- CL image of the hardground interval, sample Q6. In the framework pores, three generations of calcite cement are seen (c1, b1, b4). The boundary between c1 and b1 is sharp, and the early lithified dense micrite (m2) has moderate to bright CL. (**H**)- Another CL image of the hardground interval, sample Q6. Brachiopods (br) and thrombolitic microbial limestone (m1) show no CL, and their intragranular porosity is filled in microspar (msp) display moderate to bright CL. The fragments of echinoderms (er) have patchy CL. All scale bars are 500 μm.

5.4. Carbon and oxygen isotopes

Results of isotope analyses are shown in figure 11 and Table. 3. Carbon and oxygen isotopes from bulk rock (Bm, n=39) have $\delta^{13}C$ values ranging from -1.16 ‰ to +3.80 ‰, and $\delta^{18}O$ values ranging from -8.88 ‰ to -2.89 ‰. In the hardground (hg), $\delta^{13}C$ values range from -1.56 ‰ to +0.23 ‰, and $\delta^{18}O$ values from -5.18 ‰ to -2.89 ‰. Microbial carbonates (M1, n=38) have $\delta^{13}C$ values ranging from +1.15 ‰ to +3.59 ‰, $\delta^{18}O$ values ranging from -7.85 ‰ to -2.23 ‰. The brachiopods were subdivided into two groups. Articulate brachiopods (Abr, n=12) with less than 7 % punctae (see below) have $\delta^{13}C$ values ranging from +2.07 ‰ to +3.70 ‰ and $\delta^{18}O$ values from -3.13 ‰ to -2.05 ‰. Brachiopods having > 7 % of punctae, and those with cracks filled by cement or showing evidence of dissolution, were lumped together with brachiopods that could not be screened with SEM into a category of less reliable brachiopods (Ubr). Their stable isotope composition is ranging from +2.00 ‰ to +4.04 ‰ for $\delta^{13}C$ and -4.62 ‰ to -1.39 ‰ for $\delta^{18}O$. The isotopic values obtained from v2 veins (v2, n=6) are between +1.99 ‰ and +2.60 ‰ for $\delta^{13}C$, and have $\delta^{18}O$ ranging -11.02 ‰ to -9.04 ‰. In contrast, dog tooth to fibrous calcite cements (c2, n=3) show $\delta^{13}C$ ranging from +3.25 ‰ to 3.30 ‰ and $\delta^{18}O$ from -4.21 ‰ to -2.28 ‰. These values are similar to those of the screened brachiopods. The isotopic ratios in crinoids (Cr, n=4) are between +1.29 ‰ and +3.32 ‰ in $\delta^{13}C$, -7.50 ‰ and -5.61 ‰ in $\delta^{18}O$. Ooids (Oo, n=5) have $\delta^{13}C$ values from +2.43 ‰ to +3.02 ‰, $\delta^{18}O$ values from -

6.57 ‰ to -2.86 ‰.

Carbon and oxygen stable isotopic values of bulk rock, microbial grains, and brachiopods of the HWQ section are shown in figure 12. Isotope values of bulk rock display a strong > 4 ‰ $\delta^{13}C$ negative excursion in coincidence with the hardgroud in Bed 4. This apparent CIE is present, although strongly damped, also in the microbial carbonate grain profile. In contrast to $\delta^{13}C$, $\delta^{18}O$ of bulk rock and microbial grains display a positive trend in the same interval (gray band in Fig. 12). A slight negative shift may be observed in articulate brachiopods $\delta^{13}C$ as well, which however is grounded on a single analysis and is offset with respect to that on bulk and microbial grains. This possible shift should be taken with caution because of the low spatial resolution of brachiopod isotope data in the lower part of the section.

Above, $\delta^{13}C$ values of bulk rock and microbial grains gradually return to the high values recorded at the base of the HWQ. A negative shift of $\delta^{18}O$ > 3 ‰ in magnitude occurs both in bulk rock and microbial grains (OIE in Fig. 12). In contrast, no clear $\delta^{18}O$ excursion appears in articulate brachiopods and altered-unchecked brachiopods.

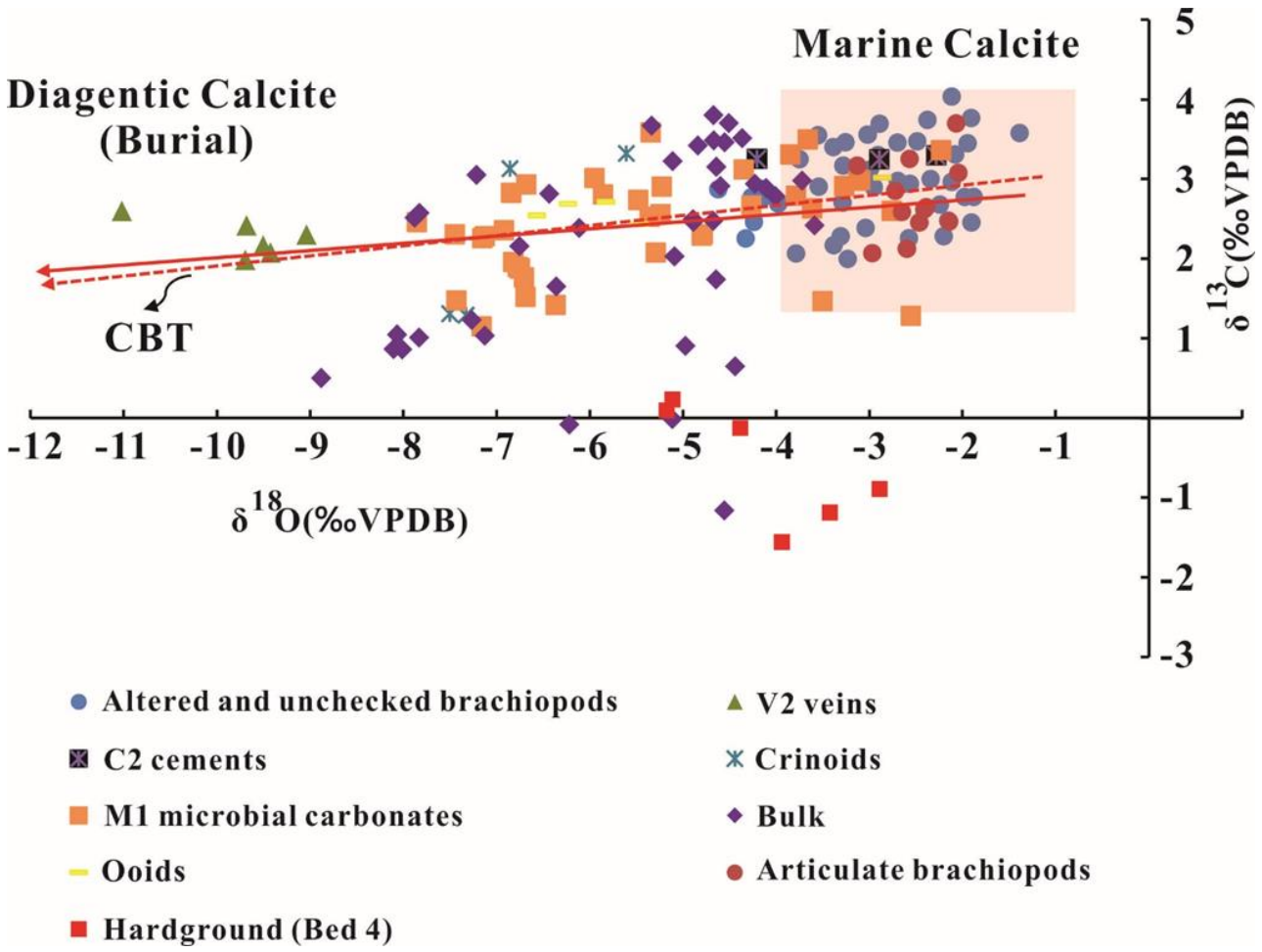

Fig. 11. Isotopic compositions of different carbonate components in the HWQ. Pink box represents isotopic variation of Carnian well brachiopods (Korte *et al.*, 2005). The dashed line represent contemporaneous burial trend (CBT, Hasuik *et al.*, 2016). The red continuous line is the linear fit to the data in this study (Slope = 0.17; R^2 = 0.1057).

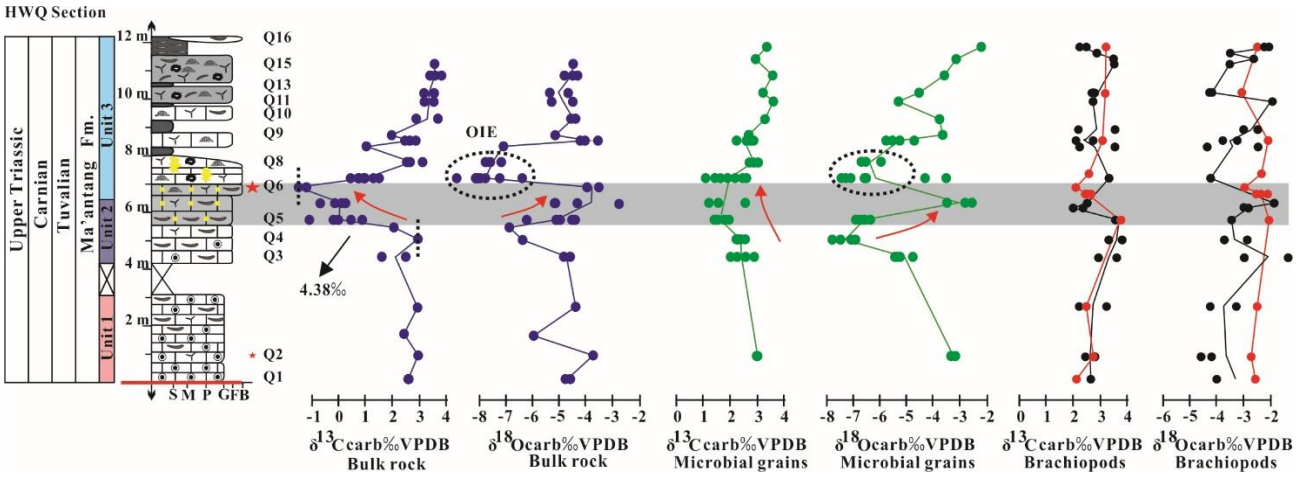

Fig. 12. Carbonate carbon and oxygen stable isotopes in bulk rock, microbial grains, and brachiopods in the HWQ section. The negative shifts in microbial grains and matrix in $\delta^{13}C$ synchronize with hardground formation (big red star). Red dots represent articulate brachiopods, black dots represent altered-unchecked brachiopods. "OIE"= oxygen isotopic excursion.

6. Discussions

6.1. Facies interpretation and depositional profile

The facies distribution and depositional profile of the HWQ are shown in figure 13. The basal ooid grainstone can be interpreted as a high-energy shallow shoal or bank environment, above the wave base in the inner ramp (Fig. 13).

The following bioclastic-oolitic packstone and grainstone are assigned to RMF 28 (Fig. 13: Q2) and consist of mixed components including intraclasts, bioclasts and microbial grains, exhibiting a disorganized fabric that can be recognized both in outcrop and thin section (Fig. 4B and 5B). The mixed components and bimodal distribution may be attributed to storm overprint that commonly occurs in the ramp environments (e.g., Burchette and Wright, 1992; Flügel, 2010). The occurrence of siliceous sponge fragments in Unit 1 (Fig. 5B) suggests that sponge mounds were growing in the vicinities. This facies may have been deposited between the inner to mid ramp and still represents a high energy environment. Cm-scale intraclastic breccia elements are to be ascribed to early cementation and may indicate the formation of poorly developed hardground surfaces (Christ *et al.*, 2015).

Bioclastic and intraclastic floatstones of Unit 2 (Fig. 5C) are attributed to RMF 15. The abundant microbial grains, ooids which commonly have intraclasts as nuclei, diverse marine organisms and reef-derived intraclasts and skeletal grains indicate a high energy environment compatible with open marine conditions. Li *et al.* (2014) speculated on the water depth of oolitic shoals and bioclastic dominated facies of the Sichuan Basin, and concluded that it may range from 2 m to 30 m, with the

bioclastic dominated facies being deeper than oolites, based on fossil assemblages.

The microbial boundstones of the lower Unit 3, classified in RMF 12, may occur from the distal part of inner ramp to the whole middle ramp according to Flügel (2010).

In sample Q6, a hardground is identified. Various skeletal grains are bound by dense micrite or microbialite with irregular shape, and bioclasts and intraclasts are commonly coated by clotted peloidal micrite (Fig. 5F, 6A, B). Similar microbial coatings were found in a Miocene hardground of central Italy by Mutti and Bernoulli (2003) and were interpreted to have been deposited in the middle ramp.

Above, reef-builders within the microbial boundstone are not dominant but diverse, framework pores are widespread and are filled by microsparite containing pyrite framboids and crystals (Fig. 5I), some of which are oxidized thus forming yellow patches. Shi *et al.* (2017) interpreted framework pores with yellow infills as dissolution features caused by subaerial exposure. However, the bounding walls of yellow patches are surrounded by worm tubes, siliceous sponge and microbialite with thrombolitic fabric that are neither abraded nor dissolved, as it would be expected for karst cavities or dissolution-enhanced fractures. Moreover, the infillings of yellow patches have bright CL (Fig. 10E) and contain marine fossils, which is opposite to what would be expected if these were filled in a meteoric environment.

Above, in Unit 3 bioclastic- thrombolitic floatstones attributed to RMF 9 are found interbedded with clays (Fig. 3 and Fig. 4G). These floatstones are dominated by poorly sorted allochthonous bio- and intraclasts, with the majority of intraclasts being made of fragments of thrombolitic boundstone with high sphericity (Fig. 5K, L). These features strongly suggest an intra-reef (or inter-bioherm) environment (Wu, 1989). The microbial floatstones in the upper part of Unit 3 are formed by worm tubes, thrombolite fragments and siliceous hexactinellid sponges (Wu, 1989). These sponge microbial floatstones at the HWQ are correlated to the massive sponge mound in the HWG section and the sedimentary environment is referred to the outer part of a middle-ramp, in agreement with Wu (2009). On the base of the original thickness of in situ sponge reefs in this area, Li *et al.* (2014) estimated the depth of sea water surrounding the reefs to more than 150 m. Fine quartz silt becomes common starting from the upper sponge reef beds (Fig. 4H). This terrigenous sediment supply has been attributed to episodic storms (Yang *et al.,* 2010). Turbid and muddy waters may have provided nutrients for siliceous sponges and other heterotrophs (Wang *et al.*, 2012, 2015).

Subsequently, marly siltstone attributed to RMF 11 and RMF 2 (Flügel, 2010), rich in open marine fossils as ammonoids, indicate that local sea level kept rising. Dm-scale pebbles made of sponge-bearing boundstone are found within the marly siltstone and probably come from an upper part of the ramp. The following dark grey shales at the base of Unit 4 contain cm-scale pyrite nodules, and ammonoids which again indicate a deep water environment. Then a thick succession of laminated

and bioturbated siltstone follows, with marine fossils. This facies represents an outer ramp to basinal depositional environment. The seawater depth may have exceeded 300 m in this interval (Li *et al.*, 2014), which was deposited into a foredeep according to Li *et al.* (2003, 2011a). The presence of a nearby emerged land being actively eroded explains the common occurrence of plants along with open marine fossils.

In short, from the basal oolitic grainstones to the top shales and silts, a transgressive sequence is documented. This overall deepening-upward trend may have been punctuated by shorter episodes of sea-level change as suggested by Shi *et al.* (2017), but we could not find unambiguous evidence from facies analysis that may indicate a karst surface in the lower part of Unit 3. Yellow patches, formerly interpreted as karst cavities, are instead framework pores (Fig. 5I) with features suggestive of formation in seawater. We thus interpreted these yellow patches, and similar gray patches, as the sediment and cement infilling of primary framework cavities of a porous microbial-sponge boundstone.

The increase of terrigenous input is widely recognizable during the Carnian in the western Sichuan Basin (Li *et al.*, 2014; Shi *et al.*, 2017) and is considered as a possible cause of the demise of sponge reefs and carbonate platforms in the area (Wu, 2009). It has been compared to the Carnian Pluvial Event of western Tethys (Shi *et al.*, 2009, 2017; Wang *et al.*, 2015).

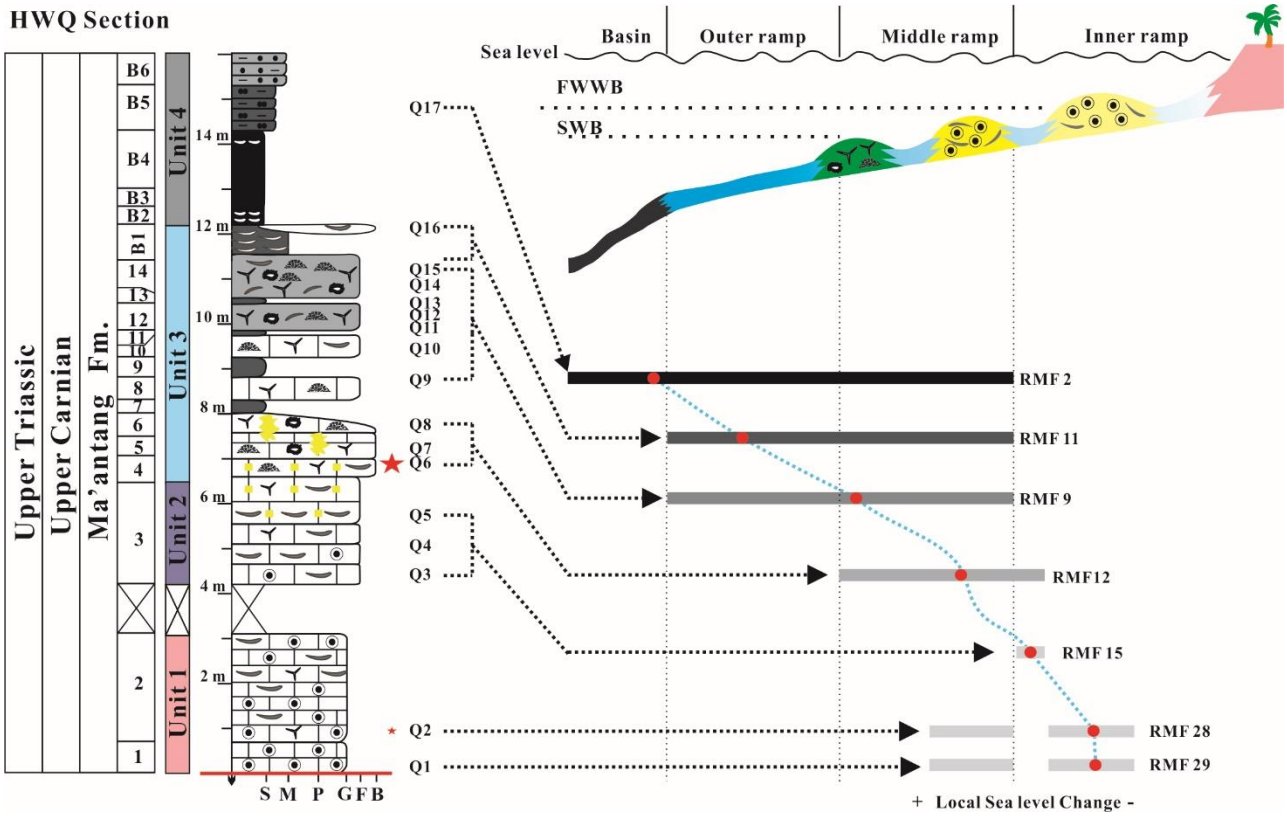

Fig. 13. Facies distribution and depositional profile from Q1 to Q17 in the HWQ section. FWWB= fair weather wave base; SWB= storm wave base. "RMF"= Ramp Microfacies Types (Flügel, 2010).

6.2. Biostratigraphic age

A conodont assemblage consisting of *Paragondolella noah*, *Carnepigondolella angulata* and *Hayashiella tuvalica* was collected from Bed 2 in Unit 1 (A in Fig. 3; see also Fig. 7). In particular, In Bed 3 (B and C in Fig. 3), a conodont association composed by *Paragondolella noah*, *Carnepigondoella orchardi*, *Epigondolella miettoi* and *Carnepigondoella* cf. *orchardi* (C in Fig. 3) was recovered.

The conodont associations recovered from units 1 and 2 of the HWQ section are known from several localities in Europe and North America, such as Pizzo Mondello (Sicily, southern Italy) (Mazza *et al.*, 2012); Lagonegro Basin (southern Apennines, Italy) (Rigo *et al.*, 2012, 2018); Black Bear Ridge (British Colombia, Canada) (Orchard, 2014). The distribution of these species is best known from Pizzo Mondello in Sicily, a candidate stratotype section for the Carnian/Norian boundary (e.g., Mazza *et al.*, 2012; Rigo *et al.*, 2018). *C. angulata*, found in Unit 1 at the HWQ, characterizes the lower part of the *Carnepigondolella orchardi* zone (Mazza *et al.*, 2012; Rigo *et al.*, 2018) at Pizzo Mondello, while *E. orchardi* and *E. miettoi* (found in Unit 2 of the HWQ) show a narrow, slightly higher stratigraphic distribution still in the *C. orchardi* zone within the upper part of the Upper Carnian.

Shi *et al.* (2017) illustrated platform conodont elements from the nearby HWG section that are all determined as belonging to a single taxon, *Quadralella polygnathiformis* (=*Paragondolella polygnathiformis* in this work). Unfortunately, our attempt at obtaining conodonts from the HWG section yielded only fragmented specimens that could not be determined with confidence. Nevertheless, we here contend that the taxon *Q. polygnathiformis* has a broad meaning and includes taxa that in other taxonomical schemes belong to distinct species, like *Paragondolella praelindae* (Fig. 9/3 in Shi *et al.*, 2017) or *Paragondolella noah* (Fig. 9/2, 6 in Shi *et al.*, 2017), the age of which could or should be Late Carnian (e.g., Orchard, 2010; Mazza *et al.*, 2012; Rigo *et al.*, 2018).

This new age determination would imply a new correlation of the paleomagnetic stratigraphy of Zhang *et al.* (2015). However, only three fossiliferous horizons could be dated so far and in a short portion of the section. More biostratigraphic data are needed in order to propose a new correlation of the magnetic stratigraphy of the HWQ with the standard Triassic APTS.

6.3. Alteration of carbonate $\delta^{13}C$ and $\delta^{18}O$ in punctated brachiopods

The majority of sampled articulate brachiopods in this study have punctae (Fig. 8C, D, E), which are filled by carbonate cement exhibiting bright CL (Fig. 8J). Punctae are one of the most characteristic morphological features in terebratulide brachiopods (Pérez Huerta *et al.*, 2009). They

penetrate through both calcitic primary and secondary layers, and biomineralization processes different with respect to those forming the fiber structure are thought to be involved in their genesis (Pérez Huerta *et al.*, 2009). If precipitated during burial, cement in punctae may have high concentrations of Fe and Mn but low Sr content (Bruckschen, *et al.*, 1995; Veizer *et al.*, 1999; Riechelmann *et al.*, 2016). This feature, when punctae are particularly abundant, is thought to be responsible of the high Fe and Mn enriching that is found in terebratulid brachiopod shells (Voigt *et al.*, 2003). Due to the presence of cement within the punctae, a potential alteration of the otherwise pristine oxygen and carbon isotopic composition of brachiopod calcite can be expected (Voigt *et al.*, 2003). Since punctae are small and abundant, contamination due to unwanted collection of the post-depositional materials that fills them during sampling for isotope analyses cannot be avoided.

The proportion of punctae revealed a strong correlation with $\delta^{18}O$ (R^2= 0.77), however, for a proportion of punctae of 7 % or less, $\delta^{18}O$ values are indistinguishable from those of non-punctated brachiopod shells (Fig. 9B). We set this threshold as a criterion of unaltered brachiopods in this study (Abr, see in Table 3). Instead, no significant correlation was found between $\delta^{13}C$ and the area of punctae (R^2 = 0.001). This is likely due the fact that the material infilling the punctae underwent diagenetic alteration that altered the oxygen isotopic composition, but was not severe enough to impact on the $\delta^{13}C$. This simple test demonstrates that punctae are probably a negative factor when using $\delta^{18}O$ to reconstruct paleotemperatures (Cusack *et al.*, 2012), but also provides a mean to exploit at least some of the punctated brachiopod shells. It also suggests that $\delta^{13}C$ from all brachiopod shells in this study are mostly pristine, despite a significant contamination from the cement infilling of punctae.

	$\delta^{13}C$ (min)	$\delta^{13}C$ (max)	$\delta^{13}C$ (mean)	$\delta^{13}C$ (stdev)	$\delta^{18}O$ (min)	$\delta^{18}O$ (max)	$\delta^{18}O$ (mean)	$\delta^{18}O$ (stdev)	*n*
Bm	-1.16	3.80	2.14	1.22	-8.88	-2.89	-5.65	1.48	39
Hg	-1.56	0.23	-0.57	0.74	-5.18	-2.89	-4.15	0.92	6
M1	1.15	3.59	2.48	0.63	-7.85	-2.23	-5.32	1.68	38
Abr	2.07	3.70	2.75	0.48	-3.13	-2.05	-2.51	0.34	12
Ubr	2.00	4.04	2.95	0.51	-4.62	-1.39	-3.01	0.84	45
V2	1.99	2.60	2.26	0.23	-11.02	-9.04	-9.73	0.68	6
C2	3.25	3.30	3.27	0.03	-4.21	-2.28	-3.13	0.98	3
Cr	1.29	3.32	2.26	1.11	-7.50	-5.61	-6.82	0.85	4
Oo	2.43	3.02	2.68	0.22	-6.57	-2.86	-5.39	1.47	5

Table. 3. Minimal, maximal, standard deviation and mean values of $\delta^{13}C$ and $\delta^{18}O$ from different components. Bm: homogenous bulk rock; Hg: sediments in hardground; Abr: articulate brachiopods; Ubr: less reliable brachiopods; Cr: crinoids; Oo: Ooids; M1: microbial carbonates; V2: calcite veins; C2: calcite cements (described in Table 2).

6.4. Carbonate diagenesis records in $\delta^{13}C_{carb}$ and $\delta^{18}O_{carb}$

Marine abiotic carbonates are composed of high magnesium calcite (HMC) or aragonite which are easily dissolved and re-precipitated as low magnesium calcite (LMC) during diagenetic processes (Matthews, 1968). Because of this, it is not easy to discern the pristine stable isotopic signal in Mesozoic carbonates from one that is altered by late diagenetic processes (e.g., Irwin *et al.*, 1977; Dickson and Coleman, 1980; Swart, 2015). The most appropriate substrates for stable isotope analyses are biogenic low-Mg calcites, like that of articulate brachiopods (Veizer *et al.*, 1986; Brand, 1989; Wadleigh *et al.*, 1992; Veizer *et al.*, 1999; Brand *et al.*, 2003; Korte *et al.*, 2005). The low-permeability of micritic sediments is thought to preserve their primary geochemical signals as well (Weissert, 1989; Marshall, 1992; Batt *et al.*, 2007; Brand *et al.*, 2012). Notwithstanding these general guidelines, it is advisable to assess the reliability of stable isotopic data using independent observations before making a conclusion on their preservation (Brand *et al.*, 2011; Ullmann and Korte, 2015).

All isotopic data of this study are plotted in figure 11, along with the field of pristine calcite precipitated from Carnian seawater according to Korte *et al.* (2005). The isotopic data of bulk rock cover a large field of values and display a positive correlation between $\delta^{13}C$ and $\delta^{18}O$ values. Bulk rock data may be modeled with a linear fit originating in the region of pristine carbonate precipitated from seawater (i.e., the Carnian seawater of Korte *et al.*, 2005 and the isotopic composition of articulate brachiopods) and with a slope of 0.17, which is close to the "contemporaneous burial trend" (CBT) of Hasiuk *et al.* (2016). The similarity of this bulk carbonate dataset with the CBT suggests alteration of carbon and oxygen stable isotopes due to burial diagenesis, rather than meteoric or marine-meteoric mixing (Marshall, 1992; Hasiuk *et al.*, 2016).

Although the majority of brachiopods locate in the range of pristine Carnian calcite (pink square in Fig. 11), those that were defined as altered (on the base of > 7 % punctae, or having cracks, or dissolution features) have sometimes lower $\delta^{18}O$.

Ooids which have moderate to bright CL (Fig. 10B) display depleted $\delta^{18}O$ values with respect to unaltered brachiopods, but similar $\delta^{13}C$ values (Fig. 14). One non-luminescent ooid (Fig. 10A) displays isotopic values similar to unaltered brachiopods (Fig. 14). This is in agreement with the statement of Sellwood and Beckett (1991) who suggest that pristine radial ooids could be reliable substrates for stable isotopic analysis. During sampling, it is difficult to avoid both the external lamina and the nucleus, thus making these ooids unpractical as a target for isotopic analyses. However, most ooids in this study are micritized with a blackish outer lamina that may have resulted from microbial activity after the ooid formed in seawater (Li *et al.*, 2017a). Micritization may have altered the original isotopic composition of the ooid, and the possibly microbial lamina accreted on the ooid may have

formed in different seawater conditions than the ooid itself.

Microbial grains like oncoids below Bed 7 (middle part of Unit 3, see Fig. 3) often have moderate to bright CL (Fig. 10C). They often have more negative $\delta^{18}O$ than brachiopods, and slightly depleted $\delta^{13}C$ (Fig. 14). Above Bed 7, the majority of microbial grains have dull to no luminescence (Fig. 10D), and have stable isotope compositions that are close to those of articulate brachiopods (Fig. 14). This probably relates to the increase of clay (Fig. 3), which plays a role in slowing the circulation of diagenetic fluids, implying that the diagenesis of these carbonates occurred in a closed or semi-closed diagenetic environment. In the presence of clay, the diagenetic system was near to close, so that the isotopic values of oxygen were affected by higher burial temperature causing depletion of $\delta^{18}O$ (e.g., Algeo *et al.*, 1992), while $\delta^{13}C$ values were minimally affected (Marshall, 1992). Similar considerations can be done for v2 calcite veins exhibiting dull CL (Fig. 10E). Their mean $\delta^{13}C$ of +2.26 ‰ is close to that of articulate brachiopods (+2.75 ‰, see in Table 3), but $\delta^{18}O$ is much more depleted (-9.73 ‰ on average comparing to -2.51 ‰ of brachiopods). The v2 veins are pervasive in samples Q7 and 8, probably causing the oxygen isotope excursion (OIE) that occur in microbial grains and bulk rock (Fig. 12). Crinoids often have patchy CL (Fig.10A), and their stable isotopic data deviate significantly from those of brachiopods (Fig. 11). This is probably due to the typical fossilization of echinoderms, which involves impregnation by syntaxial calcite cement during burial.

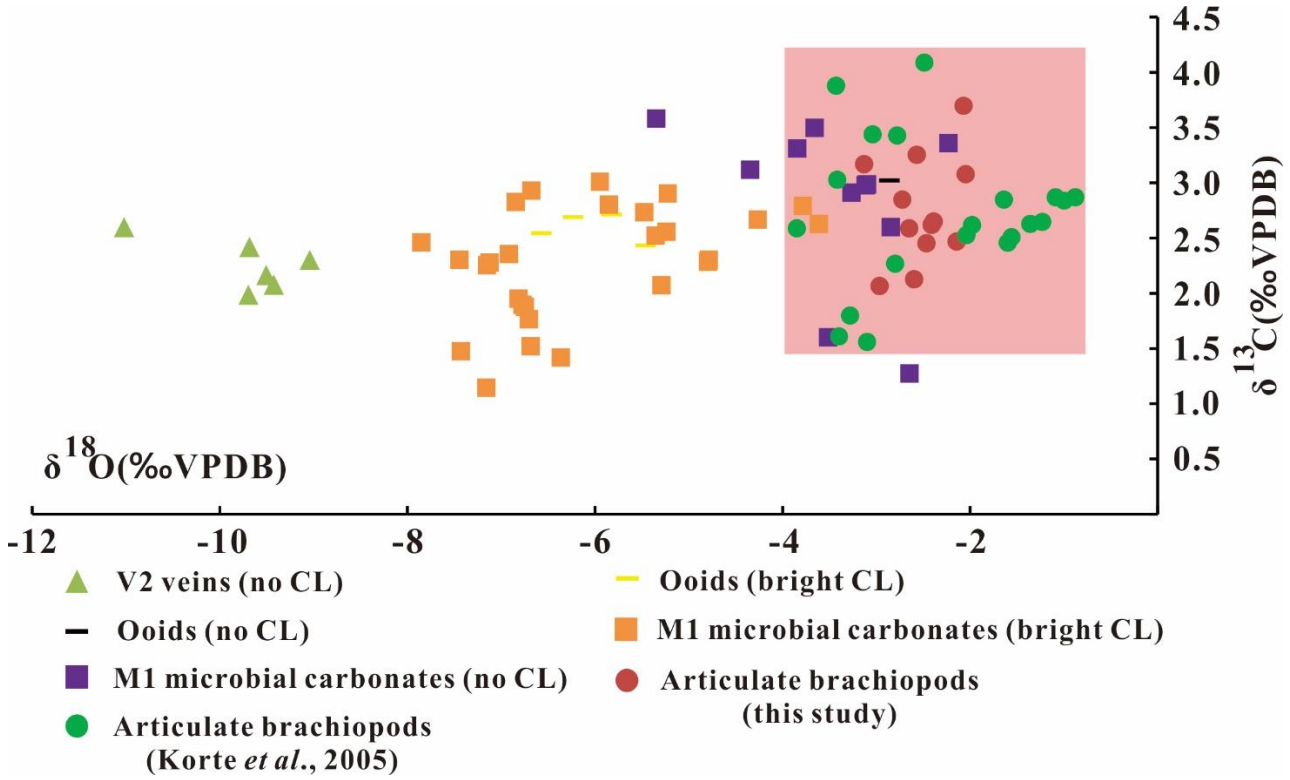

Fig. 14. $\delta^{13}C$ and $\delta^{18}O$ data of microbial carbonates (m1), ooids, unaltered brachiopods, calcite veins (v2) and well preserved from Carnian (Korte *et al.*, 2005). They are classified by different luminescence characters.

6.5. Negative $\delta^{13}C$ perturbation in the Qingyan Gou section

The $\delta^{13}C$ record of the HWQ section displays a sharp negative perturbation at meter level 5.5-7 m (Fig. 12, gray band). The magnitude of the negative shift, which is > 4 ‰ in bulk rock and < 2 ‰ in microbial grains, and the early Carnian age formerly attributed to the lower part of this section (Wu, 1989; Shi *et al.*, 2017) may suggest to correlate this CIE with the CHE. However, the new biostratigraphic data presented in this work allow dating the CIE at the HWQ to the late Tuvalian (late Carnian), therefore much younger than the onset of the CHE, which has been dated between Julian 1 and Julian 2 (early Carnian) (Hornung and Brandner, 2005; Hornung *et al.*, 2007b; Breda *et al.*, 2009; Dal Corso *et al.*, 2015).

It has been shown that the carbonate carbon isotope record can be heavily affected by diagenesis, which is essentially ubiquitous and can vary in severity (e.g., Irwin *et al.*, 1977; Dickson and Coleman, 1980; Swart, 2015; Hasiuk *et al.*, 2016).

Our data show that if isotopic compositions from brachiopods are taken into consideration, the isotope shift at the HWQ is more moderate than what is seen in bulk rocks and microbial grains, and possibly negligible (Fig. 12). Although a 1 ‰ magnitude shift is still found, this cannot be considered a major Tuvalian CIE, and may actually fall within the natural range of isotopic variability of brachiopod shells.

The large-amplitude shift in the bulk carbonate can be rather imputed to diagenesis. It is notable that in the HWQ section, facies across the negative perturbation are characterized by a hardground (Fig. 3).

Hardground formation is quite common in carbonate platforms (Christ *et al.*, 2015) and may feature crusts of microbial micrites (Nelson and James 2000; Mutti and Bernoulli, 2003) and early diagenetic precipitation of iron oxides (Mutti and Bernoulli, 2003). In Q6, dense micrite crusts with clotted peloidal fabric bind the various bioclasts and oncoids, subsequently forming a lithified sea bottom (dm in Fig. 5G; 6A, B). The clotted peloidal micrites surround what is inferred to be autochthonous sediments (cm in Fig. 5F; 6A, B), meanwhile thin rims of c1 cements, which have no CL, were precipitated. This cement includes abundant oxidized pyrite (Fig. 5E). Clotted peloidal micrites in hardgrounds were related to bacterial activity (Riding, 2000). Aerobic decomposition of organic matter by bacteria may have released ^{13}C-depleted CO_2, which then mixed with dissolved inorganic carbon in pore water and lead to precipitation of a ^{13}C-depleted hardground cement (Dickson *et al.*, 2008). ^{13}C-depleted carbonates are not rare in hardgrounds of ramps; as an example, two similar cases are reported from the Lower Cretaceous of Abu Dhabi (Dickson *et al.*, 2008) and from the Miocene of southern Italy (Mutti and Bernoulli, 2003). They both show apparent CIEs in hardground intervals, which have been ascribed to decomposition of organic matter. Mutti and

Bernoulli (2003) proposed a model of hardground formation and carbon isotopic composition of hardground carbonates that could be also applied to the Carnian ramp of the Hanwang region. According to these authors, abundant organic matter was carried by cool upwelling waters to shallow carbonate environments, which fed microbial organisms which in turn contributed to a hardground formation. The respiration of organic matter released negative carbon which was stored in coeval cements, thus depleting their carbon isotope composition. The slightly positive oxygen isotopes of these cements may relate to the cool temperature of upwelling waters.

The dull to non-luminescent c1 cements are likely to have formed in a marine phreatic to shallow burial diagenetic environment. This cement is abundant in intraparticle pores or within the microbial grains (Fig. 10C, J), it is only concentrated in the interval with hardgrounds (Q5 and Q6, see in Table 1), and is probably the source of the carbon isotopic negative perturbation.

6.6. Carbonate platform crisis of upper Carnian in South China

In the HWQ section, the sponge mounds suddenly disappeared in the late Carnian, and were covered by dark grey shales and a thick terrigenous succession with plant debris. This demise was formerly interpreted as the effect of the CHE in South China (Shi *et al.*, 2009, 2017). These macroscopic facies-changes, resemble those characteristic of the CHE worldwide: increased terrigenous input and abrupt demise of shallow-water carbonate production (Simms and Ruffell, 1989; Hornung and Brandner, 2005; Keim *et al.*, 2006; Hornung *et al.*, 2007a, b, c; Rigo *et al.*, 2007; Kozur and Bachmann, 2010; Sýkora *et al.*, 2011; Lukeneder *et al.*, 2012; Gattolin *et al.*, 2015). However, new conodonts from the HWQ section imply a late Tuvalian age for the demise of sponge mounds and the deposition of terrigenous sediments, i. e., well after the CHE.

Nevertheless, it would be arbitrary to conclude that the CHE did not have effects in Sichuan Basin, because the presence of extensive subaerial erosion in the basal HWG section (Fig. 3), which separates the Middle Triassic dolomite from Tuvalian limestones, is suggestive of a large hiatus, comprising most of the Julian. In Nanpanjiang Basin, South China, that was located approximately 550 km south of the area studied in this work, Sun *et al.* (2016) identified a carbon isotope excursion (CIE) synchronized with the deposition of black shales and marls dated to Julian 2, thus probably corresponding to the CHE. The carbonate platform underwent a crisis at this time and drowned, but the complete shutdown of carbonate production and deposition of coarse siliciclastics only occurred in the Tuvalian. Siliciclastic influx was attributed in the Nanpanjiang Basin to the development of a foreland basin, and was probably not related to climate change as in Western Europe. A similar mechanism was proposed to explain the demise of carbonate platforms in Sichuan Basin. According to Li *et al.* (2014), increased subsidence rates in a foreland basin were responsible of the drowning of

sponge mounds and the later progradation of thick siliciclastic deposits. In the HWQ, the superposition of basal oolitic grainstone, bioclastic packstone, deep water sponge mounds (Wendt *et al.*, 1989; Li *et al.*, 2014) and then dark shales rich in ammonoids make a clear deepening upward trend (Fig. 3, 13). The siliciclastic input is coeval with that observed in the Nanpanjiang Basin, suggesting that the development of a foreland basin may had a major role in the shutdown of carbonate production in the Sichuan Basin as well.

7. Conclusions

Carbonate facies of the Ma'antang Formation in the HWQ section, are assigned to seven Ramp Microfacies Types representing sedimentary environments from inner ramp to basin. Facies associations are arranged in an overall transgressive sequence.

Stable carbon and oxygen isotopes were investigated on microbial grains, bulk rock and brachiopods. The preservation of brachiopods was assessed with optical and SEM petrography, which revealed that many of the well preserved brachiopods have punctated shells. Since the punctae may be filled by late diagenetic cements and could not be avoided during sampling, the correlation between the area of punctae and isotopic composition was tested. A strong correlation (R^2= 0.77) was found between $\delta^{18}O$ and punctae area, while $\delta^{13}C$ resulted insensitive to the presence-abundance of punctae. This suggests that $\delta^{18}O$ from shells of punctated brachiopods should consider with caution in paleotemperature reconstructions. However, the area of punctae was used to assess the degree of diagenetic alteration of brachiopod samples and revealed to reasonably predict the deviation of $\delta^{18}O$ from expected Carnian values.

An ample carbon isotopic excursion is apparent in bulk rock data, which is damped in microbial grains and even more moderate or absent in well preserved brachiopods. It is thus inferred that there is no major carbon isotopic excursion in the Ma'antang Formation in Hanwang, and the excursion that is apparent in bulk rock data is a product of diagenetic alteration. It is proposed that the oxidation of organic matter of the hardground formation resulted in the precipitation of diagenetic calcite with carbon isotopic composition depleted in $\delta^{13}C$.

The more precise timing of carbonate production crisis in Hanwang area is constrained by conodont biostratigraphy to the late Tuvalian (late Carnian), indicating that it is not related to the Carnian Humid Episode. The abrupt facies changes and sudden demise of hexactinellid sponge mounds in Hanwang area might therefore be linked to the paleoenvironmental changes due to the development of a foreland basin.

Acknowledgements

We thank for Stefano Castelli (University of Padova) for realizing the conodont plate, Leonardo Tauro (University of Padova) for the thin sections. We also thank the two referees, Yadong Sun (Universität Erlangen-Nürnberg) and an anonymous, for the useful comments which improved our manuscript. We also thank Editor Diane Chung for her professional editorial work. This research was supported by the National Natural Science Foundation of China grants (Grant numbers 41272131, 41572085) and China Scholarship Council (Grant number 201508510096). This work is also in part supported by Liu Baojun Geological Science Foundation for Young Scholars (Grant number DMSM2017022).

CHAPTER 3

The aftermath of the CPE and the Carnian/Norian transition in northwestern Sichuan Basin, South China

Xin Jin [1, 2] *, Christopher A. McRoberts [3], Zhiqiang Shi [2], Paolo Mietto [1], Manuel Rigo [1], Guido Roghi [1, 4], Stefano Manfrin [1], Marco Franceschi [1], Nereo Preto [1]

1. Dipartimento di Geoscienze, Università degli Studi di Padova, Via G. Gradenigo 6, Padova, Italy
2. State Key Laboratory of Oil and Gas Reservoir Geology and Exploitation, Chengdu University of Technology, Chengdu, Sichuan 610059, China
3. Department of Geology, State University of New York at Cortland, P.O. Box 2000, Cortland, USA
4. Institute of Geosciences and Georesources, C.N.R., Via G. Matteotti 30, I-35137 Padova, Italy
*Corresponding author. E-mail address: xin.jin@studenti.unipd.it, Tel: +39 3891476394

Received 23 May 2018; Revised 31 October 2018; Accepted 1 November 2018

Abstract

The northwestern Sichuan Basin (South China) was a portion of eastern Tethys where, during the Late Triassic, a sharp lithological transition from oolitic-bioclastic limestones and sponge reef mounds to dark grey terrigenous clays, siltstones and sandstones is visible in several localities. The timing and significance of this major facies transition is still unclear. Here we report new biostratigraphic and carbon stable isotope data from Hanwang and Jushui, northwestern Sichuan Basin. Sporomorphs, ammonoids, conodonts, and halobiid bivalves show that the lithological change is Late Carnian to Early Norian in age. This amended age determination facilitates recalibration of the magnetostratigraphy in the area allowing correlation between the Late Triassic of the Sichuan Basin and the Astrochronology Polarity Time Scale. A carbon stable isotopic perturbation across the CNB is missing in our sections, or it is concealed because of the mixed organic matter sources. Our findings pinpoint the position of the Carnian/Norian Boundary to a short stratigraphic interval of ~12 m thick in the Sichuan Basin. The studied sections greatly extend the paleogeographic documentation of the Carnian/Norian Boundary and provide novel information on biostratigraphy and chemostratigraphy that should be considered to define the best position of the Norian GSSP.

Keywords: Ammonoids; Conodonts; Sporopollen; Carnian Pluvial Episode; GSSP

1. Introduction

At least two main episodes of biotic crisis and environmental change are documented during the Late Triassic, the Carnian Pluvial Episode (CPE) (Simms and Ruffell, 1989, 2018) and the end-Triassic mass extinction which is one of "big five" mass extinctions in the Phanerozoic (Raup and Sepkoski, 1982). Both are associated with major negative $\delta^{13}C$ perturbations (CIEs) (Whiteside *et al*., 2010; Dal Corso *et al*., 2018, and references therein). The CIE at the Carnian Pluvial Episode has been so far documented in a few bulk organic carbon and n-alkane records (Dal Corso *et al*., 2012, 2015, 2018; Mueller *et al*., 2015, 2016; Sun *et al.*, 2016; Miller *et al.*, 2017; Baranyi *et al.*, 2018; Shi *et al.*, 2018), and also reported in carbonate records (Sun *et al.*, 2016, 2018), while the carbon isotopic record of the end-Triassic mass extinction has been extensively studied (e.g., Hesselbo *et al.*, 2002; Schoene *et al.*, 2010; Whiteside *et al.*, 2010). In both cases, the biotic and environmental changes were possibly related to emissions of CO_2 as a consequence of the eruption of a Large Igneous Province (Furin *et al.*, 2006; Schoene *et al.*, 2010; Whiteside *et al.*, 2010; Dal Corso *et al.*, 2012, 2015, 2018; Sun *et al.*, 2016, 2018).

The stratigraphic interval after the CPE is relatively poorly studied, and the definition of the boundaries between the three Upper Triassic stages (Carnian, Norian and Rhaetian) are still matter of debate (Lucas, 2018). Two main GSSP candidate sections of Carnian/Norian Boundary (CNB) have been proposed and studied for their biostratigraphy and carbon stable isotopic stratigraphy: Black Bear Ridge in British Columbia (e.g., Orchard *et al.*, 2001; McRoberts, 2007, 2011; Orchard, 2007, 2014; Williford *et al.*, 2007; Zonneveld *et al.*, 2010; Onoue *et al.*, 2016), and Pizzo Mondello in Sicily, Southern Italy (e.g., Muttoni *et al.*, 2001; Nicora *et al.*, 2007; Mazza *et al.*, 2010, 2012, 2018; Balini *et al.*, 2012). Magnetostratigraphy is available from Pizzo Mondello (Muttoni *et al.*, 2004), and it has been suggested to locate the Norian GSSP at the first occurrence (FO) of the conodont *Metapolygnathus parvus* (Mazza *et al.*, 2018; Rigo *et al.*, 2018). *Halobia* faunas (bivalves) at Pizzo Mondello were studied and correlated to ammonoid biozones by Levera (2012), showing the *Halobia austriaca* is the best halobiid marker for defining the base of the Norian GSSP.

We here document stratigraphic sections which are younger than the Ma'antang section (Shi *et al.*, 2018) including the aftermath of CPE and CNB interval from the Longmen Shan area in northwestern Sichuan Basin, a region far from the two proposed GSSP localities of Black Bear Ridge and Pizzo Mondello (BBR and PMS in Fig. 1A).

The Sichuan Basin hosts a thick succession of Upper Triassic rocks, from Carnian ramp carbonates to Carnian-Norian marginal marine and continental siliciclastic rocks (Li *et al.*, 2003; Wu,

2009). Their sequence stratigraphic correlation has been discussed by He *et al*. (2011) and Mei and Li (2017), mainly combining outcrop with core data. Fragmentary biostratigraphic data include ammonoids and bivalves (Wu, 1989; Wang, 1992; Shi *et al.*, 2017), foraminifera (He, 1980), conodonts (Shi *et al.*, 2017; Jin *et al.*, 2018a) and palynofloras (Li and Wang, 2016; Li *et al.*, 2016, 2017b). The CNB in the area was so far positioned on the basis of these scarce biostratigraphic data and is still poorly constrained. Recently, Li *et al.* (2017c) investigated the magnetostratigraphy of an overlying siliciclastic succession and constrained its age from Norian to Rhaetian. Zhang *et al.* (2015) and Shi *et al.* (2017) provided magnetostratigraphic and biostratigraphic data from the Qingyan Gou section in the Sichuan Basin and considered the sharp lithological transition from carbonates to shales as related to the CPE. However, Jin *et al.* (2018a) reported a Tuvalian 3 (late Carnian) conodont association from the carbonate units of the Qingyan Gou section, which would exclude the presence of the CPE.

In an effort to better constrain this stratigraphic interval, new ammonoids, bivalves, conodonts, and palynomorphs were collected and determined from the sections considered in this study. Carbon isotopic composition of organic matter (OM) was analyzed on bulk rock and wood, in order to assess the stable isotope record in this stratigraphic interval in the Sichuan Basin and compare it to other regions. Although not coincident with major shifts in the isotope record or major extinction events, the CNB is placed in a time when important biotic changes were occurring, for instance the major differentiation of conifers (Miller, 1982; Renner, 2009). Therefore, investigations aimed at better characterizing this interval are needed. Results presented in this paper go in this direction and clarify the Upper Triassic stratigraphic framework of the northwestern Sichuan Basin, allowing better correlations with sections in the western Tethys. Our findings help shed light on a relatively neglected interval of geological time and may provide a contribution to the process of identifying a GSSP for the Norian.

2. Geological setting

The northwestern Sichuan Basin is a portion of the Longmen Shan foreland basin that now crops out as part of the Longmen Shan thrust belt, at the boundary between the western Sichuan Basin and Songpan-Ganzi fold belt (Fig. 1B). It was surrounded by emerged land during the Late Triassic and was connected to the Paleotethys through a large bay (Fig. 1C, Deng *et al.*, 1982; Wu, 1984). At the end of Middle Triassic, collision between the North China and South China plates resulted in an extensive unconformity (Zhang *et al.*, 1996; Li *et al.*, 2003, 2011b) with the addition of NE-striking, NW-dipping extensional faults with strike-slip components (Liu *et al.*, 1995). This unconformity marks the transition from the Paleozoic-Middle Triassic passive continental margin to the Longmen

Shan foreland basin (Li *et al.*, 2003, 2011b). In the early Carnian, a transgression brought the coastline from the Ganzi open marine region towards the western Sichuan Basin as far as Chengdu (Deng *et al.*, 1982; Wu, 1989) (Fig. 1C), and a carbonate ramp, dipping west and surrounded by locally uplifted areas, formed in the middle to western Sichuan Basin (Wu, 2009; Li *et al.*, 2011a, 2014). The Triassic stratigraphy in this region includes thick marine carbonates (~ 350 m in thickness) from Ladinian (Middle Triassic) to Carnian (Late Triassic) and Carnian to Norian siliciclastic rocks (Wu, 1989; Li *et al.*, 2003; Mei and Li, 2017; Shi *et al.*, 2017; Jin *et al.*, 2018a).

Three sections have been studied in this area. The Qingyan Gou section (HWQ) (N31°27′46.85″/E104°09'35.40″), and Guanyin Ya (HWG) (N31°28'18.4"/ E104°08'50.4″), around 1.5 Km (each) from the HWQ, situated in the Hanwang region. The third section is Jushui (JS) (N31°30'44.6"/E104°13'54.5") near the town of Jushui (Fig. 1C). All of these sections were previously studied for their lithostratigraphy and microfacies (Wu, 2009; Jin *et al.*, 2015, 2018a; Shi *et al.*, 2017), biostratigraphy (Wu, 1989; Wang, 1992; Shi *et al.*, 2017; Jin *et al.*, 2018a) and paleomagnetic stratigraphy (Zhang *et al.*, 2015).

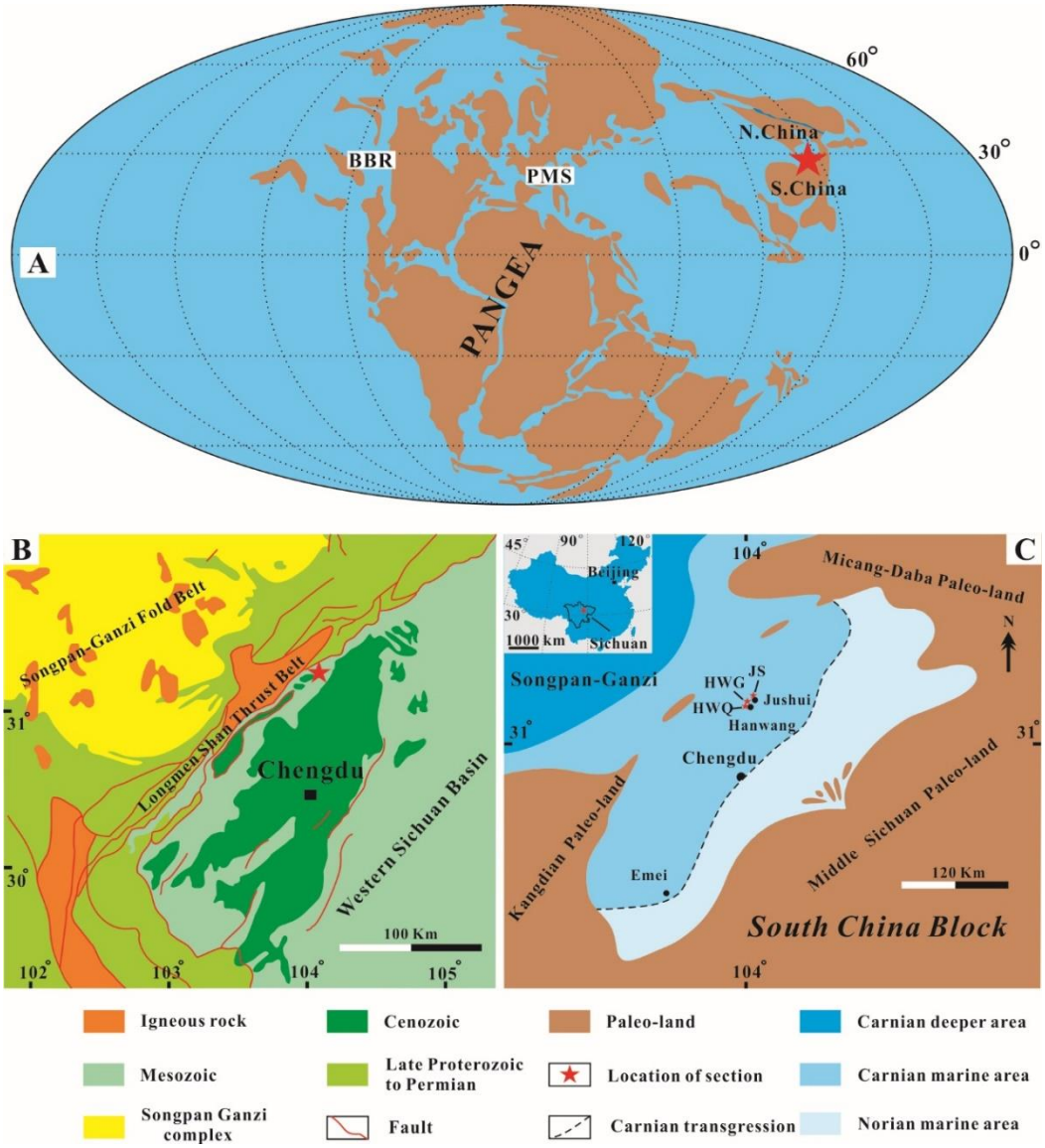

Fig. 1. Location of the study area and sections during the Late Triassic. (**A**), The position of study area (star) in eastern Tethys during the Late Triassic (simplified from Golonka, 2007). Two Norian/Carnian GSSP candidate sections are BBR: Black Bear Ridge, British Columbia; PMS: Pizzo Mondello in Sicily, Southern Italy. (**B**), Geological and tectonic map of the Sichuan Basin and adjacent areas (simplified from Shi *et al.,* 2017). (**C**), Late Triassic paleogeography of the western Sichuan Basin and locations of study sections in the Hanwang and Jushui areas (simplified from Wu, 1989). HWQ, Qingyan Gou section; HWG, Guanyin Ya section; JS, Jushui section.

2.1. The Middle Triassic in the northwestern Sichuan Basin

The uppermost Middle Triassic stratigraphic unit in the northwest of Sichuan Basin is the Tianjingshan Formation (T_{2j}), which is mainly composed of stromatolitic-bioclastic limestones or dolostones. The presence of limestone coexisting with dolostone is considered a lithological marker to identify T_{2j}. Such a lithology is markedly different from the overlying Carnian rocks, which comprise oolitic-bioclastic limestones and overlying hexactinellid sponge-bearing limestones (Wu, 1989; Wendt, 2001). The depositional environment of T_{2j} is interpreted as an evaporitic tidal flat (Wu, 1989). Wu (1989) assigned T_{2j} to the Ladinian (Middle Triassic) on the basis of bivalve and brachiopod faunas. However, He (1980) reported a Carnian foraminiferal association including *Diplotremina* sp., *Turritellella* sp., *Ophthalmidium exiguum*, *Eoguttulina* sp., *Palaeomiliolina tibetica*, *Involutina* sp., *P. tenuis*, *Aulotortus* sp., *Gaudryina* sp., *Nodosariidae* (*Astacolus, Frondicularia, Lenticulina, Nodosaria* etc.), in the upper portion of the unit. Furthermore, ammonoids (*Thisbites* sp.) and conodonts (*Neogondolella polygnathiformis*, *N. navicula*) from Wang and Dai (1981) suggest an upper Carnian age, but those fossils were not illustrated and are more typical of the overlying Ma'antang Formation (T_{3m}) (e.g., Wang, 1992; Shi *et al.*, 2017). The top of the Tianjingshan Formation is marked by an extensive, basin-scale unconformity surface within the stromatolitic limestone (Li *et al.*, 2003, 2011b). This unconformity is clearly seen in the lowest part of the HWG section (Fig. 2).

2.2. The Upper Triassic (Carnian and Norian) in the northwestern Sichuan Basin

The Tianjingshan Formation is overlain by the Ma'antang Formation (T_{3m}) of Carnian age (Wu, 1989; Wang, 1992). The Carnian succession consists of two parts (Li *et al.*, 2003, 2014). In our studied sections, the lower part is ~ 55 m thick, and it begins with oolitic-bioclastic limestones, followed by hexactinellid sponge-bearing limestones and sponge mounds in an upward - deepening succession (Jin *et al.,* 2018a). Its sedimentary environment comprises a carbonate ramp (Wu, 2009; Jin *et al.,* 2018a). The upper part is > 65 m thick and is composed of dark grey shales, mudstones and siltstones (Li *et al.,* 2003). Its sedimentary environment is controversial, having been interpreted as a

gulf (Wu, 1989), foredeep (Li *et al.*, 2014) and lagoon (Shi *et al.*, 2015). In this paper we use the facies model of Li *et al.* (2014) (Fig. 2). The abrupt lithological change from limestone to shale has been associated with the Carnian Pluvial Episode (Shi *et al.*, 2009, 2017; Wang *et al.*, 2015). On the basis of conodont biostratigraphy, Jin *et al.* (2018a) suggested instead that the whole T_{3m} succession in the Hanwang area is Tuvalian (late Carnian) and the carbonate crisis in this region is thus unrelated to the CPE.

The T_{3m} is subdivided into four units (Shi *et al.*, 2017; Jin *et al.*, 2018a): Unit 1 comprises oolitic limestones; Unit 2 consists of bioclastic limestones; Unit 3 is mainly composed of microbial sponge mounds; Unit 4 consists of siltstones and shales (Fig. 2). The oolitic-bioclastic units (Unit 1 and Unit 2 in Fig. 2) in Hanwang area have been assigned to the lower Carnian (Julian), based on ammonoids *Protrachyceras* cf. *P. victoria*, *Clionites* sp., *Sandlingites* sp., *Californites*? sp. (Wu, 1989) and conodont *Paragondolella* (=*Quadralella*) *polygnathiformis*. Recently (Jin *et al.*, 2018a), suggested that the conodont associations from the HWQ section were consisted of *Carnepigondolella angulata*, *Hayashiella tuvalica*, *Paragondolella noah*, *Carnepigondoella orchardi*, *Epigondolella miettoi* and *Carnepigondoella* cf. *C. orchardi*. These are typical late Tuvalian (late Carnian) conodonts (Mazza *et al.*, 2012; Rigo *et al.*, 2012, 2018). Wang (1992) reported ammonoids above the sponge mounds (lower part of Unit 4) in Hanwang area that were determined as *Thisbites borellii*, *T. haushoferi*, *T.* cf. *borni*, *T. agricolae*, *Anatomites herici*, *Discotropites plinii*, *Timortropites dubvosus*, *Anatibetites* sp., *Thisbites* sp. and *Juvavites* sp. In particular, the ammonoid *Discotropites plinii* defines the uppermost late Carnian (Tuvalian 3) biochronozone (Krystyn, 1982).

The overlying thick succession (~ 500 m thick in studied area) of coarser terrigenous rocks is the Xiaotangzi Formation (Fig. 2). Li *et al.* (2003) attributed this stratigraphic interval to the Xujiahe Formation (T_{3x}). In this work, we use the term "Xujiahe Formation" only for the upper, coarse grained siliciclastic unit within the Late Triassic of the Sichuan Basin.

The Xiaotangzi Formation (T_{3xt}) is dated as Norian based on ammonoids (Wu, 1989) and bivalves (Gou, 1998). The uppermost T_{3xt} is characterized by quartz-lithic arenites with calcite cement. Its sedimentary environment is thought to vary from shelf to littoral (Mei and Liu, 2017). So far, the biostratigraphy was poor across the CNB interval. Some authors propose the occurrence of coarse quartzose sandstone as a marker of the CNB (Deng *et al.*, 1982; Li *et al.*, 2003; Shi *et al.*, 2015). Zhang *et al.* (2013) suggested that a local unconformity exists between the T_{3m} and T_{3xt}, and this unconformity could correspond to the CNB (Fig. 2). In some localities, such as the Emei area (Fig. 1C), the upper part of T_{3m} consists of shales and siltstones, and this unit is locally named Kuahongdong Formation (Wu, 1989).

Li and Wang (2016) investigated the palynological assemblages in the Western Sichuan Basin, including the area of this study. These authors recognized three assemblages: a *Dictyophyllidites*–

Corollisporites–Micrhystridium (DCM) assemblage mainly occurring in the Ma'antang Formation, a *Dictyophyllidites–Kyrtomisporis–Canalizonospora* (DKC) assemblage mainly in the Kuahongdong Formation (upper Ma'antang Formation) and a *Dictyophyllidites–Lunzisporites–Chasmatosporites* (DLC) assemblage that is the main association in the Xiaotangzi and Xujiahe formations.

In summary, only sparse biostratigraphic data from the Ma'antang, Xiaotangzi and Xujiahe formations are available, which suggests that the Carnian and Norian are both present in studied area.

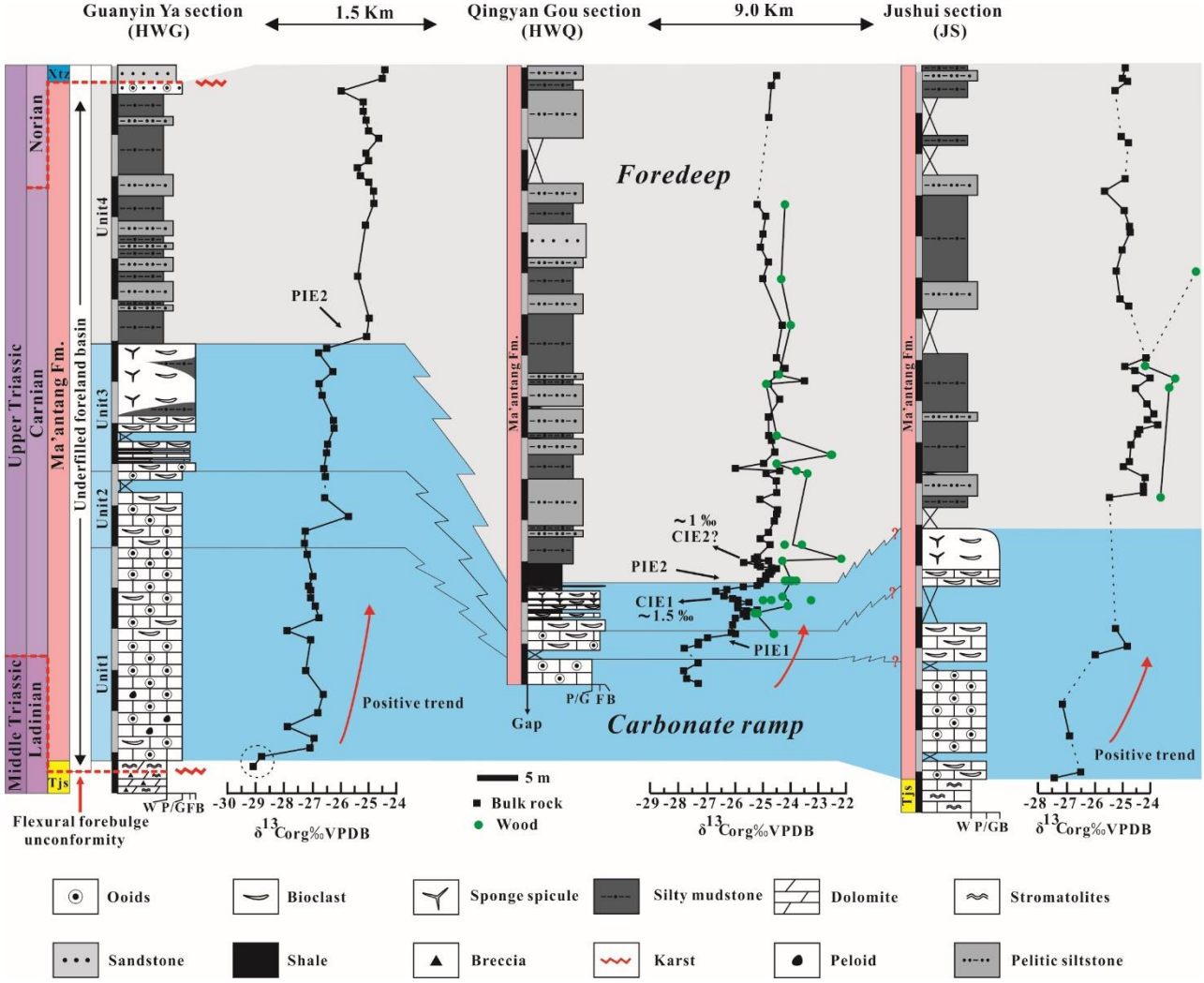

Fig. 2. Facies correlations (jagged line) and $\delta^{13}C_{org}$ values of bulk rock and wood from the HWG, HWQ, and JS sections. Lithological units (Unit 1, Unit 2, Unit 3, and Unit 4) were introduced by Shi *et al.* (2017) and Jin *et al.* (2018a). The term "Flexural forebulge unconformity" follows Li *et al.* (2003), and facies model follows Li *et al.* (2014). W, Wackestone; P/G, Packstone-Grainstone; F, Floatstone; B, Boundstone; CIE, Carbon isotopic excursion; PIE, Positive isotopic excursion; Tjs, Tianjingshan Formation; Xtz, Xiaotangzi Formation.

2.3. Magnetostratigraphy in the HWQ section, Hanwang area

The HWQ section has been also investigated for its magnetic polarity pattern (Zhang *et al.*, 2015) and tentative correlations with the Triassic astrochronological polarity time scale have been proposed

(Zhang *et al.*, 2015; Shi *et al.*, 2017). The latest proposed correlation implies that the HWQ section spans the lower to upper Carnian with a short interruption due to a hiatus, which was ascribed to a karstic surface, in the middle of our Unit 3 (corresponding to the middle of Unit 2 in the HWQ section in Shi *et al.*, 2017). These authors suppose that the late Julian is missing on the basis of their magnetostratigraphy. However, no petrographic and field evidence of karst was found by Jin *et al.* (2018a).

3. Methods

3.1. Ammonoids, bivalves and conodonts

Ammonoids were collected from the HWQ and JS sections (A-H horizons in Fig. 3). Tens of bivalves were collected from the HWQ and JS sections in 2012 (Ba and Bb horizons in Fig. 3), but only a few of them were illustrated in Shi *et al.* (2017). Collected specimens were cleaned and photographed at the Department of Geosciences, Padova University. Two rock samples, 3-5 kg each, were also collected from the lowest part of the JS section for conodont biostratigraphy (a and b positions in Fig. 3). The conodont samples were etched with formic acid, and the residues dried at the Institute of Sedimentary Geology, Chengdu University of Technology. Conodonts were concentrated by heavy liquid treatment, separated manually by binocular microscope and photographed with a CamScan MX 2500 SEM in the Department of Geosciences, Padova University.

3.2. Palynology

Three palynological samples (PA-PC) were collected in the HWG and one (PD) in the HWQ section (Fig. 3). The samples were ground and approximately 10 g of powder was treated with 10 % HCl to remove the sulfates and carbonates, followed by 47 % HF at 55°, to remove silicate minerals. Residues were washed with deionized water until neutrality was reached, and were then sieved at 15 µm. The residue was stored in glycerin jelly. All the slides were studied and photographed in the Geoscience Department of Padova University.

3.3. Organic carbon isotopes

Seventy-six bulk rock samples and 30 wood fragments from the HWQ section, 51 bulk rock samples from the HWG section, 40 bulk rock samples and 5 wood fragments from the JS section were collected to be analyzed for their $\delta^{13}C$. From now on, the notation $\delta^{13}C_{org}$ will be used for the stable

isotopic composition of organic carbon. Bulk rock samples were first cleaned with deionized water, then oven-dried at 50° for one night and pulverized with an agate mortar. Subsequently, the carbonates were removed by putting ca. 2 g of powder into a polypropylene falcon tube with 50 ml of 10 % HCl. Desulfurization was carried out for sulphurous samples with 37 % HCl poured in the same tubes at 55°C for four hours. The process was repeated until the solution lost its yellow color. The residuals were rinsed with deionized water and centrifuged until neutrality was reached, then oven-dried again. Approximately 1-5 mg of sample were weighed in tin capsules. Wood samples were separated from bulk rock, etched with 10 % HCl and oven-dried. Approximately 0.04 mg of treated wood were weighted in tin capsules. All samples were ran in duplicate. The $\delta^{13}C_{org}$ analyses were performed in the Department of Geosciences, University of Padova, with a Thermo Flash 2000 Elemental Analyzer linked to a Thermo-delta V advantage isotopic ratio mass spectrometer. Results were calibrated to the international VPDB scale, by analyzing contemporaneously two international standards CH-7 (-32.151 ‰) and CH-6 (-10.449 ‰). A quality control standard was also run along with the samples (ZER sucrose from a C3 plant). The accuracy was ca. ± 0.15 ‰ (1 σ) during the period of the analyses.

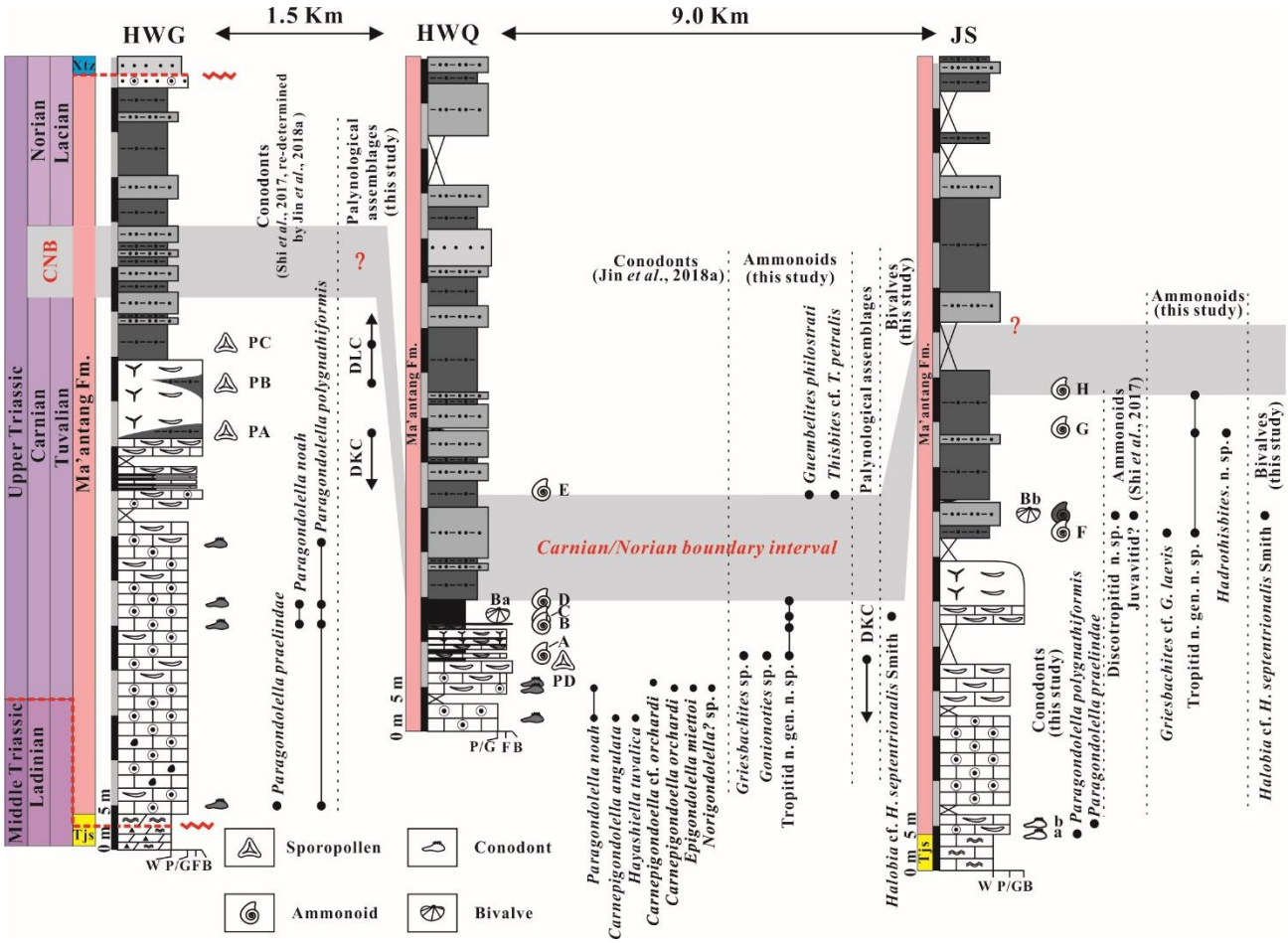

Fig. 3. Biostratigraphic data (ammonoids, conodonts, bivalves and palynological assemblage zones) and tentative correlation. The CNB (in grey) at HWQ is the uncertain interval between the last Carnian ammonoid associations with tropitids and the first Norian ammonoid associations. Palynological assemblage zones DKC: *Dictyophyllidites-*

Kyrtomisporis-Canalizonospora assemblage; DLC: *Dictyophyllidites-Lunzisporites-Chasmatosporites* assemblage (Li and Wang, 2016). Letters besides fossil occurrences (A-H for ammonoids; a, b for conodonts; Ba, Bb for bivalves; PA-PD for palynomorphs) are the names of fossiliferous horizons and palynological samples used in the text.

4. Results

4.1. Biostratigraphy

4.1.1. Conodonts

Three conodonts were found in two samples from the JS section (Fig. 3). One conodont species, *Paragondolella polygnathiformis* (Fig. 4/a) occurs in a sample within the top of stromatolite bed. In sample b (Fig. 3), above the stromatolite, the conodont species *Paragondolella praelindae* (Fig. 4/b) was found. All conodonts show a Color Alteration Index (CAI) of 1.

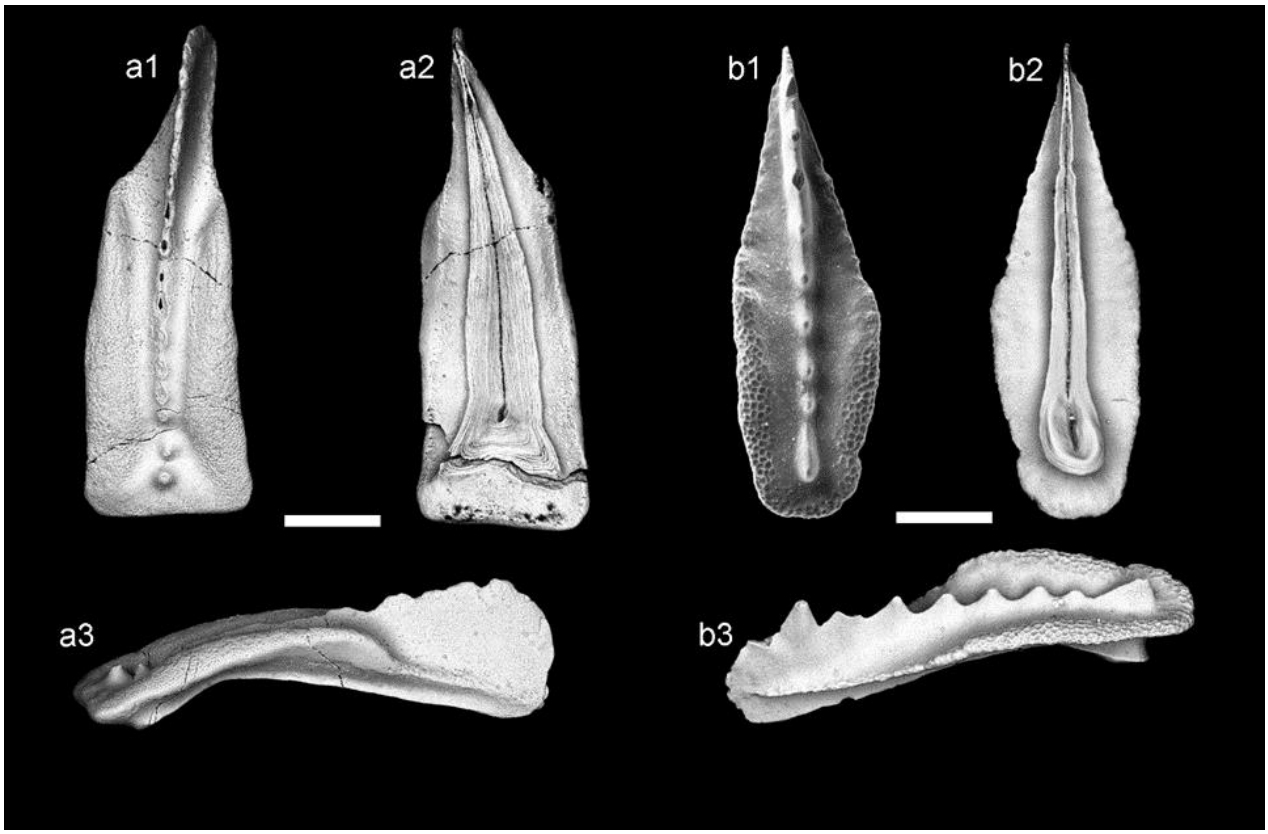

Fig. 4. Scanning Electron Microscope photomicrographs of conodonts from the JS section. (**a**) *Paragondolella polygnathiformis*; (**b**) *Paragondolella praelindae*. For each specimen: (1) upper view, (2) lower view, (3) lateral view. "a" and "b" refer to the sampling horizons (see Fig. 3). The Color Alteration Index of these conodonts is 1. All scale bars = 200 μm.

4.1.2. Ammonoids

Ammonoids were collected from five horizons in units 3 and 4 of the HWQ section (A-E in Fig. 3) and 3 horizons (F-H) of the JS section (Fig. 3). Ammonoids occur along with a diverse fauna that includes brachiopods and molluscs, including thin shelled halobiid bivalves. Ammonoids are sometimes preserved with their original aragonitic shell, sometimes shells are substituted by calcite, and suture lines are seldom visible. The distribution of all ammonoids from the HWQ and JS sections are displayed in Table. 1.

Most specimens belong to a small (< 2 cm) taxon of ammonoids with a keeled rounded venter and ventrolateral shoulders, with a moderately open umbilicus =< 30% of the shell diameter. These ammonoids are densely ribbed (Fig. 5B1, B2, G1, H), showing 10-12 ribs per quadrant on the ventrolateral margin that terminates before the keel on faint bullae or swellings. This taxon corresponds to "Discotropitid (n. gen. n. sp. 1)" in Shi *et al.* (2017) and is here identified as "Tropitid n. gen. n. sp." Some specimens expose the suture line (Fig. 5G1) which is ammonitic, confirming the attribution of this taxon to the tropitid family. Tropitid n. gen. n. sp. is by far the most abundant ammonoid in horizons A, B, C, and D (HWQ section), F, G, and H (JS section).

Involuted, smooth ammonoids were also collected that are attributed to the family Juvavitidae. A specimen from horizon A at HWQ (Fig. 5A1) is ca. 3 cm in diameter and is preserved as a compressed substituted shell. The venter and suture lines are not visible; however, weak ribs are visible in the outer part of the flank that disappear in the umbilical part. This specimen was determined as *Gonionotites* sp. Several specimens were collected of an ammonoid taxon with smooth, involute shell and an elliptical whorl section that we tentatively attribute to genus *Griesbachites* (e.g., Fig. 5A2, F1, F2). These have a rounded venter without ornamentation, and flanks with few coarse and simple ribs or plicae that near the venter are adorally projected and terminate without bullae or knots. One specimen from the JS section exhibits the suture line partially (Fig. 5F1) at a diameter of ca. 2 cm. This suture line has at least 3 lobes and 3 saddles, all deeply denticulated and squared, the first lobe being deeper that all others. This suture line and the weak ornamentation compare well with that of *Griesbachites laevis* illustrated by Tozer (1994), in which the ventrolateral bullae that are typical in large specimens of *Griesbachites* are instead missing or minimally developed. The "Juvavitid, n. gen." of Shi *et al.* (2017) most probably belongs to this taxon.

A fragment of a strongly ribbed, involuted ammonoid, preserved as an external mold, was collected from horizon E of the HWQ section (Fig. 5E1). This specimen compares well with the inner whorls of *Guembelites philostrati* illustrated by Krystyn (1982: pl. 13 fig. 6) from the Jomsom section in the Nepalese Himalaya. From the same horizon, we also collected a fragmented specimen of *Thisbites* (Fig. 5E2). This ammonoid shows a dense ribbing, with 17 ribs being counted per quadrant

at a diameter of ca. 1 cm. Ribs are falcoid, mostly simple, few are bifurcated close to the umbilical margin, and terminate on strong tubercles aside of a keeled venter. This specimen can be clearly distinguished from Discotropitid n. gen. n. sp. 1 because of the denser ribs, which terminate on strong tubercles instead of the weak bullate swellings of Tropitid n. gen. n. sp. Because of the dense ribbing and strong tubercles, this *Thisbites* has been determined as *Thisbites* cf. *T. petralis* (see Tozer, 1994, pl. 108, fig. 3, 4).

Finally, a nearly complete specimen of an ammonoid with distinctive ornamentation comes from horizon G of the JS section (Fig. 5G2). This specimen, ca. 1.5 cm in diameter, has a narrow, keeled venter bordered by bullated tubercles on the ventrolateral shoulders. The umbilicus is well open and exposes ribbed inner whorls. The last whorl, probably a habitation chamber, is not ribbed, and only shows very weak tubercles elongated radially that mimic faint ribs. Of the suture line, only part of an entire saddle is visible. We attribute this ammonoid to a species of *Hadrothisbites* different from *H. taylori* of Tozer (1994).

The association of tropitids, *Hadrothisbites* n. sp., *Gonionotites* sp. and *Griesbachites* sp. at HWQ and JS indicates a late Tuvalian (late Carnian) age. In particular, tropitids are only known so far from the upper Carnian. It should be noted, however, that the tropitids illustrated in this work are a new taxon, whose distribution is thus unknown. The ammonoids from horizon E of the HWQ section suggest instead a lower Norian age: *Guembelites philostrati* is so far only known from the Norian, while the species of genus *Thisbites* occur in a short stratigraphic interval across the Carnian-Norian boundary; *T. petralis*, however, is only known from the lower Norian (Tozer, 1994).

Ammonoid species	Horizons	Occurrence	Section
Tropitid n. gen. n. sp.	A	XX	HWQ
Tropitid n. gen. n. sp.	B	XX	HWQ
Tropitid n. gen. n. sp.	C	X	HWQ
Tropitid n. gen. n. sp.	D	X	HWQ
Tropitid n. gen. n. sp.	F	X	JS
Tropitid n. gen. n. sp.	G	XX	JS
Tropitid n. gen. n. sp.	H	XX	JS
Gonionotites sp	A	X	HWQ
Griesbachites sp	A	X	HWQ
Griesbachites cf. G. *laevis*	F	X	JS
Guembelites philostrati	E	X	HWQ
Thisbites cf. *T. petralis*	E	X	HWQ
Hadrothisbites n. sp.	G	X	JS

Table. 1. List of Late Triassic ammonoids in northwestern Sichuan Basin, China

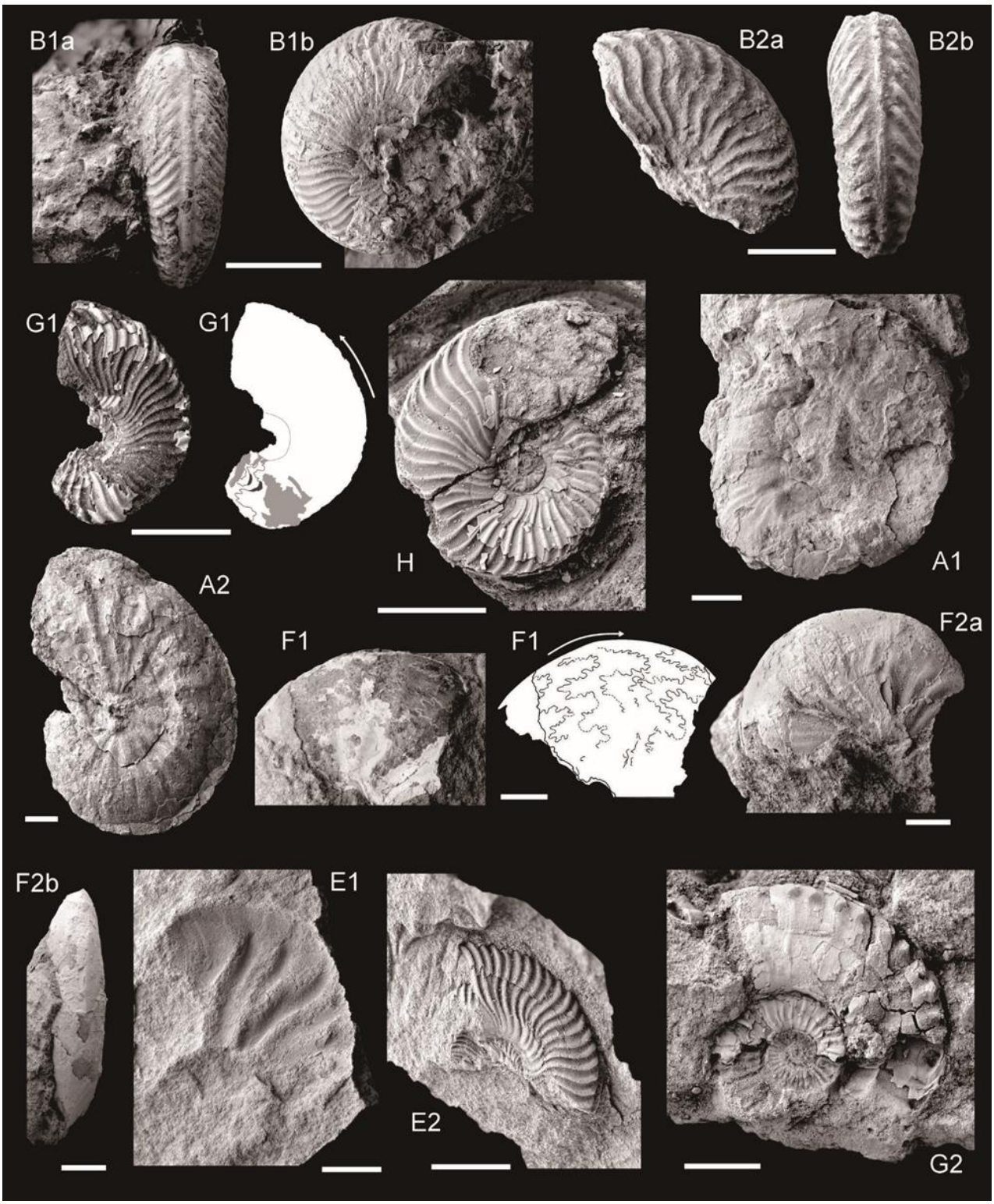

Fig. 5. Photographs of ammonoids from the HWQ and JS sections. Letters refer to sampling horizons (see Fig. 3). (**B1**, **B2**, **G1** and **H**) Tropitid n. gen. n. sp.; (**A1**) *Gonionotites* sp.; (**A2** and **F2**) *Griesbachites* sp.; (**F1**) *Griesbachites* cf. *G. laevis*; (**E1**) *Guembelites philostrati*; (**E2**) *Thisbites* cf. *T. petralis*; (**G2**) *Hadrothisbites* n. sp. For B1, B2 and F2 specimens: (a) upper view, (b) lateral view. All scale bars = 5 mm.

4.1.3. Bivalves

Halobiid bivalves occur at several levels (Ba and Bb) within both the HWQ and JS sections (Fig. 3). Most of the specimens are preserved as partial skeletons of recrystallized calcite which exposes the outer surface of a middle skeletal layer. While this surface (between the shell layers) does preserve some of the original ornament of the individuals (e.g., commarginal growth banding and at least the general course and direction of the radial ornament), but details of the external expression of radial ribs from the outer skeletal layer are obscured precluding definitive species-level identification.

Based on shell outlines, commarginal growth banding, the angular breadth of the anterior tube, and generalized course of the ribbing of the specimens, it appears highly probably that they belong to a single species, here referred to as *Halobia* cf. *H. septentrionalis* Smith (Fig. 6) and may therefore may serve as a robust correlation datum between the two sections. The HWQ and JS specimens are similar to those that have been attributed to both *Halobia qaboensis* Zhang and *Halobia septentrionalis* Smith. There is a strong possibility for these two taxa of being synonymous. Chen and Ba (1986, pl. 2, figs. 6, 8, 11, 14) illustrated *Halobia septentrionalis* Smith 1927 from middle to late Carnian of Zedang (south Xizang). This species is known from several localities throughout North America perhaps best represented in southeastern Alaska and western Canada in the upper Carnian (*K. macrolobatus* ammonoid zone) as discussed by McRoberts (2010, 2011). This morphotype is also similar to *Halobia qaboensis* Zhang (in Zhang *et al.,* 1985, pl. 33, figs. 1-9) known from the Bolila Formation, near Kangba and Chengdu. However, the preservation of Zhang's illustrated specimens is rather poor, making direct comparisons to *H. septentrionalis* not possible. Additionally, the HWQ and JS halobias may be compared to those Ma *et al.* 1976 (pl. 33, fig. 6) referred to as *Halobia rugosa* Gümbel from the Yunnanyi Formation, Xiangyun County, Yunnan. More recent evaluations of *Halobia rugosa* (see McRoberts, 2011; Levera, 2012) suggest that "*H. rugosa*" from the upper Carnian are distinctively different from true *Halobia rugosa* which is earliest Carnian (=*Trachyceras* ammonoid zone) from the western Tethys. Therefore, it is possible that the Yunnanyi "*H. rugosa*" are also conspecific with those described as *Halobia* cf. *H. septentrionalis* in this report (Fig. 6).

The morphologic affinities of the HWQ and JS *Halobia* cf. *H. septentrionalis* suggest a Tuvalian age and are most likely mid to upper Tuvalian equivalent to the *Anatropites* (=*K. macrolobatus*) or slightly older *T. subbulatus* (=*T. welleri*) ammonoid zones (sensu Silberling and Tozer, 1968; Kozur, 2003; McRoberts, 2010).

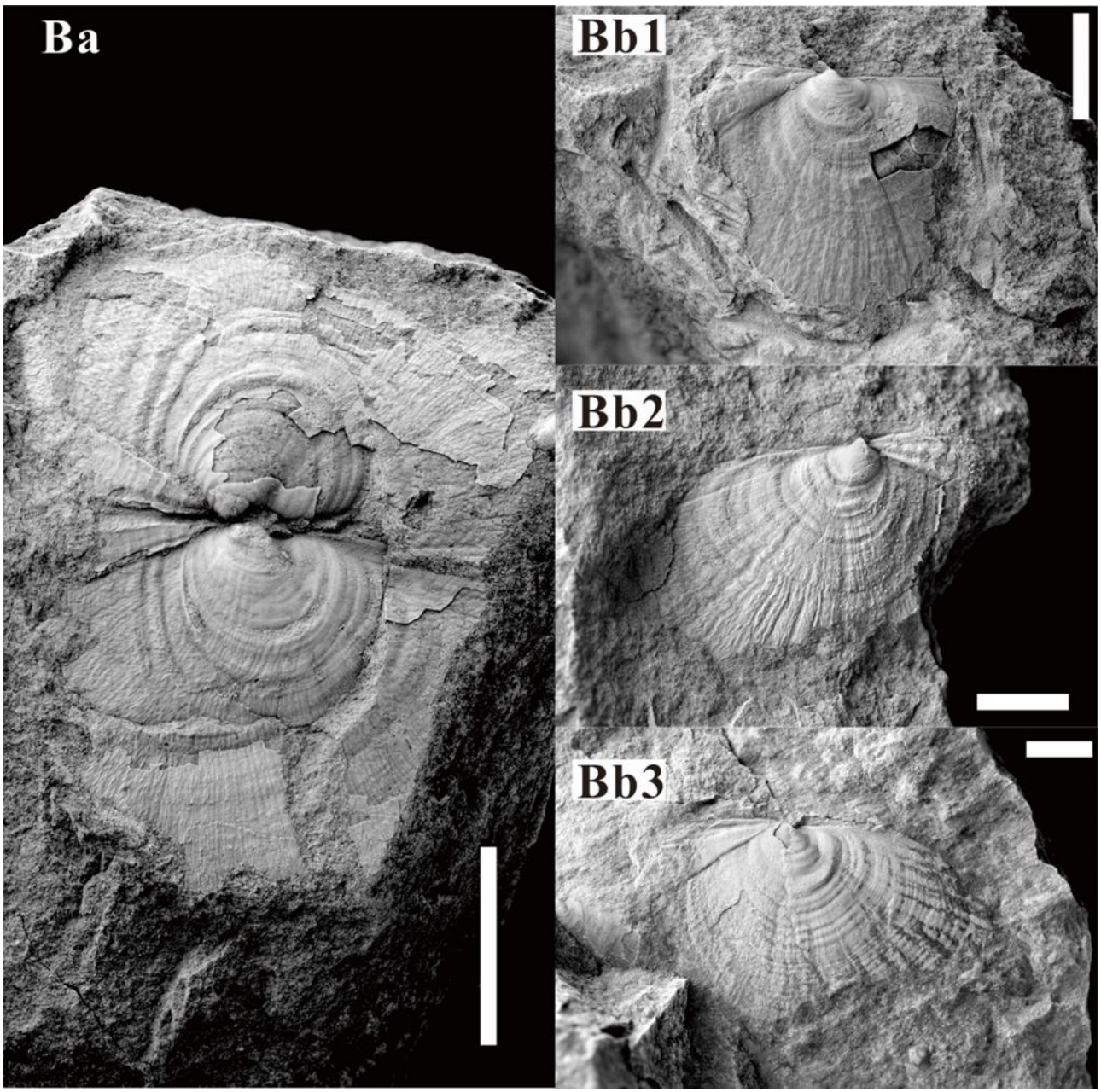

Fig. 6. Photographs of *Halobia* cf. *H. septentrionalis* Smith from the HWQ (**Ba**) and JS (**Bb1-3**) sections. Ba: articulated valve pair; Bb1: left valve; Bb2: right valve; Bb3: left valve. All scale bars = 1 cm.

4.1.4. Spores and Pollen

The sporomorphs were collected from PA-PC and PD positions from the HWG and HWQ sections (Fig. 3), respectively. The preservation of the palynological material is unfortunately not good, because of degradation on the exine. The representative sporomorphs were displayed in Fig. 7, and the distribution of all sporomorphs are showed in Table. 2.

The spores from the HWG section are composed of levigated and ornamented Azonotriletes as *Deitoidospora* sp., *Concavisporites* spp, *Dictyophyllidites* sp., *Dictyophyllidites harrisii*, *Todisporites* sp., *Punctatisporites* spp., *Converrucosisporites* spp., *Verrucosisporites* sp., *Pustulatisporites* sp.,

Leiotriletes sp.; cingulati spore as *Annulispora* sp., *Stereisporites* sp., and *Asseretospora* sp.; zonate spore as *Kraeuselisporites* sp.; cavatomonoletes as *Aratrisporites* spp., cingulicavate form as *Densosporites* sp. Pollen grains are rare including alete forms as *Psophosphaera* spp. and *Araucariacites* sp.; monocolpate forms as *Riccisporites* sp., *Cyadopites* sp., and *Chasmatosporites* spp. Bisaccates are present as *Piceites* sp. and *Pinuspollenites enodatus*. Green algae spore as *Tasmanites* sp. are present.

The spores from the HWQ section consists of Azonotriletes *Concavisporites* sp., *Converrucosisporites* sp., *Anapiculatisporites* sp., zonate spore as *Kraeuselisporites* sp., cavatomonoletes as *Aratrisporites* sp. The pollen grains contain monocolpate as *Cyadopites* sp. and *Chasmatosporites* spp., bisaccates as *Pinuspollenites* sp., *Alisporites* sp., and Algae spore: *Botryococcus* sp., *Tasmanites* sp.

palynomorph	Samples	Occurrence	Section
Alisporites sp.	PD	X	HWQ
Anapiculatisporites sp.	PD	X	HWQ
Annulispora sp.	PA	X	HWG
Aratrisporites spp.	PA,PB,PD	XX	HWG,HWQ
Araucariacites sp.	PA,PB,PC	X	HWG
Asseretospora sp.	PB	X	HWG
Bisaccates	PA,PB	X	HWG
Botryococcus sp.	PD	X	HWQ
Chasmatosporites spp.	PB,PC,PD	XX	HWG,HWQ
Concavisporites sp.	PA,PB,PC,PD	X	HWG,HWQ
Converrucosisiporites spp.	PA,PD	XX	HWG,HWQ
Cyadopites spp.	PA,PB,PD	XX	HWG,HWQ
Deitoidospre sp.	PC	X	HWG
Densosporites sp.	PA	X	HWG
Dictyophyllidites harrisii	PB	X	HWG
Dictyophyllidites sp.	PC	X	HWG
Kraeuselisporites sp.	PA,PB,PD	X	HWG,HWQ
Leiotriletes sp.	PA	X	HWG
Piceites sp.	PA	X	HWG
Pinuspollenites enodatus	PB,PD	X	HWG,HWQ
Psophosphaera spp.	PA,PB	XX	HWG
Punctatisporites spp.	PA,PB,PC	XX	HWG
Pustulatisporites sp.	PC	X	HWG
Riccisporites sp.	PC	X	HWG
Stereisporites sp.	PB	X	HWG
Tasmanites sp.	PA,PD	X	HWG,HWQ
Todisporites sp.	PB	X	HWG
Verrucosisporites sp.	PC	X	HWG

Table. 2. List of Late Triassic palynomorphs in the Hanwang area, northwestern Sichuan Basin

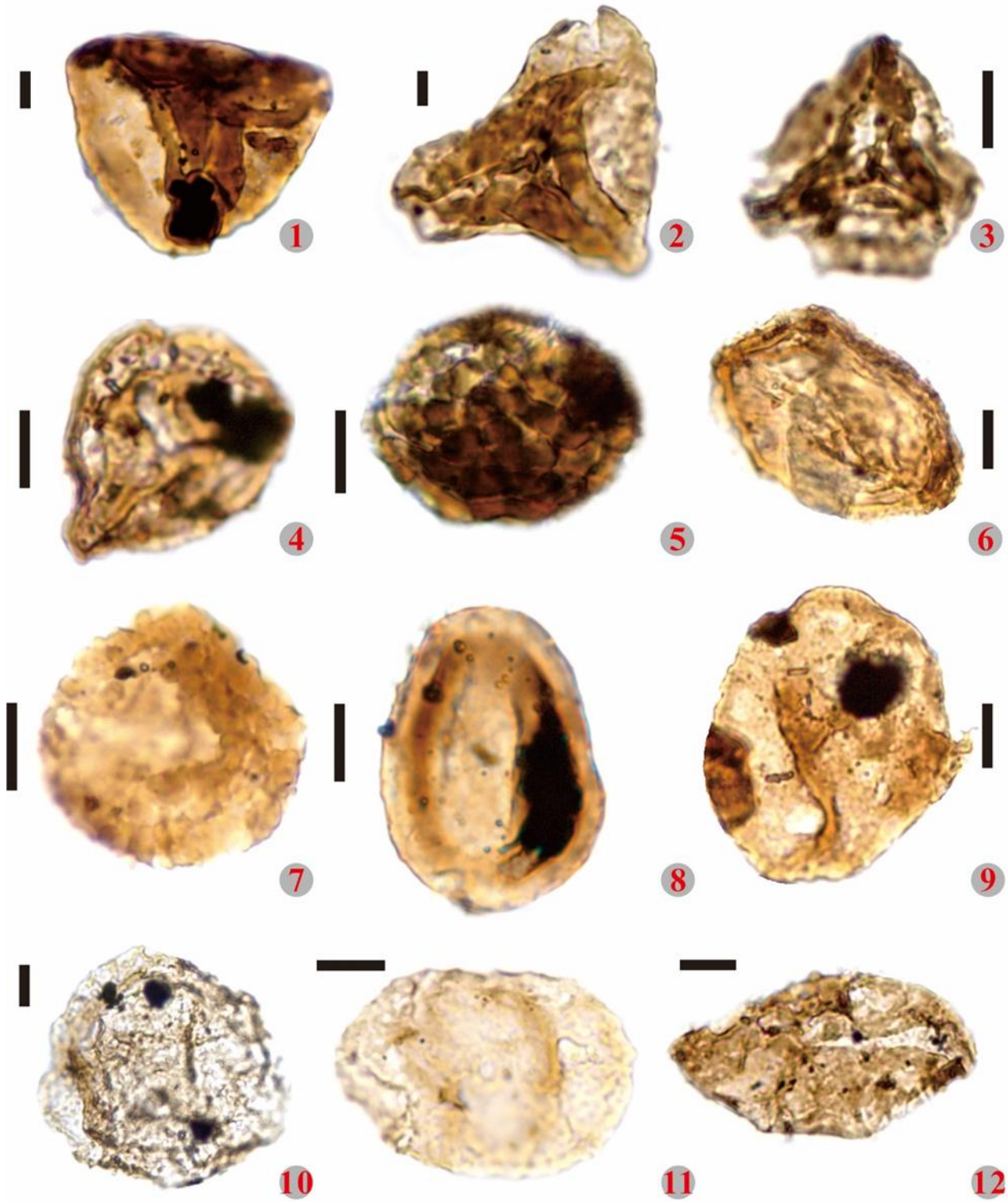

Fig. 7. Representative palynomorphs from the HWG and HWQ sections. (**1**) *Concavisporites* sp., sample PD, HWQ; (**2**) *Pustulatisporites* sp., sample PC, HWG; (**3**) *Concavisporites* sp., sample PC, HWG; (**4**) *Stereisporites* sp., sample PB, HWG; (**5**) *Verrucosisporites* sp., sample PB, HWG; (**6**) *Kraeuselisporites* sp., sample PB, HWG; (**7**) *Converrucosisporites* sp., sample PD, HWQ; (**8**) *Chasmatosporites* sp., sample PD, HWQ; (**9**) *Psophosphaera* sp., sample PB, HWG; (**10**) *Araucariacites* sp., sample PA, HWG; (**11**) *Pinuspollenites* sp., sample PD, HWQ; (**12**) *Cyadopites* sp., sample PA, HWG. All scale bars = 10 μm.

4.2. $\delta^{13}C$ of bulk organic matter from woods and bulk rock

The $\delta^{13}C_{org}$ values at the HWG section range from -29.12 ‰ to -24.39 ‰, those from the HWQ section range between -27.84 ‰ and -23.47 ‰ and from the JS section vary from -27.47 ‰ to -23.90 ‰. In the HWQ section, 30 wood fragments were collected, and their values range from -25.35 ‰ to -22.37 ‰. The values of 5 wood samples from the JS section range between -24.29 ‰ and -22.07 ‰. The $\delta^{13}C$ data from limestone, terrigenous rocks and wood are distinct (Fig. 8).

The mean value of $\delta^{13}C_{org}$ in limestones from the three sections is -26.6 ‰, while terrigenous rocks of the Ma'antang Formation have an average $\delta^{13}C_{org}$ value of -24.8 ‰. The wood fragments of the HWQ and JS sections are -24.0 ‰ on average: heavier but largely overlapping with the $\delta^{13}C_{org}$ in terrigenous rocks (Fig. 8). All sections exhibit a weak positive trend in limestone units 1 to 3 (Fig. 2), and very negative values of about -29 ‰ occur at the stromatolite in the basal part of the HWG section above the unconformity surface (dashed circle in Fig. 2).

In the HWQ section, two positive isotopic excursions (PIE1 and PIE2) are observed. The PIE1 is within the limestone unit, while the PIE2 coincides with the lithological change from limestone to shale and siltstone. The PIE2 can be observed in a comparable position also at the HWG section (Fig. 2).

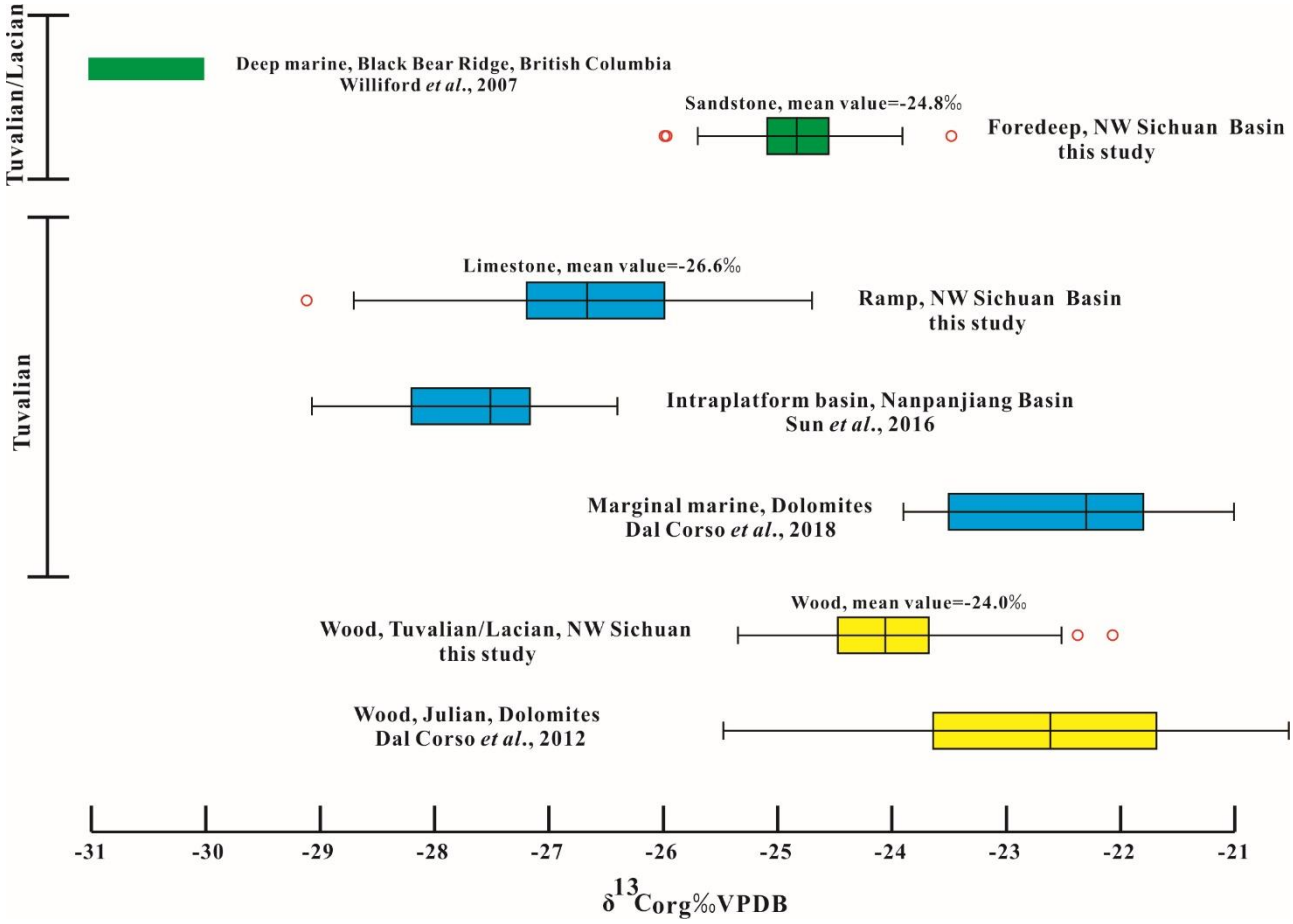

Fig. 8. Comparison of $\delta^{13}C_{org}$ values of the Carnian/Norian bulk rock and wood from western and eastern Tethys.

The boxes represent 25% and 75% quartiles, the whiskers depict 10% and 90% ranges, and the central lines in the box depict the medians. Outliers are highlighted with a red circle. For Black Bear Ridge, the full range of $\delta^{13}C_{org}$ variability is being plotted instead of box plot.

Two short-lived negative carbon isotopic excursions (CIE1 and CIE2) are observed in the HWQ section. The first is within the sponge mound interval (uppermost Unit 3) and has a magnitude of approximately 1.5 ‰. A second, negative shift of ~1 ‰ is seen just above the PIE2 (Fig. 2). These negative excursions do not occur in correlated sections, and are thus unlikely to be related to a regional signal. The wood samples are ^{13}C-enriched with respect to the coeval bulk OM, and their isotopic composition has large variability (Fig. 8).

5. Discussions

5.1. The Carnian - Norian boundary interval in northwestern Sichuan Basin

Despite their poor species diversity, ammonoids suggest that a continuous record of the CNB is preserved in northwestern Sichuan. Ammonoids were found in the Ma'antang Formation of the Sichuan Basin also by Wu (1989) and Wang (1992), albeit the precise sampling position of their findings within a stratigraphic log was not given. They found a much richer fossil association, which we could not fully recover. However, the occurrence of *Thisbites* spp., which was found also during this study in the HWQ section, was documented by both authors. Genus *Thisbites* is typical of the Carnian/Norian boundary interval (e.g., Tozer, 1994).

Shi *et al.* (2017) illustrated an ammonoid association from the JS section that is similar to the one illustrated in this work (Fig. 3). The ammonoids illustrated by Shi *et al.* (2017) were collected on a large but isolated outcrop on the eastern valley flank. However, their stratigraphic position could be determined with good approximation by tracing beds in the field (Fig. 2). These ammonoids include both smooth-shelled juvavitids and abundant tropitids; Shi *et al.* (2017) interpreted this ammonoid association as to represent the lower Tuvalian. Due to a richer ammonoid association presented in this work, and to an improved determination of smooth-shelled taxa, we are now confident that this ammonoid association instead indicates a late Tuvalian (late Carnian) to lower Norian age. This ammonoid biochronology is consistent with our age determination of halobiid bivalves and conodonts.

The palynological associations also suggest a late Carnian – Norian age. Pollen and spores from the PA horizon in the HWG section and PD layer are similar to the DKC assemblage of Li and Wang (2016) from the Kuahongdong Formation dated to late Carnian-early Norian. Pollen and spores from the PB horizon, show the appearance of some important taxa as *Psophosphaera* and *Riccisporites*

which are similar to the DLC assemblage of Li and Wang (2016) from the Xiaotangzi and Xujiahe formations, which these authors assumed to be Norian-Rhaetian. Moreover, the distinctive palynological associations described in the western Tethys during the Carnian Pluvial Episode (e.g., Roghi, 2004; Roghi *et al*., 2010; Mueller *et al*., 2016) seems to be absent, further confirming that the stratigraphic succession in Hanwang is younger than the CPE.

5.2. The amended age of stromatolitic beds of the uppermost Tianjingshan Formation

The conodonts *Paragondolella polygnathiformis* (Fig. 4/1) and *Paragondolella praelindae* (Fig. 4/2) were found within or just above the stromatolitic beds of the JS section (Fig. 3). This interval was attributed to the uppermost Tianjinshan Formation and was dated to Middle Triassic (Wu, 1989). However, *P. polygnathiformis* and *P. praelindae* are exclusive of the Julian (lower Carnian) to lower Tuvalian (upper Carnian; e.g., Mazza *et al.,* 2012). *P. polygnathiformis* first appears, in the Carnian GSSP section of Stuores Wiesen, very close to the Ladinian/Carnian boundary (Mietto *et al.,* 2012) and is routinely used as a datum to define the Carnian. Therefore, the uppermost Tianjinshan Formation at the JS should be assigned a Carnian age. This age determination would agree with those of, e.g., He (1980), Wang and Dai (1981).

5.3. A revised magnetostratigraphic correlation of the HWQ section

The most recent magnetic polarity time scale for the late Triassic (Kent *et al.,* 2017) is mostly based on data from the Newark Basin, correlated with the biostratigraphy of western Tethys. For the Tuvalian to Lacian (i.e., late Carnian to early Norian) interval a biostratigraphically calibrated record of magnetic polarity reversals has been investigated in the Pizzo Mondello section (Sicily, Muttoni *et al.,* 2001, 2004; Mazza *et al.,* 2012, 2018).

The new findings of conodonts, ammonoids and halobiid bivalves at HWQ allow an amended magnetostratigraphic correlation with western Tethys and the Newark polarity time scale. However, biostratigraphic age determinations are not fully in agreement one each other at HWQ. This led us to provide to correlation proposals, each having its advantages and drawbacks.

At Pizzo Mondello, among many other taxa, the platform conodont elements *Hayashiella tuvalica*, *Carnepigondolella zoae*, *C. angulata*, *Paragondolella noah* disappear at the top of the PM3r magnetozone, while the co-occurrence of *Epigondolella miettoi* and *Carnepigondoella orchardi* have a narrow distribution in the magnetozone PM4n, immediately below the proposed CNB defined by the FO of *Metapolygnathus parvus* (Mazza *et al.,* 2018; Rigo *et al.,* 2018) (Fig. 9). The conodonts *Epigondolella miettoi* and *Carnepigondoella orchardi* were found by Jin *et al.* (2018a) in the HWQ

section within the HQ2n, below horizons with the upper Tuvalian to lower Lacian ammonoids. This implies that the whole magnetostratigraphic record at the HWQ section is younger than suggested by Zhang *et al.* (2015) and Shi *et al.* (2017). In the HWQ section, Shi *et al.* (2017) identified a karstic surface (i.e., hiatus) within the HQ2r. It was suggested that the record of geomagnetic reversals at HWQ is thus discontinuous, and the late Julian is truncated (fig. 10 in Shi *et al.*, 2017). However, Jin *et al.* (2018a) did not find any detectable omission or erosive surface, which could correspond to an hiatus, in this interval. In light of the conodont biostratigraphy, and assuming near-constant sedimentation rates, the magnetozones in the HWQ section can be correlated to the magnetozones at Pizzo Mondello (Option A in figure 9). Assuming near-constant sedimentation rates means that the thickness ratios of magnetozones at HWQ is similar to the Newark magnetic polarity time scale.

The Option A correlation implies that the ammonoid associations of horizons A to D, which contain tropitids and *Halobia* cf. *H. septentrionalis*, are Norian. The CNB interval is to be placed between 6 m and 9.5 m from the base of the HWQ section. However, this correlation implies low sedimentation rates through the section, generally <10 m/My, which seem to be unlikely in a foreland basin system and more typical of starved open ocean environments below the Carbonate Compensation Depth (e.g., Enos, 1991).

An alternative correlation is proposed which accounts for increasing sedimentation rates at the HWQ section that could be expected in a foreland basin (Option B in figure 10). The Option B correlation maintains that ammonoid horizons with tropitids and *Halobia* cf. *H. septentrionalis* are within the Carnian, but requires that the thickness of magnetozones at HWQ is not proportional to their duration, and do not correlate to the thicknesses of magnetozones at Pizzo Mondello. The Carnian Ma'antang Formation is the initial sedimentation stage of the Longmen Shan foreland basin (Li *et al.*, 2003, 2014). The deep marine shales and mudstones of the upper Ma'antang Formation (Fig. 2) contain deep water fossils, suggesting that the basin was underfilled at this stage (Li *et al.*, 2003, 2014), but then with the siltstones and sandstones of the Xiaotangzi Formation, sedimentation was keeping up with subsidence. Along with the development of the foreland basin, the sedimentation rates were increasing, and on the basis of the upper Triassic thickness of Li *et al.* (2003) and the geological time scale of Cohen *et al.* (2013), we calculated average net sedimentation rates in the studied area of ~ 25 to ~50 m/Myrs in the Carnian, ~ 162 m/Myrs in the Norian, and > 139 m/Myrs in the Rhaetian. This suggests that sedimentation rates were increasing near the CNB in the Sichuan Basin. All calculations of net sedimentation rates do not consider compaction and denudation rates, hence the original accumulation rates may have been higher. In view of ammonoids, bivalves and sedimentation rate, the reverse polarity interval PM4r at Pizzo Mondello may correlate to the interval between HQ3r and the top of HQ4r at the HWQ section. According to Option B, the CNB interval at the HWQ section could be positioned between 14.5 m and 26.5 m. The drawback of this correlation

(Option B) is that the thickness ratios of magnetozones are not preserved, and as a result the correlation is outside of the range of biostratigraphic constraints. Further biostratigraphic investigations are needed to finally assess which of the offered correlation options is best.

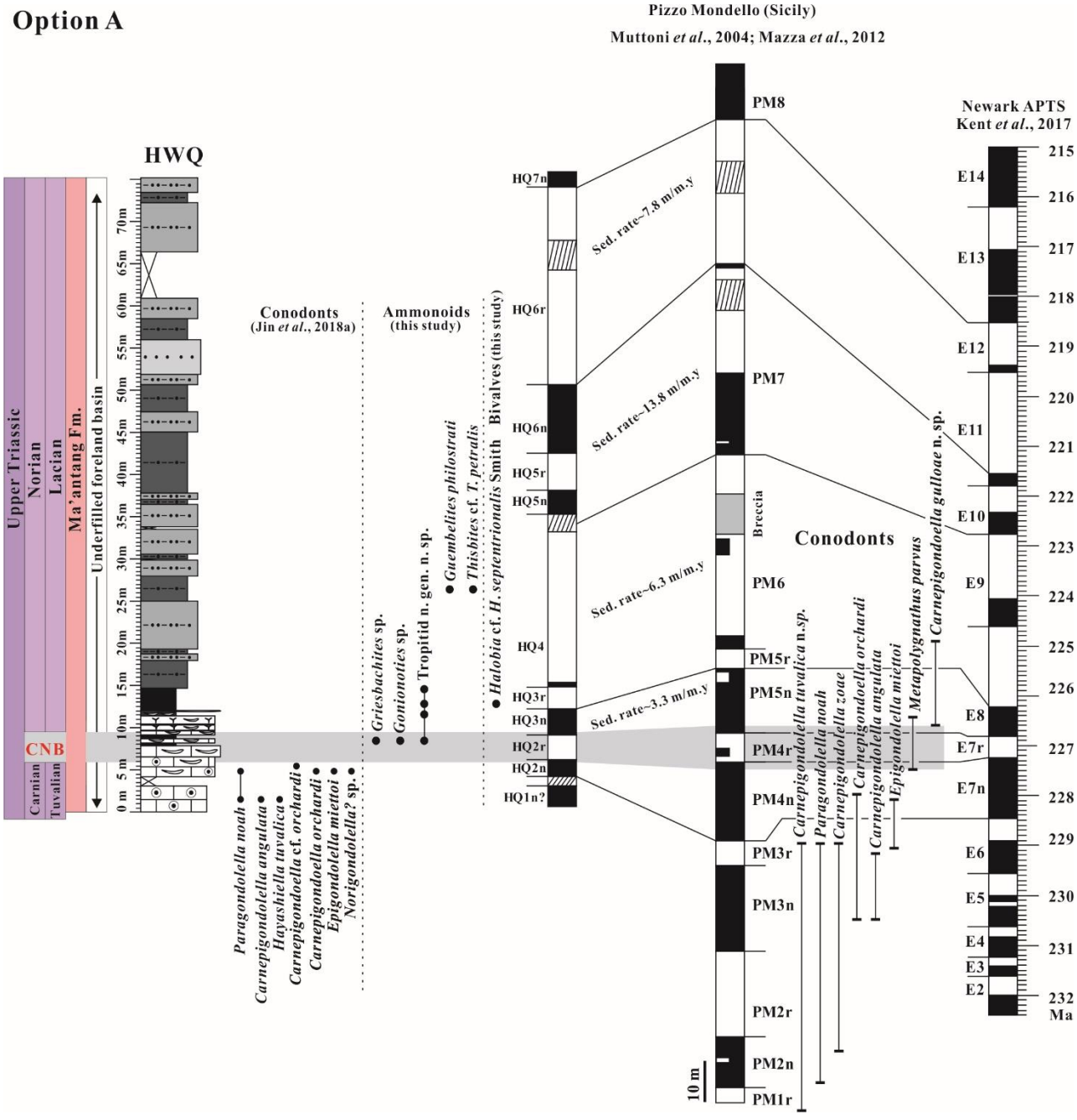

Fig. 9. Correlation of the HWQ section with the Newark APTS (Kent *et al.*, 2017) and Pizzo Mondello, Sicily (Muttoni *et al.*, 2004), based on conodont biostratigraphy and magnetostratigraphy (Zhang *et al.*, 2015; Jin *et al.*, 2018a). The Carnian/Norian boundary (CNB) interval (in grey) placed between 6 m and 9.5 m. According to this proposal, the CNB (in grey) coincides with the boundary interval of Mazza *et al.* (2012), i.e., the interval between the FO of *Metapolygnathus parvus* (conodont) and the FO of *Halobia austriaca* (bivalve) at Pizzo Mondello. This boundary interval was then correlated assuming that the HQ2r above the conodonts at the HWQ sections coincides with the PM4r at Pizzo Mondello. With this correlation, the bivalve *Halobia* cf. *H. septentrionalis* would occur in the Norian at HWQ.

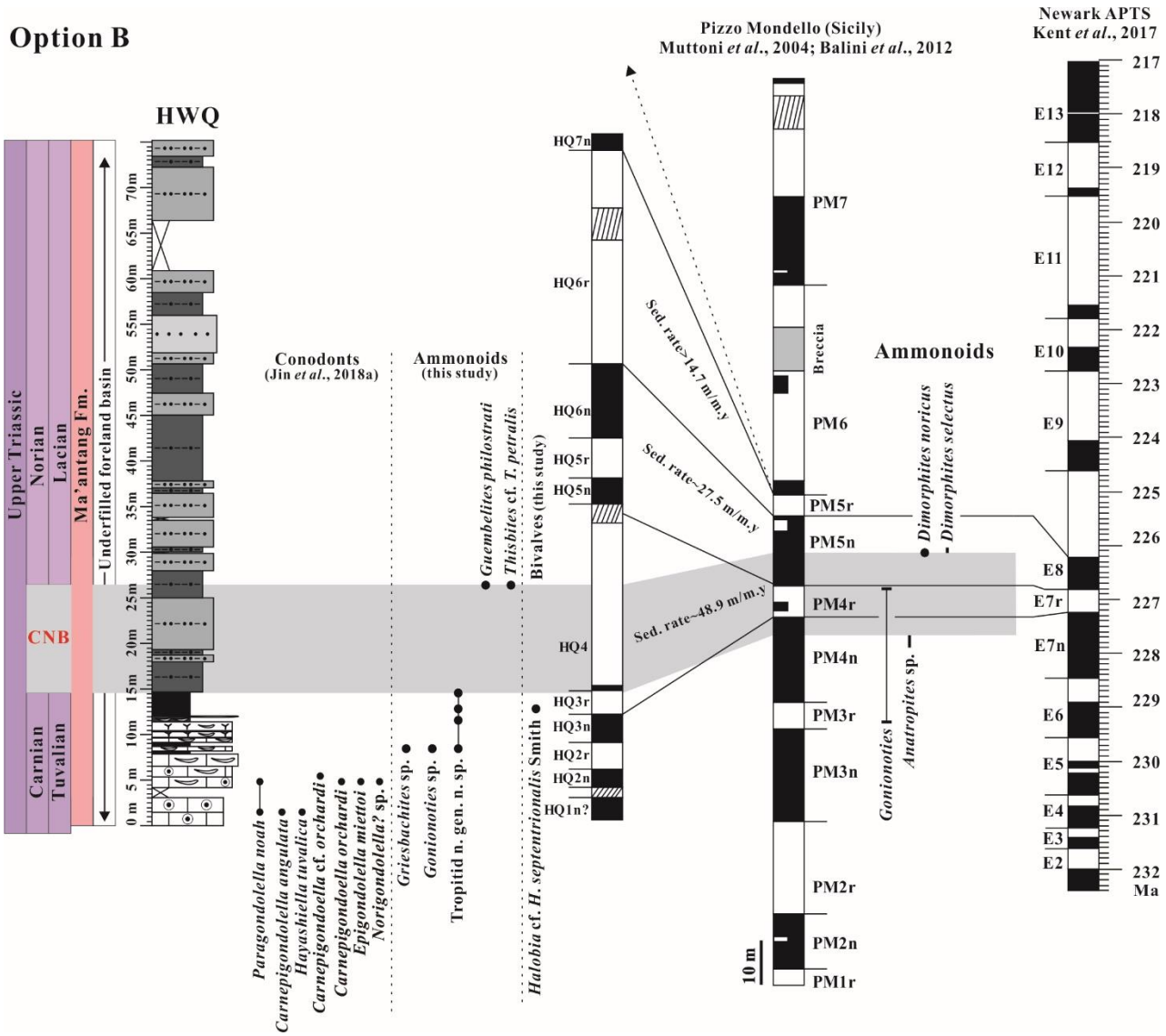

Fig. 10. Correlation of the HWQ section with the Newark APTS (Kent *et al.*, 2017) and Pizzo Mondello, Sicily (Muttoni *et al.*, 2004), based on ammonoid biostratigraphy (this study and Balini *et al.*, 2012, for Pizzo Mondello) and magnetostratigraphy (Zhang *et al.*, 2015). The Carnian/Norian boundary (CNB) interval (in grey) placed between 14.5 m and 26.5 m. In Option B, the CNB (in grey) is the uncertain interval between the last Carnian ammonoid associations with tropitids and the first Norian ammonoid associations (see also Fig. 3). This uncertain interval may not be the same between HWQ and Pizzo Mondello. Magnetozones are then correlated assuming a sedimentation rate that is increasing, on average, with time, as it must expected for a foreland basin. With this correlation, the bivalve *Halobia* cf. *H. septentrionalis* would occur in the Carnian at HWQ.

5.4. The sources of OM in the Sichuan Basin

The $\delta^{13}C_{org}$ in sedimentary rocks can result from the combination of OM from diverse sources, in particular marine or freshwater-terrestrial (Fogel and Cifuentes, 1993). A possible variability of OM sources in the investigated sections is demonstrated in figure 8, where the average carbon isotopic compositions of different components from the Sichuan Basin are compared with those of coeval

localities worldwide, where the provenance of OM could be suggested on the basis of the sedimentary environments. The $\delta^{13}C_{org}$ of sandstone across the CNB interval is much heavier than samples from coeval deep marine settings of Black Bear Ridge, but overlaps with wood samples from both the Sichuan Basin and the Southern Alps. On the contrary, the average $\delta^{13}C_{org}$ of limestones in the Sichuan Basin, which bear little terrigenous material and no wood, is closer to the carbon isotopic composition of the open marine Black Bear Ridge section. These different $\delta^{13}C_{org}$ values could be easily explained if we assume that OM in limestones is mostly marine in origin, while the wood-bearing sandstones contain mostly terrestrial organic matter.

Recent marine OM, which is mainly derived from phytoplankton, benthic and macroscopic algae (Fry *et al.,* 1977), has a $\delta^{13}C_{org}$ is less negative than -23.0 ‰ (Fry *et al.,* 1977; Anawar *et al.,* 2010). However, the terrestrial OM is more $\delta^{13}C$-enriched than marine OM during the Triassic (Hayes *et al.,* 1999; Nordt *et al.,* 2016). OM remineralization, metabolic fractionation and diagenesis could alter the isotopic composition of OM (e.g., McArthur *et al.,* 1992; Goñi *et al.,* 1997; Anawar *et al.,* 2010), but the impact of diagenetic factors should not be important in our case, because we only consider relative changes within bulk rock and wood which underwent similar diagenetic influences in each study area.

Wood fragments from the HWQ and JS sections have more positive $\delta^{13}C_{org}$ than marine OM (Fig. 8), within a wide range from -25.35 ‰ to -22.07 ‰. Although wood from the Dolomites is slightly heavier (Dal Corso *et al.,* 2011), this could be ascribed to an undetected difference in taxonomic composition. Triassic land plants were C3 plants, and today C3 plants have an average $\delta^{13}C_{org}$ of ca. -26 ‰. Even though the average $\delta^{13}C_{org}$ in the Longmen Shan area is -24.0 ‰, slightly more positive than present values, it is still in the range of what would be expected for C3 plants (Gröcke, 2002; Badeck *et al.,* 2005, and references therein). The wide range of $\delta^{13}C_{org}$ from wood fragments reflects a natural dispersion that is expected for plants (e.g., Arens *et al.,* 2000; Dal Corso *et al.,* 2017) and is common in fossil material (e.g., Dal Corso *et al.,* 2011). Due to its intrinsic variability, an erratic trend is observed in the $\delta^{13}C_{org}$ of wood of the HWQ section (Fig. 2).

The mean value of $\delta^{13}C_{org}$ in terrigenous rocks (Unit 4 in Fig. 2) is between those of wood and bulk OM of the limestone units (Fig. 8), albeit closer to the $\delta^{13}C_{org}$ of wood. These foredeep-deposited terrigenous rocks have been suggested to be related to the uplift of Longmen Mountains and other surrounding paleolands (Yang *et al.,* 2008; Liu *et al.,* 2009; Shi *et al.,* 2015), thus the $\delta^{13}C_{org}$ of bulk organic carbon in this unit may reflect the mixing of C3 plant material with marine OM. The different OM source with distinctive ranges of $\delta^{13}C_{org}$ value from limestone units and terrigenous unit may explain the PIE2 (Fig. 2).

Differences in organic carbon sources may also explain other minor features of the $\delta^{13}C_{org}$ record that could not be correlated between the three study sections. In the HWQ section, the well-bedded

sponge mound layers are inter-reef deposits that correspond to the mound-shape sponge reefs in the JS and HWG sections (Wu, 1989). A slight negative perturbation of ca 1.5 ‰ in magnitude (CIE1 in Fig. 2) is recorded within the inter-reef deposits which is not, however, reproduced in the other two sections of this study. We suggest that this local isotopic shift may be related to accumulation of marine OM in this inter-reef environment rather than to a regional or global modification of the organic carbon pools.

5.5. Is there a carbon isotopic oscillation at the CNB?

In our correlation Option A (Fig. 11A), a strong isotopic excursion of $\delta^{13}C_{carb}$ nearly coincides with the CNB. However, $\delta^{13}C_{carb}$ from carefully chosen brachiopod shells show no detectable excursion. This has been explained as the result of early diagenesis of carbonate sediments rich in organic carbon during shallow burial (Jin *et al.,* 2018a). The $\delta^{13}C_{carb}$ record from brachiopods is considered to represent a more pristine record of seawater $\delta^{13}C$ than bulk carbonate (Brand, 1989; Brand *et al.,* 2003; Korte *et al.,* 2005). Although a 1 ‰ magnitude shift is still found in brachiopod data near the CNB (Fig. 11A), this may actually derive from the natural range of isotopic variability of brachiopod shells (Korte *et al.,* 2017). A PIE in the $\delta^{13}C_{carb}$ across the CNB interval has been reported in many locations (Black Bear Ridge, Onoue *et al.,* 2016; Guri Zi, Muttoni *et al.,* 2014; Pizzo Mondello, Muttoni *et al.,* 2004; Mazza *et al.,* 2010; Wadi Mayhah, Sun *et al.,* 2018) (only the BBR and PMS sections were displayed in Fig. 11A). This PIE has different shapes and magnitudes and has only been reported from deep water setting (Fig. 11A). We could not confirm the occurrence of this PIE at the CNB on the base of our $\delta^{13}C_{carb}$ data from well preserved brachiopods.

The $\delta^{13}C_{org}$ records of wood and bulk organic carbon reported in this work from Hanwang and Jushui areas are the first from the CNB interval in South China. The only counterpart with detailed biostratigraphy is Black Bear Ridge, Canada (Williford *et al.,* 2007). A small negative isotopic perturbation, ca 0.5 ‰ in magnitude, was found at the proposed position of the CNB at Black Bear Ridge and was discussed in relation to a fossil turnover observed in the section (Williford *et al.,* 2007). In our correlation Option A (Fig. 11A), an opposite shift (PIE1) to more positive values ca. 2 ‰ in magnitude occurs in the $\delta^{13}C_{org}$ across the CNB, which is part of a general positive trend within the limestone unit, reproduced in all study sections (Fig. 2).

According to correlation Option B (Fig. 11B), a minor negative shift (CIE2) of ~ 1 ‰ is observed at 15 m, at the base of the CNB interval, which is difficult to correlate with Black Bear Ridge because biostratigraphic constraints in this part are poor. Moreover, this negative shift is found in an interval of facies transition characterized by the increase in terrigenous input and therefore might be related to the mixing of OM from continental and marine sources. As a consequence, the general flat trend

of $\delta^{13}C_{org}$ values within the CNB interval (Fig. 11B), grey band could have recorded a mixed-carbon stable isotopic composition, and the real signal of $\delta^{13}C_{org}$ across the CNB which could have been masked in our sections.

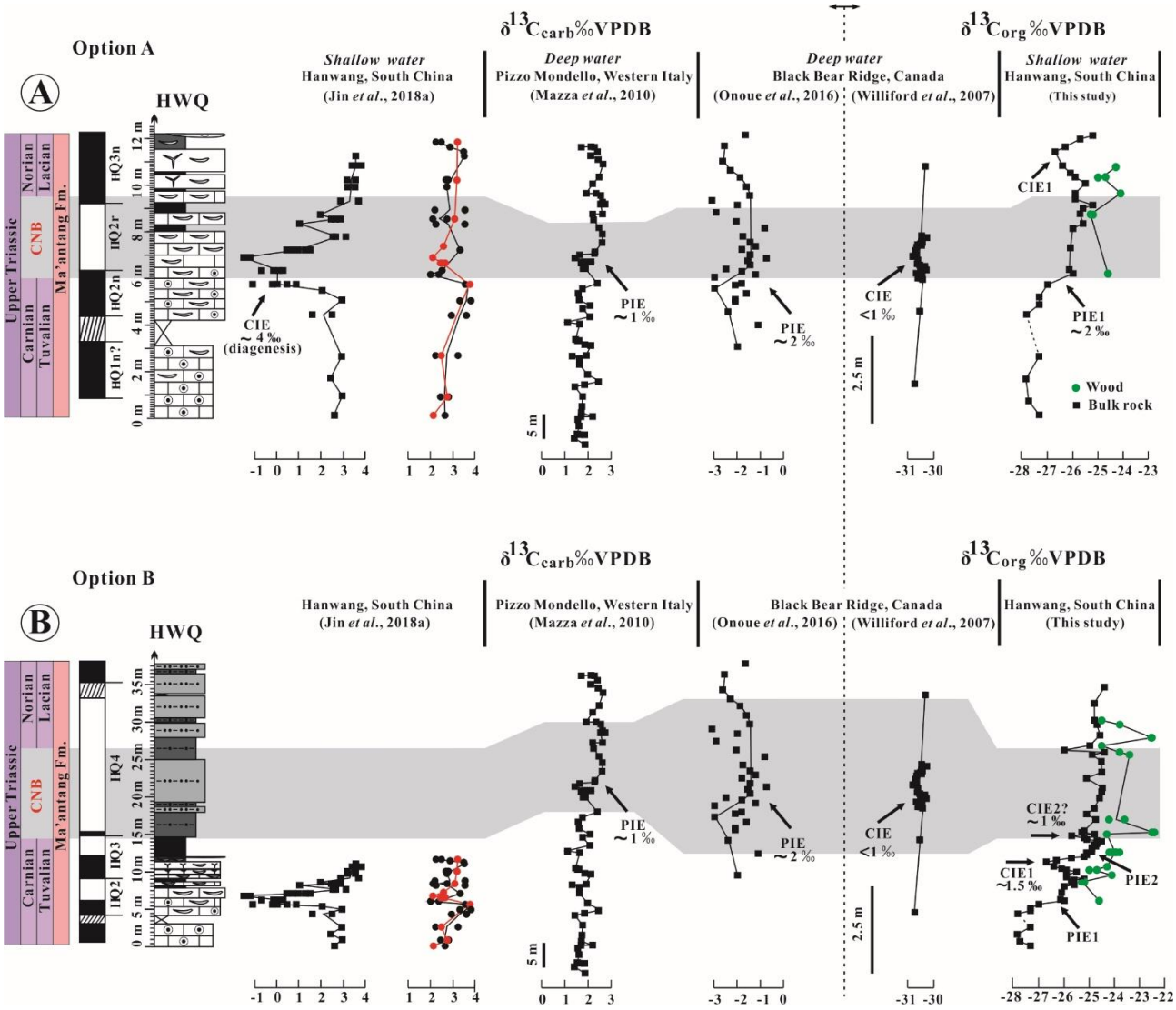

Fig. 11. Comparison of carbon isotope (organic and carbonate) records from the HWQ section, South China and other selected Carnian/Norian boundary (CNB) sections, according to the two correlation options proposed in figures 9 and 10. In option A, the grey band is the CNB interval according to Mazza *et al.* (2012), i.e., between the FO of *Metapolygnathus parvus*, below, and the FO of *Carnepigondolella gulloe* (close to the FO of *Halobia austriaca*), above. For option B, the grey band is the CNB interval according to ammonoid biostratigraphy. At Pizzo Mondello, this interval is comprised between the last occurrence of *Anatropites* sp., below, and the FO of *Dimorphites* spp., above (Balini *et al.,* 2012). At Black Bear Ridge, we drawn the CNB interval between the last occurrence of *Anatropites* sp., below, and the FO of *Guembelites jandianus*, above (Orchard *et al.,* 2014).

5.6. The end of Carnian Pluvial Episode in the northwestern Sichuan Basin

The most negative values of $\delta^{13}C_{org}$ are recorded in the lowest part of the HWG section, followed by a long-lasting positive trend (Fig. 2). As this trend is detected within the limestone units (Unit 1

to 3), we assume the OM source was not changing too much in this interval. The $\delta^{13}C_{org}$ of limestones in the Sichuan Basin overlap with values of $\delta^{13}C_{org}$ during the fading phase of the CPE from adjacent Nanpanjiang Basin (Fig. 8). We tentatively correlate the carbon isotope records between these two areas (Fig. 12).

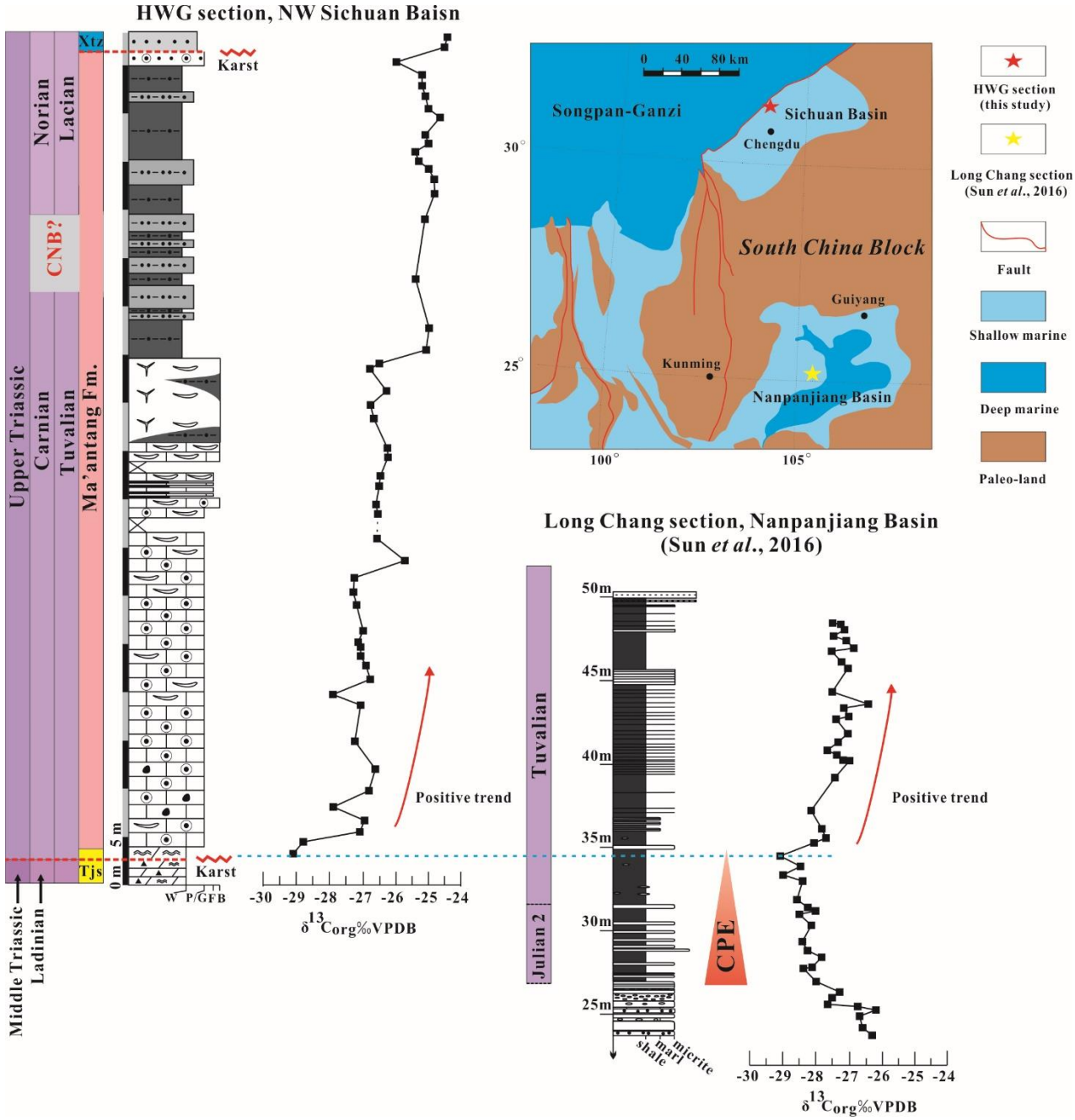

Fig. 12. Comparison of the $\delta^{13}C_{org}$ records between the HWG section, NW Sichuan Basin and Long Chang section, Nanpanjiang Basin (Sun *et al.*, 2016). The lower part of the Long Chang section was truncated. The Carnian paleogeographic map of South China (top right corner) modified from Ma *et al.* (2009). CPE, Carnian Pluvial Episode.

The biostratigraphy of the HWG section is still incomplete. The lower Ma'antang Formation yielding most negative $\delta^{13}C_{org}$ values might be corresponding to approximately the 34 m level in the

Long Chang section of Sun *et al.* (2016) and thus to the fading phase of the carbon isotopic excursion (CIE) of the Carnian Pluvial Episode. This trend was recognized clearly in the Ma'antang section, North-eastern Sichuan Basin (Shi *et al.*, 2018), and it is identifiable in the basal part of our three sections (Fig. 2). The distinctive CIE was also reported in other parts of Tethys (Dal Corso *et al.*, 2012, 2015, 2018; Mueller *et al.*, 2015, 2016; Miller *et al.*, 2017; Baranyi *et al.*, 2018; Sun *et al.*, 2018) and it is partly missing at the HWG because it corresponds to a hiatus marked by the basal karstic surface (Fig. 2, 12), which has been interpreted as the forebulge unconformity of the Longmen Shan foreland basin (Li *et al.*, 2003, 2011b). In the eastern Sichuan Basin, the whole Tianjinshan Formation and the overlying Ma'antang Formation were eroded or they never deposited (Li *et al.*, 2003; Mei and Liu, 2017).

6. Conclusions

New biostratigraphic data from the Carnian and Norian of the northwestern Sichuan Basin are provided in this work. On the basis of an existing magnetostratigraphy and new biostratigraphic age determinations, two possible correlations between the Astrochronology Polarity Time Scale of the Triassic and the magnetostratigraphy of the HWQ section are proposed, but further biostratigraphic investigations are needed to identify a preferred correlation. In Option A correlation, the CNB is located between 6 m and 9.5 m. In Option B correlation, the CNB could be positioned between 14.5 m and 26.5 m of the HWQ section. Furthermore, the occurrence of Carnian conodonts at the base of the JS section imply that some stromatolitic dolostones/limestones in the Sichuan Basin are Carnian rather than Ladinian.

Carbon stable isotopes from wood and bulk organic matter are here measured for the first time in eastern Tethys near the CNB. The recorded variability of $\delta^{13}C_{org}$ between different lithologies is explained by varying organic matter sources. A long-lasting positive trend has been recognized within a uniformly calcareous interval, which can be attributed to the slow recovery from the isotopic perturbations of the CPE and can be corrected with the isotopic record of the Nanpanjiang Basin of South China. Instead, the isotopic record of the CPE in the western Tethys and continental Europe is more complex, featuring repeated negative isotopic excursions, and its correlations with the Sichuan Basin is still uncertain.

Overall, our findings erect the northwestern Sichuan Basin as a relevant area for the study of the CNB. In particular, Carnian-Norian ammonoids, conodonts, and bivalves from the Sichuan Basin are from a much easterly position than other successions so far considered for the definition of the CNB. These new biostratigraphic data may thus reveal useful for a better-informed placement of the Norian GSSP.

Acknowledgements

We acknowledge Stefano Castelli (University of Padova) for the conodont and ammonoid plates. Piero Gianolla (University of Ferrara) and Jacopo Dal Corso (University of Leeds) are thanked for the discussions. We are grateful to two referees, Yadong Sun (Universität Erlangen-Nürnberg) and Mark W Hounslow (Lancaster University), and Editor Alastair Ruffell for the useful comments which improved our manuscript. This work was supported by Open Fund of State Key Laboratory of Oil and Gas Reservoir Geology and Exploitation (Chengdu University of Technology) (grant number PLC20180301); the National Natural Science Foundation of China grants (grant numbers 41272131, 41572085); and China Scholarship Council (grant number 201508510096).

CHAPTER 4

The Carnian Pluvial Episode at Ma'antang, Jiangyou in Upper Yangtze Block, Southwestern China

Zhiqiang Shi [a], *, Xin Jin [b], Nereo Preto [b], Manuel Rigo [b], c, Yixing Du [a, b] Lu Han [a]

a. State Key Laboratory of Oil and Gas Reservoir Geology and Exploitation, Chengdu University of Technology, Chengdu, Sichuan 610059, China
b. Department of Geosciences, University of Padova, Via Gradenigo, 6, 35131 Padova, Italy
c. IGG-CNR (Istituto di Geoscienze e Georisorse), Via Gradenigo, 6, 35131 Padova, Italy
*Corresponding author. E-mail address: szqcdut@163.com; Fax: +86 28 8407 8992; Tel: +86 28 8407 9807

Received 12 February 2018; Revised 21 October 2018; Accepted 13 November 2018

Abstract

The Ma'antang (MAT) section is located in the Jiangyou County, Upper Yangtze Block (Northwest margin of Sichuan Basin, China). The lowest MAT section is made of peritidal cycles with stromatolite layers of the Tianjingshan Formation. A subaerial exposure (karst) surface occurs in its upper part. The carbonate carbon and oxygen isotopes show a clear meteoric diagenetic trend near the karst surface. Above, the Ma'antang Formation is subdivided into 5 units on the basis of lithology. Units 1 to 3 are composed of bioclastic limestones and intercalated thin clayey siltstones. At least four intervals of sandstone are recognized in these units. A distinct lithological transition from carbonates to terrigenous clastic rocks is observed between the boundary of Units 3/4. The diagnostic fossils (ammonoids and conodonts) constrain the lower part of Unit 4 to the Julian 2 (Early Carnian), and the Julian/Tuvalian boundary is in the upper part of Unit 4. Unit 5 is mainly made of siltstone and sandstone. A broad negative carbon isotopic excursion (CIE), ca. 4 ‰ in magnitude, occurs in the lower Carnian of the MAT section, and is followed by a long positive trend. A similar carbon isotopic excursion has been reported in Nanpanjiang Basin, South China and was related to the CPE. The CIE at the MAT section is the first reported in Sichuan Basin and can be correlated to other CPE sections from western Tethys, which however record multiple and short-lived isotopic excursions. The CIE shows that the CPE started well before the main transition to siliciclastic sedimentation at the MAT section. However, it is unclear whether the occurrences of the minor

siliciclastic intervals within Units 1-3 could be correlated to similar terrigenous episodes in the western Tethys region.

Keywords: Late Triassic, Carnian Pluvial Episode, Eastern Tethys, Conodonts, Stable carbon isotopes

1. Introduction

The Carnian Pluvial Episode (CPE sensu Simms and Ruffell, 1989) was characterized by the extensive crisis of carbonate platforms in shallow marine environments, and by the sharply increased rainfall and runoff products, as terrigenous sediments. Moreover, a humid climate and carbon and oxygen isotopic perturbations were associated to the CPE, which have been widely reported in many marine and continental sections of Tethys (reviewed in Ogg, 2015 and Ruffell *et al.,* 2016; see also Chapter 1 of this thesis work).

The character of Carnian Pluvial Episode has been discussed with details in the introduction of this thesis and the front two chapters. Basing on our previous results, the crisis of carbonate platforms in the Hanwang region of the Sichuan Basin was not related to CPE because of the age, which is too young. The onset of CPE in western Tethys is near the boundary Julian 1/ Julian 2 (Hornung and Brandner, 2005; Hornung *et al.*, 2007c; Dal Corso *et al.*, 2012, 2015, 2018, and references therein), while the ammonoids and conodonts in Hanwang indicate late Tuvalian (late Carnian) to early Norian ages (Jin *et al.*, 2018a, b: see chapters 2 and 3). This conclusion negates the previous studies that related the demise of carbonate platforms and the overlain dark grey shales in Hanwang and Jushui to the CPE (Shi *et al.*, 2017). The questions remains unanswered, however, whether the CPE is documented in some part of the Sichuan Basin or not. Wang (1992) reported early Carnian ammonoids in Ma'antang, but a lithological log, precise biostratigraphy, and geochemical data are still missing. Hence, we collected and determined ammonoids and conodonts from the MAT section for its biochronology, and sampled bulk rock for its stable carbon isotopes. The results are displayed in this paper.

2. Geological setting

The Late Triassic of Sichuan Basin has been described in chapters 2 and 3. Here, additional information on the MAT section will be given. The Ma'antang section (N 32°11’22.14”/E 105°13’50.35”) is located in the Longmen Shan Thrust Belt, at the boundary between the Sichuan Basin and Tibetan Plateau (Fig. 1A). This section encompasses the Tianjingshan Formation, the

Ma'antang Formation and the Xiaotangzi Formation (Fig. 2). At Hanwang and Jushui, about 100 kilometers southwestward from the Ma'antang Section (Fig. 1B), the Carnian is less than 100 m thick and mainly composed of oolitic limestones, sponge-bearing limestones, shales and siltstones (Wu, 1989, 2009; Shi *et al.*, 2017; Jin *et al.*, 2018a). In Jiangyou, the Carnian is represented instead by the more than 200 m thick Ma'antang Formation, which is subdivided into five lithological units (Fig. 1C, Fig. 2). Deng *et al.* (1982) considered the boundary between the Tianjingshan and Ma'antang formations as a conformity surface. In the present study, however, we distinguished an erosional uncomformity marked by a deep karst within the stromatolites of uppermost Tianjingshan Formation (Fig. 2).

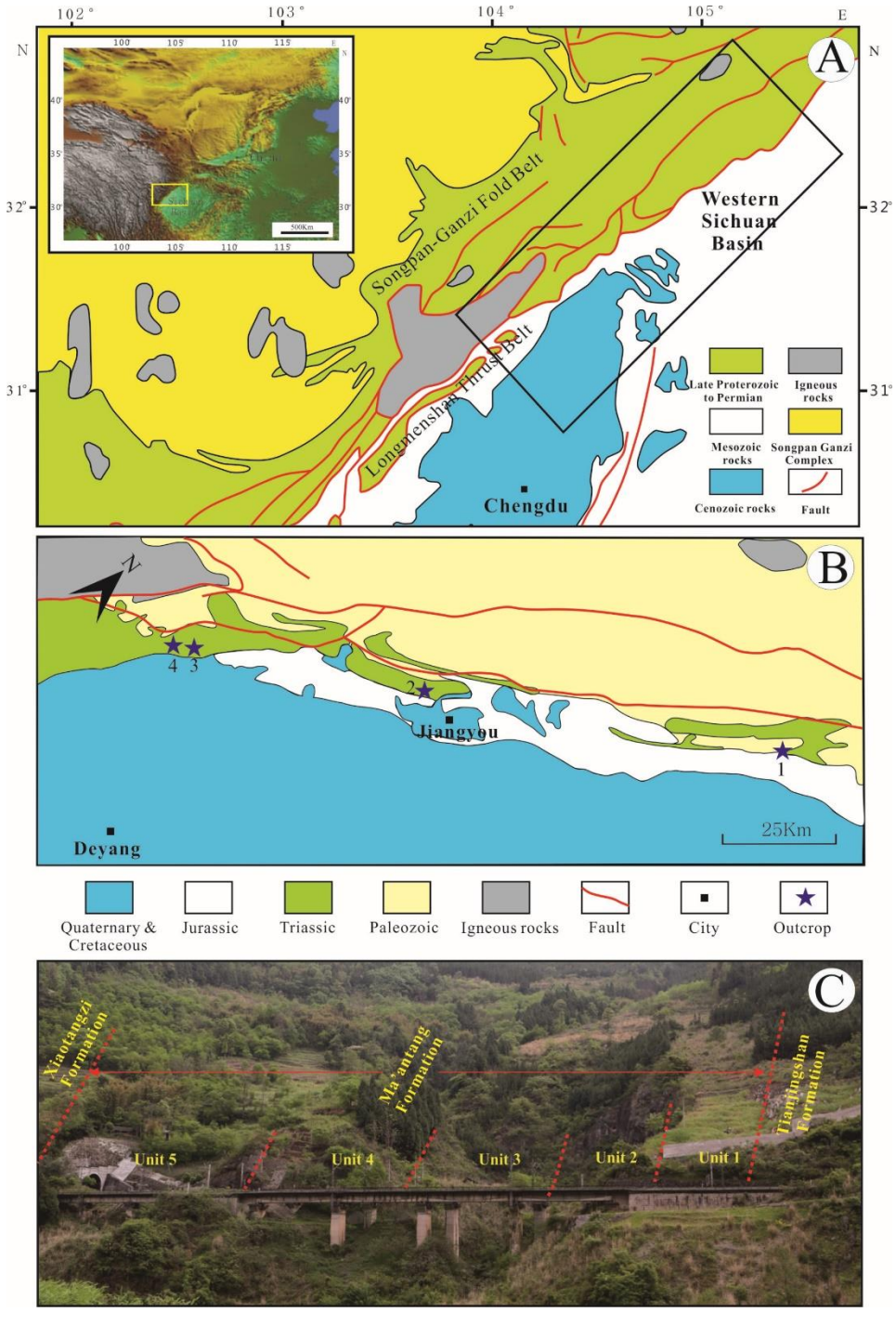

Fig. 1. General geological and tectonic map (**A**) of the western margin of Sichuan Basin (inset shows the Longmen Shan region with respect to the Tibetan Plateau), detailed geological map (**B**) showing the location of Ma'antang section and the lithological units in the outcrop (**C**). 1-Ma'antang Section; 2-Huanglianqiao Section; 3-Jushui Section; 4-Hanwang Sections.

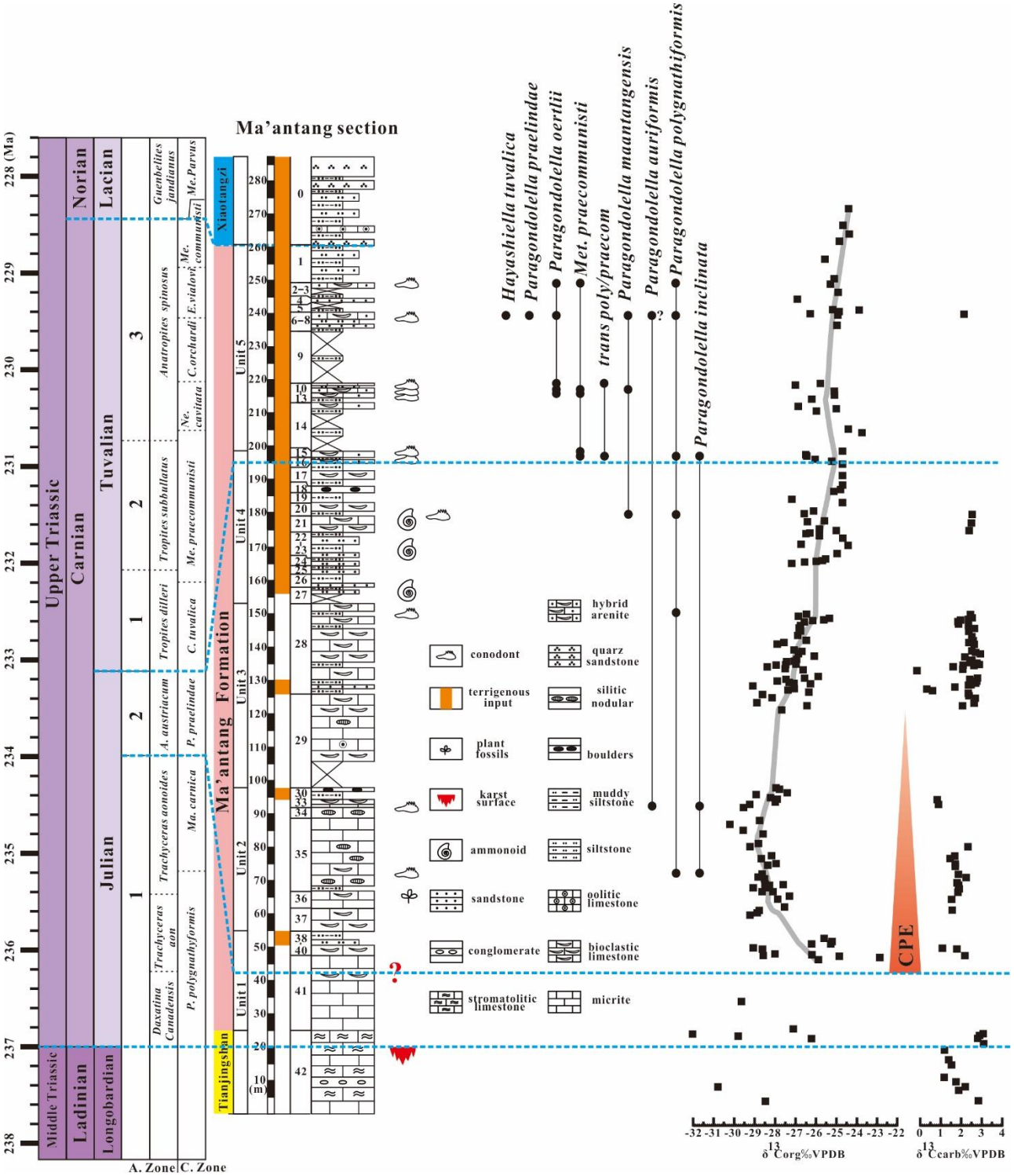

Fig. 2. Lithologic units and organic/carbonate carbon isotopic curves of the Upper Triassic Ma'antang Formation in the Ma'antang Section. Time scale as of Bernardi *et al.* (2018). The ammonoid zonation of Carnian follows Gallet *et al.* (1994) and Broglio Loriga *et al.* (1999). The conodont zonation of Carnian follows Rigo *et al.* (2018).

3. Materials and methods

3.1. Lithological study

The MAT section was measured and logged. Bulk rock samples were collected for microfacies analysis and prepared for standard thin sections. All the thin sections were studied and photographed with a polarizing microscope at the Institute of Sedimentary Geology, Chengdu University of Technology. See Chapter 5 for further details.

3.2. Ammonoids and conodonts

More than 20 ammonoid fossils were collected from the dark clayey siltstone of Unit 4 (upper Ma'antang Formation). Fossils were photographed and identified at the Department of Geoscience, Padova University. Twenty-nine samples, more than 3 kg each, were dissolved with formic acid and the residuals were concentrated by heavy liquids treatment at the Department of Geoscience, Padova University. The conodonts were photographed by the Scanning Electron Microscope (SEM) at the two State Key Laboratoris of Northwest University and Chengdu University of Technology in China.

3.3. Organic carbon isotopic analysis

One hundred and forty-six bulk rock samples were washed with deionized water, oven-dried at 50° and powdered in an agate mortar. Around 2 g were put into polypropylene Falcon tubes, acid-washed with 10% HCl and neutralized with deionized water. Between ca. 0.5 and 10 mg of powder were then weighted in tin capsules and wrapped. All samples were analyzed with the Thermo Scientific Delta V Advantage Isotopic Ratio Mass Spectrometer (IRMS) linked to a Thermo Scientific Flash 2000 Elemental Analyzer (EA) at Padova University. The international standards CH-6 ($\delta^{13}C$ = -10.449 ‰ VPDB) and CH-7 ($\delta^{13}C$ = -32.151 ‰ VPDB) were ran along the samples for normalization purposes. An internal standard ZER ($\delta^{13}C$ =-25.99+/- 0.24 ‰ VPDB) was ran repeatedly as a quality control. The precision obtained was better than +/- 0.15 ‰ (standard deviation).

3.4. Carbonate carbon and oxygen isotopic analysis

Seventy-six limestone samples were drilled by a micro-drill (0.4 mm) to manually extract ca. 0.2-2 mg of powder from freshly broken surfaces. Then, between 0.2 and 0.35 mg of sample were weighted into exetainer glass vials, which were flushed with > 400 ml of high-purity He less than 24

h before the analysis. The analyses were performed with a Delta V Advance Isotopic Ratio Mass Spetrometer at the Department of Geosciences, University of Padova, Italy. The results were normalized against an internal standard (white Carrara calcite marble Maq 1: $\delta^{13}C$=2.58 %; $\delta^{18}O$=1.15 ‰ VPDB) which is being periodically calibrated against NBS 19. The reproducibility was tested with repeated analyses of a quality control standard and resulted better than 0.1‰ (1σ) for both carbon and oxygen.

4. Results

4.1. Sedimentological and lithological description

4.1.1. Uppermost Middle Triassic Tianjingshan Formation

The uppermost Tianjingshan Formation (Bed 42 showed in Fig. 2) is mainly composed of greyish white microbialitic limestone. Its age is Middle Triassic (Wu, 1989; Li *et al.*, 2003). An irregular karst surface (Fig. 3A) was found about 5 meters below the last stromatolitic bed. The karst cavities (Fig. 3B) are filled by angular and poorly sorted breccia in a calcareous fine matrix, which are observed in the MAT section.

4.1.2. Ma'antang Formation

Ma'antang Formation can be subdivided into five units (Fig. 2). Unit 1 is made of micritic and and peloidal limestone with thick bedding (Fig. 3C). Thin bedded shelly limestone occurs at the upper part of Bed 41 (Fig. 3D), and is dominated by diverse skeletal grains (Fig. 3E). Terrigenous clasts (sand grains) are common in Beds 39-38 and mark a first siliciclastic pulse at the MAT section (Fig. 2). Abundant metazoan fossils are found in Bed 38. Unit 2 is composed of thin to middle bedded bioclastic limestone of Beds 37-36 (Fig. 3F, G), massive or thick bedded wackestone containing chert nodules of Beds 35-34, and bioclastic limestone, shale and siltstone of Beds 33-30 (Fig. 2). Plants, bivalves and foraminifera are found in Bed 36 (Fig. 3G, H). Bed 31consists of shale and siltstone, represents the onset of a second siliciclastic pulse (Fig. 2). Spherical nodules of bioclastic limestone which are 15-30 cm in diameter are common in the Bed 30 (Fig. 3I) within siliceous sandstone and claystone. The lower part of Unit 3 (Bed 29) is composed of micrite, grainstone, and oolite, while the upper part (Bed 28) is composed of bioclastic limestone containing siliceous sponge spicules (Fig. 4A) interbedded with shales and rare sandstones. Unit 4 is mainly composed of siltstone, fine sandstone, and bioclastic limestone of Beds 27-15. The bioclastic limestones (Fig. 4B, C) contain

abundant sand grains, and many marine fossils are found in siltstone and sandstone (Fig. 4D). Unit 5 mainly consists of terrigenous clasts and sandy bioclastic limestone (Fig. 2). The bioclastic limestone contains diverse fossils and fine quartz sands (Fig. 4E-G), and abundant fossils can also be found in siltstones and sandstones of this unit (Fig. 4H).

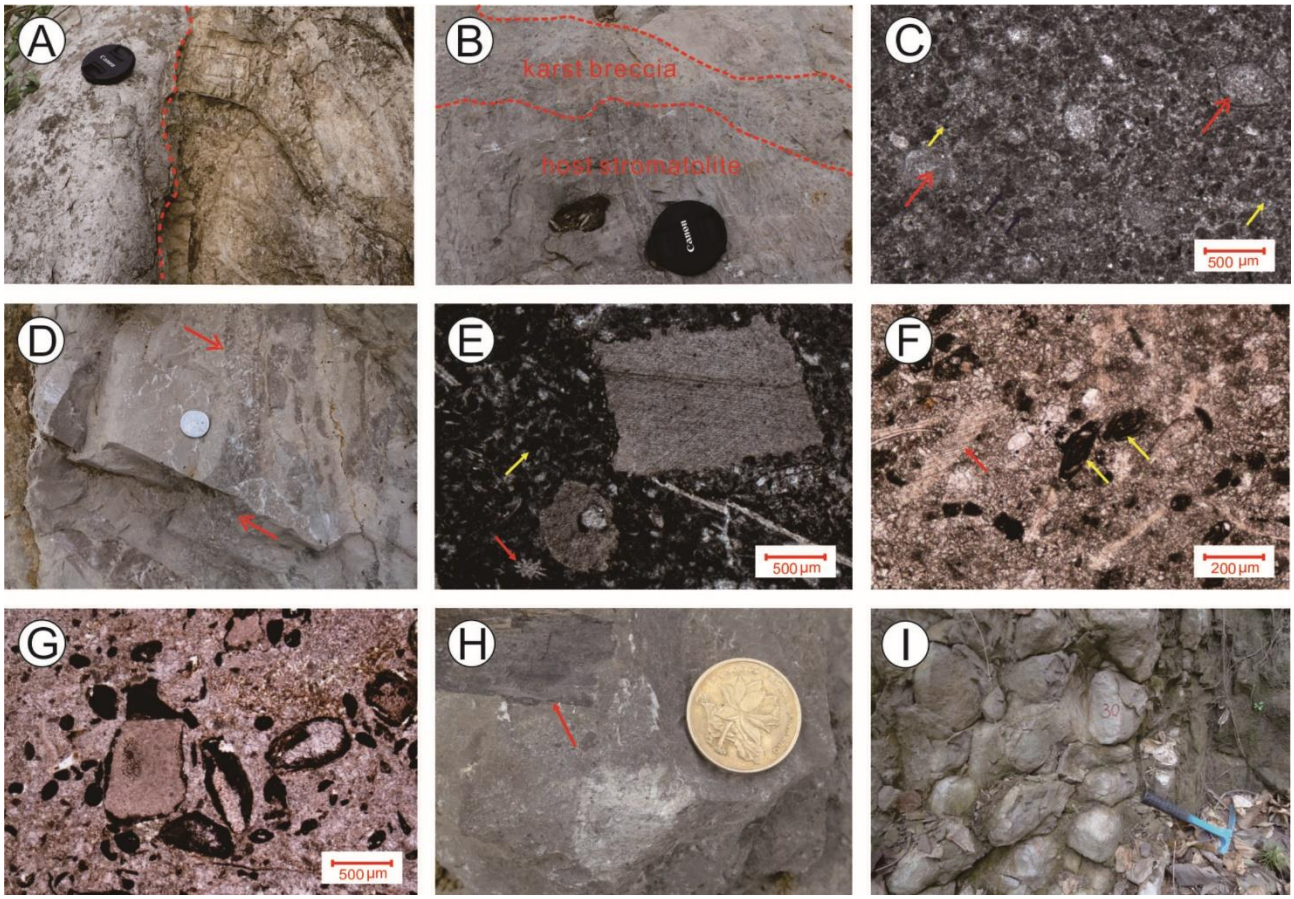

Fig. 3. Lithological and mineral characteristics of the Units 1-3, Upper Triassic Ma'antang Formation at Ma'antang, Jiangyou. (**A**), An irregular karst surface develops within the stromatolite of the uppermost Tianjingshan Formation. (**B**), Breccia filling in a karst solution groove at the uppermost Tianjingshan Formation. (**C**), Algae grains (indicated by the red arrows) and spherulite (indicated by the yellow arrows) are contained in the micrite of Bed 41. (**D**), Thin bedded shelly limestone yield as thin interlayers in the upper Bed 41 (indicated by the red arrows). (**E**), Crinoid segments, urchin spine (indicated by the red arrow) and faecal pellets (indicated by the yellow arrow) are seen from the bioclassic limestone of Bed 40. (**F**, **G**), Bivalve, foraminifer and echinodermata fossils and thrombolite are contained in Beds 37 and 36. (**H**), Plant fossils are seen in Bed 36. I-Boulders of bioclastic limestone are common in the Bed 30.

4.1.3. Upper Triassic Xiaotangzi Formation

The lower part of Xiaotangzi Formation is made of thin bedded oolite and bioclastic limestone and interlayered with brown siltstone and dark grey shale. A thin, brown ferruginous layer between the Ma'antang and Xiaotangzi Formations has been observed, which was interpreted as a possible uncomformity. Middle-thick bedded quartz sandstone was found about 20 m above the

Ma'antang/Xiaotangzi Formation boundary (Fig. 4I).

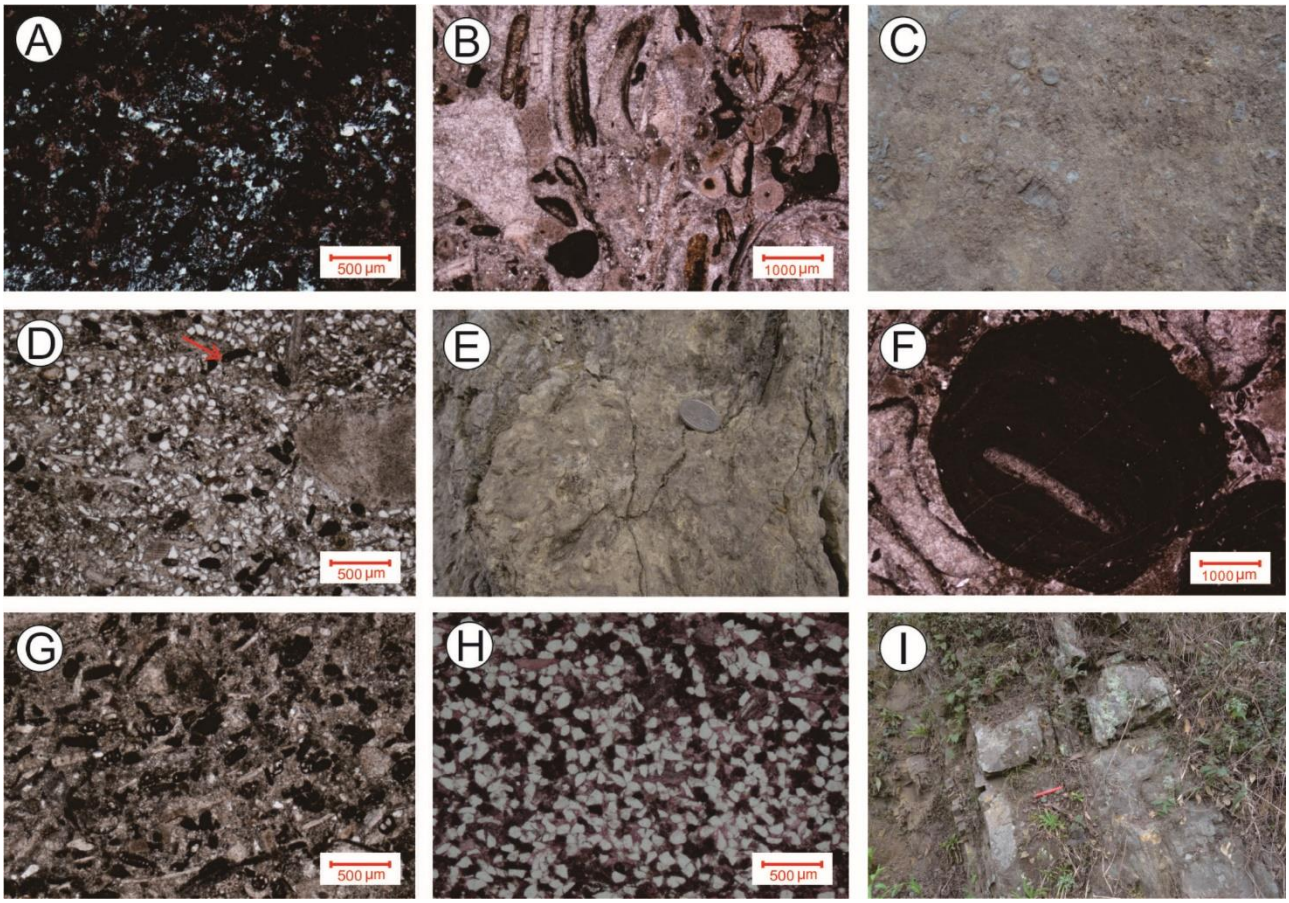

Fig. 4. Lithological and mineral characteristics of the upper Ma'antang Formation and Xiaotnagzi Formation. (**A**), Polarizing microphotograph of siliceous sponge spicules (approximately 40%) are contained in the Bed 28. (**B**, **C**), Crinoid and bivalve fragments are most common in the bioclastic limestone layers of Beds 20 (**B**) and 16 (**C**). (**D**), The sandstone of Bed 20 contains 35 % marine bioclastics of foraminifer, bivalve and crinoid, and calcite cement is common. (**E**), An oncolite is contained in the bioclastic limestone of Bed 11. (**F**, **G**), The bioclastic limstone contains plenty of crinoid, bivalve and foraminifer fossils and fine squartz sands in the Bed 10. (**H**), The sandstone of Bed 3 contains bioclastic grains and calcite cement. (**I**), The quartz sandstone sequence of middle Xiaotangzi Formation.

4.2. Biostratigraphy

4.2.1. Ammonoids

Ammonoids of the Ma'antang section are preserved as internal moulds with external impression and are present in a few horizons within a short interval of Unit 4. Unfortunately, all recovered specimens are fragmented, and many are compressed. The suture line is never visible. Only five specimens, which are relatively more complete and better preserved, were determined for this study. A comparison is attempted with western Tethysian ammonoids (e.g., Krystyn, 1978; Ulrichs, 1994;

Mietto *et al.*, 2008, 2012; Lukeneder and Lukeneder, 2013), but given the typically endemic character of many Carnian ammonoid faunas (e.g., Hao *et al.*, 2003; Xu *et al.*, 2003; Zou *et al.*, 2015), determinations were conservatively done only at the genus level.

All specimens belong to ammonoids with strong ornamentation, constituted by ribs and tubercles. One specimen (Fig. 5C) has been determined as *Austrotrachyceras* sp. because of the double row of tubercles on each side of a furrowed venter that are nearly fused and disposed diagonally, positioned at the end of strongly proverse ribs. The other four specimens (e.g., Fig. 5A, B) expose flanks that show strong ribs, larger than the inter-rib spaces, often bifurcated and ornamented by tubercles which are elongated in the spiral direction. These specimens are determined as cf. *Neoprotrachyceras* sp.

The presence of *Austrotrachyceras* indicates a late early Carnian age (e.g., Krystyn, 1978; Lukeneder and Lukeneder, 2013). This genus is common in successions of the South China Block (e.g., Hao *et al.*, 2003; Sun *et al.*, 2016).

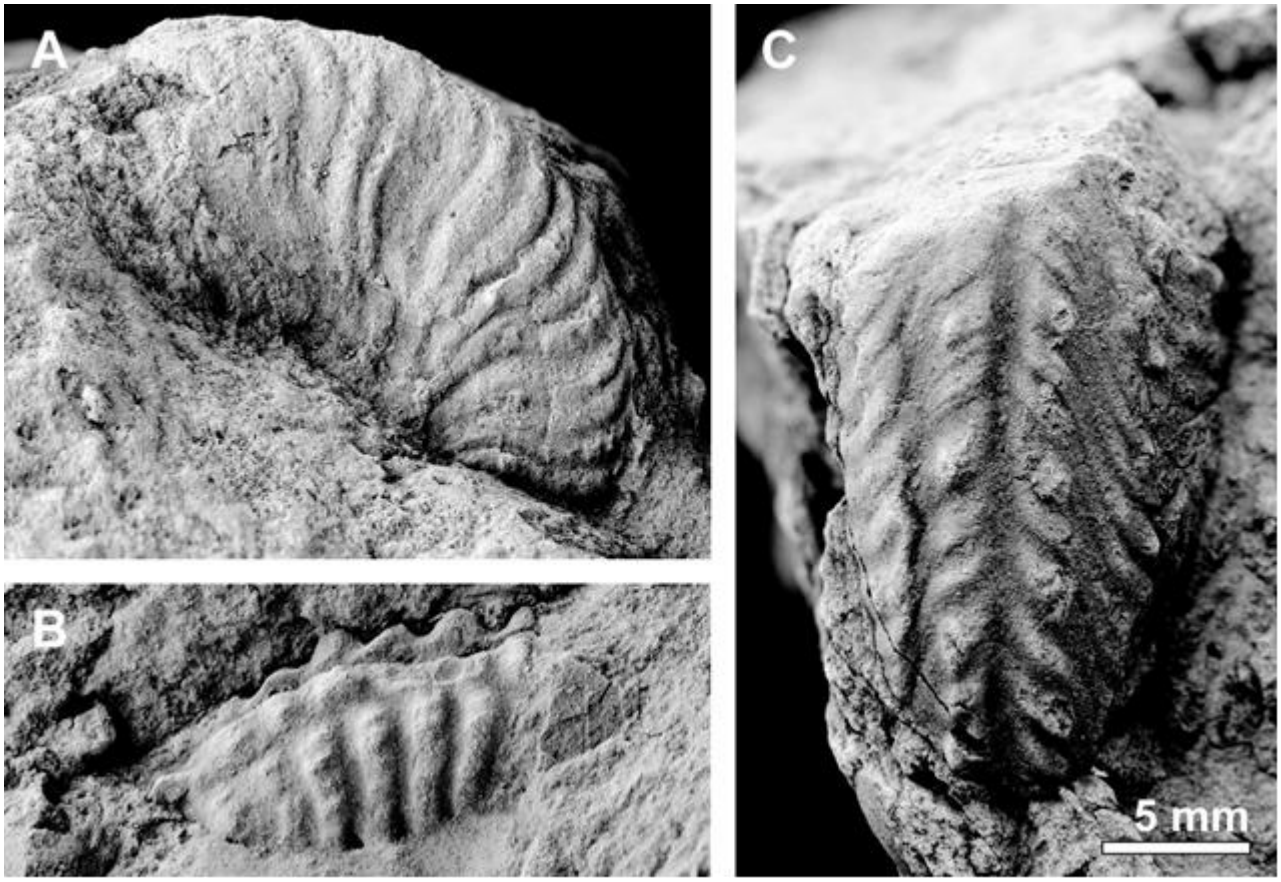

Fig. 5. Significant ammonoids from the Unit 4 of the Ma'antang Formation. (**A**, **B**). cf. *Neoprotrachyceras* sp. from the Bed 22. (**C**). *Austrotrachyceras* sp. from the Bed 22.

4.2.2. Conodonts

The studied samples yielded common to abundant conodonts, with a light pale amber color CAI=1. Two significant conodont assemblages have been recognized, the first ranging up to m 195,

and consisting of *Paragondolella polygnathiformis* (Fig. 6A, B, C), *P. inclinata* (Fig. 6D-F) and *P. auriformis*. The disappearance of *P. auriforms* in the upper part of Unit 2 of the Ma'antang Formation (Fig. 2) is commonly considered mid to uppermost Julian 1 (Rigo *et al.*, 2018). Above, this association occurs along with *Paragondolellla maantangensis* (Fig. 6G-I), which is found in younger strata also associated with typical primitive Tuvalian conodonts, such as *Metapolygnathus praecommunisti* (Fig. 6J-L) and *Paragondolella oertlii* (Fig. 6O-Q). The first occurrence of the *M. praecommunisti* was used here to define the Julian/Tuvalian boundary (upper part of Unit 4 of the Ma'antang Formation). *Paragondolella praelindae* (Fig. 6M, N) and *Hayashiella tuvalica* occur in the upper part of the studied section (Unit 5) with *P. oertlii* and *M. praecommunisti*. All of these species first occur just after the Julian/Tuvalian boundary (lower Tuvalian) (Mazza *et al.*, 2011, 2012).

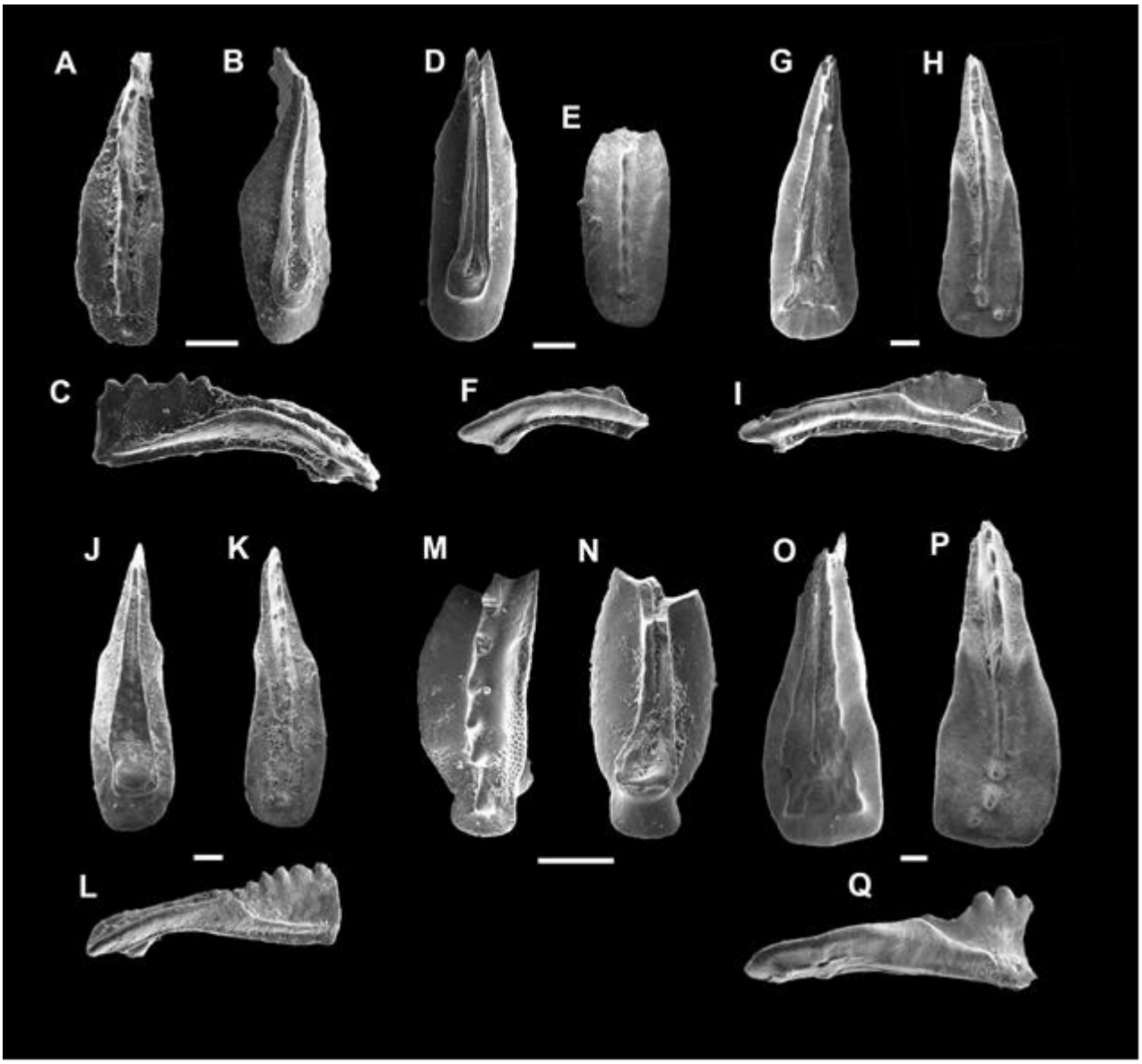

Fig. 6. Photomicrographs of conodonts from the Ma'antang Formation. (**A**, **B**, **C**). *Paragondolella polygnathiformis*. (**D**, **E**, **F**). *Paragondolella. inclinata*; (**G**, **H**, **I**). *Paragondolellla maantangensis*. (**J**, **K**, **L**). *Metapolygnathus praecommunisti*. (**M**, **N**). *Paragondolella praelindae*. (**O**, **P**, **Q**). *Paragondolella oertlii*. Scale bar 100 m. CAI=1.

4.3. Stable isotopes

Carbon and oxygen isotopes from 76 bulk carbonate samples have $\delta^{13}C_{carb}$ values ranging from -0.17 ‰ to +3.07 ‰, and $\delta^{18}O_{carb}$ values ranging from -6.29 ‰ to -0.87 ‰. Most of them are distributed in the region of isotopic composition of articulate brachiopods from Carnian seawater (Fig. 7A, Korte *et al.*, 2005). Immediately below the karst surface of the upper Tianjingshan Formation, the values of both $\delta^{13}C_{carb}$ and $\delta^{18}O_{carb}$ are strongly reduced, and gradually increase in a downward direction (Fig. 7B). Above the karst surface, neither the $\delta^{13}C_{carb}$ nor the $\delta^{18}O_{carb}$ show any discernible trend (Fig. 2).

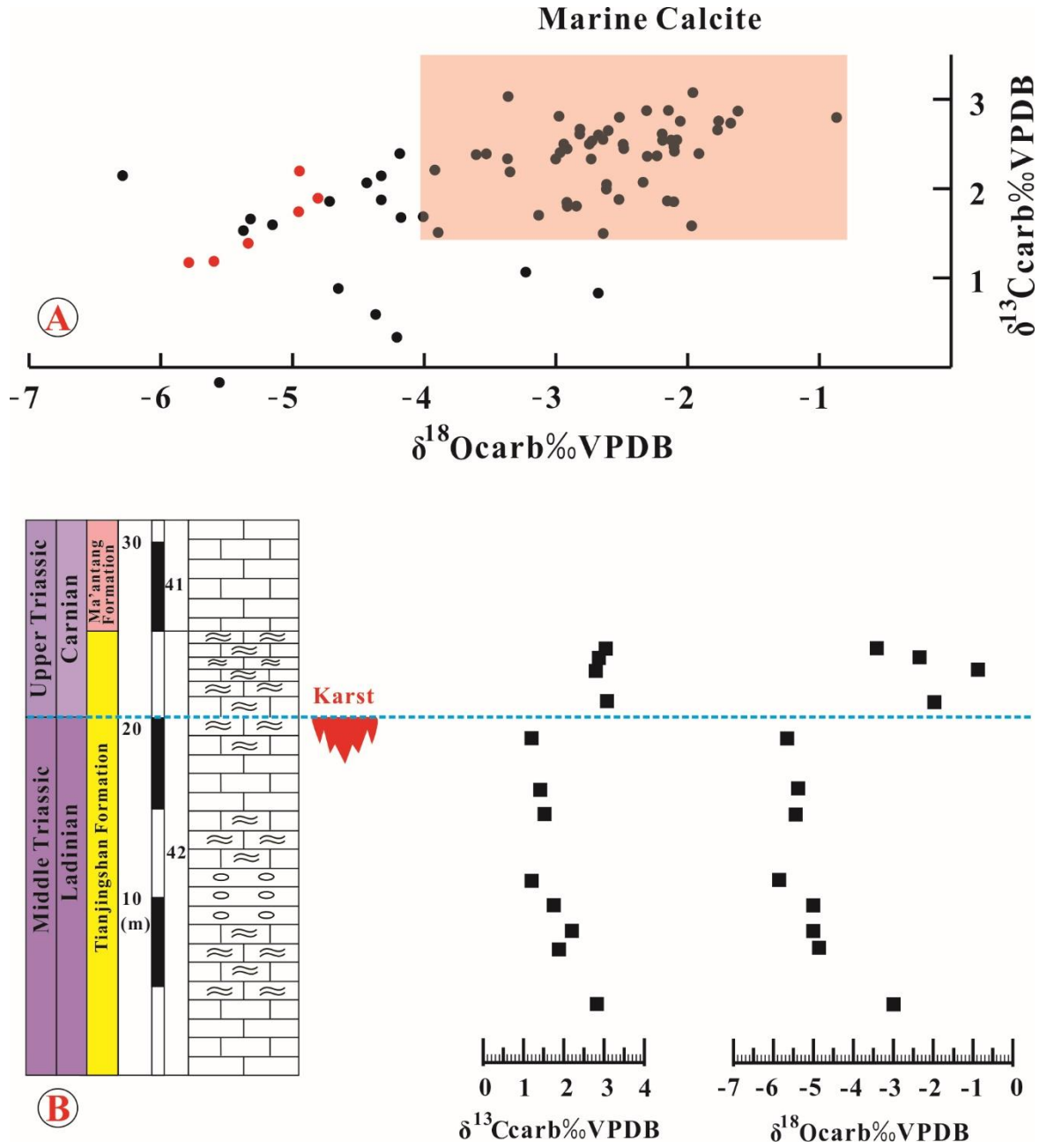

Fig. 7. Carbonate carbon-Oxygen relationship (**A**) and its values showing adjacently above and below the karst surface within the uppermost Tianjingshan Formation (**B**). Pink box represents isotopic variation of Carnian well brachiopods (Korte *et al.* 2005).

One hundred and forty-six bulk rock samples were analyzed for the $\delta^{13}C_{org}$ of bulk organic matter. The $\delta^{13}C_{org}$ values are ranging from -32.02 ‰ to -22.87 ‰. Data are scattered in the lower part of the section around an average of ca. -28 ‰ VPDB, i.e., the most negative values of the section. Organic carbon contents (TOC) were not determined for this interval but samples yielded minimal residues; it is probable that the scattering of values of $\delta^{13}C_{org}$ in this part of the section is related to the low TOC of these pale-coloured limestones. Above, a long-standing negative excursion encompasses the whole Unit 2 and a secular positive trend starts at 90 m that persists up to the top of the section (Fig. 2). The main negative carbon isotopic excursion is within the Julian (Early Carnian), based on ammonoids and conodonts.

5. Discussion

5.1. Stable isotopes of organic carbon allow to identify the CPE at Ma'antang

In many Tethysian Carnian sections, the onset of the CPE is placed at the Julian 1/Julian 2 (lower Carnian) boundary (e.g., Hornung and Brandner, 2005; Hornung *et al.*, 2007a, c; Breda *et al.*, 2009; Dal Corso *et al.*, 2015, 2018; Sun *et al.*, 2016). A sharp CIE in terrestrial and marine organic carbon isotope records occurs at this stratigraphic position and is being used to define the onset of the CPE (Dal Corso *et al.* 2012, 2015; Mueller *et al.*, 2015, 2016; Sun *et al.*, 2016). In this study, a negative perturbation in bulk organic carbon has been found in the lower part of Ma'antang Section (Unit 2 in Fig. 2), before the main lithological change from carbonate to terrigenous sedimentation (Units 4 and 5). The age of this lithological transition is Julian 2, based on ammonoids. Conodonts from the lowest horizons in the Ma'antang Formation, coinciding with the main part of the negative shift of $\delta^{13}C_{org}$, is Carnian in age, thus the isotopic excursion is dated to the Julian. Ammonoids from Unit 4 include genera *Austrotrachyceras* and *Neoprotrachyceras*, which were also found in near coincidence with the first CPE isotopic excursion at Raibl (Dal Corso *et al.*, 2018) and Long Chang section in the South China Block (Sun *et al.*, 2016). The distribution of both genera, however, continues well after this first isotopic excursion was finished.

Miller *et al.* (2017) and Dal Corso *et al.* (2018) reported multiple negative carbon isotopic oscillations (Fig. 8), recorded by *n-alkanes* and bulk organic matter. This complex organization of the carbon isotopic record during the CPE is not found at Ma'antang, which could be due to numerous gaps in data (Fig. 2). However, the negative carbon isotope excursion followed by a long-ranged positive trend ending into the upper Carnian (Tuvalian) is similar to the one recorded in the Long Chang section (Fig. 8), Nanpanjiang Basin (Sun *et al.*, 2016), approximately 800 km South of this area. It is still unclear why the bulk organic carbon of western Tethysian sections recorded multiple,

short-lived isotopic excursions while the successions of the South China Block only show one, long-lasting isotopic excursion. Sun *et al.* (2016) interpreted the differences between the $\delta^{13}C_{org}$ curves in China and western Tethys as possibly due to uneven compositions of the organic matter in sediments (e.g., different proportions of marine VS continental organic matter). The similarity of $\delta^{13}C_{org}$ curves between Ma'antang and the Nanpanjiang Basin may suggest a uniform composition and synchronous variation in the organic carbon pools around South China.

Carbonate carbon isotopes are invariant in the lower Carnian of Ma'antang, whereas the $\delta^{13}C$ of bulk organic carbon exhibits a broad negative perturbation. If such isotopic perturbation reflects a change in the isotopic composition of atmospheric carbon, it should be recorded also by marine carbonates. Its absence, however, is not unique to Ma'antang. In none of the successions that recorded multiple isotopic perturbations in Northern Italy (Dal Corso *et al.*, 2018) was possible to detect such perturbations in the carbonates as well. Dal Corso *et al.* (2015) discussed the absence of a carbonate stable isotopic record of the CPE in literature, and provided various possible explanations for it. Recently, multiple negative carbon isotopic excursions recorded by carbonates were finally found in South China and Oman (Sun *et al.*, 2016, 2018).

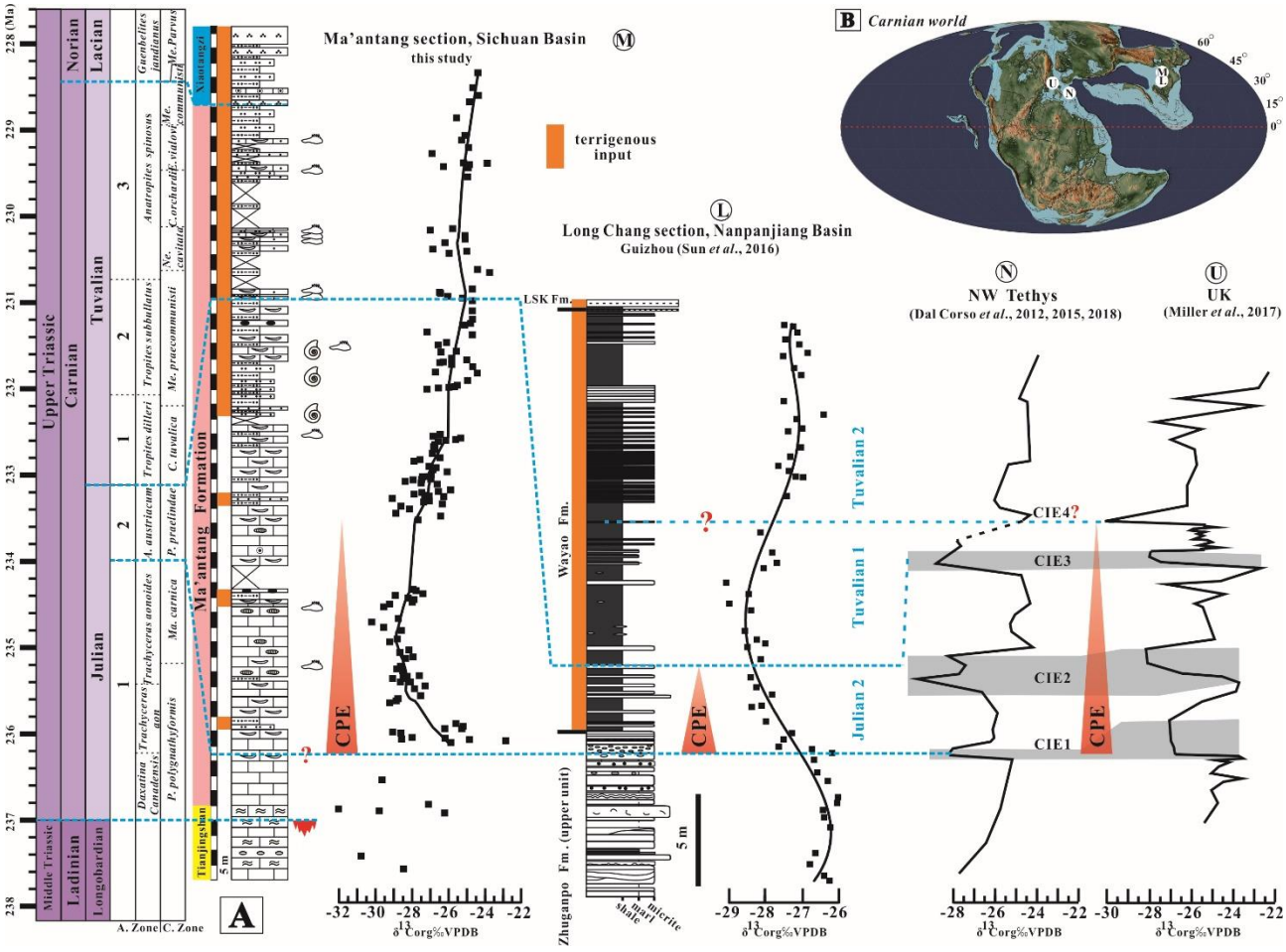

Fig. 8. Comparison of the organic carbon isotope records from Ma'antang, western Sichuan Basin (this study), Long Chang (Nanpanjiang Basin, Sun *et al.*, 2016), NW Tethys (Dal Corso *et al.*, 2012, 2015, 2018), and a lacustrine succession from the continental Central European Basin of UK (WP borehole 1, Miller *et al.*, 2017). The

biostratigraphic correlation of NW Tethys and UK follows Dal Corso *et al.* (2018). LSK Fm., Laishi Ke Formation; CIE, carbon isotopic excursion.

5.2. Carbonate VS siliciclastic sedimentation at Ma'antang and the CPE

The CPE in the Western Tethys realm was marked by the demise of carbonate platforms, or microbial carbonates were substituted by ooids and skeletal grains. Moreover, a sudden input of siliciclastics is associated to the CPE (e.g., Simms and Ruffell 1989; Hornung *et al.*, 2007a, b, c; Rigo *et al.*, 2007; Preto *et al.*, 2010; Dal Corso *et al.*, 2015; Gattolin *et al.*, 2015; Mueller *et al.*, 2015, 2016). At the MAT section, a long-lasting CIE was related to the CPE and encompasses two short siliciclastic intervals, followed by a stable terrigenous sedimentation in Units 4 and 5, which is a evolution of the sedimentation similar with the CPE in Nanpanjiang Basin (Sun *et al.*, 2016). Instead, the characters of sedimentation at the CPE in South China are not uniform with those of western Tethys (Dal Corso *et al.*, 2015), in which a shorter CIE occurred slightly before the first pulse of terrigenous sediment. Dal Corso *et al.* (2018) shown that multiple CIE occurred in western Tethys, each corresponding to a pulse of terrigenous sedimentation. It is unambiguous whether the terrigenous sedimentation is really related to the CPE at the MAT section, because the coeval development of Longmen Shan foreland basin, promoting the increase in accommodation (e.g., Shi *et al.*, 2017), and the associated strong tectonic movements may have affected terrigenous sediment supply already in the early Carnian.

5.3. The input of siliciclastic sedimentation and heteropic deposit in Sichuan Basin

Our previous research results (Chapter 2 and 3) shed light on the discharge of terrigenous sediments in Hanwang and Jushui, which was in late Carnian to early Norian (Jin *et al.*, 2018a, b). However, this main lithological transition was Julian 2 (early Carnian) at the MAT section (Unit 4 in Fig. 2). This different timing of terrigenous input between two parts of the Sichuan Basin may be related to the different paleogeography and geomorphology during the Carnian. The MAT section is more close to the continent, and many evidences showed that the onset of Indosinian orogeny was from north to south of Sichuan Basin, which implies the MAT section may have been involved in the foredeep, and received the terrigenous input earlier (Liu *et al.*, 2009; Chen *et al.*, 2011; Deng *et al.*, 2012).

The Carnian in the HWQ, HWG, and JS sections is made of oolitic shoal, bioclastic shoal, siliceous sponges and is followed by dark-grey shales and marls (Shi *et al.*, 2017; Jin *et al.*, 2018a). It deposited in a ramp environment during a time when the local sea level was rising (Wu, 2009, Li

et al., 2011a, 2014, Jin *et al.*, 2018a). However, the oolitic shoals and sponge reefs are absent in MAT section (Fig. 2). This may be ascribed to an inherited rugged paleotopography, i.e., shoals and sponge mounds nucleated on local topographic highs in Hanwang and Jushui (Shi *et al.*, 2015).

6. Conclusions

The Carnian marine succession at Ma'antang, Jiangyou, in Upper Yangtze Block has been studied for lithology, biostratigraphy, and carbon and oxygen isotopes. Two unconformities have been identified in the lower and upper part of the MAT section, and at least three terrigenous intervals are observed in the lower Carnian portion of the MAT section. The main lithological transition from prevailing carbonate to siliciclastic sedimentation occurs at the middle of the MAT section, which is dated to the uppermost part of Julian 2. A broad negative carbon isotopic excursion is recorded by bulk organic carbon in the lower part of Ma'antang section, i.e., before the main lithological change to persistent terrigenous sedimentation. This isotopic excursion is Julian (lower Carnian) in age and is attributed to the CPE, but the shape and duration of the excursion are markedly different from all western Tethys records. Instead, this negative shift is similar to shape of carbon isotopic curve within the CPE of the Nanpanjiang Basin. It is unclear whether the terrigenous input at the MAT section should be related to CPE or not. We speculate that the main terrigenous input at the MAT section was the result of the Indosinian orogeny.

Acknowledgments

We thank Prof. Dr. James G. Ogg and Yang Zhang at Purdue University, USA for their valuable suggestions in the field. We are thankful to Paolo Mietto and Stefano Manfrin (University of Padova) for their suggestions on the identification of ammonoids. We also thank Stefano Castelli (University of Padova) for realizing the conodont plates and pictures of the ammonoids. We are grateful to two anonymous referees and Editor Alastair Ruffell for the useful comments which improved this paper. This study was supported by NSF grants (No. 41572085, 41272131) of the Chinese Ministry of Science and Technology. N. P. was funded by the MIUR, PRIN grant 20107ESMX9_002.

CHAPTER 5

A new perspective for Carnian Pluvial Episode (Late Triassic): tracing of microbial carbonate abundance variations reveals synchronized modifications in shallow water carbonate production

Xin Jin [a, b], Piero Gianolla [c], Zhiqiang Shi [b, *], Marcello Caggiati [c], Marco Franceschi [a], Yixing Du [a], Nereo Preto [a]

a. Dipartimento di Geoscienze, Università degli Studi di Padova, Via G. Gradenigo 6, Padova, Italy
b. State Key Laboratory of Oil and Gas Reservoir Geology and Exploitation, Chengdu University of Technology, Chengdu, Sichuan 610059, China
c. Physics and Earth Sciences Department, University of Ferrara, Via Saragat, 1, Ferrara 44100, Italy
*Corresponding author. E-mail address: szqcdut@163.com, Tel: (+86) 28-84079807 (office).

Abstract

Quantitative petrologic analysis on carbonates was carried out on Carnian sections from northwestern Sichuan Basin, South China and from northern Italy, in stratigraphic sections encompassing the Carnian Pluvial Episode. The Carnian Pluvial Episode, or CPE, is a period of climate change that occurred between the early Carnian and the beginning of the late Carnian (Late Triassic), during which relevant biological turnovers occurred in the marine realm. The CPE was found coincident with multiple, sharp negative excursions of $\delta^{13}C$ record that are thought to be evidence of perturbations of the global carbon cycle. During the Carnian Pluvial Episode, microbial carbonate platforms, that were dominant in northwestern Sichuan Basin and throughout Tethys, underwent widespread demise and the microbial grains content in the platform carbonate sediments sharply decreased. Our results show a coincidence between the carbonate platforms demise and a switch to ooid- and skeletal grains-dominated carbonate production with the negative C-isotope shifts of the CPE in the Sichuan Basin and in the Southern Alps, i.e. in areas located at opposite sides of the Tethys Ocean. Most notably, microbial carbonate production recovered Tethys-wide in the late Tuvalian, and the timing of recovery was not influenced by the differences in basin evolution and geodynamic setting of the Southern Alps and Sichuan Basin.

Keywords: Point-counting; Carbonate platform; Microbialite; Sichuan Basin; South Alps

1. Introduction

The Carnian Pluvial Episode or CPE (sensu Simms and Ruffell, 1989) is the most distinctive biotic crisis in the Late Triassic (Preto *et al*., 2010). It was first reported in the Northern Calcareous Alps (NCA), Austria, and initially termed as "Reingrabener Wende" (Schlager and Schöllnberger, 1974). Subsequently, it has been widely documented in many regions of the Tethys (Fig. 1). Its onset was dated around the boundary between Julian 1 and Julian 2, i.e., between the *Trachyceras aonoides* ammonoid zone and the *Austrotrachyceras austriacum* ammonoid zone (e.g., Hornung and Brandner, 2005; Hornung *et al*., 2007a, b, c; Breda *et al*., 2009; Dal Corso *et al*., 2015, 2018; Sun *et al*., 2016). Lukeneder *et al*. (2012) reported a delay of the CPE on the equatorial Cimmerian terrane in Turkey, near the boundary between Julian and Tuvalian.

The CPE is mainly characterized by continental siliciclastic input and a crisis of shallow-water carbonate production in the margins of Tethys (Schlager and Schöllnberger, 1974; De Zanche *et al*., 1993, 2000; Keim *et al*., 2001, 2006; Berra and Jadoul, 2002; Hornung and Brandner, 2005; Hornung, 2007; Hornung *et al*., 2007a, c; Breda *et al*., 2009; Roghi *et al*., 2010; Stefani *et al*., 2010; Sýkora *et al*., 2011; Haas *et al*., 2012; Bialik *et al*., 2013; Soua, 2014; Dal Corso *et al*., 2015, 2018; Gattolin *et al*., 2015; Mueller *et al*., 2016; Sun *et al*., 2016). The carbonate sedimentation crisis and siliciclastic input can also be observed in hemipelagic and pelagic settings (Hornung *et al*., 2007b; Rigo *et al*., 2007; Rostási *et al*., 2011; Preto *et al*., 2013; Nakada *et al*., 2014). In continental areas, evaporitic playa-lake deposits were temporarily replaced by fluvial sandy deposits, and river systems occupied vast surfaces (Simms and Ruffell, 1989; Olsen *et al*., 1996; Prochnow *et al*., 2006; Colombi and Parrish, 2008; Kozur and Bachmann, 2010; Arche and López-Gómez, 2014; López-Gómez *et al*., 2017; Miller *et al*., 2017; Barrenechea *et al*., 2018; Lucas and Tanner, 2018).

This major lithological transition is thought to be related to increased rainfall and runoff which can be inferred from an observed change from xerophytic elements toward more hygrophytic elements of palynological assemblages (Hochuli and Frank, 2000; Roghi *et al*., 2004, 2010; Mueller *et al*., 2015, 2016) and from the episodic presence of coal beds and elevated kaolinite content in siliciclastic intervals (Simms and Ruffell, 1989, 1990; Simms *et al*., 1995; Rostási *et al*., 2011; Lucas and Tanner, 2018). In addition, salinity fluctuations, excess of nutrients, lower oxygen condition and fast regional subsidence (Keim *et al*., 2001), and the extreme humid climate associated with increase in terrestrially derived nutrients and/or organic matter during the CPE could have induced the demise of carbonate platforms in the Dolomites (Keim *et al*., 2006). Preto (2012) found that terrigenous supply did not affect the development of high relief carbonate platforms in the Dolomites before the CPE, but seems to have had an influence on carbonate grain associations, leading to the carbonate platform crisis in the Dolomites (De Zanche *et al*., 1993; Gianolla *et al*., 1998a; Bosellini *et al*., 2003).

The coincidence with the onset of the CPE and a sharp negative shift of $\delta^{13}C$ was reported in bulk organic matter and n-alkanes (e.g., Dal Corso *et al*., 2012, 2015; Mueller *et al*., 2016; Sun *et al*., 2016; Shi *et al*., 2018) and it was later shown that actually multiple carbon isotopic excursions occurred during the CPE, both in terrestrial and marine successions (Miller *et al*., 2017; Baranyi *et al*., 2018; Dal Corso *et al*., 2018). Recently, Sun *et al*. (2018) reported multiple carbon isotopic shifts in carbonate bulk rock from Oman. These major carbon isotope excursions are interpreted as related to the injection of massive amounts of isotopically light carbon into the atmosphere-ocean system that may have derived from intense volcanism, and in particular from the emplacement of the Wrangellia Large Igneous Province (Furin *et al*., 2006; Dal Corso *et al*., 2012, 2015, 2018; Xu *et al*., 2014; Mueller *et al*., 2016; Sun *et al*., 2016, 2018).

The CPE was early identified as having had a significant impact on carbonate depositional systems (e.g., Schlager and Schöllnberger, 1974; Preto and Hinnov, 2003; Hornung *et al*., 2007b, c; Stefani *et al*., 2010; Breda and Preto, 2011; Haas *et al*., 2014). More recently, it was highlighted that changes in carbonate production mode seem to have occurred across the CPE. In the carbonate platforms of the Dolomites (northern Italy, western Tethys in Fig. 1) prolific microbial carbonate production came to an end at the beginning of the CPE, and was replaced by dominant skeletal carbonate production (Dal Corso *et al*., 2015; Gattolin *et al*., 2015). This evidence seems to contradict the more established belief that microbial facies represent crisis facies testifying the opportunistic proliferation of bacteria after crises of reef building organisms (Schubert and Bottjer, 1992; Martini *et al*., 2004; Hornung and Brandner, 2005; Hornung *et al*., 2007a; Lukeneder *et al*., 2012; Haas *et al*., 2014; Peybernes *et al*., 2015). In the Southern Alps, microbial carbonate platforms recovered only in the middle-late Tuvalian (late Carnian) to Norian (e.g., Caggiati *et al*., 2018). However, this recovery is so far only inferred from the return to high relief depositional geometries of southern Alpine carbonate platforms.

Whether the drop in microbial production at the CPE observed in the Southern Alps region was a local feature confined to the western Tethys is still unclear. Further investigations are needed in order to assess if the impact on microbial producers can be considered a distinctive feature of the CPE. To reach this goal, quantitative petrologic investigations on carbonates in the northwestern Sichuan Basin (eastern Tethys) are presented and discussed in this study, and the western Tethys record has been integrated with additional petrographic investigations from the Southern Alps. This new dataset allows to clarify the scenario of modifications in carbonate production modes that occurred across the CPE at the scale of the whole Tethys.

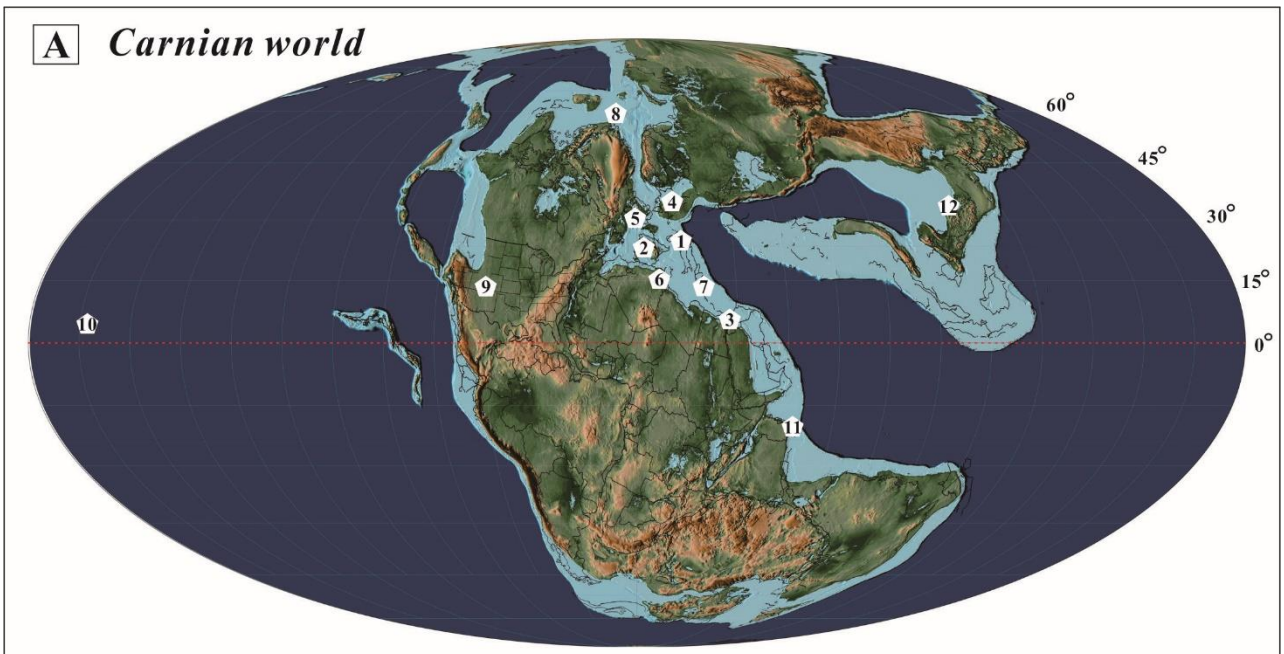

B

12	11	10	9	8	7	6	5	4	3	2	1				Locations / CPE signals
China	Indian	Japan	SW USA	Norway	Turkey	Tunisia	UK	Germany	Israel	Iberia	Slovenia	Italy	Hungary	Austria	
●	●				●						●	●	●	●	*Carbonate platform crisis*
	●	●	●	●	●		●	●		●	●	●	●	●	*Terrigenous clastic input*
●	●	●	●	●	●	●	●	●	●	●	●	●	●	●	*Humid and warm climate*
●								●		●		●	●	●	*Sea level drop and karst*
●	●					●						●		●	*Marine anoxia*
●				●			●					●	●	●	*CIEs*
												●			*CCD rise*
●					●							●	●	●	*Marine extinction*

Fig. 1. A). General palaeogeographic map of Carnian (Late Triassic) (Scotese, C. R, 2014) and some locations where the Carnian Pluvial Event (CPE) was recognized. **B**). Details of the geological record of the CPE. 1- Locations in the Alpine area: Northern Calcareous Alps (NCA), Austria (Schlager and Schöllnberger, 1974; Hornung and Brandner, 2005; Hornung, 2007; Hornung *et al.*, 2007a, c; Roghi *et al.*, 2010; Dal Corso *et al.*, 2015; Mueller *et al.*, 2016), Slovenia (Roghi *et al.*, 2010; Sýkora *et al.*, 2011), Hungary (Rostási *et al.*, 2011; Haas *et al.*, 2012; Dal Corso *et al.*, 2015, 2018); Southern Alps, Northern Italy (Julian Alps: De Zanche *et al.*, 2000; Roghi, 2004, 2010; Preto *et al.*, 2005; Dal Corso *et al.*, 2018. Dolomites: De Zanche *et al.*, 1993; Keim *et al.*, 2001, 2006; Gianolla *et al.*, 1998, 2003; Preto and Hinnov, 2003; Breda *et al.*, 2009; Stefani *et al.*, 2010; Roghi, 2010; Dal Corso *et al.*, 2012, 2015, 2018; Gattolin *et al.*, 2015. Lombardy: Garzanti *et al.*, 1995; Berra and Jadoul, 2002); Southern Italy, Lagonegro Basin (Furin *et al.*, 2006; Rigo *et al.*, 2007; Preto *et al.*, 2013). 2- Iberian Peninsula (Spain, summarized in Arche and López-Gómez, 2014; López-Gómez *et al.*, 2017; Barrenechea *et al.*, 2018). 3- Makhtesh Ramon, Southern Israel (Bialik *et al.*, 2013). 4- Germanic Basin (Kozur

and Bachmann, 2010). 5- Southern UK (Simms and Ruffell, 1989; Miller *et al.*, 2017; Baranyi *et al.*, 2018). 6- Tunisia (Soua, 2014). 7- Turkey (Lukeneder *et al.*, 2012). 8- Norway (Mueller *et al.*, 2015). 9- Southwestern USA (Prochnow *et al.*, 2006; Lucas and Tanner, 2018). 10- Japan (Nakada *et al.*, 2014). 11. Spiti Himalaya, India (Hornung *et al.*, 2007b). 12- South China: Nanpanjiang Basin (Lehrmann *et al.*, 2005; Sun *et al.*, 2016; Zhang *et al.*, 2018), Sichuan Basin (Shi *et al.*, 2018; Jin *et al.*, 2018b) and Qiangtang Basin (Wang *et al.*, 2017). "CIEs"= Carbon isotopic excursions.

2. Geological setting and stratigraphy of NW Sichuan Basin

2.1. Northwestern Sichuan Basin, South China

The Sichuan Basin is a portion of the larger tectonic plate known as South China Block. It is surrounded by the Songpan Ganzi Terrane and Longmen Shan thrust belt to the west, Micang-Daba paleo-land to the north, Kangdian paleo-land to the southwest, and the Xuefeng paleo-land to the east (Fig. 2B; Meng *et al*., 2005; Li *et al*., 2014). The Sichuan Basin hosted extensive carbonate platforms from much of the Late Precambrian to the middle Late Triassic (T_{3m}), Late Triassic (T_{3x}) to Quaternary were instead mostly times of terrigenous (Chen *et al*., 1995). During the Triassic, this plate was located in eastern Tethys, the Sichuan Basin occupying its western margin (Fig. 2B). At the end of the Middle Triassic, the collision between North China and South China plates resulted in the formation of a forebulge unconformity (Zhang *et al*., 1996; Li *et al*., 2003, 2011b), which brought about an extensive erosion of the Middle Triassic Tianjingshan Formation in most parts of the Sichuan Basin (Li *et al*., 2003, 2011b). This unconformity marks the transition from Paleozoic-Middle Triassic passive continental margin to the Sichuan Foreland Basin (Li *et al*., 2011b). The lower portion of the overlying Ma'antang Formation (Carnian, Late Triassic) is missing in Hanwang area (Fig. 2A). During the early Carnian, the Longmen Shan thrust belt was a submarine chain separating the western Sichuan Basin and Ganzi deep basin (Deng *et al*., 1982; Wu, 1984, 1989). An early Carnian transgression allowed water masses from the Tethys ocean to pass through this chain, then entering the western Sichuan Basin and forming a semi-enclosed bay (Deng *et al*., 1982; Wu, 1984, 1989) and allowing the onset of a carbonate ramp setting (Wu, 2009; Li *et al*., 2011a, 2014; Jin *et al*., 2018a). The relative sea level was rising until the late Carnian (Li *et al*., 2011a, 2014): the contemporary paleoclimate change and the development of flexural deformation of the western margin of the South China Block, associated to the accelerated loading of Longmen Shan orogenic wedge, subsequently triggered the drowning of carbonate platforms in Sichuan Basin (Li *et al*., 2011a, 2014; Jin *et al*., 2018a).

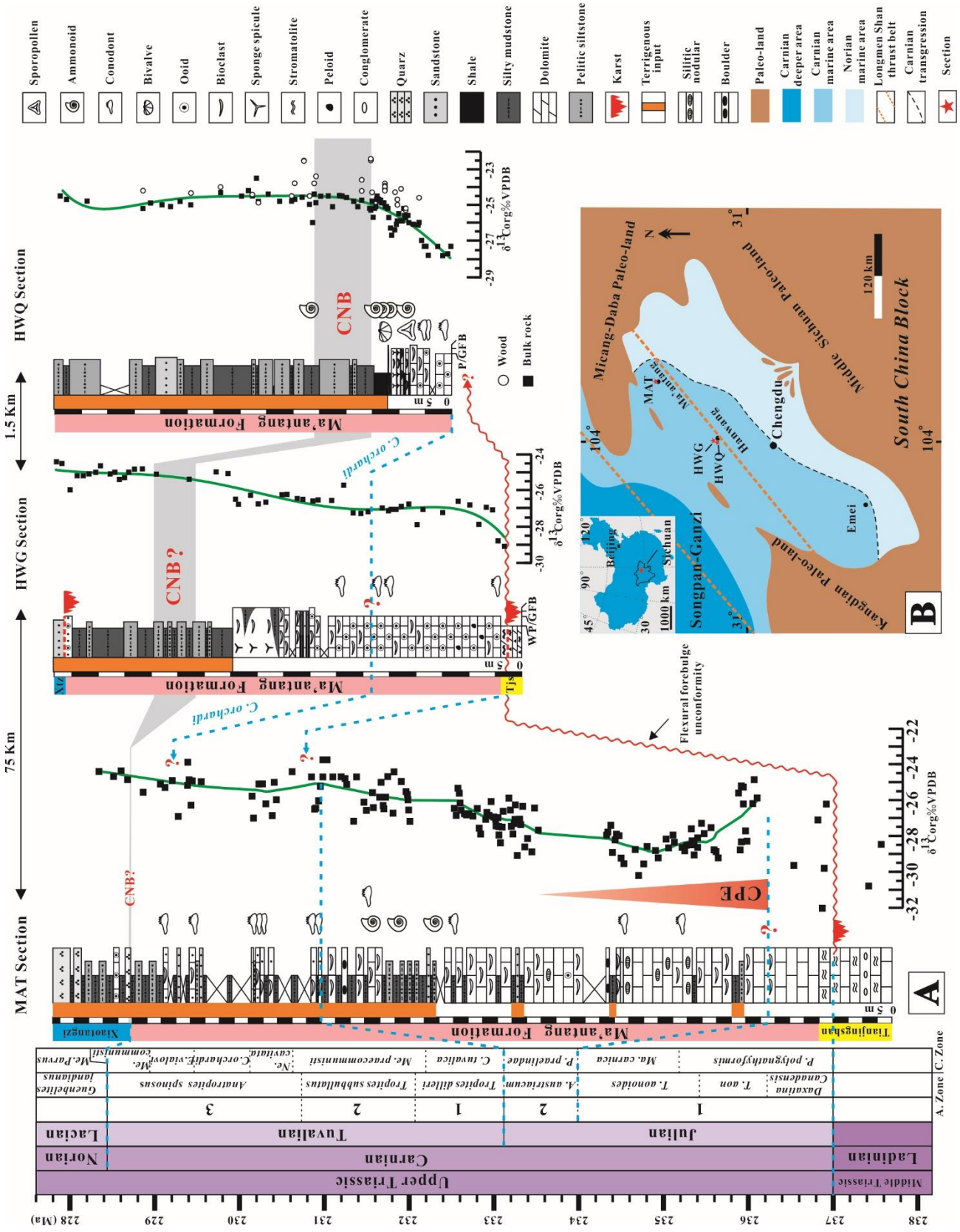

Fig. 2. A). The bulk organic carbon isotope records and biostratigraphic correlation of the MAT, HWG, and HWQ sections from northwestern Sichuan Basin. The MAT section follows Shi *et al.* (2018). The biostratigraphy and isotopic geochronology of the HWG and HWQ sections are based on Jin *et al.* (2018a, b). **B**). Carnian paleogeography of western Sichuan Basin and locations of study sections (simplified from Wu, 1989). Time scale as of Bernardi *et al.* (2018). The ammonoid zonation of Carnian follows Gallet *et al*. (1994) and Broglio Loriga *et*

al. (1999). The conodont zonation of Carnian follows Rigo *et al*. (2018). “CNB” = Carnian/Norian boundary, “CPE” = Carnian Pluvial Episode, “W” = Wackestone, “P/G” = Packstone-grainstone, “F” = Floatstone, “B” = Boundstone, “Tjs” = Tianjingshan Formation, “Xtz” = Xiaotangzi Formation.

2.2. Ma'antang Formation in western Sichuan Basin

Petrological and facies studies have been carried out by many researchers in the Carnian of the Sichuan Basin (Wu, 2009; Wang *et al*., 2015; Jin *et al*., 2015, 2018a; Shi *et al*., 2017, 2018). The Ma'antang Formation in Hanwang area consists of oolitic-bioclastic limestone, microbial-sponge boundstones locally forming mounds, followed by fossil-rich mudstones (Fig. 2A). In Ma'antang area, it is mainly composed of bioclastic limestones, and the typical microbial-sponge bioconstructions are absent (Shi *et al*., 2018). Wu (2009) proposed a carbonate ramp depositional environment for this unit in Hanwang, an interpretation that was confirmed by Jin *et al*. (2018a). Based on a diverse fossil association, the Ma'antang Formation has been attributed to the Carnian (Wendt, 1989, 2001; Wu, 1989; Wang, 1992 and particularly Jin *et al*., 2018a, b; Shi *et al*., 2018). At its top, the Ma'antang Formation makes a sharp transition to terrigenous lithologies. These were considered as related to the CPE by Shi *et al*. (2017) based on the magnetostratigraphy of Zhang *et al*. (2015) and biostratigraphy (conodonts, and ammonoids), pointing to an Early Carnian age. Shi *et al*. (2018) reported a > 2 ‰ wide negative shift of the stable carbon isotopes of organic matter in the lower part of Ma’antang section, below early Carnian ammonoids and conodonts, which allowed it to be correlated to the CPE (Fig. 2A). The carbon isotopes from bulk organic matter and wood from Qingyan Gou (HWQ) and Guanyin Ya (HWG) sections didn't show this negative shift; instead, they exhibit a long positive trend which was inferred to correspond to the end of the CPE in Hanwang area (Jin *et al*., 2018b). Jin *et al*. (2018a, b) obtained instead that the age of the carbonate platform crisis is late Carnian to early Norian, and therefore cannot be related to the CPE.

3. Geological setting and stratigraphy of Southern Alps

3.1. Northern Italy

The Dolomites and Julian Alps are the part of the Southern Alps thrust-and fold belt, and are located in Northern Italy and western Slovenia (Fig. 6B). During the Middle-Late Triassic, they were part of the Tethys western passive margin (Stampfli *et al*., 2013) and were affected by different tectonic pulses with differential subsidence originating horst and graben structures, often associated with volcano-magmatic stages, followed by a relatively more stable setting characterizing the Upper

Triassic (Doglioni, 1987; De Zanche *et al*., 1993; Gianolla *et al*., 1998a; Preto *et al*., 2011; Abbas *et al*., 2018). During this time-span, several generations of high-relief carbonate platforms grew in the Southern Alps (Bosellini *et al*., 2003; Stefani *et al*., 2010; Preto *et al*., 2017). Toward the end of the early Carnian, a sharp input of siliciclastics coupled with a sea-level drop and change of carbonate production (Keim *et al*., 2001; Bosellini *et al*., 2003; Gattolin *et al*., 2013) and occurred and high-relief carbonate platforms suddenly changed to low-relief carbonate ramps (e.g., Heiligkreuz Fm.; Preto and Hinnow, 2003), often laterally passing to shallow water mixed systems (Heiligkreuz Fm., Rio del Lago, Conzen and Tor Fm.; De Zanche, 2000; Preto *et al*., 2005; Breda *et al*., 2009) connected to a southern and western terrigenous shoreline (Brusca *et al*., 1981; Jadoul *et al*., 2004). Since the Late Carnian (Upper Tuvalian), a depositional system characterized by a northward transition of alluvial-plain, flood-basin and shallow-lagoon dominated the Eastern Southern Alps (Travenanzes Fm., Breda and Preto, 2011) and was connected northeastward to a margin-slope system (Caggiati *et al*., 2018). From the northern part of the Southern Alps, the carbonate platforms expanded landward on the former flood basin during the late Carnian to Norian, and prograded northeastward (basinward) for a few kilometers, originating huge peritidal successions in northern Italy and western Slovenia (Dolomia Principale and Dachstein Limestone; Bosellini and Hardie, 1984; Ciarapica and Passeri, 1990; Celarc and Kolar- Jurkovšek, 2008; Gale *et al*., 2015).

3.2. Stratigraphy in the eastern Southern Alps

The late Early Carnian in the Dolomites is commonly documented by the transition from Cassian Dolomite and the heteropic San Cassiano Formation, representing high-relief carbonate platforms and the adjacent basinal carbonate-siliciclastic sediments, to the Heiligkreuz Fm., related to deposition in a carbonate ramp setting (Bosellini *et al*., 2003). In the Cortina area (Dibona-Milieres sections, “D” in figure. 6B), the transition from the San Cassiano Fm. and the Heiligkreuz Fm. is characterized by the progressive shallowing of the basin, coupled with a strong increase in sandstones and the occurrence of subtidal carbonate mounds (Gattolin *et al*., 2015). This transition, by constrained biostratigraphy (ammonoids, conodonts) and palynomorphs to the base of Julian 2, is preceded by a strong shift in the organic carbon isotopic ratio (Dal Corso *et al*., 2015). At least other two isotopic shifts have been detected in the overlying part of carbonate ramp succession, followed by similar increases in the siliciclastic input shed in deeper environments (Dal Corso *et al*., 2018). Transgressive alluvial and mud-flat facies associations of Tuvalian age (Travenanzes Fm.) lay unconformably on the Heiligkreuz Fm. and are in turn overlaid by carbonate peritidal cycles of the Dolomia Principale (Breda and Preto, 2011).

The area south of Santo Stefano di Cadore lies in a relatively complex shear zone, dominated by

high-angle faults originated during the Alpine orogeny, and it was likely located northeastward to the Dolomites in the Triassic. The sedimentary succession is similar to the Dolomites, but essentially dominated by basinal units deposited during the Early to Late Carnian. The transition from the San Cassiano Formation to the overlying unit is gradual, marked first by an increase of terrigenous sandstones and then by the occurrence of almost regular carbonate-siliciclastic alternations, and eventually by shallow water limestones. The latter are suddenly overlaid by an upper Tuvalian pelagic succession, dominated by marls a calciturbidite intercalations.

In the Cave del Predil (Raibl) area (Julian Alps), the Carnian succession is up to 650 m-thick (De Zanche *et al*., 2000). Here, the terrigenous input related to the CPE is evidenced by the superposition of the Rio del Lago Fm., consisting of shales, siltstones and limestones alternations deposited in an outer ramp setting, on the basinal micrites of Predil Limestone, with organic carbon-isotope shift located in the basal barren beds of the Rio del Lago Formation (Dal Corso *et al*., 2018). The Rio del Lago Fm. is characterized by a shallowing upward trend, with transition to the Conzen Limestones, and constrained to the Austriacum zone by ammonoids (De Zanche *et al*., 2000; Roghi *et al*., 2004). Sedimentation in ramp continued until the early Late Carnian (lower Tuvalian: Tor Fm. and Portella Dolomite; De Zanche *et al*., 2000; Preto *et al*., 2005) but subsequently, drowning of the platform led to the development of pelagic conditions, on which a new epicontinental carbonate platform prograded (Gianolla *et al*., 2003; Caggiati *et al*., 2018). Recently, the multi-phase character of the isotopic signal and of humid pulses has been highlighted also in this area (Dal Corso *et al*., 2018).

The Mt. Škrlatica (ŠK) section is located in the Julian Alps (NW Slovenia), but in a different tectonic nappe respect to the Cave del Predil area (Fig. 6B), and it was probably placed in a slightly northeastward position during the Late Triassic. The base of the section is composed of Razor bedded limestones, for which Ramovš (1987) proposed an early Carnian in age. The Razor bedded limestones represent two different depositional settings, the first is subtidal which consists of thick-bedded packstone and grainstone with diverse skeletal grains; the second is intertidal-supratidal and characterized by laminated grainstones and horizontal microbial laminites (Celarc and Kolar-Jurkovšek, 2008). They are followed by the Martuljek platy limestones, upper Tuvalian to lower Norian in age according to conodonts and ammonoids (Ramovš, 1987; Celarc and Kolar- Jurkovšek, 2008). Two members of Martuljek platy limestones are observed (Celarc and Kolar- Jurkovšek, 2008). The lower member is characterized by reddish bioclastic wackestone to packstone, the upper member is made of light grey to white platy and thin-bedded, grainstones and rudstones. On these deep water micritic limestones, a carbonate platform prograded in the early Norian (Dachstein reef limestones representing the slope to margin facies; Celarc and Kolar- Jurkovšek, 2008).

4. Methods

Thirteen samples were collected from the Dolomites, Northern Italy in the Santo Stefano di Cadore section (N46°32'49.05"/E12°34'59.15"). In the Julian Alps area, three samples were collected from: Mt. Škrlatica (ŠK) section (N46°24'54.27"/E13°48'2.96") and 16 samples were collected from Cave del Predil section (E46°26'21.05"/E13°35'59.35"). Standard, 30 μm thin sections were prepared at the Department of Physics and Earth Sciences, Ferrara University and at the Department of Geosciences, University of Padova. Forty-five samples were collected from three localities in northwestern Sichuan Basin: Ma'antang (MAT) (N32°11'22.14"/E105°13'50.35″), Guanyin Ya (HWG) (N31°28'18.4"/E104°08'50.4″) and Qingyan Gou (HWQ) (N31°27′46.85″/E104°09′35.40″). Thin sections from the Sichuan Basin were made at the Institute of Sedimentary Geology, Chengdu University of Technology (China). All thin sections were studied and photographed with a polarizing microscope at the Department of Geosciences, Padova University.

The detailed methods and principles of point counting followed Flügel (2010). This work is carried out on the photographs of thin sections. A regular two-dimensional grid was used and each component (the non-carbonate particles and cracks are included in this study) which falls under a grid point was counted. In this study, the principles of "grain-bulk measurements" is used. The nuclei of coated grains or ooids were counted as specific grains (i. e., whatever bioclasts or others sediments constitute the nuclei). A total of 300 points per thin section were counted with the help of the software JMicroVision 1.2.7 (https://www.jmicrovision.com). The point-counting of some thin sections was repeated with a graduated stage under a binocular microscope, but the results were comparable. Complete point counting data are shown in the data table (supplementary material).

For a more comprehensive interpretation of the evolution of carbonate systems across the CPE, the original data produced for this work were integrated with those of Preto (2012) and Gattolin *et al*. (2015), which were acquired with similar methods.

5. Results

In this study, we distinguished terrigenous components (clay and quartz), skeletal grains (including siliceous sponge spicules, bivalves, gastropods, brachiopods, foraminifers, calcareous sponges, echinoderms, ostracods, corals, stromatoporoids, bryozoans, and other undetermined skeletal grains), microbial grains (including clotted peloidal micrite, thrombolites, oncoids, calcimicrobes, *Tubiphytes*, worm tubes, and pure leiolites), ooids and peloids. Worm tubes in these samples are cf. *Terebella* sp., which walls have clotted peloidal fabric. The origin of carbonate in these tubes was interpreted as microbial because of their fabric.

5.1. Ma'antang section

The lowest part of Ma'antang section (MAT), earliest Julian in age, is dominated by stromatolites (Fig. 3A, 4), and is not suitable for point-counting. In sample M1, carbonate grains are mainly composed of shells of aragonitic bivalves (Fig. 3B), the total content of which is nearly 50 % (Fig. 4). Microbial grains are rare, and small oncoids are found. Calcimicrobes are present (Fig. 3C) but are less than 5 % (Fig. 4). Most of these calcimicrobes are fragments of *Girvanella* sp. In the following Julian (lower Carnian) portion of the section, the skeletal grains are less abundant, generally ≤ 25 % excluding siliceous sponge spicules (Fig. 4), but microbial grains are scarce as well. Carbonate microfacies in this interval, coinciding with the negative shift in $\delta^{13}C$ of organic matter, are dominated by interstitial micrite or microsparite and scarce metazoans which are mainly brachiopods, foraminifera, bivalves, and fewer ostracods (sample M7, Fig. 3D, 4). In one sample (M13), siliceous sponge spicules reach 20 % of the rock volume (Fig. 3E, 4). In thin section, siliceous sponge spicules often show elongated shapes and wavy extinction (Fig. 3E). Small oncoids, peloids, and fragments of bioclasts are found (Fig. 3E). In the interval after the main carbon isotopic excursion, which is uppermost Julian to Tuvalian in age, the skeletal grain content increases at the expense of interstitial components. In sample M17 (Fig. 3F), bioclasts are diverse, with echinoderms contributing 25 % of the whole rock volume (Fig. 4). Brachiopods, foraminifera, bivalves, ostracods, bryozoans, and gastropods are present as well. Microbial grains rarely occur and are mainly small thrombolite fragments and oncoids. Calcimicrobes are found throughout the Tuvalian of the MAT section (Fig. 3C, 4). Generally, their abundance is less than 10 %. The terrigenous component is abundant in the upper part, up to ≥ 50 % at the top of the MAT section. Ooids are scarce and only occur in samples M20 and 21 (Fig. 4).

5.2. Guanyin Ya section

Guanyin Ya section (HWG) has been studied by Jin *et al*. (2015, 2018a, b) and Shi *et al*. (2017, 2018). The age of the HWG section is still debated, but conodonts roughly restrained it to the Tuvalian (Shi *et al*., 2017; Jin *et al*., 2018a). The HWG section is composed of oolitic-bioclastic shoals and sponge reef mounds. Towards the base of the section, oolites are interfingering with bioclastic grainstones and packstones (Fig. 5). In sample G7 within this interval, bioclasts are made of bivalves, brachiopods, foraminifera, echinoderms and gastropods (Fig. 3G). Micrite ooids are also seen. Carbonate mud may be found in interstices between bioclasts and ooids (Fig. 3G). Ooids are dominant in the middle of the section, and their content can be up to 60 % (Fig. 5). In sample G10, the majority of ooids are radial and concentric (Fig. 3H), with many exhibiting bioclasts at their nuclei (e.g.,

foraminifera, brachiopods, echinoderms, crinoids). Interparticle spaces are filled with clotted peloidal micrite (interstitial) and cements (Fig. 3H). The microbial grains are increasing from bottom to top in this interval. Close to the sponge mound layer at the top of the section, the content of microbial carbonates is increased to 60 % (excluding calcimicrobes, Fig. 5). At the base of the sponge mound, carbonate grains are mainly intraclasts made of thrombolite (sample G14, Fig. 3I), which amount to 25 %. Bioclasts are seen, including bivalves, brachiopods, and echinoderms (Fig. 3I). The siliceous sponge spicules are prevalent in the upper part of the HWG section, while calcimicrobes are only present in the lower part (Fig. 5).

5.3. Qingyan Gou section

The carbonate portion of Qingyan Gou section (HWQ) is late Tuvalian (*Carnepigondolella orchardi* conodont zone), and thus younger than the MAT section. The lithology of this section, which is around 1.5 Km apart from the HWG, has been described by Jin *et al*. (2018b). At the base of the section, the composition of carbonate microfacies is nearly the same as in the upper part of the HWG section, which is coeval (Fig. 5). The skeletal grains (excluding siliceous sponge spicules) are generally rare. The microbial grains (excluding *Tubiphytes* sp.) are much more abundant than in the MAT section, reaching up to 60 % of the total rock volume in the upper part of the HWQ section. Siliceous sponge spicules are common in the HWQ section. In sample Q3, microbial grains are mainly composed of big oncoids and fragments of thrombolites. Bioclasts are present which often have oncolitic coatings (Fig. 3J). Interparticle spaces are filled with microspar and peloids. Above in the section, the content of microbial grains could reach 40 % (Fig. 5), and are mostly fragments of thrombolites (sample Q8, Fig. 3K). The skeletal grains are less abundant and made of bivalves and brachiopods (Fig. 3K). The sample Q9 is made of leiolites, worm tubes and fragments of siliceous sponges. *Tubiphytes* sp. are found within the top sponge reef layers, but their content is often less than 10 % (sample Q9, Fig. 3L).

5.4. Santo Stefano di Cadore section

The Santo Stefano di Cadore section has been attributed an age from Julian to Tuvalian, which is comparable with the MAT section. The skeletal grains are diverse, their contents are around 10% to 25% (Fig. 6A). The microbial grains are abundant in the lower part (GG14 and XSS01), which dates to before the Carnian Pluvial Episode. Ooids are distributed discontinuously through the section. Sample GG 18, lower Tuvalian, is dominated by peloids and intraclasts (Fig. 3M); microbial grains, mostly thrombolites and oncoids, make less than 15 % of the rock volume (Fig. 6A). In sample GEY

13, microbial grains are mainly composed of small thrombolite fragments which amount to 16 % of the rock volume. The skeletal grains are made of bivalves and gastropods.

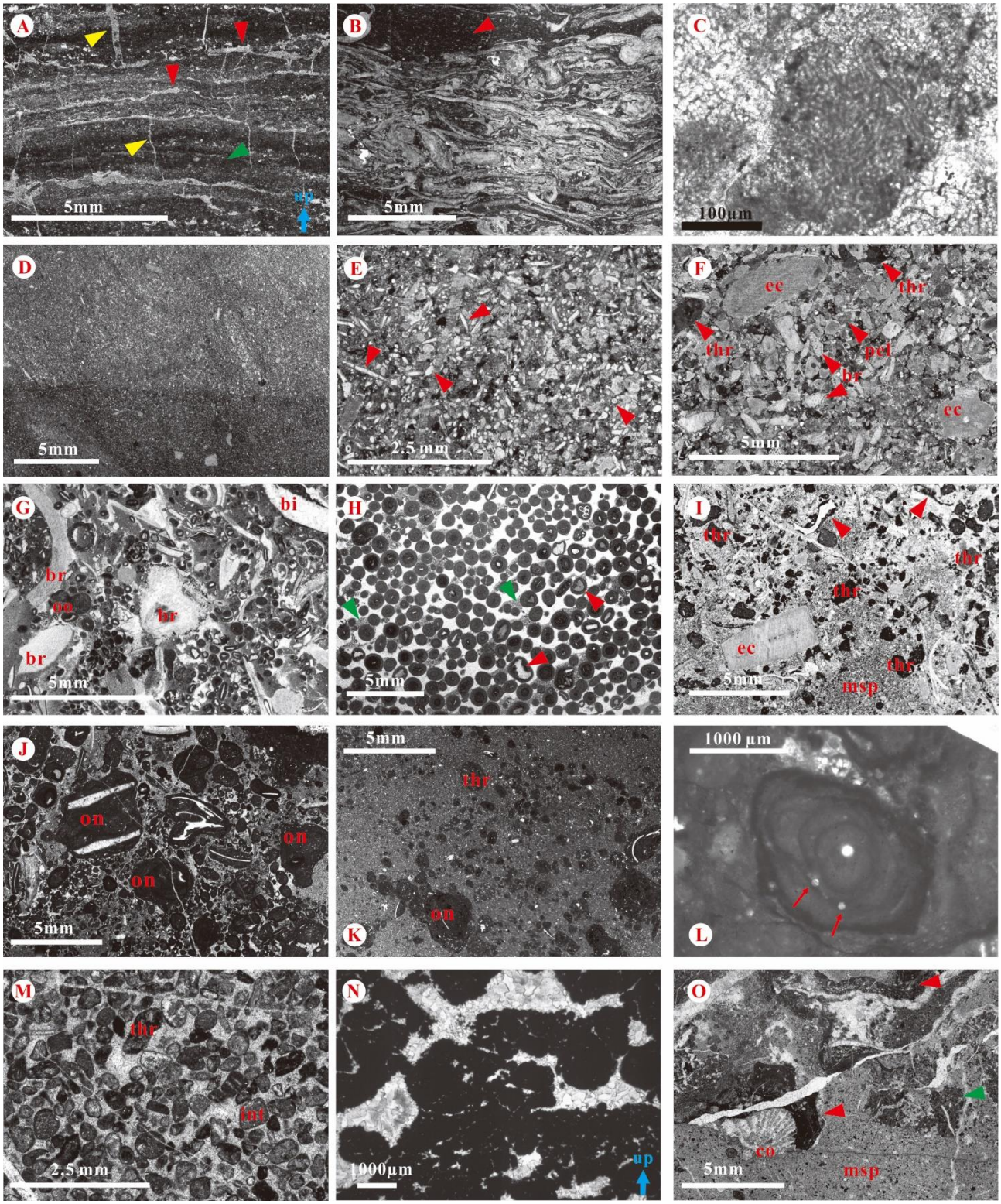

Fig. 3. Thin-section microphotographs of the Carnian successions in Tethyan region. MAT section: (**A**)- Stromatolitic dolomitic boundstone, from the lowest part of the MAT section (Fig. 4). The dark stromatolitic layers (green arrow) are interbedded with fenestral structures (red arrow). They are often cut by vertical calcite veins (yellow arrow). (**B**)- Bioclastic grainstone, sample M1. It is mainly made of aragonitic bivalves. The classification of these bivalves is impossible because their shells are substituted by late calcite cement. Intergranular spaces are

filled with small peloids (red arrow). (**C**)- Detail of *Girvanella* sp. (from sample M11 of Fig. 4). (**D**)- Bioclastic wackestone, sample M7. It is mainly composed of fine carbonate mud and bioclasts. Small fragments of bivalves, brachiopods, echinoderms are visible. This mud-rich interval (M6 to M9) is coincident with the carbon isotopic negative curve (Fig. 4). (**E**)- Bioclastic grainstone, sample M13. Siliceous sponge spicules are dominant (red arrow). Bivalves, echinoderms and brachiopods are also seen. Intergranular spaces are filled with micrite, peloids and fine terrigenous sediment. (**F**)- Bioclastic grainstone, sample M17. It is mainly made of diverse bioclasts such as bivalves, gastropods, brachiopods (br), foraminifera, echinoderms (ec). Also peloids (pel), thrombolites (thr) and terrigenous clasts are seen. Intergranular spaces are filled with blocky and microsparry cement. HWG section: (**G**)- Bioclastic-oolitic grainstone, sample G7. Bioclasts and ooids (oo) are dominant. The fragments of brachiopods (br) and bivalves (bi) are seen. Some of ooids have bioclastic nuclei. Intergranular spaces are filled with micrite, or microsparry cement. (**H**)- Oolitic grainstone, sample G10. Some of the ooids have bioclastic nuclei such as echinoderms and bivalves (red arrow). Interstitial clotted peloidal micrite (green arrow) is commonly present in the intergranular spaces. The cements are blocky calcites. (**I**)- Bioclastic- thrombolitic grainstone, sample G14. Fragments of echinoderms (ec), foraminifera, bivalves and brachiopods are present. Some of them have oncolitic-microbial coating (red arrow). Dominant are fragments of thrombolite (thr), and the pore space is filled with microsparry cement (msp). HWQ section: (**J**)- Bioclastic and intraclastic floatstone, sample Q3. It is mainly composed of fragments of bioclasts which often have oncolitic-microbial coating (on) with irregular shape. Locally, the soft parts of reworked siliceous sponges are substituted with clotted peloidal micrite. Microbial grains with thrombolite fabric, ooids and peloids are seen. Intergranular spaces are filled by microsparry cement. (**K**)- Bioclastic and intraclastic floatstone, sample Q8. It is mainly composed of fragments of thrombolites, bioclasts and intraclasts. Allochthonous thrombolites (thr, intraclast) are more common and identified because they are worn and mildly rounded. Oncoids (on) have bioclastic nuclei and are encrusted by sessile foraminifera, which display an irregular shape. Fine terrigenous sediments and peloids are found in interstices between bioclasts. (**L**)- Detail of *Tubiphytes* sp. (from sample Q9). The red arrows are the traces of *in situ* laser ablation. Santo Stefano di Cadore section: (**M**)- Bioclastic- intraclastic grainstone, GG18. It is mainly composed of intraclasts and bioclasts. Intraclasts (int) are mainly made of carbonate mud and have round shape. Bioclasts are mainly foraminifera and bivalves, with fewer brachiopods and echinoderms. Oncoids, peloids and thrombolites (thr) are seen. Intergranular spaces are filled with blocky cement. Cave del Predil section: (**N**)- Boundstone, sample CZ1, consists of thrombolites, the intergranular spaces are filled with blocky cement, and bioclasts are rare. Mt. Škrlatica section: (**O**)- Bioclastic and intraclastic rudstone, sample Mk11. Reef builders are common, such as corals (co) and which are often encrusted by oncolitic-microbial coatings (red arrow). Intertitial clotted peloidal micrite (green arrow) and fragments of thrombolites are visible.

5.5. Cave del Predil section

Cave del Predil section is composite, located in the Cave del Predil (Raibl) area of Northern Italy and comprises a Julian to early Tuvalian succession. The lithology and biostratigraphy were studied by De Zanche *et al*. (2000) and Dal Corso *et al*. (2018). The point-counting starts synchronously with the CPE (Fig. 6A). The skeletal grains are dominant throughout the section, their contents are around

7 % to 56 %. On the contrary, microbial grains are rare. A sharp peak of microbial grain content was observed in CZ1 sample. This sample consists of thrombolites, skeletal are rare (Fig. 3N).

5.6. Mt. Škrlatica section

Mt. Škrlatica (ŠK) section is late Tuvalian to early Norian, which is analogous to the HWQ section. The contents of microbial grains are slightly higher than skeletal grains. In sample Mk11, abundant fragments of reef-builders are found, such as corals (Fig. 3O). Other bioclasts are mainly foraminifera, brachiopods and echinoderms. There is interstitial clotted peloidal micrite, and the most common microbial grains are large oncoids (Fig. 6A).

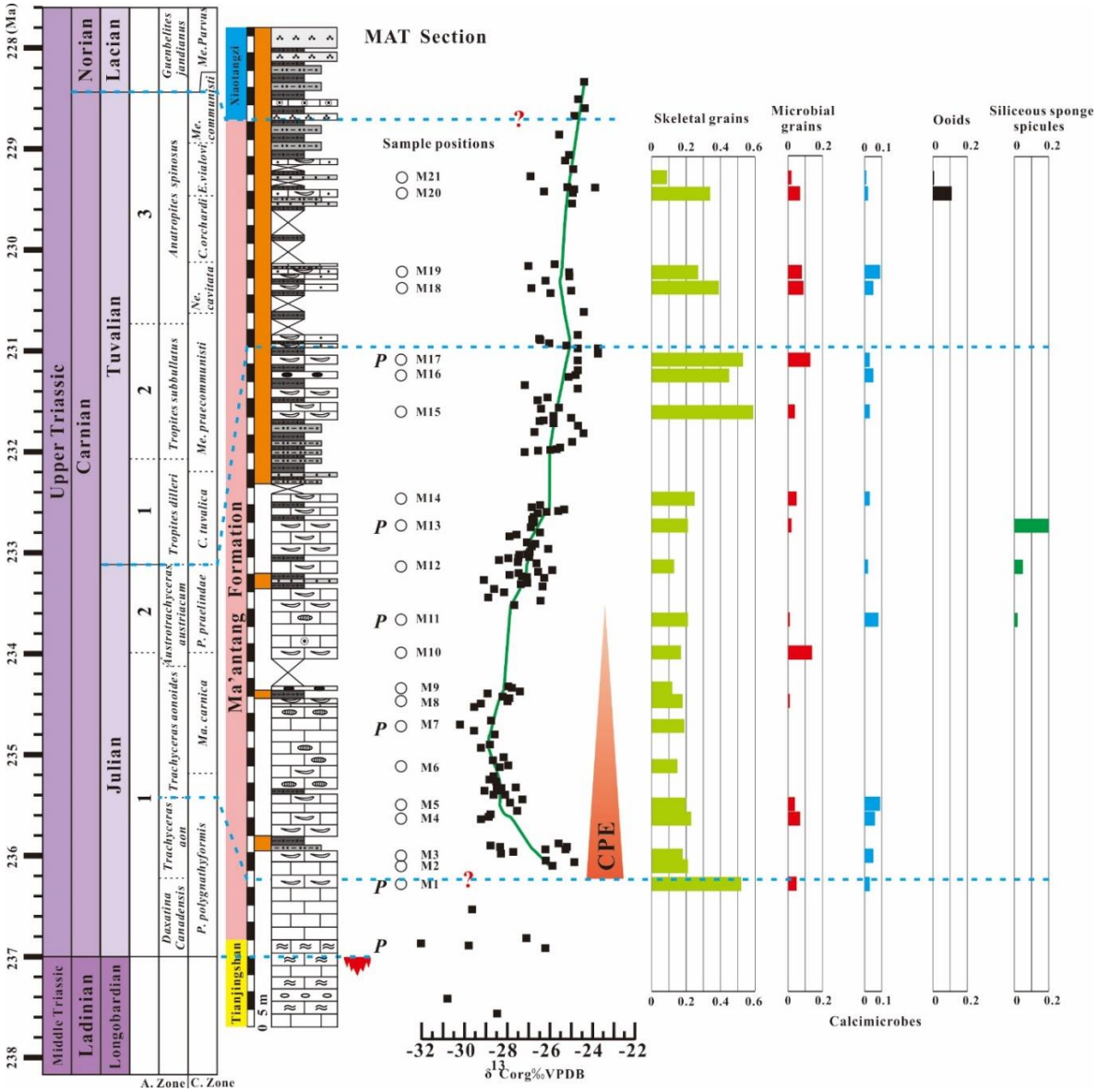

Fig. 4. Modal abundance of carbonate skeletal grains, microbial grains and calcimicrobes, ooids and siliceous sponge spicules of the MAT section, northwestern Sichuan Basin, South China. "P" means the positions of described thin sections (see Fig. 3). The biostratigraphy and isotopic geochronology follow Shi *et al.* (2018). "CPE" = Carnian Pluvial Episode.

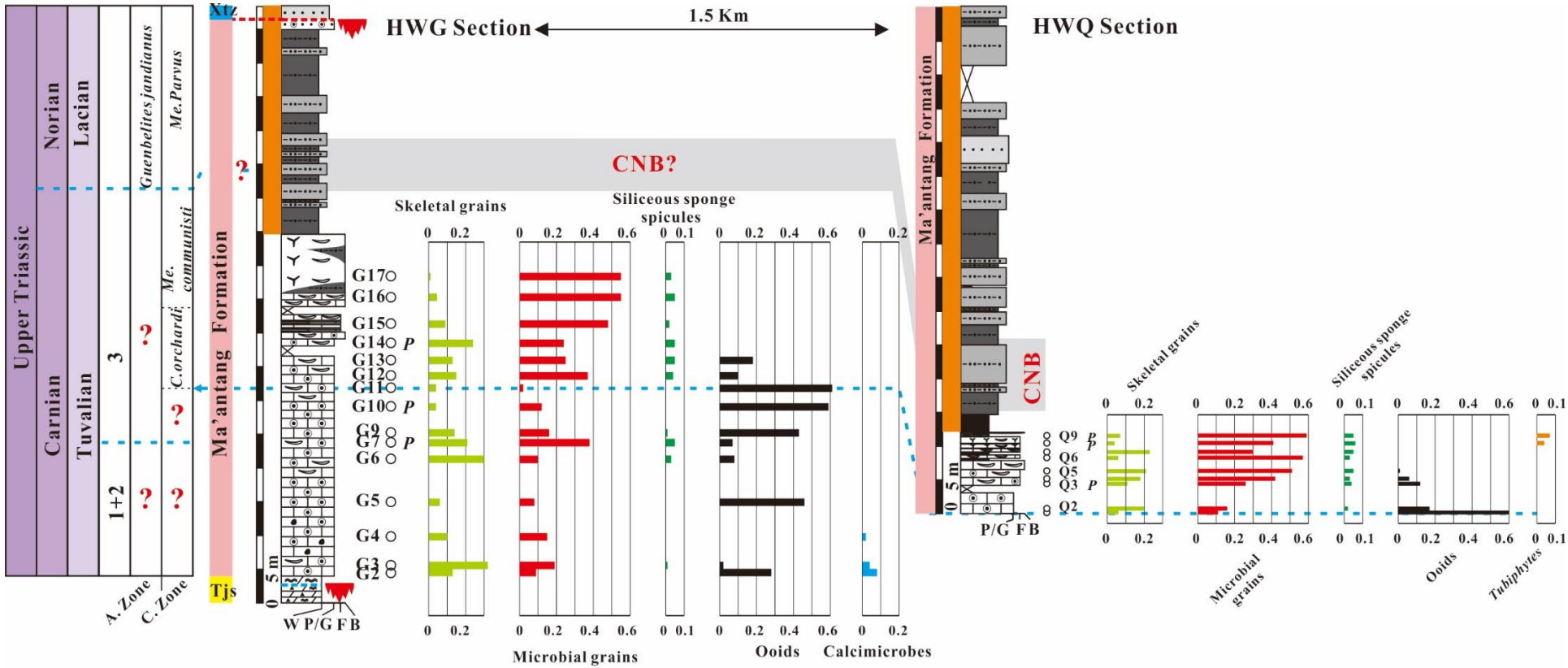

Fig. 5. Modal abundance of carbonate skeletal grains, microbial grains and calcimicrobes, ooids, siliceous sponge spicules and *Tubiphytes* of the HWG and HWQ sections, northwestern Sichuan Basin, South China. "P" means the positions of described thin sections (see Fig. 3). The grain compositions of the HWG and HWQ sections are nearly identical above the middle blue dashed line. The biochronology follows Jin *et al*. (2018a, b).

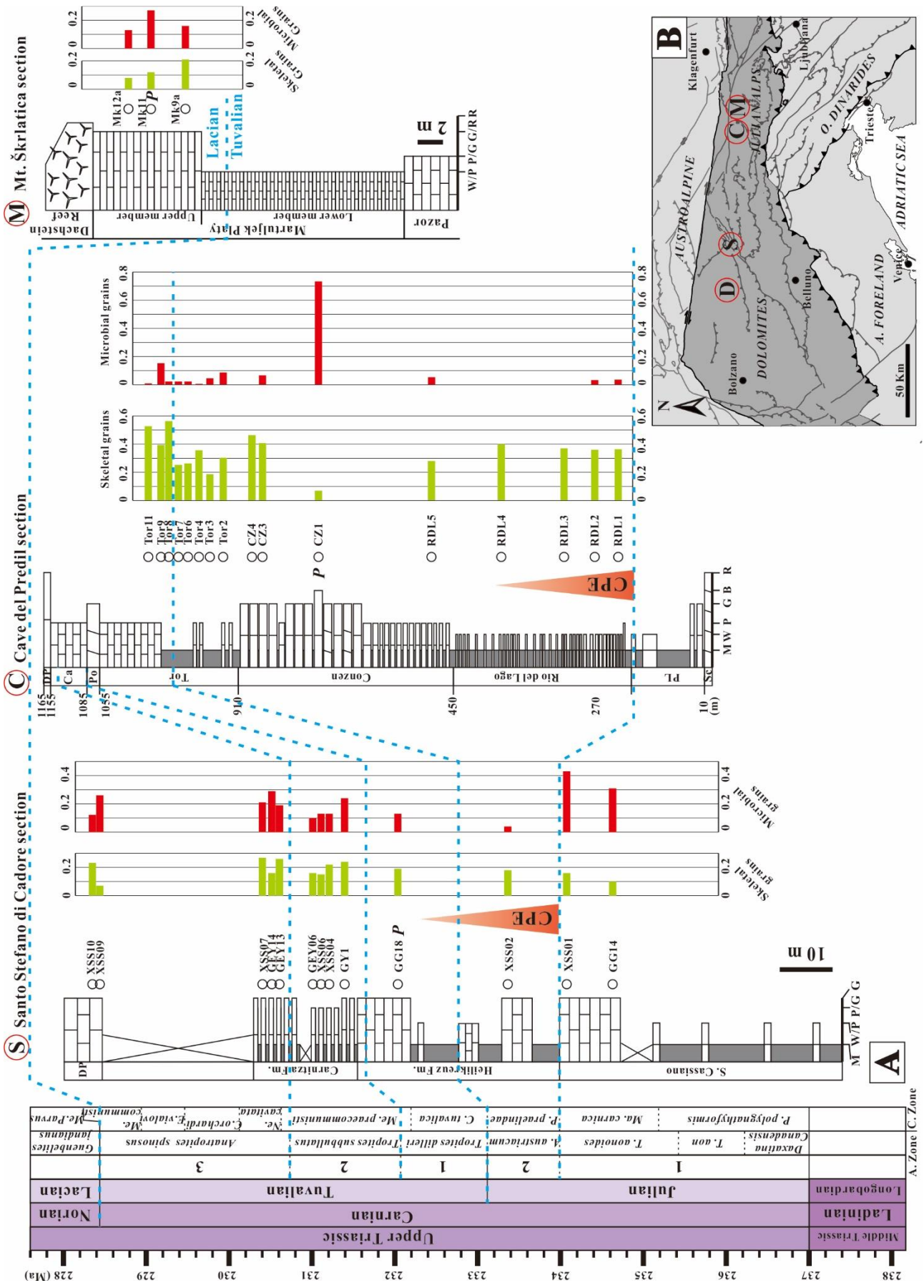

Fig. 6. A). Modal abundance of skeletal grains and microbial grains from Santo Stefano di Cadore section (Dolomites, North Italy), Cave del Predil section (Julian Alps, North Italy) and Mt. Škrlatica section (Julian Alps, NW Slovenia) (The Mt. Škrlatica section was simplified from Celarc and Kolar-Jurkovšek, 2008). **B**). Locations of

Carnian sections in Southern Alps. The biochronology follows De Zanche *et al*. (2000) and Dal Corso *et al*. (2018). "Sc= Sciliar Fm.", "PL"= Predil Limestone, "Po"= Portella Fm.", "Ca"= Carnizza Fm.", "DP"= Dolomia Principale", "M" =Marl, "W/P" = Wackestone-packstone, "P/G" = Packstone-grainstone, "B" = Boundstone, "R" = Rudstone.

6. Discussion

6.1. The Carnian transgression in northwestern Sichuan Basin

A local sea level rise has been documented by microfacies analysis in the Carnian of Hanwang, northwestern Sichuan Basin (Wu, 2009; Jin *et al*., 2018a), which is also in agreement with the results of Li *et al*. (2011a and 2014). The modal composition of carbonate components in the HWQ and HWG sections could also be interpreted in terms of sea level rise. Calcimicrobes, which are interpreted as fossilized cyanobacterial colonies (e.g., Riding, 2000), are abundant in the lower part of the HWG section and throughout the MAT section (Fig. 3C, 4). This type of microbialites, widespread in Paleozoic and Mesozoic, are associated to tidal and subtidal carbonate platforms. They are considered indicators of shallow water conditions because modern microbial communities in these environments are dominated by cyanobacteria which photosynthesizing (Riding *et al*., 2000; Flügel, 2010). *Tubiphytes* is a problematic fossil known to occur from Permian to Triassic. It was of primary importance as reef builder from Anisian to Carnian (Flügel, 2010). It occurs in layers from the HWQ section along with siliceous (Hexactinellida) sponges (Fig. 3L and Fig. 5). Senowbari-Daryan (2013) interpreted most Triassic *Tubiphytes* as consortia of a foraminifer and heterotrophic, probably sulfate-reducing bacteria. As such, *Tubiphytes* should not require sunlight, and in fact in the Dolomites, *Tubiphytes* was reported in deep water sediments at depths ≥250 m (Keim and Schlager, 1999; Marangon *et al*., 2011; Preto, 2012). The associated hexactinellid sponges were mainly reported in deep water in Jurassic (Leinfelder, 2001). The siliceous sponge reefs in Longmen Shan area reached more than 80 m in height above the surrounding sea bottom (Li *et al*., 2011a), which implies a water depth of at least 80 m at the foot of the mounds. Therefore, the substitution of calcimicrobes by *Tubyphites* in the Carnian of Hanwang may indeed record a transgression and local sea-level rise. The closure of the Palaeotethys and the collision between Cathaysia and drifting Cimmerian plates, which led to the Indosinian orogeny (Golonka, 2007), may have been responsible for global sea level fluctuations (Hornung *et al*., 2007c).

6.2. The Carnian Pluvial Episode and microbial factory crisis and recovery

The Carnian Pluvial Episode induced one of the most distinctive biological crises in the Triassic

(Preto *et al*., 2010; Ruffell *et al*., 2016; Ogg, 2015, and references therein). Shallow water carbonates were temporarily polluted, or sometimes replaced, by terrigenous sediments in the Dolomites of Northern Italy (Keim *et al*., 2001, 2006; Preto and Hinnov, 2003; Preto *et al*., 2005; Breda *et al*., 2009, and references therein). At the same time, a temporary demise of carbonate platforms is also documented in depositional environments ranging from shelf to basin in the Northern Calcareous Alps (Schlager and Schöllnberger, 1974; Hornung and Brandner, 2005; Hornung, 2007; Mueller *et al*., 2016). The crisis of carbonate platforms is documented in other regions of Tethys: Spiti Basin, northwestern India (Hornung *et al*., 2007b), the Anatolian terrane, southwestern Turkey (Lukeneder *et al*., 2012) and the Nanpanjiang Basin, South China (Sun *et al*., 2016). However, it has been suggested that the crisis of shallow carbonate platforms was not synchronous and coincident with the onset of the CPE. Hornung *et al*. (2007b) dated the lithological change marked by laminated shale associated to anoxic conditions to the Julian 1 (uppermost *Trachyceras aonoides* Zone), which is slightly younger than western Tethys (lowermost *Trachyceras aonoides* Zone). Lukeneder *et al*. (2012) found that argillaceous sediments substituted hemipelagic limestones in Turkey approximately 2 Myr later than in western Tethys and interpreted this as due to the different paleolatitude of the two areas. In the Nanpanjiang Basin (Sun *et al*., 2016), the time of termination of carbonate platforms was close to that of western Tethys (Hornung and Brandner, 2005; Hornung *et al*., 2007c; Breda *et al*., 2009), however the carbonate production never recovered in Nanpanjiang Basin. Although a connection between the increase in siliciclastic input and the carbonate platform crisis could be envisaged, a direct link between the two phenomena is challenged by evidence from the Sichuan Basin. There the arrival of terrigenous material into the basin occurred in the late Julian to late Tuvalian, much later than in the Dolomites (Fig. 2A). Furthermore some carbonate platforms in the Dolomites were hit by the crisis, but did not suffer from a significant terrigenous contamination (e.g., Preto and Hinnov, 2003).

Actually, shallow water carbonate precipitation did not stop everywhere at the CPE. Modal analysis on thin sections from carbonate platforms in the Southern Alps, quantitatively showed that relative abundance of microbial carbonates dropped sharply, but was replaced by ooids and skeletal grains that took over and became the dominant carbonate components during the CPE (Dal Corso *et al*., 2015; Gattolin *et al*., 2015). Our results from further stratigraphic sections in the Southern Alps reinforce this observation (Fig. 7A).

The correlation of stratigraphic successions here examined can be correlated within the Sichuan Basin (Fig. 2A) and within the western Tethys with the construction of two composite series displaying the variations in the abundances of carbonate constituents in the two areas across the CPE in the upper Julian – Tuvalian interval (Fig. 7A).

A low content of microbial carbonate is found during the CPE both in the Chinese and Italian

sections. In the Dolomites, the microbial content dropped in coincidence with the negative shift in $\delta^{13}C_{org}$ at the onset of the CPE (Gattolin *et al*., 2015). Shi *et al*. (2018) discuss the isotope record inform the Ma'antang section, in the northwestern Sichuan Basin (Fig. 4), and refer the negative carbon isotopic excursion in the Ma'antang Formation to the CPE. The biostratigraphic resolution of the Ma'antang section does not allow discrimination of the multiple carbon isotopic excursions recognized elsewhere, and the negative carbon isotope excursion can be referred to the Julian, hence the low microbial carbonate content observed in the section is at least in part coeval to the microbial-poor interval in the Dolomites.

This evidence suggests that the decline in microbial production associated to the early stages of the CPE was not a local feature, confined to carbonate platforms of the western Tethys, but was instead a large scale phenomenon that interested shallow water carbonate platform at the scale of the entire Tethys. There is, however, a dichotomy in the way the crisis of platform carbonates at the CPE is described in literature. Most work (Keim *et al*., 2001, 2006; Hornung and Brandner, 2005; Hornung, 2007; Hornung *et al*., 2007a, b, c; Breda *et al*., 2009) describe a shutdown, or demise of the shallow water carbonate production. Instead, others (Dal Corso *et al*., 2015; Gattolin *et al*., 2015 and this study) describe a change in the type of carbonate produced by the carbonate factory: shallow water carbonate depositional systems did not stop producing carbonate, but the type of carbonates changed, possibly along with a diminution (as opposed to a complete halt) of carbonate production rates.

A similar evolution of carbonate platforms and its similarities with what is observed across the CPE is also reported in the Early Jurassic, when a change from a microbial-dominated to a skeletal-dominated carbonate production occurs at the Sinemurian-Pliensbachian (S-P) boundary Event (Franceschi *et al*., 2018). Franceschi *et al*. (2018) pointed out that a similar evolution pattern in carbonates across negative carbon isotopic excursions observed in different times suggested cause effect-relationships between the environmental changes associated to negative carbon isotopic perturbations and the observed modifications in the carbonate factory. Results presented in this paper corroborate this hypothesis by demonstrating that those effects occurred Tethys-wide and point phenomena able to impact carbonate systems at global scale.

What is observed in the Carnian and in the Early Jurassic is somewhat in contrast with the idea that microbial carbonates could be considered "crisis facies", that become widespread in the geologic record after biotic crises have impacted other carbonate producers (e.g., Schubert and Bottjer, 1992; Webb, 1996; Whalen *et al*., 2002).

Shallow-marine microbial carbonate platforms in the western Tethyan regions recovered in late Carnian to early Norian (Caggiati *et al*., 2018). Our new data from the Sichuan Basin show that microbial content suddenly increases in the Tuvalian to Early Norian (Fig. 7A) in eastern Tethys as well. With all the caveats due to the differences in biostratigraphic resolution, this timing is in good

agreement with that observed in the western Tethyan sections. This implies that it took at least one million year before the perturbations of palaeoenvironment and/or seawater chemistry associated with the CPE fade out and suggests that the recovery of the microbial carbonate factory was not a local phenomenon and might be due to a Tethys-wide re-establishment of seawater conditions suitable to the development of microbialites after the CPE.

6.3. Shallow water carbonate production and sea level during the CPE

The CPE impacted on the microbial platforms in western Tethys (Dolomites) and eastern Tethys (north western Sichuan Basin). In the Dolomites, the crisis of the microbial factories was nearly synchronous with a sea level drop, the onset of a more humid climate, terrigenous input and the first of multiple carbon isotopic excursions (Roghi, 2004, 2010; Dal Corso *et al*., 2012, 2015 and 2018, and references therein). The regression and the input of siliciclastics in the early Carnian were previously suggested as the main reasons of the carbonate platform crisis (e.g., De Zanche *et al*., 1993; Gianolla *et al*., 1998a; Bosellini *et al*., 2003).

It is true that sea level fluctuations may greatly influence carbonate production (Keim *et al*., 2001), and increased influx of terrigenous sediments would be associated to an increase in nutrients (Hallock and Schlager, 1986; Keim, 2001) that could be detrimental to shallow water carbonate ecosystems. However, data from the Dolomites area show that the demise of high-relief carbonate platforms occurred before the sea-level fall and the increase of terrigenous input, Gattolin *et al*. (2015). Furthermore, microbial carbonate production is less influenced by sea-level variations than modern tropical reefs, because the microbial carbonate factory is productive at a wide range of water depths (Kenter *et al*., 2005).

In the Sichuan Basin a large-scale regression was reported during late Ladinian, followed by a Carnian transgression, and this local sea-level change was attributed to the formation of a forebulge like to Ladinian regression followed by the onset of foreland basin sedimentation in the Carnian (Deng *et al*., 1982; Wu, 1984; Zhang, 1996; Li *et al*., 2003). As a consequence, the upper part of the Middle Triassic (most of Sichuan Basin) and the lower part of the Upper Triassic (i.e., Hanwang area) are missing. The subaerial exposure surface corresponding to this hiatus is found in the Ma'antang and Guanyin Ya sections (Fig. 2A). The different magnitudes of erosion in these two areas are probably to be attributed to their positions in different zones of the Longmen Shan forebulge (Li *et al*., 2011b, 2014) and to the inherited rugged landform (Shi *et al*., 2015). Above the unconformity, local sea level kept rising during the whole Carnian, as demonstrated by facies analysis (Wu, 2009, Li *et al*., 2003, 2014; Jin *et al*., 2018a, also see the discussion in 6.1).

There are thus profound differences between the geological history of the Sichuan Basin and the

Dolomites. Firstly, the sea level drop occurred before the beginning of the CPE in the Sichuan Basin (Fig. 2A), while it occurs after it in the Dolomites (Gattolin *et al*., 2015). The other is that the decrease in microbial grains occurs during a long-lived Carnian transgression in Sichuan, while in the Dolomites oolitic-skeletal grain associations persisted during a time interval punctuated by multiple relative sea-level oscillations, which implied also repeated subaerial exposures (e.g., De Zanche *et al*., 1993; Gianolla *et al*., 1998a; Preto and Hinnov, 2003; Breda *et al*., 2009). Therefore, sea level fluctuations did not influence the microbial carbonate production significantly across the CPE.

Another potential mechanism able to impact on carbonates by changing seawater chemistry could be ocean acidification. Rigo *et al*. (2007) described a rise in the Carbonate Compensation Depth in the Lagonegro Basin of Southern Italy at the time of the CPE. This could be in agreement with an ocean acidification scenario, however, no definitive proof has been provided so far that the pH of seawater was reduced during the CPE. Moreover, the duration of the microbial carbonate factory crisis, which apparently lasted for > 1 Myrs from the late Julian to the late Tuvalian (Fig. 7A), seems not compatible with the average duration of an ocean acidification event that should not exceed 100 kyrs (Hönisch *et al*., 2012).

6.4. The crisis of platforms is not platform drowning

The CPE was marked by an increased runoff and the input of siliciclastics to shallow water carbonate platforms (Keim *et al*., 2001; Preto and Hinnov, 2003; Preto *et al*., 2005; Breda *et al*., 2009, and references therein), which was associated to the change in carbonate production and to a reorganization of depositional environments in the whole Tethys (Fig. 8A/B).

A typical response of carbonate platforms to climatic or environmental crises is drowning, i.e., the superposition of pelagic sediments on shallow water carbonates as the top of platforms subsides to higher depths (e.g., Schalger, 1981). Rapid eustatic sea-level rises and regional tectonics were considered as possible factors for drowning (Schlager, 1981; Crevello *et al*., 1989; Mutti *et al*., 1997; Weissert *et al*., 1998; Marino and Marin, 2010, and references therein).

It is clear that not all carbonate platforms were drowning during CPE (Fig. 8A), yet some drowning events were documented at ages close to or coinciding with the CPE. In the Qinyan Gou (HWQ) section (Fig. 8A), the abrupt lithological change from Carnian microbial-sponge boundstones, forming reef mounds, to dark grey shales with a deep water faunal association has been deemed a drowning event associated to the CPE (Shi *et al*., 2009, 2017; Li *et al*., 2011a). However, recent studies indicated that the age of sponge reefs is Tuvalian 3 (late Carnian), which implies the drowning is much younger than the CPE in this part of the Sichuan Basin (Jin *et al*., 2018a, b).

In Nanpanjiang Basin, Guizhou province, approximately 550 km south of Sichuan Basin, two

carbonate platform drowning events are documented (Lehrmann *et al*., 2005; Enos *et al*., 2006; Wang *et al*., 2008; Minzoni *et al*., 2015). A first drowning event started with nodular-bedded, ammonoid bearing, dark-gray lime mudstones of the Zhuganpo Formation (Enos *et al*., 1998; Lehrmann *et al*., 2005; see also Fig. 8A), which overlie the shallow water, peritidal carbonates of the Yangliujing Formation (Minzoni *et al*., 2015). Based on the record of magnetic polarity inversions and biostratigraphy of Minzoni *et al*. (2015), Zhang *et al*. (2015) and Sun *et al*. (2016), this drowning event is early Carnian and predates the CPE. However, the drowning was not complete and isolated or pinnacle platforms were still growing around the Nanpanjiang Basin at this time. Subsequently, black shales of the lower part of Wayao Formation deposited on the drowned platform succession of the Zhuganpo Formation, and also draped the residual surviving isolated platforms (Minzoni *et al*., 2015). This second drowning event roughly coincides with the onset of the CPE (Sun *et al*., 2016), and the Wayao Formation bears sedimentological evidence of reduced carbonate productivity (Wang *et al*., 2008).

The carbonate platform crisis in Aşağiyaylabel section (Taurus Mountains, southwest Turkey) described by Lukeneder *et al*. (2012) is a drowning event. The early Julian coral reef was substituted by fine carbonates with deep water fauna (ammonoids, conodonts, *Halobia*), through an oxides-rich surface (fig. 3 in Lukeneder *et al*., 2012). This surface could correspond to a drowning event which is nearly synchronous with the age of the CPE (Fig. 8A).

In the Julian Alps, the Conzen Formation is interpreted as a carbonate- terrigenous platform and consists of the lower subtidal and upper intra- peritidal deposits (De Zanche *et al*., 2000). The subsequent Tor Formation is characterized by shallow-water terrigenous-carbonate ramp deposits, and dominated by thin-layered shallow-water limestones with abundant fossils. The dolomite-dominated Portella Formation still represents a shallow water environment (De Zanche *et al*., 2000). These shallow water facies are suddenly substituted by the deep water facies of the Carniza Formation, which is mainly composed by thin-shelled bivalves, radiolarians and chert-nodular limestones. This sharp facies change was considered to a drowning event, offer to the Tuvalian1/2 in Julian Alps (Fig. 8A), which is after the CPE.

The different timeframe of drowning in South China Block, early Carnian in Nanpanjiang Basin (Minzoni *et al*., 2015, and references therein) and late Carnian in Sichuan Basin (Jin *et al*., 2018a) may be related to the different local structural arrangements and distances from the Indosinian orogeny. Also in western-central Tethys, some platforms drowned but the drowning events were not synchronous. Nevertheless, the Carnian carbonate platforms change from microbial to oolitic-skeletal production was nearly synchronous, and also bounced back to microbial dominated platforms at the same time in western and eastern Tethys.

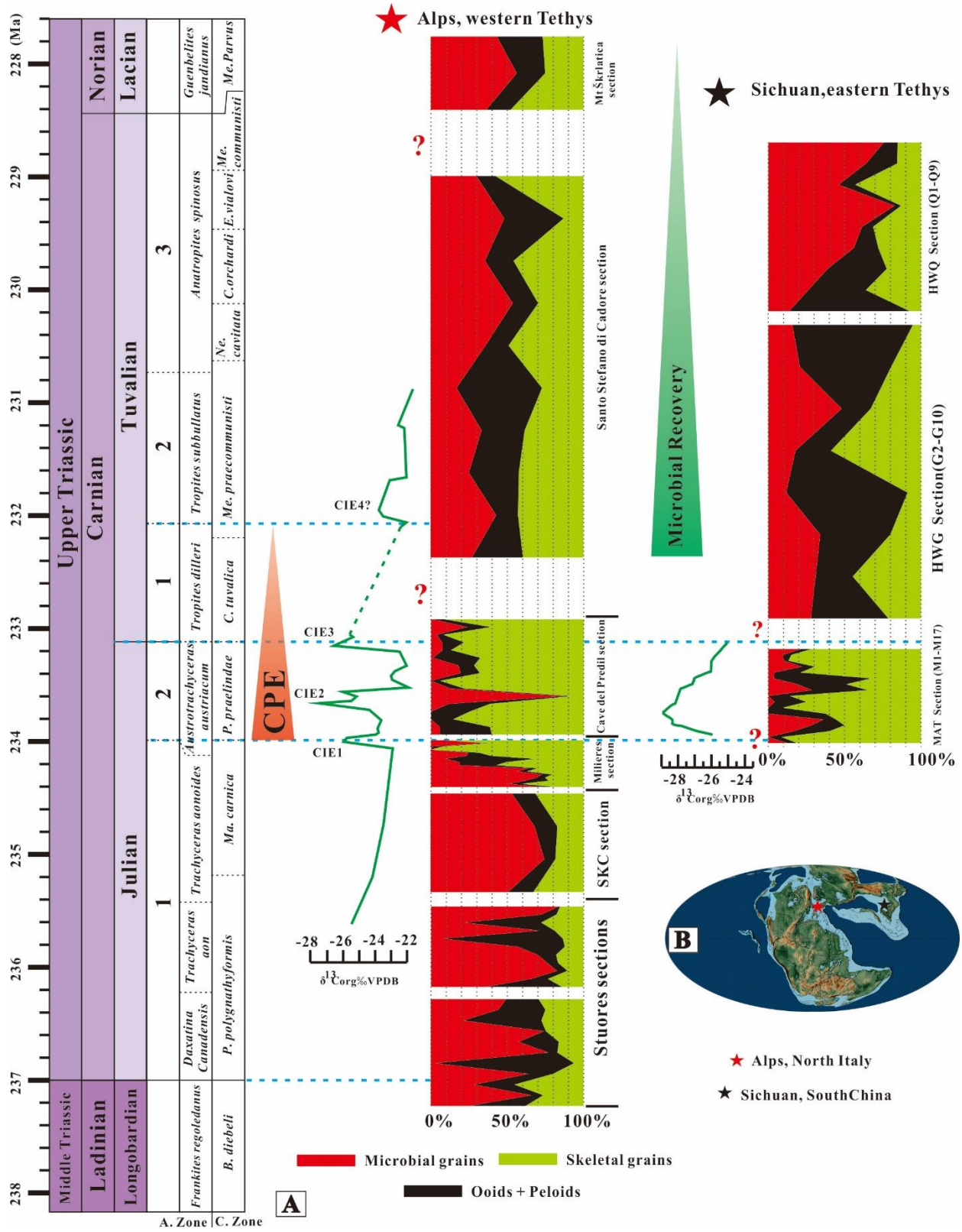

Fig. 7. A). The comparison of modal abundance of skeletal grains and microbial grains (excluded others components) in carbonates from Ladinian to Norian in Alpine regions (western Tethys) and Sichuan Basin (eastern Tethys). The published data from Stuores Wiesen section (Preto, 2012) and Milieres section (Dal Corso *et al.*, 2015) are merged with the new results of this study. The unpublished data of SKC section were donated by Nereo Preto. The dramatic decrease of abundance in microbial grains coinciding with the negative CIE is both observed in Alpine regions and Sichuan Basin, as well as the recovery of microbial grains is in late Carnian to earlier Norian. **B**). Locations of Southern Alps and Sichuan Basin during the Carnian.

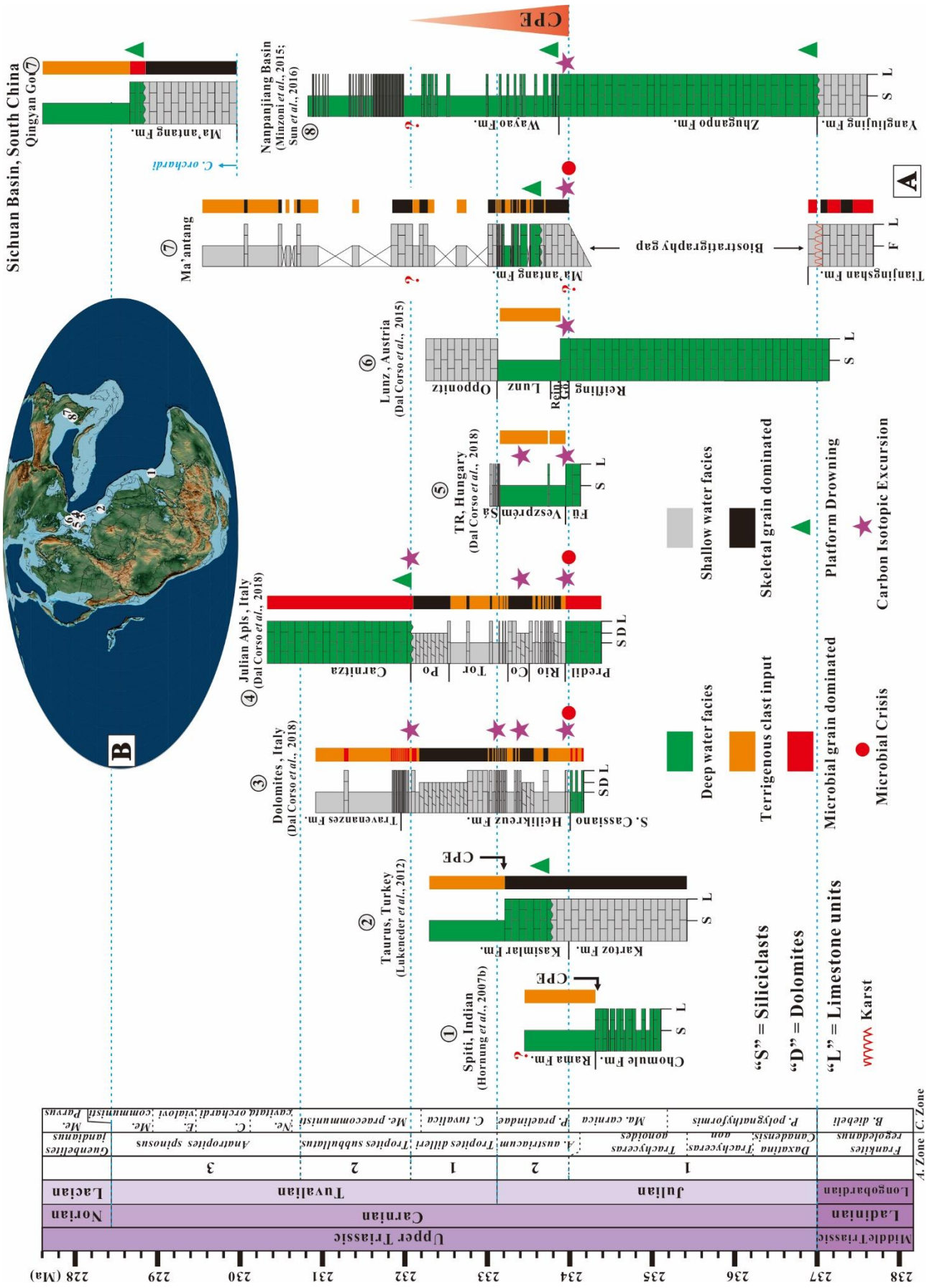

Fig. 8. A). The major changes of Carnian carbonate platforms during the CPE in Tethys. **B**). Locations of Carnian sections in Tethys, the palaeogeographic map of Carnian from Scotese, C. R (2014). "Predil" = Predil Limestone, "Rio" = Rio del Lago Formation., "Co" = Conzen Formation., "Tor" = Tor Formation., "Po" = Portella Limestone,

“Fü” = Füred Formation., “Sá” = Sándorhegy Formation., “Gö” = Göstling Formation., “Rein.” = Reingraben Formation..

7. Conclusions

The Carnian Pluvial Event coincided with widespread modifications in carbonate platform sedimentary systems.

Modal analysis carried out on shallow water carbonate series encompassing the CPE in Sichuan Basin (eastern Tethys) and in the Southern Alps (western Tethys) show that carbonate production switched from microbial-dominated to bioclastic-oolitic The recovery of microbial carbonate factory occurred in the late Tuvalian/early Norian both in the Southern Alps and Sichuan Basin. Thus, a synchroneity of crisis and recovery of microbial carbonate factories is observed at the scale of the entire Tethys and irrespective of the different local environmental conditions. Hence, the crisis of microbial shallow water carbonates points to changes in climate, oceanographic or seawater chemistry related to the CPE as the drivers of the observed global scale modifications in shallow water carbonate systems.

Acknowledgements

We acknowledge Leonardo Tauro (University of Padova) for the thin sections, Stefano Castelli (University of Padova) for photographing thin sections. Manuel Rigo (University of Padova) is thanked for the discussions. This work was supported by Open Fund of State Key Laboratory of Oil and Gas Reservoir Geology and Exploitation (Chengdu University of Technology) (grant number PLC20180301); the National Natural Science Foundation of China grants (grant numbers 41272131, 41572085); and China Scholarship Council (grant number 201508510096).

OVERALL DISCUSSIONS AND CONCLUSIONS

1. Some considerations on the regional geology of the Northwestern Sichuan Basin

1.1. The age of hexactinellid sponge reef mounds (Ma'antang Formation) and Carnian/Norian boundary in northwestern Sichuan Basin

The hexactinellid sponge reef mounds are a unique character of the carbonate platforms in Hanwang and Jushui areas and were initially investigated by Wu (1989). These reef mounds sit on a basal unit of oolitic-bioclastic limestones (units 1 and 2 in chapters 2 and 3), and were initially dated to early Carnian; the upper sponge reef mounds and the overlaying dark shales/mudstones were dated to late Carnian (Wu, 1989). However, there is no illustration of diagnostic fossils in Wu (1989). In light of the magnetic polarity pattern, finding of *Q. polygnathiformis* and ammonoid taxa of the Discotropitid and Juvavitid families, Shi *et al*. (2017) raised the overlain terrigenous sedimentations were lower upper Carnian, and their occurrence was related to the CPE in northwestern Sichuan Basin. Our conodonts association: *Paragondolella noah*, *Carnepigondolella angulata*, *Hayashiella tuvalica*, *Epigondolella miettoi*, *Carnepigondoella orchardi* was collected from below the sponge reef mounds and is dated to late Tuvalian (*Carnepigondolella orchardi zone* Zone) (Fig. 1). The palynological assemblages *Dictyophyllidites-Kyrtomisporis-Canalizonospora* and *Dictyophyllidites-Lunzisporites-Chasmatosporites*, associated with the bivalve *Halobia* cf. *H. septentrionalis*, were found in similar positions. The ammonoids association Tropitid n. gen. n. sp., *Gonionotites* sp., *Griesbachite*s sp., *Griesbachites* cf. G. *laevis*, *Guembelites philostrati*, *Thisbites* cf. T. *petralis*, *Hadrothisbites* n. sp. which were collected from below and above the sponge reef mounds are dated to a short interval between the late Carnian and early Norian (Fig. 1). These new biostratigraphic data convincingly indicate the hexactinellid sponge reef mounds are much younger (late Tuvalian) than previous determinations (Shi *et al.*, 2017), as a result, the abrupt facies changes and sudden demise of hexactinellid sponge mounds in Hanwang and Jushui areas are not ascribed to the CPE, and are instead linked to the paleoenvironmental changes due to the development of the Sichuan foreland basin.

Moreover, according to the new biostratigraphy and two recalibrations of the magnetostratigraphy of the HWQ section, the Carnian/Norian boundary is pinpointed in a short interval in the HWQ section (Fig. 1). The study of the Carnian/Norian boundary with a detailed succession of ammonoids, conodonts, and bivalves biostratigraphy is the first report in northwestern Sichuan Basin which provides a much easterly position than other successions so far considered in

the Tethys. These new biostratigraphic data may reveal useful for a better-informed placement of the Norian GSSP.

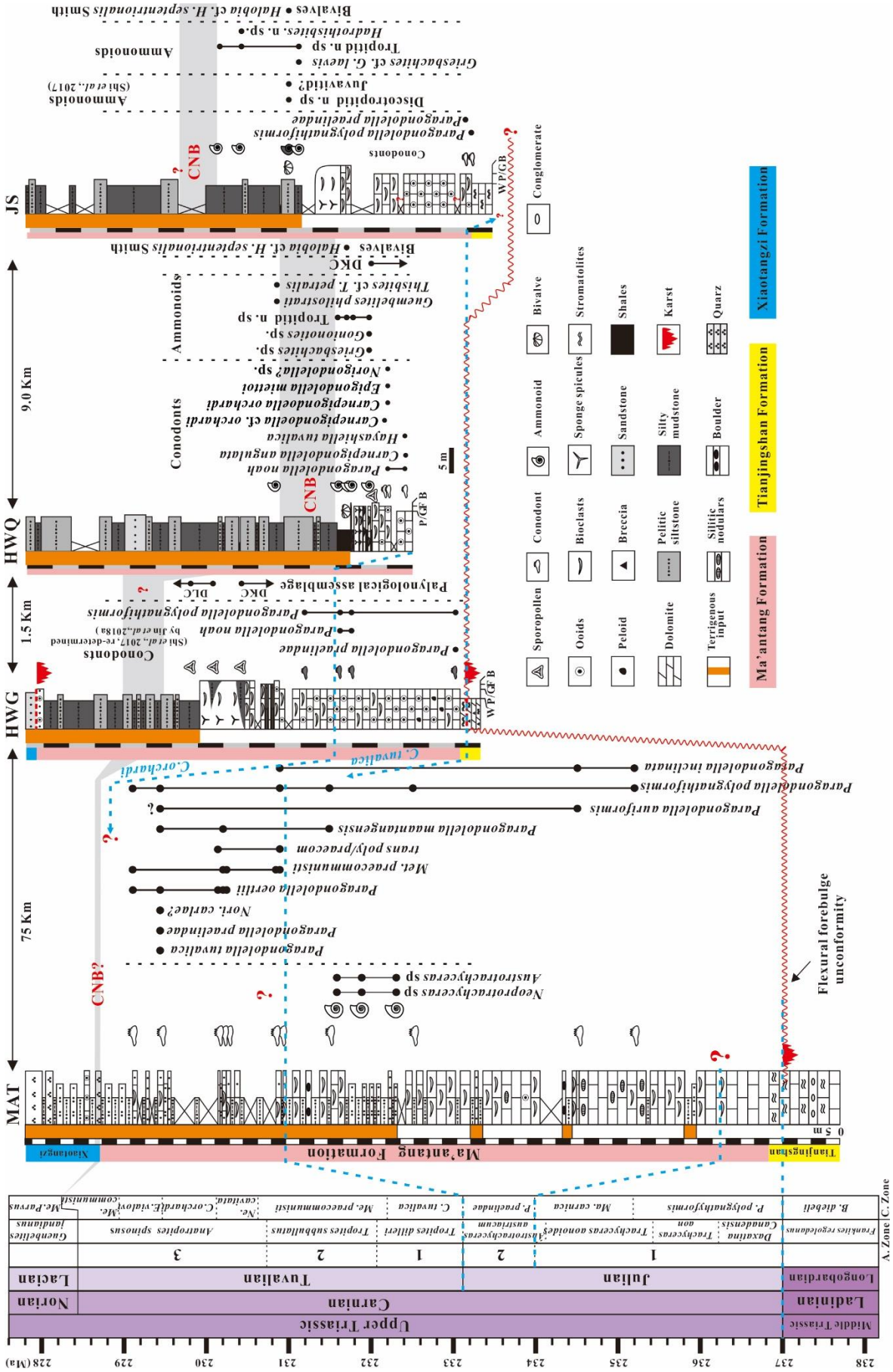

Fig. 1. The Carnian biostratigraphic correlation in northwestern Sichuan Basin, South China. The biostratigraphy of MAT section follows Shi *et al*. (2018). The biostratigraphy of the HWG and HWQ sections follows Jin *et al*. (2018a, b). The Tianjingshan Formation shows a contradictory age according to our new biostratigraphic data. Time scale as of Bernardi *et al*. (2018). The ammonoid zonation of Carnian follows Gallet *et al*. (1994) and Broglio Loriga *et al*. (1999). The conodont zonation of Carnian follows Rigo *et al*. (2018). "W" = Wackestone, "P/G" = Packstone-grainstone, "F" = Floatstone, "B" = Boundstone.

1.2. The age of upper stromatolites (Tianjingshan Formation?) in northwestern Sichuan Basin

The boundary between Middle and Late Triassic in western Sichuan Basin is marked by extensive karst (Wu, 1989; Li *et al.*, 2003, 2011b; Mei and Liu, 2017, and references therein). The karst developed during a tectonically driven subaerial exposure episode, and the relative exposure surface and hiatus are interpreted as the forebulge unconformity of the Sichuan foreland basin (e.g., Li *et al.*, 2003). The stromatolitic dolostones/limestones of the Tianjingshan Formation are below this karst surface, and are easily differentiated from the overlaying oolitic-bioclastic limestones of Ma'antang Formation (Wu, 1989). In this simple lithological evolution, stromatolitic facies always predate the onset of the Sichuan foreland basin. In regional geology work, thus, stromatolitic facies are used as a marker of the Middle Triassic, and to identify the Tianjingshan Formation in the field. We found instead that the contact between the middle and upper Triassic in northwestern Sichuan Basin is more complex. First, the conodonts *Paragondolella polygnathiformis* and *Paragondolella praelindae* were collected within the top of or just above stromatolite beds at the JS section. These conodonts are positively Carnian in age (e.g., Mietto *et al.*, 2012; Rigo *et al.*, 2007, 2018), and are suggested to most probably indicate a Tuvalian (Late Carnian) age (Fig. 1). If the stromatolites are used to define the Tianjingshan Formation, this implies that the Tianjingshan Formation is Carnian (Fig. 1). This age determination is in agreement with findings of Carnian foraminiferal and conodont associations reported in similar layers of Tianjingshan Formation (He, 1980 and Wang, 1981). Second, the paleokarst surface was found within the top of stromatolite beds of Tianjingshan Formation in MAT and HWG sections, but the stratigraphic position of this karst is possibly not the same across the Sichuan Basin. The lower Carnian is present in the lower part of the Ma'antang Formation at the MAT section, while it is omitted in Hanwang and JS sections (Fig. 1). This might be attributed to different magnitudes of erosion because of their positions in different zones of the Longmen Shan forebulge (Li *et al.*, 2011b, 2014) and to the inherited rugged landforms (Shi *et al.*, 2015).

With the current lithostratigraphic nomenclature, the stromatolite-bearing Tianjingshan Formation occurs both below and above the forebulge uncomformity of the Sichuan Foreland basin. This apparent inconsistency derives from the practice of using stromatolites as a lithological marker

for the Tianjingshan Formation (Fig. 1). We here suggest that the stromatolite-bearing carbonates above the forebulge uncomformity should not included in the Tianjingshan Formation, and a lithostratigraphic revision of the Carnian of the Sichuan Basin is needed.

2. A global comparison of Carnian carbon stable isotopes

The new biostratigraphic data collected with this work so far excluded the presence of the lower Carnian in the Ma'antang Formation of Hanwang and Jushui, and contradict the inference that the crisis of carbonate platforms was caused there by the CPE. The MAT section is about 100 kilometers northwestward from Hanwang and Jushui sections, located at Ma'antang town, Jiangyou city, in Upper Yangtze Block. It was studied for lithology, biostratigraphy, and carbon and oxygen isotopes. The MAT section is mainly made of bioclastic limestones and micrites in the lower part and by terrigenous sedimentary rocks upwards. However, the main lithological transition occurs at the middle of the MAT section which is dated to upper Julian and is older than lithologically similar horizons at the HWQ, HWG and JS sections (Fig. 1). The asynchronous demise of carbonate platforms in these two areas is probably related to a complex inherited Carnian paleotopography and to the effects of Indosinian orogeny and the consequent formation of the Sichuan foreland basin. A single broad negative carbon isotopic excursion (CIE) is recorded by bulk organic carbon in the lower part of Ma'antang Section (Fig. 2), i.e., before the main lithological change to persistent terrigenous sedimentation. This CIE, due to its age as determined with conodonts and ammonoids biostratigraphy, has been associated to the CPE. In the HWQ, HWG, and JS sections, carbon stable isotopes from wood and bulk organic matter were measured in the late Carnian to early Norian interval for the first time in eastern Tethys. The evidence from the Sichuan Basin is that no carbon isotopic excursions occur at the Carnian/Norian boundary (Fig. 2). The most negative bulk organic carbon $\delta^{13}C$ values occur at the lowest part of the HWG section, which might be corresponding to the fading phase of the CIE of the Carnian Pluvial Episode. This would correspond to the youngest parts of the CIEs in the MAT section, northwestern Sichuan Basin, and in the Longchang section, Nanpanjiang Basin approximately 550 km south of Sichuan Basin (Sun *et al.*, 2016). Prolonged positive d13C trends were recognized in the HWQ, HWG, and JS sections, and were tentatively correlated to the uppermost MAT and Longchang sections (Fig. 2). The occurrence of a single CIE, followed by a long-lasted positive trend of organic carbon isotopes in South China is different from the multiple CIEs reported both in terrestrial and marine CPE sections in western Tethys (Miller *et al.*, 2017; Baranyi *et al.*, 2018; Dal Corso *et al.*, 2018) (Fig. 2). To ascertain the causes of this difference, more precise biostratigraphy and high-density sampling are needed.

Nevertheless, the CIE associated with CPE is interpreted as being caused by the injection of massive amounts of $\delta^{13}C$-depleted carbon into the atmosphere-ocean system, that may have derived from contemporary volcanism, and in particular from the emplacement of the Wrangellia Large Igneous Province (Furin *et al.*, 2006; Dal Corso *et al.* 2012, 2015, 2018; Xu *et al.*, 2014; Sun *et al.*, 2016, 2018; Mueller *et al.*, 2016).

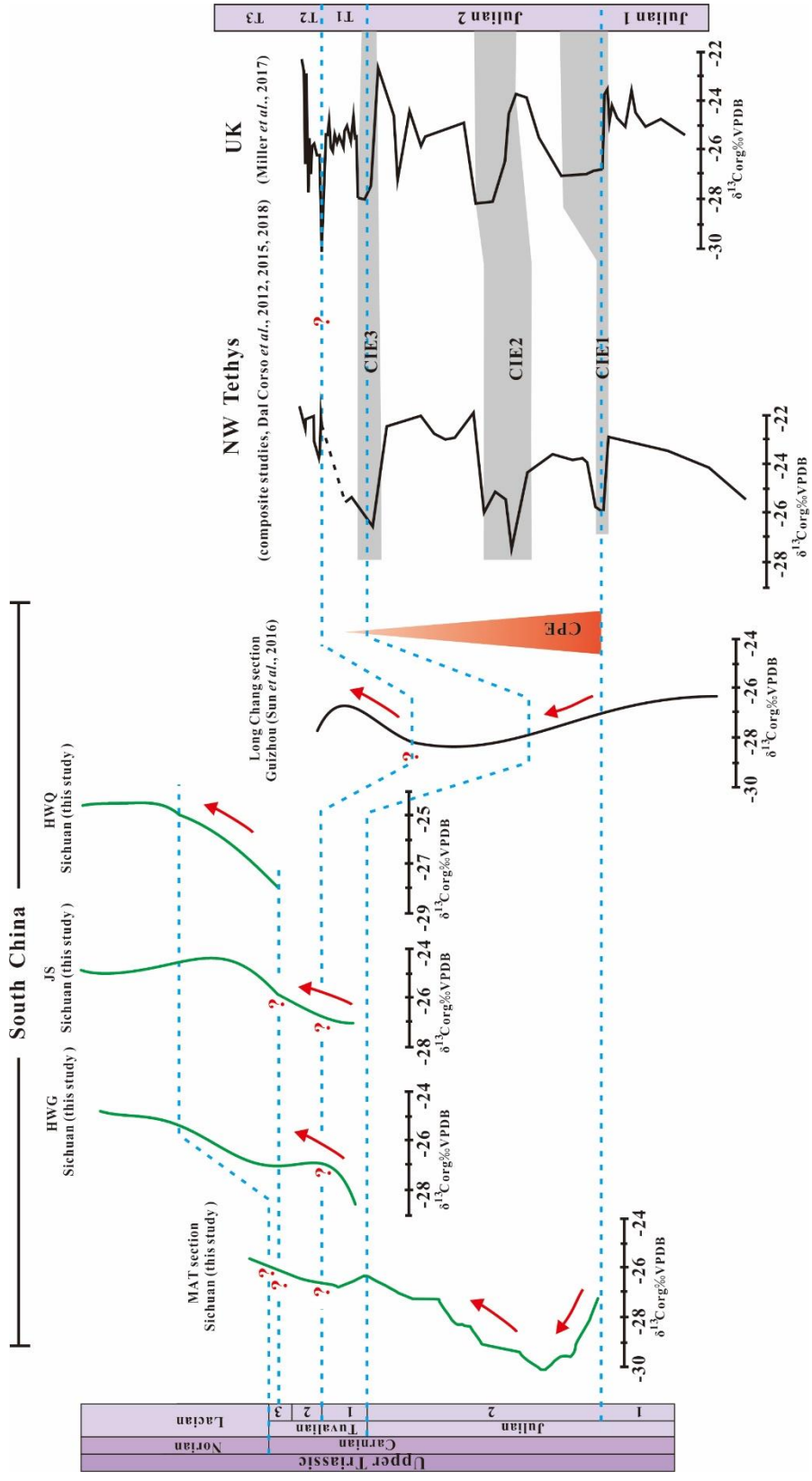

Fig. 2. Correlation of the carbon stable isotopes from eastern Tethys (Sichuan Basin, this study; Guizhou Basin, Sun *et al.*, 2016), western Tethys (Dal Corso *et al.*, 2012, 2015, 2018), and a lacustrine succession from the continental Central European Basin of UK (WP borehole 1, Miller *et al.*, 2017). The biochronology scale follows that of the MAT section, Sichuan Basin (Shi *et al.*, 2018). The upper parts of the HWG, HWQ and JS sections are not shown. The boundary of biochronostratigraphic subdivisions of the Tuvalian (T1, T2 and T3) in Sichuan Basin is still unclear. The lower part of Long Chang section is not shown. The biostratigraphic correlation of NW Tethys and UK follows Dal Corso *et al*. (2018).

3. The Carbonate diagenesis records of $\delta^{13}C_{carb}$ and $\delta^{18}O$ and microfacies studies in the HWQ section

Stable carbon and oxygen isotopes were investigated on microbial grains, bulk rock, and brachiopods in the HWQ section. The preservation of brachiopods was assessed with optical and Scanning Electron Microscope (SEM) petrography, which revealed that many of the well-preserved brachiopods have punctated shells. Since the punctae may be filled by late diagenetic cement and could not be avoided during sampling, the correlation between the area of punctae and isotopic composition was tested. A strong correlation ($R^2 = 0.77$) was found between the $\delta^{18}O$ of sampled brachiopod calcite and punctae area, while the $\delta^{13}C$ values resulted insensitive to the presence-abundance of punctae. This suggests that the cement filling the punctae had a relatively low $\delta^{18}O$, and calls for caution when punctated brachiopods are used in paleotemperature reconstructions. However, the area of punctae was used to assess the degree of diagenetic alteration of brachiopod samples in this case and revealed to reasonably predict the deviation of $\delta^{18}O$ from expected Carnian values. The screening of punctae density of brachiopod shells is here suggested as a new method to assess the reliability stable isotopic data.

A CIEs with magnitude of > 4 ‰ in bulk rock and < 2 ‰ in microbial grains was found in the lower part of the HWQ section. This CIE should not be considered to relate to the CPE because of its age, younger than the CPE. This ample CIE is apparent in bulk rock data, is less intense in coeval microbial grains, and there is no CIE in the same interval in well-preserved brachiopods. Hence, we concluded that there was no major carbon isotopic excursion in the Ma'antang Formation in Hanwang. This abrupt CIE is instead a product of diagenetic alteration, in light of petrological checking of SEM imaging and cathodoluminescence (CL). It is ascribed to decomposition of organic matter during hardground formation which resulted in the precipitation of diagenetic calcite with carbon isotopic composition depleted in $\delta^{13}C$. Oxidized pyrite was found within fine calcite cement in framework pores of hardground and overlain leiolites, which exhibits dull CL and has moderately low carbon and oxygen isotopic composition. No evidence of karst dissolution, as suggested by Shi *et al*. (2017), was found instead. More evidence from carbonate microfacies and quantitative petrography analyses

of the Ma'antang Formation in the MAT, HWQ and HWG sections support this conclusion. In fact, facies associations are arranged in an overall transgressive sequence representing sedimentary environments from inner ramp to basin. This Carnian transgression can also be inferred from the shallow water organism association, including calcimicrobes in the lower part, which shifts to deep water hexactinellid sponges and *Tubiphytes* in the upper part.

4. The microbial factory crisis and recovery and drowning event in CPE

During the CPE, a temporary demise of carbonate platforms occurred worldwide (Ogg *et al.*, 2015; Ruffel *et al.*, 2016, and references therein), however not all carbonate platforms died out; instead, some carbonate platforms changed in type, i. e., the microbial carbonate production was replaced by dominant skeletal carbonate production (Dal Corso *et al.*, 2015; Gattolin *et al.*, 2015). Carnian successions were sampled in the Southern Alps, north Italy and northwestern Sichuan Basin, South China for quantitative petrologic analysis. The modal abundance of microbial grains in Sichuan Basin (eastern Tethys) dropped sharply, with ooids and skeletal grains becoming dominant on carbonate platforms coinciding with the CIE of organic matter which is associated with the CPE. This is agreement with previous studies in the Southern Alps (western Tethys) (Dal Corso *et al.*, 2015; Gattolin *et al.*, 2015). The difference is that the crisis of microbial carbonates in the Southern Alps coincide with multiple CIEs (Dal Corso *et al.*, 2018) and occurs immediately before a sea level drop. In Sichuan Basin, a single and long-lasting CIE coexists with the fading of microbial production and occurs after a sea level drop. Notably, the new data from the Sichuan Basin show that microbial carbonate production recovered in the late Tuvalian to Early Norian, which is in good agreement with observations in the coeval sections of the Southern Alps. This might be due to the re-establishment of seawater conditions suitable to the growth of microbialites after the CPE. The contemporary crisis and recovery of microbial carbonate production in eastern and western Tethys reveals that the crisis and recovery of microbial factories are Tethys-wide at least, and might be not affected by such factors as: the different paleolatitudes, sea level fluctuations, subsidence rates, geodynamic settings, and the timing of the terrigenous input. All these factors are, indeed, dramatically different between the two investigated areas.

Drowning events were documented during the CPE. Initially, the crisis of hexactinellid sponge reef mounds and subsequent deposition of fossil-rich dark grey shales in Hanwang area were attributed to the CPE (Shi *et al.*, 2017). This lithological transition is to be considered a drowning episode (Li *et al.*, 2011a, 2014), but is not related to the CPE in this work because of its age. Two drowning events were recorded in Nanpanjiang Basin (Lehrmann *et al.*, 2005; Enos *et al.*, 2006; Wang *et al.*, 2008; Minzoni *et al.*, 2015). One occurs near the Ladinian/Carnian boundary and is younger

than CPE, and the other is nearly synchronized with CPE (Minzoni *et al.*, 2015). The complex history of carbonate platform drowning on the margin of the South China Block thus suggests that the occurrence of drowning events cannot be correlated worldwide during the Carnian. Instead, the crisis of microbial carbonate production and its substitution with skeletal grains and ooids is here identified as a Tethys-wide response to the CPE.

References

Abbas, H., Michail, M., Cifelli, F., Mattei, M., Gianolla, P., Lustrino, M., Carminati, E., 2018. Emplacement modes of the Ladinian plutonic rocks of the Dolomites: Insights from anisotropy of magnetic susceptibility. J. Struct. Geol., 113, 42-61.

Algeo, T. J., Wilkinson, B. H., Lohmann, K. C., 1992. Meteoric-burial diagenesis of Middle Pennsylvanian limestones in the Orogrande Basin, New Mexico: water/rock interactions and basin geothermics. J. Sediment. Res., 62, 652-670.

Allan, J. R., Matthews, R. K., 1982. Isotope (C, O) signatures associated with early meteoric diagenesis. Sedimentology, 29, 797-817.

Anawar, H. M., Yoshioka, T., Konohira, E., Akai, J., Freitas, M. C., Tareq, S. M., 2010. Sources of organic carbon and depositional environment in the Bengal delta plain sediments during the Holocene period. Limnology, 11, 133-142.

Arens, N. C., Jahren, A. H., Amundson, R., 2000. Can C3 plants faithfully record the carbon isotopic composition of atmospheric dioxide? Paleobiology, 26, 137–164.

Arche, A., López-Gómez, J. L., 2014. The Carnian Pluvial Event in Western Europe: new data from Iberia and correlation with the Western Neotethys and Eastern North America–NW Africa regions. Earth. Sci. Rev., 128, 196-231.

Badeck, F.W., Tcherkez, G., Nogues, S., Piel, C., Ghashghaie, J., 2005. Post-photosynthetic fractionation of stable carbon isotopes between plant organs—a widespread phenomenon. Rapid Communications in Mass Spectrometry 19, 1381-1391.

Balini, M., Krystyn, L., Levera, M., Tripodo, A., 2012. Late Carnian-Early Norian ammonoids from the GSSP candidate section Pizzo Mondello (Sicani Mountains, Sicily). Riv. Ital. Paleontol. Stratigr., 118, 47-84.

Baranyi, V., Miller, C. S., Ruffell, A., Hounslow, M. W., Kürschner, W. M., 2018. A continental record of the Carnian Pluvial Episode (CPE) from the Mercia Mudstone Group (UK): palynology and climatic implications. J. Geol. Soc. London, in press.

Barrenechea, J. F., López-Gómez, J., De La Horra, R., 2018. Sedimentology, clay mineralogy and palaeosols of the Mid-Carnian Pluvial Episode in eastern Spain: insights into humidity and sea-level variations. J. Geol. Soc. London, in press.

Bates, N. R., Brand, U., 1990. Secular variation of calcium carbonate mineralogy; an evaluation of ooid and micrite chemistries. Geol. Rundschau 79, 27-46.

Batt, L. S., Montañez, I. P., Isaacson, P., Pope, M. C., Butts, S. H., Abplanalp, J., 2007. Multi-carbonate component reconstruction of mid-carboniferous (Chesterian) seawater $\delta^{13}C$. Palaeogeogr. Palaeoclimatol. Palaeoecol., 256, 298-318.

Bellanca, A., Di Stefano, P., Neri, R., 1995. Sedimentology and isotope geochemistry of Carnian deep-water marl/ limestone deposits from the Sicani Mountains, Sicily: environmental implications and evidence for a planctonic source of lime mud. Palaeogeogr. Palaeoclimatol. Palaeoecol., 114, 111-129.

Benton, M. J., 1991. What really happened in the Late Triassic? Hist. Biol., 5, 263-278.

Benton, M. J., 2004. Origin and relationships of Dinosauria. In: Weishampel, D.B., Dodson, P., Osmólska, H. (Eds.), the Dinosauria. University of California Press, Berkeley, pp. 7-19.

Benton, M. J., Bernardi, M., Kinsella, C., 2018. The Carnian Pluvial Episode and the origin of dinosaurs. J. Geol. Soc. London, in press.

Bernardi, M., Gianolla, P., Petti, F. M., Mietto, P., Benton, M. J., 2018. Dinosaur diversification linked with the Carnian Pluvial Episode. Nat. Commun., 9, 1499.

Berra, F., Jadoul, F., 2002. Evidence of a ‘‘mid-Carnian’’ transgression in the western Southern Alps (Lombardy, Italy): stratigraphic and paleogeographic implications. Riv. Ital. Paleontol. Stratigr., 108, 119-131.

Bialik, O. M., Korngreen, D., Benjamini, C., 2013. Carnian (Triassic) aridization on the Levant margin: evidence from the M1 member, Mohilla Formation, Makhtesh Ramon, south Israel. Facies, 59, 559-581.

Bosellini, A., 1984. Progradation geometries of carbonate platforms: examples from the Triassic of the Dolomites, Northern Italy. Sedimentology, 31, 1-24.

Bosellini, A. Hardie, L. A., 1985. Facies e cicli della Dolomia principale delle Prealpi venete. Mem. Soc. Geol. It., 30, 245–266

Bosellini, A., Gianolla, P., Stefani, M., 2003. Geology of the Dolomites. Episodes, 26, 181-185.

Brand, U., 1989. Biogeochemistry of Late Paleozoic North American brachiopods and secular variation of seawater composition. Biogeochemistry, 7, 159-193.

Brand, U., Logan, A., Hiller, N., Richardson, J., 2003. Geochemistry of modern brachiopods: applications and implications for oceanography and paleoceanography. Chem. Geol., 198, 305-334.

Brand, U., Logan, A., Bitner, M.A., Griesshaber, E., Azmy, K., Buhl, D., 2011. What is the ideal proxy of Palaeozoic seawater chemistry? Mem. Assoc. Australas. Palaeontol, 9-24.

Brand, U., Jiang, G., Azmy, K., Bishop, J., Montañez, I. P., 2012. Diagenetic evaluation of a Pennsylvanian carbonate succession (Bird Spring Formation, Arrow Canyon, Nevada, U.S.A.) - 1: Brachiopod and whole rock comparison. Chem. Geol, 308., 26-39.

Breda, A., Preto, N., Roghi, G., Furin, S., Meneguolo, R., Ragazzi, E., Fedele , P., Gianolla, P., 2009. The Carnian Pluvial Event in the Tofane area (Cortina d’Ampezzo, Dolomites, Italy). Geo. Alp., 6, 80-115.

Breda, A., Preto, N., 2011. Anatomy of an Upper Triassic continental to marginal-marine system: the mixed siliciclastic–carbonate Travenanzes Formation (Dolomites, Northern Italy). Sedimentology, 58, 1613-1647.

Broglio, L. C., Cirilli, S., De Zanche, V., Di, B. D., Gianolla, P., Laghi, M. F., Lowrie, W., Manfrin, S., Mastandrea, A., Mietto, P., Muttoni, G., Neri, C., Posenato, C., Rechichi, M. C., Rettori, R., Roghi, G., 1999. The Prati di Stuores/Stuores Wiesen Section (Dolomites, Italy): a candidate Global Stratotype section and point for the base of the Carnian stage. Riv. Ital. Paleont. Strat, 105., 37-78.

Bruckschen, P., Bruhn, F., Meijer, J., Stephan, A., Veizer, J., 1995. Diagenetic alteration of calcitic fossil shells: Proton microprobe (PIXE) as a trace element tool. Nucl. Instrum. Meth. B., 104, 427-431.

Brusca, C., Gaetani, M., Jadoul, F., Viel, G., 1981. Paleogeografia Ladino- Carnica e metallogenesi nel Sudalpino. Mem. Soc. Geol. It., 22,65–82.

Burchette, T. P., Wright, V. P., 1992. Carbonate ramp depositional systems. Sediment. Geol., 79, 3-57.

Caggiati, M., Gianolla, P., Breda, A., Celarc, B., Preto, N., 2018. The start-up of the Dolomia Principale/Hauptdolomit carbonate platform (Upper Triassic) in the eastern Southern Alps. Sedimentology, 65, 1097-1131.

Celarc, B., Kolar- Jurkovšek, T., 2008. The Carnian-Norian basin-platform system of the Martuljek Mountain Group (Julian Alps, Slovenia): progradation of the Dachstein carbonate platform. Geologica Carpathica-Bratislava, 59, 211.

Chen, J. h., Ba, D. Z., 1986, *Halobia* fauna from Zedang of South Xizang with a discussion on the Halobia assemblages in China. Acta Geol. Sin., 25, 1-9.

Chen, S. F., Wilson, C. J., Worley, B. A., 1995. Tectonic transition from the Songpan-Garze fold belt to the Sichuan Basin, south-western China. Basin Res., 7, 235-253.

Chen, Y., Liu, S. G., Li, Z. W., Deng, B., Zeng, X. L., Lin, J., 2011. LA-ICP-MS detrital ziron U-Pb geochronology approaches to the sediment provenance of west Sichuan foreland basin and limited uplift the Longmen mountains during the early stage of late Triassic. Geotectonica Et Metallogenia 35, 315-323 (In Chinese with English Abstract).

Chen, Y., Krystyn, L., Orchard, M. J., Lai, X. L., Richoz, S., 2015. A review of the evolution, biostratigraphy, provincialism and diversity of Middle and early Late Triassic conodonts. Pap. Palaeontol., 2, 235-263.

Christ, P. A., Immenhauser, A., Wood, R.A., Darwich, K. and Niedermayr, A., 2015. Petrography and environmental controls on the formation of Phanerozoic marine carbonate hardgrounds. Earth-Sci. Rev., 151, 176-226.

Ciarapica, G., L. Passeri., 1990. The Dachstein limestone of the Mt. Canin (Julian Alps) and its paleogeographic meaning. Boll. Soc. Geol. It. 109., 239-47.

Cohen, K. M., Finney, S. C., Gibbard, P. L., Fan, J. X., 2013. The ICS International Chronostratigraphic Chart. Episodes, 36, pp. 199-204.

Colombi, C. E., Parrish, J. T., 2008. Late Triassic Environmental evolution in Southwestern Pangea: plant taphonomy of the Ischigualasto Formation. Palaios, 23, 778-795.

Crevello, P. D., Wilson, J. L., Sarg, J. F., Read, J. F., 1989. Controls on carbonate platform and basin development. SEPM Special Publication 44, 15-25.

Cusack, M., Huerta, A. P., Eimf., 2012. Brachiopods recording seawater temperature-A matter of class or maturation? Chem. Geol, 334., 139-143.

Dal Corso, J., Preto, N., Kustatscher, E., Mietto, P., Roghi, G., Jenkyns, H.C., 2011. Carbonisotope variability of Triassic amber, as compared with wood and leaves (Southern Alps, Italy). Palaeogeogr. Palaeoclimatol. Palaeoecol., 302, 187-193.

Dal Corso, J., Mietto, P., Newton, R. J., Pancost, R. D., Preto, N., Roghi, G., Wignall, P. B., 2012. Discovery of a major negative ^{13}C spike in the Carnian (Late Triassic) linked to the eruption of Wrangellia flood basalts. Geology, 40, 79-82.

Dal Corso, J., Gianolla, P., Newton, R.J., Franceschi, M., Roghi, G., Caggiati, M., Raucsik, B., Budai, T., Haas, J., Preto, N., 2015. Carbon isotope records reveal synchronicity between carbon cycle perturbation and the "Carnian Pluvial Event" in the Tethys realm (Late Triassic). Glob. Planet. Change., 127, 79-90.

Dal Corso, J., Schmidt, A. R., Seyfullah, L. J., Preto, N., Ragazzi, E., Jenkyns, H. C., Delclòs, X., Néraudeau, D., Roghi, G., 2017. Evaluating the use of amber in palaeoatmospheric reconstructions: The carbon-isotope variability of modern and Cretaceous conifer resins. Geochim. Cosmochim. Ac., 199, 351-369.

Dal Corso, J., Gianolla, P., Rigo, M., Franceschi, M., Roghi, G., Mietto, P., Manfrin, P., Raucsik, B., Budai, T., Jenkyns, H. C., Reymond, C. E., Caggiati, M., Gattolin, G., Breda, A., Merico, A., Preto, N., 2018. Multiple negative carbon-isotope excursions during the Carnian Pluvial Episode (Late Triassic). Earth. Sci. Rev, in press.

De Zanche, V., Gianolla, P., Mietto, P., Siorpaes, C., Vail, P. R., 1993. Triassic sequence stratigraphy in the Dolomites (Italy). Mem. Sci. Geol., 45, 1-27.

De Zanche, V., Gianolla, P., Roghi, G., 2000. Carnian stratigraphy in the Raibl/Cave del Predil area (Julian Alps, Italy). Eclogae. Geol. Helv., 93, 331-348.

Deng, K.L., He, L., Qin, D.Y., He, Z.G., 1982. The earlier late Triassic sequence and its sedimentary environment in western Sichuan basin. Oil and Gas Geology, 3, 204-210 (In Chinese with English abstract).

Deng, B., Liu, S.G., Jansa, L., Cao, J.X., Cheng, Y., Li, Z.W., Liu, S., 2012. Sedimentary record of Late Triassic transpressional tectonics of the Longmenshan Thrust Belt, SW China. J. Asian Earth. Sci. 48., 43–55.

Dickson, J. A. D., Coleman, M., 1980. Changes in carbon and oxygen isotope composition during limestone diagenesis. Sedimentology, 27, 107-118.

Dickson, J. A. D., Wood, R.A., Bu Al Rougha, H., Shebl, H., 2008. Sulphate reduction associated with hardgrounds: lithification afterburn! Sediment. Geol., 205, 34-39.

Doglioni, C., 1987. Tectonics of the Dolomites (Southern Alps, Northern Italy). J. Struct. Geol., 9, 181–193.

Enos, P., 1991. Sedimentary parameters for computer modeling. Sedimentary Modeling: Computer Simulations and Methods for Improved Parameter Definition: Kansas Geological Survey, Bulletin, 233, 63–99.

Enos, P., Wei, J. Y., Lehrmann, D. J., 1998. Death in Guizhou-Late Triassic drowning of the Yangtze carbonate platform. Sediment. Geol., 118, 55-76.

Enos, P., Lehrmann, D. J., Wei, J. Y., Yu, Y. Y., Xiao, J. F., Chaikin, D. H., Minzoni, M., Berry, A. K., Montgomery, P., 2006. Triassic evolution of the Yangtze platform in Guizhou Province, People's Republic of China. Geol. Soc. Am. Spec. Pap., 417, 1-105.

Erba, E., 2006. The first 150 million years history of calcareous nannoplankton: Biospheregeosphere interactions. Palaeogeogr. Palaeoclimatol. Palaeoecol., 232, 237-250.

Flügel, E., 2010. Microfacies of Carbonate Rocks. Analysis, Interpretation and Application. Springer-Verlag, Berlin.

Fogel, M., Cifuentes, L., 1993. Isotope fractionation during primary production. In: Engel, M., Macko, S. (Eds.), Organic Geochemistry. Springer, US, pp. 73-98.

Fry, B., Scalan, R. S., Parker, P. L., 1977. Stable carbon isotope evidence for two sources of organic matter in coastal sediments: seagrasses and plankton. Geochim. Cosmochim. Ac., 41, 1875-1877.

Furin, S., Preto, N., Rigo, M., Roghi, G., Gianolla, P., Crowley, J. L., Bowring, S. A., 2006. High-precision U-Pb zircon age from the Triassic of Italy: Implications for the Triassic time scale and the Carnian origin of calcareous nannoplankton and dinosaurs. Geology, 34, 1009. doi:10.1130/g22967a.1

Franceschi, M., Dal Corso, J., Cobianchi, M., Roghi, G., Penasa, L., Picotti, V., Preto, N., 2018. Tethyan carbonate platform transformations during the Early Jurassic (Sinemurian-Pliensbachian, Southern Alps); comparison with the Late Triassic Carnian Pluvial Episode. Geol. Soc. Am. Bull, in press.

Franz, M., Kustatscher, E., Heunisch, C., Niegel, S., Röhling, H. G., 2018. The schilfsandstein and

its flora-arguments for a humid mid-Carnian episode?. J. Geol. Soc. London, in press.

Gale, L., Celarc, B., Caggiati, M., Kolar-J Jurkovšek, T., Jurkovšek, B., Gianolla, P., 2015. Development and palaeogeographic meaning of the Late Triassic basinal succession of the Tamar Valley, northern Julian Alps, Slovenia. Geol. Carpath., 66, 269–283.

Gallet, Y., Besse, J., Krystyn, L., Theveniaut, H., Marcoux, J., 1994. Magnetostratigraphy of the Mayerling section (Austria) and Erenkolu Mezarlik (Turkey) section: improvement of the Carnian (late Triassic) magnetic polarity time scale. Earth. Planet. Sci. Lett., 125, 173-191.

Garzanti, E., Gnaccolini, M., Jadoul, F., 1995. Anatomy of a semiarid coastal system: the Upper Carnian of Lombardy (Italy). Riv. Ital. Paleontol. Strat., 101, 17-36.

Gattolin, G., Breda, A., Preto, N., 2013. Demise of Late Triassic carbonate platforms triggered the onset of a tide-dominated depositional system in the dolomites, northern Italy. Sediment. Geol., 297, 38–49.

Gattolin, G., Preto, N., Breda, A., Franceschi, M., Isotton, M., Gianolla, P., 2015. Sequence Stratigraphy after the demise of a high-relief carbonate platform (Carnian of the Dolomites): sea-level and climate disentangled. Palaeogeogr. Palaeoclimatol. Palaeoecol., 423, 1-17.

Gerry, E., Honigstein, A., Rosenfeld, A., Hirsch, F., Eshet, Y., 1990. The Carnian salinity crisis: ostracods and palynomorphs as indicators of palaeoenvironment. In: Whatley, R., Maybury, C. (Eds.), Ostracoda and Global Events. Chapman and Hall, London, pp. 87-97.

Gianolla, P., De Zanche, V., Mietto, P., 1998a. Triassic sequence stratigraphy in the Southern Alps (northern Italy): definition of sequences and basin evolution. In: De Graciansky, P.C., Hardenbol, J., Jacquin, T., Vail, P.R. (Eds.), Mesozoic and Cenozoic Sequence Stratigraphy of European Basins. SEPM Special Publication, 60, 719-748.

Gianolla, P., Ragazzi, E., Roghi, G., 1998b. Upper Triassic amber from the dolomites (northern Italy). A paleoclimatic indicator? Riv. Ital. Paleontol. Stratigr., 104, 381-389.

Gianolla, P., De Zanche, V., Roghi, G., 2003. An upper Tuvalian (Triassic) platform–basin system in the Julian Alps: the start-up of the Dolomia Principale (Southern Alps, Italy). Facies, 49, 135-150.

Golonka, J., 2007. Late Triassic and early Jurassic palaeogeography of the world. Palaeogeogr. Palaeoclimatol. Palaeoecol. 244, 297-307.

Goñi, M., Ruttenberg, K., Eglinton, T., 1997. Sources and contribution of terrigenous organic carbon to surface sediments in the Gulf of Mexico. Nature, 389, 275-278.

Gou, Z., 1998. The bivalve faunas from the Upper Triassic Xujiahe Formation in the Sichuan Basin. Sedimentary Facies Palaeogeography, 18, 20–31. (In Chinese with English Abstract).

Greene, A. R., Scoates, J. S., Weis, D., Katvala, E. C., Israel, S., Nixon, G. T., 2010. The architecture of oceanic plateaus revealed by the volcanic stratigraphy of the accreted Wrangellia oceanic

plateau. Geosphere, 6, 47-73.

Gröcke, D.R., 2002. The carbon isotope composition of ancient CO_2 based on higher-plant organic matter. Philosophical Transactions of the Royal Society of London A: Mathematical, Physical and Engineering Sciences, 360, 633-658.

Grossman, E. L., Mii, H.-S., Zhang, C., Yancey, T. E., 1996. Chemical variation in Pennsylvanian brachiopod shells; diagenetic, taxonomic, microstructural, and seasonal effects. J. Sediment. Res., 66, 1011-1022.

Haas, J., Budai, T., Raucsik, B., 2012. Climatic controls on sedimentary environments in the Triassic of the Transdanubian Range (Western Hungary). Palaeogeogr. Palaeoclimatol. Palaeoecol., 353-355, 31-44.

Haas, J., Budai, T., Győri, O., Kele, S., 2014. Multiphase partial and selective dolomitization of Carnian reef limestone (Transdanubian Range, Hungary). Sedimentology, 61, 836-859.

Hao, W. C., Sun, Y. L., Jiang, D. Y., Yang, S. R., Wang, X. P., 2003. Cephalopods of the "Falang Formation" (Triassic) from Guanling and Zhenfeng Counties, Guizhou Province, China. Acta Geol. Sin., 77, 430-439.

Hasiuk, F. J., Kaczmarek, S. E., Fullmer, S. M., 2016. Diagenetic Origins of the Calcite Microcrystals That Host Microporosity in Limestone Reservoirs. J. Sediment. Res., 86, 1163-1178.

Hallock, P., Schlager, W., 1986. Nutrient excess and the demise of coral reefs and carbonate platforms. Palaios, 1, 389-398.

Hayes, J. M., Strauss, H., Kaufman, A. J., 1999. The abundance of ^{13}C in marine organic matter and isotopic fractionation in the global biogeochemical cycle of carbon during the past 800 Ma. Chem. Geol., 161, 103-125.

He, Y., 1980. Sketch of the Triassic foraminiferal biostratigraphy of northwestern Sichuan (Szechuan), China. Riv. Ital. Paleontol. Stratigr., 85, 1167-1174.

He, L., Li, M., Xiong, L., Ran, F., Liao, Z., 2011. Re-discussion on the sequence division schemes of Upper Triassic Formations in the Sichuan basin. Natural Gas Industry, 31, 28-33. (In Chinese with English Abstract).

Hesselbo, S. P., Robinson, S. A., Surlyk, F., Piasecki, S., 2002. Terrestrial and marine extinction at the Triassic-Jurassic boundary synchronized with major carbon-cycle perturbation: A link to initiation of massive volcanism? Geology, 30, 251-254.

Hönisch, B., Ridgwell, A., Schmidt, D. N., Thomas, E., Gibbs, S. J., Sluijs, A., Zeebe, R., Kump, L., Martindale, R. C., Greene, S. E., Kiessling, W., Ries, J., Zachos, J. C., Royer, D. L., Barker, S., Marchitto, T. M., Moyer, R., Pelejero, C., Ziveri, P., Foster, G. L., Williams, B., 2012. The geological record of ocean acidification. Science, 335, 1058–1063.

Hornung, T., Brandner, R., 2005. Biochronostratigraphy of the Rheingraben Turnover (Hallstatt

Facies Belt): local black shale events controlled by regional tectonics, climatic change and plate tectonics. Facies, 51, 460-479.

Hornung, T., Spatzenegger, A., Joachimski, M. M., 2007a. Multistratigraphy of condensed ammonoid beds of the Rappoltstein (Berchtesgaden, southern Germany): unravelling palaeo-environmental conditions on“Hallstatt deep swells” during the Reingraben event (late Lower Carnian). Facies, 53, 267-292.

Hornung, T., Krystyn, L., Brandner, R., 2007b. A Tethys-wide mid-Carnian (Upper Triassic) carbonate productivity crisis: Evidence for the Alpine Reingraben Event from Spiti (Indian Himalaya)? J. Asian. Earth. Sci., 30, 285-302.

Hornung, T., Brandner, R., Krystyn, L., Joachimski, M. M., Keim, L., 2007c. Multistratigraphic constraints on the NW Tethyan “Carnian Crisis”. New Mexico Mus. Nat. Hist. Sci. Bull., 4, 9-67.

Hornung, T., 2007. Multistratigraphy of the Draxllehen quarry near Berchtesgaden (Tuvalian-Lacian 2): implications for Hallstatt Limestone-sedimentation and palaeoclimate in the aftermath of the “Carnian Crisis”. Austr. J. Earth. Sci., 100, 82-99.

Hochuli, P. A., Frank, S. M., 2000. Palynology (dinoflagellate cysts, spore-pollen) and stratigraphy of the Lower Carnian Raibl Group in the Eastern Swiss Alps. Eclogae. Geol. Helv., 93, 429-443.

Huang, X. F., Mo, X. X., Yu, X. H., Li, X. W., Ding, Y., Wei, P., He, W. Y., 2013. Zircon U-Pb chronology, geochemistry of the Late Triassic acid volcanic rocks in Tanchang area, West Qinling and their geological significance. Acta. Petrol. Sin., 29, 3968-3980 (in Chinese with English abstract).

Irwin, H., Curtis, C., Coleman, M., 1977. Isotopic evidence for source of diagenetic carbonates formed during burial of organic-rich sediments. Nature, 269, 209-213. doi:10.1038/269209a0

Jadoul, F., Galli, M.T., Berra, F., Cirilli, S., Ronchi, P., Paganoni, A., 2004. The Late Triassic-Early Jurassic of the Lombardy Basin: Stratigraphy, Palaeogeography and Palaeontology. 32nd IGC Florence August 20–28 2004, Excursion Guide book, 68, 36 pp.

Jin, X., Ji, G. F., Shi, Z. Q., Wang, Y. Y., 2015. The sedimentary facies of Guanyinya Section in Hanwang, Mianzhu: implications for the environment evolution ahead of and after the Triassic Carnian Pluvial Event. Geological Science and Technology Information, 34, 1174-1182 (In Chinese with English abstract).

Jin, X., Shi, Z. Q., Rigo, M., Franceschi, M., Preto, N., 2018a. Carbonate platform crisis in the Carnian (Late Triassic) of Hanwang (Sichuan Basin, South China): insights from conodonts and stable isotope data. J. Asian. Earth. Sci., 164, 104-124.

Jin, X., McRoberts, A, C., Shi, Z. Q., Mietto, P., Rigo, M., Roghi, G., Manfrin, S., Franceschi, M.,

Preto, N., 2018b. The aftermath of the CPE and the Carnian/Norian transition in northwestern Sichuan Basin, South China. J. Geol. Soc. London, in press.

Keim, L., Schlager, W., 1999. Automicrite facies on steep slopes (Triassic, Dolomites, Italy). Facies, 41, 15-25.

Keim, L., Brandner, R., Krystyn, L., Mette, W., 2001. Termination of carbonate slope progradation: an example from the Carnian of the Dolomites, Northern Italy. Sediment. Geol, 143, 303–323.

Keim, L., Spötl, C., Brandner, R., 2006. The aftermath ofthe Carnian carbonate platform demise: a basinal perspective (Dolomites, Southern Alps). Sedimentology, 53, 361-386.

Kent, D. V., Olsen, P. E., Muttoni, G., 2017. Astrochronostratigraphic polarity time scale (APTS) for the Late Triassic and Early Jurassic from continental sediments and correlation with standard marine stages. Earth. Sci. Rev., 166, 153-180

Kenter, J. A. M., Harris, P. M., Della Porta, G., 2005. Steep microbial boundstone- dominated platform margins — examples and implications. Sediment. Geol., 178, 5-30.

Korte, C., Kozur, H., Joachimski, M., Strauss, H., Veizer, J. N., Schwark, L., 2004. Carbon, sulfur, oxygen and strontium isotope records, organic geochemistry and biostratigraphy across the Permian/Triassic boundary in Abadeh, Iran. Int. J. Earth. Sci. 93., 565-581.

Korte, C., Kozur, H. W., Veizer, J., 2005. $\delta^{13}C$ and $\delta^{18}O$ values of Triassic brachiopods and carbonate rocks as proxies for coeval seawater and palaeotemperature. Palaeogeogr. Palaeoclimatol. Palaeoecol, 226, 287–306.

Korte, C., Hesselbo, S. P., 2011. Shallow marine carbon and oxygen isotope and elemental records indicate icehouse-greenhouse cycles during the Early Jurassic. Paleoceanography, 26.

Korte, C., Thibault, N., Ullmann, C., Clémence, M. E., Mette, W., Olsen, T., Rizzi, M; Ruhl, M., 2017. Brachiopod biogeochemistry and isotope stratigraphy from the Rhaetian Eiberg section in Austria: potentials and limitations. Neues Jahrbuch für Geologie und Paläontologie – Abhandlungen, 284, 117-138.

Kozur, H., 2003. Integrated ammonoid, conodont and radiolarian zonation of the Triassic. Hallesches Jahrbuch der Geowissenschaften, 25, 49–79.

Kozur, H. W., Bachmann, G. H., 2010. The Middle Carnian Wet Intermezzo of the Stuttgart Formation (Schilfsandstein), Germanic Basin. Palaeogeogr. Palaeoclimatol. Palaeoecol., 290. 1-4, 107-119.

Krautter, M., Conway, K. W., Barrie, J. V., 2006. Recent Hexactinosidan Sponge Reefs (Silicate Mounds) Off British Columbia, Canada: Frame-Building Processes. J. Paleontology., 80, 38-48.

Krystyn, L., 1978. Eine neue Zonengliederung im alpin-mediterranen Unterkarn. Schriftenreihe der Erdwissenschaftlichen Kommissionen. Osterreichische Akademie der Wissenschaften, 4, 37-

75.

Krystyn, L., 1980. Triassic conodont localities of the Salzkammergut region (northern Calcareous Alps). In: Schonlaub HP (ed) Second European Conodont Symposium ECOS II: Guidebook and Abstracts. Abh- lung Geologisch Bundes, 35, 61-98.

Krystyn, Leopold., 1982. Obertriassische Ammonoideen aus dem zentralnepal-esischen Himalaya (Gebiet von Jomsom). Abhandlungen der Geologischen Bundesanstalt in Wien, 36, 1-63.

Lehrmann, D. J., Enos, P., Payne, J. L., Montgomery, P., Wei, J., Yu, Y., Xiao, J., Orchard, M., 2005. Permian and Triassic depositional history of the Yangtze platform and Great Bank of Guizhou in the Nanpanjiang Basin of Guizhou and Guangxi, south China. Albertiana, 33, 149-168.

Leinfelder, R. R., 2001. Jurassic reef ecosystems. In: Stanley Jr., G.D. (Ed.), The History and Sedimentology of Ancient Reef Systems. Kluwer Academic/Plenum Publishers, New York, pp. 251-302.

Levera, M., 2012. The halobiids from the Norian GSSP candidate section of Pizzo Mondello (Western Sicily, Italy): systematics and correlations. Riv. Ital. Paleontol. Stratigr., 18, 3-45.

Li, F., Yan, J., Burne, R. V., Chen, Z. Q., Algeo, T. J., Zhang, W., Tian L., Gan Y. L., Liu, K., Xie, S. C., 2017a. Paleo-seawater REE compositions and microbial signatures preserved in laminae of Lower Triassic ooids. Palaeogeogr. Palaeoclimatol. Palaeoecol., 486, 96-107.

Li, L. Q., Wang, Y. D., 2016. Late Triassic palynofloras in the Sichuan Basin, South China: Synthesis and perspective. Palaeoworld, 25, 212-238.

Li, L., Wang, Y., Liu, Z., Zhou, N., Wang, Y., 2016. Late Triassic palaeoclimate and palaeoecosystem variations inferred by palynological record in the northeastern Sichuan Basin, China. PalZ, 90, 327-348.

Li, L., Wang, Y., Vajda, V., Liu, Z., 2017b. Late Triassic ecosystem variations inferred by palynological records from Hechuan, southern Sichuan Basin, China. Geol. Mag., 1-18.

Li, M., Zhang, Y., Huang, C., Ogg, J., Hinnov, L., Wang, Y., Zou, Z., Li, L., 2017c. Astronomical tuning and magnetostratigraphy of the Upper Triassic Xujiahe Formation of South China and Newark Supergroup of North America: implications for the Late Triassic time scale. Earth. Planet. Sci. Lett., 475, 207-223.

Li, Y., Allen, P. A., Densmore, A. L., Qiang, X., 2003. Evolution of the Longmen Shan foreland basin (western Sichuan, China) during the Late Triassic Indosinian orogeny. Basin. Res., 15, 117-138.

Li, Y., Sun, D. C., Dong, S. L., Sun, W., Yang, R. J., Liu, S. G., Yan, Z. K., Yan, L., 2011a. Dynamic of drowning of the carbonate ramp and sponge build-up in the early stage (Carnian) of Longmen Shan foreland basin, Late Triassic, China. Acta. Petrol. Sin., 27, 3460-3470. (In Chinese with English Abstract).

Li. Y., Su, D. C., Dong, S. L., Yan, Z. K., He, P., Yan, L., 2011b. The recognition of the basal

unconformity in the Longmenshan foreland basin: Transition from passive cintinet margin to foreland basin. Acta. Petrol. Sin., 27, 2413-2422 (in Chinese with English abstract).

Li, Y., Yan, Z., Liu, S., Li, H., Cao, J., Su, D., Dong, S. L., Sun, W., Yang, R. J., Yan, L., 2014. Migration of the carbonate ramp and sponge buildup driven by the orogenic wedge advance in the early stage (Carnian) of the Longmen Shan foreland basin, China. Tectonophysics, 619, 179-193.

Li, Z. Q., Ying, D. L., Li, H. K., Yang, G., Zeng, Q., Guo, X. Y., Chen, X., 2011c. Evolution of the western Sichuan basin and its superimposed characteristics, China. Acta. Petrol. Sin., 27, 2362-2370. (In Chinese with English Abstract).

Liu, S. G., Tong, Z. G., Luo, Z. L., Dai, S. L., Pang, J. L., Zhang, G. Z., He, L., 1995. The formation and evolution of Late Triassic foreland basin in West Sichuan. Natural Gas Industry, 15, 11-15. (In Chinese with English Abstract).

Liu, S. G., Yang, R. J., Wu, X. C., Sun, W., Chen, Y., 2009. The Late Triassic transition from marine carbonate rock to clastics in the western Sichuan Basin. Oil and Gas Geology, 30, 556-566 (In Chinese with English Abstract).

López-Gómez, J., Escudero-Mozo, M. J., Martín-Chivelet, J., Arche, A., Lago, M., Galé, C., 2017. Western Tethys continental-marine responses to the Carnian Humid Episode: palaeoclimatic and palaeogeographic implications. Glob. Planet. Chang., 148, 79-95.

Lucas S. G. 2018. The Late Triassic Timescale. In: Tanner, L. H. (ed.). The Late Triassic World: Earth in a Time of Transition. Springer International Publishing, Cham, 1-25.

Lucas, S. G., Tanner, L. H., 2018. Record of the Carnian wet episode in strata of the Chinle Group, western USA. J. Geol. Soc. London., in press.

Lukeneder, S., Lukeneder, A., Harzhauser, M., İslamoğlu, Y., Krystyn, L., Lein, R., 2012. A delayed carbonate factory breakdown during the Tethyan-wide Carnian Pluvial Episode along the Cimmerian terranes (Taurus, Turkey). Facies, 58, 279-296.

Lukeneder, S., Lukeneder, A., 2013. A new ammonoid fauna from the Carnian (Upper Triassic) Kasimlar Formation of the Taurus Mountains (Anatolia, Turkey). Palaeontology, 57, 357–396.

Luo, Z., Long, X., 1992. The uplifting of the Longmenshan orogenic zone and the subsidence of the west Sichuan foreland basin. Acta. Geologica. Sichuan, 12, 1-17. (In Chinese with English Abstract).

Ma, Q. H., Chen, J. H., Lan, X., Gu. Z. W., Chen, C. C., Lin, M. J., 1976. Triassic Lamellibranchia. In: Mesozoic Lamellibranchia of Yunnan, Mesozoic Fossils of Yunnan, Volume A, Nanjing Institute of Geology and Palaeontology, Academia Sinica (eds.), Science Press, Beijing. Pp 161-386 (in Chinese).

Ma, Y., Chen, H., Wang, G., 2009. Atlas of Tectonics and Sequence Lithofacies Palaeogeography in

South China from Sinian to Neogene. Science Press, Beijing. Pp 1-301 (in Chinese).

Marangon, A., Gattolin, G., Della Porta, G., Preto, N., 2011. The Latemar: a flat topped, steep fronted platform dominated by microbialites and synsedimentary cements. Sediment. Geol., 240, 97-114.

Marino, M., Santantonio, M., 2010. Understanding the geological record of carbonate platform drowning across rifted Tethyan margins: examples from the Lower Jurassic of the Apennines and Sicily (Italy). Sediment. Geol., 225, 116-137.

Marshall, J. D., 1992. Climatic and oceanographic isotopic signals from the carbonate rock record and their preservation. Geol. Mag., 129, 143-160.

McArthur, J. M., Tyson, R. V., Thomson, J., Mattey, D., 1992. Early diagenesis of marine organic matter: Alteration of the carbon isotopic composition. Mar. Geol., 105, 51-61.

Martínez-Pérez, C., Cascales-Miñana, B., Plasencia, P., Botella, H. 2015. Exploring the major depletions of conodont diversity during the Triassic. Hist. Biol., 27, 503-507.

Martini, R., Zaninetti, L., Lathuilliere, B., Cirilli, S., Cornée, J. J., Villeneuve, M., 2004. Upper Triassic carbonate deposits of Seram (Indonesia): palaeogeographic and geodynamic implications. Palaeogeogr. Palaeoclimatol. Palaeoecol., 206, 75-102.

Matthews, R. K., 1968. Carbonate diagenesis: Equilibration of sedimentary mineralogy to the subaerial environment: Coral Cap of Barbados,West Indies. J. Sediment. Res., 38, 1110-1119.

Mazza, M., Furin, S., Spötl, C., Rigo, M., 2010. Generic turnovers of Carnian/Norian conodonts: Climatic control or competition? Palaeogeogr. Palaeoclimatol. Palaeoecol., 290, 120-137.

Mazza, M; Rigo, M., Nicora, A., 2011. A new Metapolygnathus platform conodont species and its implications for Upper Carnian global correlations. Acta. Palaeontol. Pol., 56, 121-131.

Mazza, M., Rigo, M., Gullo M., 2012. Taxonomy and stratigraphic record of the Upper Triassic conodonts of the Pizzo Mondello section (Western Sicily, Italy), GSSP candidate for the base of the Norian. Riv. Ital. Paleontol. Stratigr., 118, 85-130.

Mazza, M., Nicora, A., Rigo, M., 2018. *Metapolygnathus parvus* Kozur, 1972 (Conodonta): a potential primary marker for the Norian GSSP (Upper Triassic). B. Soc. Paleontol. Ital., 57, 82.

McRoberts, C. A., 2007. The halobiid bivalve succession across a potential Carnian/Norian GSSP at Black Bear Ridge, Williston Lake, northeast British Columbia, Canada. Albertiana 36, 142-145.

McRoberts, C. A., 2010. Biochronology of Triassic bivalves, pp. 201-219. In: Lucas S.G. (ed.) The Triassic Time Scale. Geol. Soc. Lond., Spec. Publ., 334.

McRoberts, C. A., 2011. Late Triassic Bivalvia (chiefly Halobiidae and Monotidae) from the Pardonet Formation, Williston Lake area, northeast British Columbia, Canada. J. Paleontol., 85, 615-666.

Mei, M., Liu, S., 2017. The Late Triassic Sequence-Stratigraphic Framework of the Upper Yangtze Region, South China. Acta. Geol. Sin (English Edition), 91, 51-75.

Meng, Q. R., Wang, E., Hu, J. M., 2005. Mesozoic sedimentary evolution of the northwest Sichuan basin: Implication for continued clockwise rotation of the South China block. Geol. Soc. Am. Bull., 117, 396-410.

Merkel, C., Deuschle, J., Griesshaber, E., Enders, S., Steinhauser, E., Hochleitner, R., Brand. U., Schmahl, W. W., 2009. Mechanical properties of modern calcite- (Mergerlia truncata) and phosphate-shelled brachiopods (Discradisca stella and Lingula anatina) determined by nanoindentation. J. Struct. Biol., 168, 396-408.

Mietto, P., Manfrin, S., Preto, S., and Gianolla, P., 2008. Selected ammonoid fauna from Prati di Stuores/Stuores Wiesen and related sections across the Ladinian–Carnian boundary (Southern Alps, Italy). Riv. Ital. Paleontol. Stratigr., 114. 377–429.

Mietto, P., Manfrin, S., Preto, N., Rigo, M., Roghi, G., Furin, S., Gianolla, P., Posenato, R., Muttoni, G., Nicora, A., Buratti, N., Cirilli, S., Spötl, C., Ramezani, J., Bowring, S.A., 2012. The global boundary stratotype section and point (GSSP) of the Carnian stage (Late Triassic) at Prati di Stuores/Stuores Wiesen section (Southern Alps, NE Italy). Episodes-Newsmagazine of the International Union of Geological Sciences, 35, 414.

Miller, C.N., 1982. Current status of Paleozoic and Mesozoic conifers. Rev. Palaeobot. Palynol., 37, 99–114.

Miller, C. S., Peterse, F., da Silva, A. C., Baranyi, V., Reichart, G. J., Kürschner, W. M., 2017. Astronomical age constraints and extinction mechanisms of the Late Triassic Carnian crisis. Sci. Rep., 7, 2557.

Minzoni, M., Lehrmann, D. J., Dezoeten, E., Enos, P., Montgomery, P., Berry, A., Qin, Y., Meiyi, Y., Ellwood, B. B., Payne, J. L., 2015. Drowning of the Triassic Yangtze Platform, South China, by Tectonic subsidence into toxic deep waters of an anoxic basin. J. Sediment. Res., 85, 419-444.

Mojsisovics von Mojsvár, E., 1869. Ueber die Gliederung der oberen Triasbildungen der östlichen Alpen. Jahrb Geolog Reichsan, 19, 91-150.

Mojsisovics von Mojsvár E., Waagen, W. H., Diener, C., 1895. Entwurf einer Gliederung der pelagischen Sediments des Trias-Systems. Akad Wissensch Wien Mathemat-naturwiss Klasse Sitzungsber, 104, 1279-1302.

Mueller, S., Hounslow, M. W., Kürschner, W. M., 2015. Integrated stratigraphy and palaeoclimate history of the Carnian Pluvial Event in the Boreal realm; new data from the Upper Triassic Kapp Toscana Group in central Spitsbergen (Norway). J. Geol. Soc. London., 173, 186-202.

Mueller, S., Krystyn, L., Kürschner, W. M., 2016. Climate variability during the Carnian Pluvial Phase — A quantitative palynological study of the Carnian sedimentary succession at Lunz am See, Northern Calcareous Alps, Austria. Palaeogeogr. Palaeoclimatol. Palaeoecol., 441, 198-

211.

Mutti, M., Weissert, H., 1995. Triassic Monsoonal Climate and its signature in Ladinian– Carnian carbonate platforms (Southern Alps, Italy). J. Sediment. Res., B65, 357-367.

Mutti, M., Bernoulli, D., Stille, P., 1997. Temperate carbonate platform drowning linked to Miocene oceanographic events: Maiella platform margin, Italy. Terra Nova, 9, 122-125.

Mutti, M., Bernoulli, D., 2003. Early marine lithification and hardground development on a Miocene Ramp (Maiella, Italy): key surfaces to track changes in trophic resources in nontropical carbonate settings. J. Sediment. Res., 73, 296-308.

Muttoni, G., Kent, D. V., Di Stefano, P., Gullo, M., Nicora, A., Tait, J., Lowrie, W., 2001. Magnetostratigraphy and biostratigraphy of the Carnian/Norian boundary interval from the Pizzo Mondello section (Sicani Mountains, Sicily). Palaeogeogr. Palaeoclimatol. Palaeoecol., 166, 383-399.

Muttoni, G., Kent, D. V., Olsen, P. E., Di Stefano, P., Lowrie, W., Bernasconi, S. M., Hernández, F. M., 2004. Tethyan magnetostratigraphy from Pizzo Mondello (Sicily) and correlation to the Late Triassic Newark astrochronological polarity time scale. Geol. Soc. Am. Bull., 116, 1043-1058.

Nagy, Z. R., 1999. Platform-basin transition and depositional models for the Upper Triassic (Carnian) Sa´ndorhegy Limestone, Balaton Highland, Hungary. Acta. Geol. Hung., 42, 267-299.

Nakada, R., Ogawa, K., Suzuki, N., Takahashi, S., Takahashi, Y., 2014. Late Triassic compositional changes of aeolian dusts in the pelagic Panthalassa: response to the continental climatic change. Palaeogeogr. Palaeoclimatol. Palaeoecol., 393, 61-75.

Nelson, C.S., James, N.P., 2000. Marine cements in mid-tertiary cool-water shelf limestones of New Zealand and southern Australia. Sedimentology, 47, 609-629.

Nicora, A., Balini, M., Bellanca, A., Bertinelli, A., Bowring, S. A., Di Stefano, P., Dumitrica, P., Guaiumi, C., Gullo, M., Hungerbuehler, A., Levera, M., Mazza, M., McRoberts, C. A., Muttoni, G., Preto, N., Rigo, M., 2007. The Carnian/Norian boundary interval at Pizzo Mondello (Sicani Mountains, Sicily) and its bearing for the defnition of the GSSP of the Norian Stage. Albertiana 36, 102-129.

Nordt, L., Tubbs, J., Dworkin, S., 2016. Stable carbon isotope record of terrestrial organic materials for the last 450 Ma yr. Earth. Sci. Rev., 159, 103-117.

Ogg, J. G., 2015. The mysterious mid-Carnian “wet intermezzo” global event. J. Earth. Sci., 26, 181-191.

Olsen, P. E., Kent, D. V., 1996. Milankovitch climate forcing in the tropics of Pangea during the Late Triassic. Palaeogeogr. Palaeoclimatol. Palaeoecol., 122, 1-26.

Onoue, T., Zonneveld, J. P., Orchard, M. J., Yamashita, M., Yamashita, K., Sato, H., Kusaka, S.,

2016. Paleoenvironmental changes across the Carnian/Norian boundary in the Black Bear Ridge section, British Columbia, Canada. Palaeogeogr. Palaeoclimatol. Palaeoecol., 441, 721–733.

Orchard, M. J., McRoberts, C. A., Tozer, E. T., Johns, M. J., Sandy, M. R., Shaner, J. S., 2001. An intercalibrated biostratigraphy of the Upper Triassic of Black Bear Ridge, Williston Lake, northeast British Columbia. Geological Survey of Canada, Current Research 2001-A 6, p. 21

Orchard, M., 2007. A proposed Carnian-Norian boundary GSSP at Black Bear Ridge, northeast British Columbia, and a new conodont framework for the boundary interval. Albertiana, 36, 130-141.

Orchard, M.J., 2010. Triassic conodonts and their role in stage boundary definition. Geol. Soc. Lond., Spec. Publ., 334, 139-161.

Orchard, M.J., 2014. Conodonts from the Carnian–Norian boundary (Upper Triassic) of Black Bear Ridge, Northeasern British Columbia, Canada. N. M. Mus. Nat. Hist. Sci. Bull. 64, 1-139.

Panuska, B. C., 1990. An overlooked, world class Triassic flood basalt event. Geological Society of America, Abstracts with Programs, 22, 168.

Parrish, J. T., 1993. Climate of the supercontinent Pangea. J. Geol., 101, 215-233.

Pérez Huerta, A., Cusack, M., McDonald, S., Marone, F., Stampanoni, M., MacKay, S., 2009. Brachiopod punctae: a complexity in shell biomineralisation. J. Struct. Biol., 167, 62-67.

Peybernes, C., Chablais, J., Martini, R., 2015. Upper Triassic (Ladinian?-Carnian) reef biota from the Sambosan Accretionary Complex, Shikoku, Japan. Facies, 61, 20.

Pratt, B. R., 1995. The origin, biota and evolution of deep-water mud-mounds. Carbonate mud-mounds, their origin and evolution. Int. Assoc. Sedimentologists., Spec. Publ., 23, 49-123.

Preto, N., Hinnov, L. A., 2003. Unraveling the origin of carbonate platform cyclothems in the Upper Triassic Durrenstein Formation (Dolomites, Italy). J. Sediment. Res., 73, 774-789.

Preto, N., Spötl, C., Mietto, P., Gianolla, P., Riva, A., Manfrin, S., 2005. Aragonite dissolution, sedimentation rates and carbon isotopes in deep-water hemipelagites (Livinallongo Formation, Middle Triassic, northern Italy). Sediment. Geol., 181, 17-194.

Preto, N., Kustatscher, E., Wignall, P. B., 2010. Triassic climates—state of the art and perspectives. Palaeogeogr. Palaeoclimatol. Palaeoecol., 290, 1-10.

Preto, N., Franceschi, M., Gattolin, G., Massironi, M., Riva, A., Gramigna, P., Bertoldi, L., Nardon, S., 2011. The Latemar: a Middle Triassic polygonal fault-block platform controlled by synsedimentary tectonics. Sediment. Geol., 234, 1–18.

Preto, N., 2012. Petrology of carbonate beds from the stratotype of the Carnian (Stuores Wiesen section, Dolomites, Italy): the contribution of platform-derived microbialites. Geo. Alp., 9, 12-29.

Preto, N., Willems, H., Guaiumi, C., Westphal, H., 2013. Onset of significant pelagic carbonate accumulation after the Carnian Pluvial Event (CPE) in the western Tethys. Facies, 59, 891-914.

Preto, N., Breda, A., Dal Corso, J., Franceschi, M., Rocca, F., Spada, C., Roghi, G., 2017. The Loppio Oolitic Limestone (Early Jurassic, Southern Alps): a prograding oolitic body with high original porosity originated by a carbonate platform crisis and recovery. Mar. petrol. Gaol., 79, 394–411.

Prochnow, S. J., Nordt, L. C., Atchley, S. C., Hudec, M. R., 2006. Multi-proxy paleosol evidence for Middle and Late Triassic climate trends in eastern Utah. Palaeogeogr. Palaeoclimatol. Palaeoecol., 232, 53-72.

Ramovš. A., 1987, Ausbildung der Karn-Stufe im östlichen Teil der nördlichen Julischen Alpen. Geologija, 30, 67-82 (in Slovenian with German summary).

Raup, D. M., Sepkoski, J. J., 1982. Mass extinctions in the marine fossil record. Science, 215, 1501-1503.

Renner, S. S., 2009. Gymnosperms. In: Hedges, S.B., Kumar, S. (Eds.), The Time tree of Life Book. Oxford University Press, New York, pp. 157–160

Reolid, M., Márquez-Aliaga, A., Belinchón, M., García-Forner, A., Villena, J., Martínez-Pérez, C., 2018. Ichnological evidence of semi-aquatic locomotion in early turtles from eastern Iberia during the Carnian Humid Episode (Late Triassic). Palaeogeogr. Palaeoclimatol. Palaeoecol., 490, 450-461.

Riding, R., 2000. Microbial carbonates: the geological record of calcified bacterial-algal mats and biofilms. Sedimentology, 47, 179-214.

Riechelmann, S., Mavromatis, V., Buhl, D., Dietzel, M., Eisenhauer, A., Immenhauser, A., 2016. Impact of diagenetic alteration on brachiopod shell magnesium isotope (δ^{26} Mg) signatures: Experimental versus field data. Chem. Geol., 440, 191-206.

Rigo, M., Preto, N., Roghi, G., Tateo, F., Mietto, P., 2007. A rise in the Carbonate Compensation Depth of western Tethys in the Carnian (Late Triassic): Deep-water evidence for the Carnian Pluvial Event. Palaeogeogr. Palaeoclimatol. Palaeoecol., 246, 188-205.

Rigo, M., Joachimski, M. M., 2010. Palaeoecology of Late Triassic conodonts: constraints from oxygen isotopes in biogenic apatite. Acta. Palaeontol. Pol., 55, 471-478.

Rigo, M., Preto, N., Franceschi, M., Guaiumi, C., 2012. Stratigraphy of the Carnian-Norian Calcari con Selce Formation in the Lagonegro Basin, Southern Apennines. Riv. Ital. Paleontol. Stratigr., 118, 143- 154.

Rigo, M., Mazza, M., Karádi, V., Nicora, A., 2018. New Upper Triassic Conodont Biozonation of the Tethyan Realm. In L.H. Tanner (Ed.), The Late Triassic World: Earth in a Time of Transition, Springer, Berlin, pp. 189-235.

Roghi, G., 2004. Palynological investigations in the Carnian of the Cave del Prdil area (Julian Alps, NE Italy). Rev. Palaeobot. Palynol., 132, 1-35.

Roghi, G., Ragazzi, E., Gianolla, P., 2006. Triassic amber of the Southern Alps (Italy), Palaios, 21, 143-154.

Roghi, G., Gianolla, P., Minarelli, L., Pilati, C., Preto, N., 2010. Palynological correlation of Carnian humid pulses throughout western Tethys. Palaeogeogr. Palaeoclimatol. Palaeoecol., 290, 89-106.

Rostási, A., Rausik, B., Varga, A., 2011. Paleoenvironmental controls on the clay mineralogy of Carnian sections from the Transdanubian Range (Hungary). Palaeogeogr. Palaeoclimatol. Palaeoecol., 300, 101-112.

Ruffell, A., Simms, M. J., Wignall, P. B., 2016. The Carnian Humid Episode of the late Triassic: a review. Geol. Mag., 153, 271-284.

Schlager, W., Schöllnberger, W., 1974. Das Prinzip straigraphischer Wenden in der Schichtfolge del Nördlichen Kalkalpen. Mitt. Geol. Ges., 66-67, 165-193.

Schlager, W., 1981. The paradox of drowned reefs and carbonate platforms. Geol. Soc. Am. Bull., 92, 197-211.

Schoene, B., Guex, J., Bartolini, A., Schaltegger, U., Blackburn, T. J., 2010. Correlating the end-Triassic mass extinction and flood basalt volcanism at the 100 ka level. Geology, 38, 387-390.

Schubert, J. K., Bottjer, D. J., 1992. Early Triassic stromatolites as post-mass extinction disaster forms. Geology, 20, 883-886.

Scotese, C. R., 2014. Atlas of Middle & Late Permian and Triassic Paleogeographic Maps, maps 43 - 48 from Volume 3 of the PALEOMAP Atlas for ArcGIS (Jurassic and Triassic) and maps 49 – 52 from Volume 4 of the PALEOMAP PaleoAtlas for ArcGIS (Late Paleozoic), Mollweide Projection, PALEOMAP Project, Evanston, IL.

Sellwood, B. W., Beckett, D., 1991. Ooid microfabrics: the origin and distribution of high intra-ooid porosity; Mid-Jurassic reservoirs, S. England. Sediment. Geol., 71, 189-193.

Senowbari-Daryan, B., 2013. Tubiphytes Maslov, 1956 and description of similar organisms from Triassic reefs of the Tethys. Facies, 59, 75–112.

Seyfullah, L. J., Roghi, G., Dal Corso, J., Schmidt, A. R., 2018. The Carnian Pluvial Episode and the first global appearance of amber. J. Geol. Soc. Lond., in press.

Shi, Z. Q, Ou, L., Luo, F., Li, Y., Qian, L., 2009. Black shale event during the Late Triassic Carnian Age: implications of sedimentary and palaeontological records in Longmen Mountains region. J. Palaeogeogr, 11, 375-383. (In Chinese with English Abstract).

Shi, Z. Q, Preto, N., Jiang, H. S, Krystyn, L., Zhang, Y., Ogg, J. G., Jin, X., Yuan, J.L., Yang, X. K., Du, Y. X., 2017. Demise of Late Triassic sponge mounds along the northwestern margin of the

Yangtze Block, South China: Related to the Carnian Pluvial Phase? Palaeogeogr. Palaeoclimatol. Palaeoecol., 474, 247-263.

Shi, Z. Q., Jin. X., Preto. N., Rigo, M., Du, Y. X., Han, L., 2018. The Carnian Pluvial Episode at Ma'antang, Jiangyou in Upper Yangtze Block, Southwestern China. J. Geol. Soc. Lond, in press.

Shi, Z. S., Wang, Z. H., Hao, C. G., Guo, C. M., Mo, W. L., 2015. Sedimentary facies of the Upper Triassic Ma'antang Formation in Sichuan Basin. J. Palaeogeogr., 17, 772-786. (In Chinese with English Abstract).

Silberling, N. J., Tozer, E. T., 1968. Biostratigraphic classification of the marine Triassic in North America. Geological Society of America Special Paper 110, 1–63.

Simms, M. J., Ruffell, A. H., 1989. Synchroneity of climatic change and extinctions in the Late Triassic. Geology, 17, 265.

Simms, M. J., Ruffell, A. H., 1990. Climatic and biotic change in the late Triassic. J. Geol. Soc. Lond., 147, 321-327.

Simms, M. J., Ruffel, A. H., Johnson, L. A., 1995. Biotic and climatic changes in the Carnian (Triassic) of Europe and adjacent areas. In: Fraser, N.C., Sues, H.D. (Eds.), In the Shadow of the Dinosaurs: Early Mesozoic Tetrapods. Cambridge University Press, pp. 352-365.

Simms, M. J., Ruffell, A. H., 2018. The Carnian Pluvial Episode: From discovery, through obscurity, to acceptance. J. Geol. Soc. Lond., in press.

Soua, M., 2014. Early Carnian anoxic event as recorded in the southern Tethyan margin, Tunisia: an overview. Int. Geol. Rev., 56, 15, 1884-1905.

Stampfli, G. M., Hochard, C., Vérard, C., Wilhem, C., vonRaumer, J., 2013. The formation of Pangea. Tectonophysics, 593, 1–19

Stanley Jr, G. D., 2003. The evolution of modern corals and their early history. Earth. Sci. Rev., 60, 195-225.

Stefani, M., Furin, S., Gianolla, P., 2010. The changing climate framework and depositional dynamics of Triassic carbonate platforms from the Dolomites. Palaeogeogr. Palaeoclimatol. Palaeoecol., 290, 43-57.

Stenzel, S., James, N., 1995. Shallow-Water Stromatactis Mud-Mounds on a Middle Ordovician Foreland Basin Platform, Western Newfoundland. Carbonate Mud-Mounds: Their Origin and Evolution, 125-149.

Sun, Y. D., Wignall, P. B., Joachimski, M. M., Bond, D. P. G., Grasby, S. E., Lai, X. L., Wang. L. N., Zhang, Z. T., Sun, S., 2016. Climate warming, euxinia and carbon isotope perturbations during the Carnian (Triassic) Crisis in South China. Earth. Planet. Sc. Lett., 444, 88-100.

Sun, Y., Richoz, S., Krystyn, L., Zhang, Z., Joachimski, M., 2018. Perturbations in carbon cycle during the Carian Humid Episode: Carbonate carbon isotope records from southwestern China

and northern Oman. J. Geol. Soc. Lond, in press.

Swart, P. K., 2015. The geochemistry of carbonate diagenesis: The past, present and future. Sedimentology, 62, 1233-1304.

Sýkora, M., Siblı´k, M., Sotak, J., 2011. Siliciclastics in the Upper Triassic dolomite formations of the Krizna unit (Mala Fatra mountains, western Carpathians): constraints for the Carnian Pluvial Event in the Fatric basin. Geol. Carpath, 62,121-138.

Tozer, E. T., 1994. Canadian Triassic Ammonoid Faunas. Geological Survey of Canada Bulletin, 467, 1-663.

Trotter, J. A., Williams, I. S., Nicora, A., Mazza, M., Rigo, M., 2015. Long-term cycles of Triassic climate change: a new δ18Orecord from conodont apatite. Earth. Planet. Sci. Lett., 415, 165–174.

Ullmann, C. V., Korte, C., 2015. Diagenetic alteration in low-Mg calcite from macrofossils: a review. Geol. Q., 59, 3-20.

Ulrichs, M., 1994. Trachyceras laube 1869 (Ammonoidea) aus dem Unterkarn (Obertrias) der Dolomiten (Italien). Stuttgarter Beitrage zur Naturkunde Serie B (Geologie und Palaeontologie), 217, 1–55.

Veizer, J., Fritz, P., Jones, B., 1986. Geochemistry of brachiopods: Oxygen and carbon isotopic records of Paleozoic oceans. Geochim. Cosmochim. Ac., 50, 1679-1696.

Veizer, J., Ala, D., Azmy, K., Bruckschen, P., Buhl, D., Bruhn, F., Carden, G. A. F., Diener, A., Ebneth, S., Godderis, Yves., Jasper, T., Korte, C., Pawellek, F., Podlaha, O. G., Strauss, H., 1999. $^{87}Sr/^{86}Sr$, $\delta^{13}C$ and $\delta^{18}O$ evolution of Phanerozoic seawater. Chem. Geo., 161, 59-88.

Visscher, H., Van Houte, M., Brugman, W. A., Poort, R. J., 1994. Rejection of a Carnian (late Triassic) “pluvial event” in Europe. Rev. Palaeobot. Palynol., 83, 217-226.

Voigt, S., Wilmsen, M., Mortimore, R., Voigt, T., 2003. Cenomanian palaeotemperatures derived from the oxygen isotopic composition of brachiopods and belemnites: evaluation of Cretaceous palaeotemperature proxies. Int. J. Earth. Sci., 92, 285-299.

Wadleigh, M. A., Veizer, J., 1992. $^{18}O^{16}O$ and $^{13}C^{12}C$ in lower Paleozoic articulate brachiopods: Implications for the isotopic composition of seawater. Geochim. Cosmochim. Ac., 56, 431-443.

Wang, Q., Wu, X., Yang, X., 2012. Clay and shaly claystones in the Upper Triassic Siliceous sponge-microbe reef mounds and oolitic bank complex in NW Sichuan, China. Carbonate. Evaporite., 27, 19-32.

Wang, Q., Zhang, Y., Wu, X., 2015. Triassic (Carnian) hexactinellid-thrombolite reef mounds and oolitic bank complex in NW Sichuan, China. Carbonate. Evaporite., 30, 187-205.

Wang, X., Bachmann, G., Hagdorn, H., Sander, M., Cuny, G., Xiaohong, C., Chuanshang, W., Lide, C., Long, C., Fansong, M., Guanghong, X., 2008. The Late Triassic black shales of the Guanling

area, Guizhou province, south-west China: a unique marine reptile and pelagic crinoid fossil lagerstätte. Palaeontology, 51, 27–61.

Wang, Y. S., 1992. The earlier late Triassic ammonties from Longmen Mountains. J. Chengdu. Colleg. Geol, 19, 28-35. (In Chinese with English Abstract).

Wang, Z. H., Dai, J. Y., 1981. Triassic conodonts from the Jiangyou-Beichuan area, Sichuan province. Acta Palaeontologica Sinica, 20, 138-152 (In Chinese with English Abstract).

Wang, Z. W., Wang, J., Fu, X. G., Zhan, W. Z., Yu, F., Feng, X. L., Song, C. Y., Chen, W. B., Zeng, S. Q., 2017. Organic material accumulation of Carnian mudstones in the North Qiangtang Depression, eastern Tethys: controlled by the paleoclimate, paleoenvironment, and provenance. Mar. Pet. Geol., 88, 440-457.

Webb, G. E., 1996. Was Phanerozoic reef history controlled by the distribution of non-enzymatically secreted reef carbonates (microbial carbonate and biologically induced cement)? Sedimentology, 43, 947-971.

Weissert, H., 1989. C-Isotope stratigraphy, a monitor of paleoenvironmental change: A case study from the early cretaceous. Surv. Geophys., 10, 1-61.

Weissert, H., Lini, A., Föllmi, K. B., Kuhn, O.,1998. Correlation of Early Cretaceous carbon isotope stratigraphy and platform drowning events: a possible link? Palaeogeogr. Palaeoclimatol. Palaeoecol., 137, 189-203.

Wendt, J., Wu, X., Reinhardt, J., 1989. Deep-water hexactinellid sponge mounds from the Upper Triassic of northern Sichuan (China). Palaeogeogr. Palaeoclimatol. Palaeoecol., 76, 17-29.

Wendt, J., Belka, Z., Kaufmann, B., Kostrewa, R., Hayer, J., 1997. The world's most spectacular carbonate mud mounds (Middle Devonian, Algerian Sahara). J. Sediment. Res., 67, 424-436.

Wendt, J., 2001. Upper Triassic (Carnian) mud mounds from northern Sichuan (China). Acta. Geol. Pol., 51, 1-13.

Whalen, M. T., Day, J., Eberli, G. P., and Homewood, P.W., 2002, Microbial carbonates as indicators of environmental change and biotic crises in carbonate systems: Examples from the late Devonian, Alberta basin, Canada: Palaeogeogr. Palaeoclimatol. Palaeoecol., 181, 127-151.

Whiteside, J.H., Olsen, P.E., Eglinton, T., Brookfield, M.E., Sambrotto, R.N., 2010. Compound-specific carbon isotopes from Earth’s largest flood basalt eruptions directly linked to the end-Triassic mass extinction. Proc. Natl. Acad. Sci. U S A., 107, 6721-6725.

Williford, K. H., Orchard, M. J., Zonneveld, J. P., McRoberts, C., Beatty, T. W., 2007. A record of stable organic carbon isotopes from the Carnian–Norian boundary section at Black Bear Ridge, Williston Lake, British Columbia, Canada. Albertiana, 36, 146-148.

Wu, X., 1984. Paleoecological characteristics of Late Triassic sponge patch reefs in northwestern Sichuan. China. J. Chengdu. Colleg. Geol., 43-54. (In Chinese with English Abstract).

Wu, X., 1989. Carnian (upper triassic) sponge mounds of the Northwestern Sichuan Basin, China: Stratigraphy, facies and paleoecology. Facies, 21, 171-187.

Wu, X., 2009. Sedimentary facies analysis of the Late Triassic Carnian siliceous sponge reef-oolitic bank complex in northwestern Sichuan province. J. Palaeogeogr, 11, 125-142. (In Chinese with English Abstract).

Xu, G. H., Niu, Z. J., Chen, H. M., 2003. Triassic cephalopods from the Zhuganpo and Xiaowa Formations in Guanling, Guizhou, with a discussion on the age of the Guanling biota. Reg. Geol. China, 22, 254-265 (In Chinese with English Abstract).

Xu, G., Hannah, J. L., Stein, H. J., Mørk, A., Vigran, J. O., Bingen, B., Schutt, D. L., Lundschien, B. A., 2014. Cause of Upper Triassic climate crisis revealed by Re-Os geochemistry of Boreal black shales. Palaeogeogr. Palaeoclimatol. Palaeoecol., 395, 222-232.

Yang, R. J., Liu, S. G., Wu, X. C., Zhao, X. F., Peng, J. S., Sun, W., 2008. Distribution characteristics and controlling factors of Upper Triassic Ma'antang Formation in the front of Longmen Mountians, Sichuan, China. Journal of Chengdu University of Technology (Science & Technology Edition), 38, 455-462 (In Chinese with English abstract).

Yang, R., Liu, S., Wu, X., 2010. Distribution and formation mechanism of lime mudstone in Upper Triassic in northwestern Sichuan, China. Carbonate. Evaporite., 25, 275-281.

Zeng, Y. F., Li, Y., 1995. The formation and evolution of Longmen Mountains foreland basin. Journal of Mineralogy and Petrology, 15, 40-49. (in Chinese with English Abstract).

Zhang, B., Wang, Z.J., Shi, Z.Q., Cheng, M., Duan, X., Jin, X., Cui, L., 2013. Discovery and geological significance of unconformity surface between Upper Triassic Ma'antang formation and Xiaotangzi formation in Hanwang of Mianzhu in Northwest Sichuan, China. J. Chengdu. Univ. Tech. (Science and Technology Edition) 40, 80–88 (In Chinese with English abstract).

Zhang, G., Meng, Q., Yu, Z., Sun, Y., Zhou, D., Guo, A., 1996. Orogenesis and dynamics of the Qinling orogen. Science in China Series D-Earth Sciences, 39, 225-234. (In Chinese with English Abstract).

Zhang, Y., Li, M. S., Ogg, J. G., Montgomery, P., Huang, C., Chen, Z. Q., Shi, Z. Q., Enos, P., Lehrmann, D. J., 2015. Cycle-calibrated magnetostratigraphy of middle Carnian from south China: implications for Late Triassic time scale and termination of the Yangtze platform. Palaeogeogr. Palaeoclimatol. Palaeoecol., 436, 135-166.

Zhang, Z. M., Chen, C. Z., Wen, S. X., 1985. Fossil lamellibranchs from Eastern Xizang, Western Sichuan and Western Yunnan. In: Stratigraphy and Palaeontology in Western Sichuan Western Xizang, China, Part 3, Regional Geological Survey of Sichuan Bureau of Geology, Nanjing Institute of Geology and Palaeontology, and Academia Sinica (eds.), People's Publishing House of Sichuan, Chengdu, Pp. 25-150 (in Chinese).

Zhang, Z. T., Sun, Y. D., Wignall, P. B., Fu, J. L., Li, H. X., Wang, M. Y., Lai, X. L., 2018. Conodont size reduction and diversity losses during the Carnian (Late Triassic) Humid Episode in SW China. J. Geol. Soc. Lond, in press.

Zonneveld, J.P., Beatty, T.W., Williford, K.H., Orchard, M.J., McRoberts, C.A., 2010. Stratigraphy and sedimentology of the lower Black Bear Ridge section, British Columbia: candidate for the base-Norian GSSP. Stratigraphy, 7, 61–82.

Zou, X., Balini, M., Jiang, D. Y., Tintori, A., Sun Z. Y. And Sun Y. L., 2015. Ammonoids from the Zhugampo Member of the Falang Formation at Nimaigu and their relevance for dating the Xingyi fossil-lagerstatte (late Ladinian, Guizhou, China). Riv. Ital. Paleontol. Stratigr., 121,135-161